13th Spanish Conference on Electron Devices
Sevilla, Spain, 9-11 June 2021

CDE 2021

Sevilla

PROGRAM AND ABSTRACTS

http://www.cde-conf.org

AICIA

IEEE Electron Devices Society | IEEE

INDEX OF CONTENTS

ORGANIZING AND SCIENTIFIC COMMITTEES

Local organizing committee (University of Seville)

- José M. Quero
- Antonio Luque
- Carmen Aracil
- Francisco Perdigones
- Juan García
- Andrea Esteban

Scientific committee

• Montserrat Nafría (Chair)	Universidad Autónoma de Barcelona
• Ramón Alcubilla	Universidad Politécnica de Cataluña
• Carlos Algora	Universidad Politécnica de Madrid
• Angel Luis Álvarez-Castillo	Universidad Rey Juan Carlos
• Xavier Aymerich	Universidad Autónoma de Barcelona
• Joan Bausells	IMB-CNM-CSIC
• Alejandro Braña	Universidad Autónoma de Madrid
• Fernando Calle	Universidad Politécnica de Madrid
• Francesca Campabadal	CSIC
• Carles Cané	IMB-CNM-CSIC
• Helena Castán	Universidad de Valladolid
• Enrique Castaño	CEIT
• Carmen Coya	Universidad Rey Juan Carlos
• Salvador Dueñas	Universidad de Valladolid
• Eduardo Fernández	Universidad de Jaén
• Beatriz Galiana	Universidad Carlos III de Madrid
• Francisco Gámiz	Universidad de Granada
• Antonio García-Loureiro	Universidad de Santiago de Compostela
• Benito González	Universidad de Las Palmas de Gran Canaria
• Tomás González	Universidad de Salamanca
• Carmen Horrillo	ITEFI-CSIC
• J.A. López Villanueva	Universidad de Granada

• Lluis Marsal	Universitat Rovira i Virgili
• Ignacio Mártil	Universidad Complutense de Madrid
• Enrique Maset	Universidad de Valencia
• Rodrigo Picos	Universidad de las Islas Baleares
• José Manuel Quero	Universidad de Sevilla
• José Ramón Ramos	Universidad de Málaga
• Cándid Reig	Universidad de Valencia
• Albert Romano	Universidad de Barcelona

GENERAL INFORMATION

About CDE 2021

For more than 20 years the Spanish Conference on Electron Devices (CDE) has served as the main venue for the presentation and discussion of current and emerging electron devices and technologies developed by Spanish research groups. In 2021, CDE will be held in Seville, from 9 to 11 June, following the successful events in Salamanca (2018), Barcelona (2017), Aranjuez (2015), Valladolid (2013), Palma de Mallorca (2011), Santiago de Compostela (2009), El Escorial (2007), Tarragona (2005), Calella de la Costa (2003), Granada (2001), Madrid (1999) and Barcelona (1997).

The 13th edition of the CDE will be held online to ensure all security measures. The safety and well-being of our participants are our priorities.

Conference topics

The aim of the conference is to review the advances in the field of electronic devices, according to the following topics:

HORIZONTAL TOPICS (TECHNIQUES AND PROCESSES)

H1. Materials and processing technology

Manufacturing techniques for bulk or 2D layered materials (LPE, MBE, MOVPE, CVD, ALD …). Development of semiconductor materials: carbon-based materials: graphene, CNT, fibers… New organic semiconductors. Technological processes and their simulation: bulk substrates treatment, photolitography, e-beam lithography, etching, FIB, diffusion, ion implantation, insulator and metal deposition, ohmic contacts, etc. Ink-jet, 3D and other new printing techniques for electronic devices.

H2. Device modelling and simulation

Statistical, numerical or analytical models for electronic, optical or physical device aspects. Physical and circuital device models and their interconnection.

H3. Characterization and reliability

Physical and chemical characterization of electronic materials: SIMS, XPS, photoluminescence, Hall Effect, XRD, SEM, TEM, STM, AFM, AES, RBS, etc. Electrical and optical device characterization: quantum efficiency, I-V, C-V, impedance, TLM, etc. Device reliability, fault analysis, electromigration, real time and fast degradation experiments, etc.

VERTICAL TOPICS (DEVICE TYPES)

V1. Sensors, actuators and micro/nano systems

Structures and their integration into devices for sensors, actuators and micro/nanosystems, MEMS/NEMS. It includes sensors for physical, chemical, gas, electrochemical, mass … detection. Integrated sensors. Hybrid integration with optical components. Energy harvesting. Electronic noses.

V2. Photovoltaic and optoelectronic/photonics devices and displays

Single crystal technologies (Si, III-V), thin film technologies (chalcogenides, a-Si, perovskites…), organic PV, third generation based concepts. Optoelectronic devices: LEDs, lasers, optical modulators, photodiodes, CMOS or CCD array detectors. Photonic Crystals structures. Displays: TFT, LCD, OLEDs…

V3. Biomedical devices and Lab-on-Chip

Sensors for biomedical detection. SPR. DNA chips. Micro-optofluidics. Micro- and nano separation technologies. Micro- and nano total analysis systems (uTAS, nTAS). Biological fuel-cells. Implantable medical devices and drug delivery devices. Medical diagnostic microsystem. Bioelectronics applications.

V4. New device concepts: quantum devices, nano-devices, RF, microwave and power devices

New functional devices based in nanostructures: nanotubes, nanowires, quantum dots, graphene, etc. Magnetic, nano-photonic, spintronic, and molecular devices. Memristive switching devices. Devices for micro-energy harvesting. Terahertz operating devices. Discrete and integrated devices for high power/voltage/current operation, including FETs, HBTs for high power, RF, microwave and integrated switches, capacitors, inductors, and components for batteries.

PRESENTATIONS

All accepted contributions included in the program are expected to be presented by one of their authors during the conference. Two types of presentations will be scheduled: oral and poster sessions

Two online conferencing platforms, WebEx and SpatialChat, will be used during CDE 2021. Connection links will be sent by email to all the registered attendees in the days prior to the start of the conference. In addition, on Tuesday 8 June from 16:00 to 20:00h CEST, attendees will have the possibility of testing the platforms during a session with staff.

Oral sessions

Oral presentations will last 12 minutes plus 3 for questions and will be made via WebEx.

Poster sessions

Poster sessions will be held in Spatial Chat.

AWARDS

Two types of prizes will be awarded during the conference: Best papers, and PhD competition.

Best papers awards

The best presentations at each session (oral and poster) will be awarded. The winners will be announced during the closing ceremony and a prize will be handed out to them.

Thanks to our partner Sensors, an open access journal from MDPI, for collaborating in this award.

PhD competition

The conference will also host the PhD Research Competition, sponsored by the IEEE CEDA Spain Chapter. PhD students will present briefly their PhD research advances in a short talk, and the best one as selected by a jury will receive an award valued in 150 euro.

Competition rules:

- Maximum length for the presentation: 5 minutes.
- Participants will be allowed to share their screen with slides or videos.
- Only the first 15 participants to register will be included.
- Presentations will take place on Thursday 10 June at 17:00 CEST.
- Proof of enrollment on a PhD program will be requested.
- Register until 31 May.

INVITED TALKS

Heike Riel *IBM Research Europe, Zurich*

9:00-9:45 Wednesday 9

Towards Next Generation of Computing - Nano-Devices on Silicon

Semiconductor nanodevices are at the core of almost all technologies we use from computing, to appliances, to communication devices, automotive, and critical infrastructure. The quest for increased chip performance and energy efficiency continues to rise whereas dimensional scaling is coming to an end. In this presentation I will give an overview of our research in the area of new materials and devices integrated on the silicon platform for next generation computing systems as well as hardware for artificial intelligence and quantum computing.

Yiran Chen *Duke University, U.S.A.*

15:00-15:45 Thursday 10

Hardware/Software Co-design for AI Systems

The rapid growth of modern neural network (NN) models' scale generates ever-increasing demands for high computing power of artificial intelligence (AI) systems. Many specialized computing devices have been also deployed in the AI systems, forming a truly application-driven heterogenous computing platform. In this talk, we discuss the importance of hardware/software co-design in AI system designs. We first use resistive memory based NN accelerators to illustrate the design philosophy of AI computing systems, and then present several hardware friendly NN model compression and optimization techniques.

Manuel Dominguez-Pumar *Universitat Politècnica de Catalunya, Spain*

9:00-9:45 Friday 11

Mars 2020: the third NASA mission with Spanish wind sensing technology in Mars

Wind sensing instrumentation with Spanish technology has reached Mars in three NASA missions: Mars Science Laboratory (the REMS instrument in the Curiosity rover), InSight (TWINS instrument) and Mars 2020 (MEDA instrument in the Perseverance rover). The talk will describe the sensors and how they are operated in the challenging Martian environment. It will also describe new instrumentation available for future missions.

PANEL DISCUSSION

Spin-Off: From research to society

15:00-16:30 Wednesday 9

Four Spin-Offs from the sector will participate in the panel discussion: A4CELL, Energiot Devices, VLC Photonics, Solar MEMS Technologies and the Spanish state agency CDTI. During this session, various topics will be discussed and questions will be put to the guests.

A4CELL *Elena Rivas Pérez*

A4CELL develops New technology named SPAchip (Suspended Planar-Array Chips) offering a perfect way to monitorize single cell alive. SPAchips are intracellular silicom microchips for monitoring extraordinarily small volumes as a single cell.

Energiot Devices *Gonzalo Murillo*

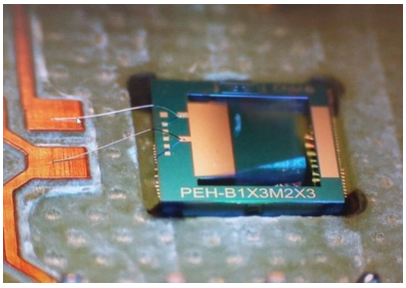

Energiot develops microgenerators to harvest ambient energy for smart wireless sensors, making possible a self-powered Internet of Things (IoT). Energiot is now focused on 24/7 end-to-end monitoring of overhead electric lines to create a smarter grid. They can also create customized monitoring solutions to enable predictive maintenance for applications in other utility services such as water and gas distribution.

VLC Photonics *Íñigo Artundo*

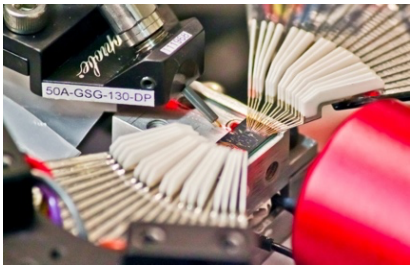

While VLC Photonics was born as a design house for photonic integrated circuits, it has evolved along the years to respond to the market needs. Currently, it provides all kinds of services spanning the whole photonic integration process, from initial evaluation to design, manufacturing, test, and packaging.

Solar MEMS Technologies *José Miguel Moreno López*

Solar MEMS is a Spanish technological-based company, specialized in Micro Electro Mechanical Systems technology (MEMS) and its application to the design and development of high accurate sun sensors for space and other high technology markets.

CDTI *Andrés Ubierna*

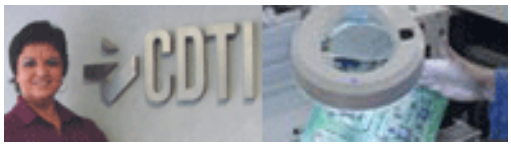

The Centre for the Development of Industrial Technology (CDTI) is a Public Business Entity, answering to the Ministry of Science and Innovation, which fosters the technological development and innovation of Spanish companies. It is the entity that channels the funding and support applications for national and international R&D&i projects of Spanish companies.

SPONSORS AND ACKNOWLEDGEMENTS

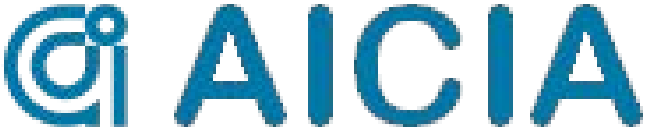

Co-sponsored by AICIA (Asociación de Investigación y Cooperación Industrial de Andalucía)

Technically co-sponsored by IEEE Electron Devices Society Spain Chapter

PARTNERS

Final Program

8 June 2021, Tuesday

10:00-12:30 ***PLATFORMS TESTING***

12:30-14:00 ***MINI-COLLOQUIUM***

12:30-13:15
M. Lanza.
KAUST, Saudi Arabia.
Hexagonal boron nitride based electronic devices and circuits: status and prospects

13:15-14:00
E. Simoen.
IMEC, Leuven, Belgium.
Low-frequency noise in advanced CMOS devices

14:00-15:30 ***Break***

15:30-18:00 ***MINI-COLLOQUIUM***

15:30-15:50
L. F. Marsal.
URV, Spain.
Polymer Solar Cells: Advances and Challenges

15:50-16:10
E. Miranda.
UAB, Spain.
The memdiode model for RRAM devices and its application to neuromorphic computing

16:10-16:30
B. Iñiguez.
URV, Spain.
Compact Modeling of Organic and Amorphous Oxide Thin Film Transistors (TFTs) from 150K to 350K

16:30-17:15
I. Kymissis.
Columbia University, NY, USA.
Electronics on anything: How Thin Film Electronics can Instrument the World

17:15-18:00
H. de los Santos.
NanoMEMS Research, Irvine CA, USA.
Theory of Nano-Electron-Fluidic Logic (NFL): A New Digital “Electronics” Concept

9 June 2021, Wednesday

Session We I: Materials: Processing and characterization

Chairperson Oral Session: Á. L. Álvarez-Castillo (Universidad Rey Juan Carlos)
Chairperson Poster Session: F. Campabadal (CSIC)

8:45-9:00 ***OPENING***

Chairperson: M. Nafría (UAB)

9:00-9:45 ***INVITED TALK***

H. Riel.
IBM Research Europe, Zurich.
Towards Next Generation of Computing - Nano-Devices on Silicon

9:45-11:00 ***ORAL SESSION I (Materials: Processing and characterization)***

ID-60 **9:45-10:00**
D. Caudevilla[1], Y. Berencén[2], S. Algaidy[1], F. Zenteno[1], J. Olea[1], E. San Andrés[1], R. García-Hernansanz[1], A. del Prado[1], D. Pastor[1] and E. García-Hemme[1].
[1]Universidad Complutense de Madrid, Spain, [2]HZDR, Dresden, Germany.
Overcoming the solid solubility limit of Te in Ge by ion implantation and pulsed laser melting recrystallization

ID-24 **10:00-10:15**
F. Jiménez[1], H. García[2], M. B. González[3], S. Dueñas[2], H. Castán[2], E. Miranda[4], F. Campabadal[3] and J. B. Roldán[1].
[1]Universidad de Granada, Spain, [2]Universidad de Valladolid, Spain, [3]IMB-CNM (CSIC), Barcelona, Spain, [4]Universitat Autònoma de Barcelona, Spain.
Fabrication, characterization and modeling of TiN/Ti/HfO2/W memristors: programming based on an external capacitor discharge

ID-78 **10:15-10:30**
J. Martín[1], G. Pedreira[1], P. Saraza[2], J. Díaz[3], R. Castro-López[4], R. Rodriguez[1], E. Roca[2], X. Aymerich[1], F. Vidal[2] and M. Navafría[1].
[1]Universitat Autònoma de Barcelona, Spain, [2]IMSE-CNM, Sevilla, Spain, [3]IMEC, Belgium, [4]Nil.
A complete smart approach for the RTN characterization and modelling of scaled MOSFETs

ID-89 **10:30-10:45** (ID:89)
A. L. Álvarez[1], F. Borrás[1], S. J. Quesada[1], A. López[1], A. de Andrés[2] and C. Coya[1].
[1]Universidad Rey Juan Carlos, Madrid, Spain, [2]ICMM, Madrid, Spain.
Massive covalent functionalization of graphene by local electric-fields: a path for multianalyte biosensors

ID-20 **10:45-11:00** (ID:20)
M. Bargalló[1], M. Zabala[1], K. Kalam[2], A. Tamm[2], F. Jiménez[3], J. B. Roldán[3] and F. Campabadal[1].
[1]IMB-CNM (CSIC), Barcelona, Spain, [2]University of Tartu, Estonia, [3]Universidad de Granada, Spain.
Analysis of the Characteristic Current Fluctuations in the High Resistance State of HfO2-based Memristors

11:00-11:30 ***Meet with friends***

11:30-13:15 POSTER SESSION I (Materials: Processing and characterization)

H1. MATERIALS AND PROCESSING TECHNOLOGY

ID-12 G. López-Rodríguez[1], G. Masmitjà[1], I. Martín[1], J. M. Moreno[2], M. Rodríguez[2], J. M. Quero[3], J. García[3] and P. R. Ortega[1].
[1]Universitat Politècnica de Catalunya, Barcelona, Spain, [2]Solar MEMS Technologies S.L., Sevilla, Spain, [3]Universidad de Sevilla, Spain.
Base and work vacuum pressure influence during sputtering of Al films for sun sensor applications

ID-14 A. Torrens, G. Masmitjà, R. E. Almache, B. Pusay, E. Ros, G. López-Rodriguez, I. Martín, C. Voz, J. Puigdollers and P. R. Ortega.
Universitat Politècnica de Catalunya, Barcelona, Spain.
Atomic layer deposition of SnO2 films for c-Si solar cells

ID-15 E. San Andrés[1], R. García[1], E. García[1], R. Barrio[2], I. Torres[2], D. Caudevilla[1], D. Pastor[1], J. Olea[1], A. del Prado[1], S. M. Algaidy[1] and F. Pérez[1].
[1]Universidad Complutense de Madrid, Spain, [2]CIEMAT, Madrid, Spain.
High Pressure Sputtering of materials for selective contacts in emerging photovoltaic cells

ID-56 R. Barrio.
CIEMAT, Madrid, Spain.
Light-trapping improvement of limited-quality silicon wafers for silicon heterojunction solar cell applications

ID-73 S. Sánchez.
Ceit, Donostia-San Sebastián, Spain.
Nanosecond laser assisted chemical vapor deposition process for the growth of ZnO thin films

ID-80 K. B. Saddik[1], J. Grandal[2], B. J. García[1] and S. Fernández-Garrido[3].
[1]Universidad Autónoma de Madrid, Spain, [2]Instituto de Sistemas Optoelectrónicos y Microtecnología, Universidad Politécnica de Madrid, Spain, [3]Dpto. Física Aplicada, Universidad Autónoma de Madrid, Spain.
Chemical beam epitaxy of GaP1-xNx for the integration of III-V solar cells and light-emitting devices on Si(001)

H3. CHARACTERIZATION AND RELIABILITY

ID-18 A. Pacheco[1] and D. Jiménez[2].
[1]Dpto. Ingeniería Electrónica., Universitat Autònoma de Barcelona, Spain, [2]Universitat Autònoma de Barcelona, Spain.
A contact resistance extraction method of 2D-FET technologies without test structures

ID-29 M. Maestro-Izquierdo[1], M. B. González[1], P. Martín-Holgado[2], Y. Morilla[2], and F. Campabadal[1].
[1]IMB-CNM (CSIC), Spain, [2]CNA, Sevilla, Spain.
Gamma Radiation Effects on HfO2-based RRAM Devices

ID-32 V. M. Orejuela.
IES, Universidad Politécnica de Madrid, Spain.
Advances in the development of high efficiency III-V multijunction solar cells on Ge|Si virtual substrates

ID-43 S. Fernández-Garrido[1], C. Pisador[1], J. Lähnemann[2], S. Lazic[3], A. Ruiz[4] and A. Redondo-Cubero[1].
[1]Dpto. Física Aplicada, Universidad Autónoma de Madrid, Spain, [2]Paul-Drude-Institut für Festkörperelektronik, Berlin, Germany, [3]Dpto. de Física de Materiales, Universidad Autónoma de Madrid, Spain, [4]Instituto de Ciencia de Materiales de Madrid, CSIC, Spain.
Coalescence, crystallographic orientation and luminescence of ZnO nanowires grown on Si(001) by chemical vapour transport

ID-45 A. Ruiz[1], N. Seoane[2], S. Claramunt[1], A. J. García-Loureiro[2], M. Porti[1] and M. Nafría[1].
[1]Universitat Autònoma de Barcelona, Spain, [2]Universidad de Santiago de Compostela, Spain.
Analysis of metal gate workfunction fluctuations on MOSFETs variability using KPFM characterization and device simulation tools

ID-51 K. B. Saddik[1], J. Lähnemann[2], M. Pérez[1], M. A. Pampillón[1], J. Grandal[3], B. J. García[1] and S. Fernández-Garrido[4].
[1]Universidad Autónoma de Madrid, Spain, [2]Paul-Drude-Institut für Festkörperelektronik, Berlin, Germany, [3]Intituto de Sistemas Optoelectrónicos y Microtecnología, Universidad Politécnica de Madrid, Spain, [4]Dpto. Física Aplicada, Universidad Autónoma de Madrid, Spain.
Luminescence of GaP1-xNx grown by chemical beam epitaxy: correlation with growth conditions

ID-91 L. Martínez-Herraiz, E. Ruiz, A. F. Braña y J.L. Plaza.
LCC, Madrid, Spain.
Effects of Surface Treatments on the Performance of CdZnTeSe Radiation Detectors

15:00-16:30 ***PANEL DISCUSSION (Spin Off: From research to society)***

16:30-17:00 ***Meet with friends***

17:00-18:30 ***SOCIAL EVENT***

10 June 2021, Thursday

Session Th II: Photovoltaic, optoelectronic and photonic devices

Chairperson Oral Session: J. R. Ramos-Barrado (Universidad de Málaga)

Chairperson Poster Session: J. Pallares (Universitat Rovira i Virgili)

9:00-10:15 ***ORAL SESSION II (Photovoltaic, optoelectronic and photonic devices)***

ID-9 **9:00-9:15**

A. J. García-Loureiro[1], E. Fernández[2], N. Seoane[1], P. Rodrigo[2], E. Comesaña[1] and F. Almonacid[2].

[1]Universidad de Santiago de Compostela, Spain, [2]Universidad de Jaén, Spain.

High-efficiency intrinsic-Vertical-Tunnel-Junction multi-band-gap concentrator solar cells up to 15,000 suns

ID-16 **9:15-9:30**

L. F. Marsal, J. Pallares and E. Moustafa.

Universitat Rovira i Virgili, Tarragona, Spain.

Influence of Spray Pyrolysis Deposition Technique on the Performance and stability of Polymer Solar Cells

ID-27 **9:30-9:45**

E. Navarrete-Astorga[1], J. Rodríguez-Moreno[1], M. C. López-Escalante[1], J. J. Peinado[1], F. Martín[1], E. Dalchiele[2] and J. R. Ramos-Barrado[1].

[1]Universidad de Málaga, Spain, [2]Instituto de Física, Facultad de Ingeniería de Montevideo, Uruguay.

Flexible and transparent supercapacitors based on ZnO nanowires

ID-46 **9:45-10:00**

C. Coya[1], C. D. Redondo-Obispo[1], T. Ripolles[1], E. Climent-Pascual[2], A. de Andrés[3] and A. L. Álvarez[1].

[1]Universidad Rey Juan Carlos, Madrid, Spain, [2]Universidad Politécnica de Madrid, Spain, [3]ICMM, Madrid, Spain.

Influence of graphene on hybrid perovskites-based solar cells performance

ID-63 **10:00-10:15**

D. Sánchez[1], J. D. López[1], M. Delgado[2], R. Altuna[1], C. Vázquez[1], A. Fresno[1], P. Contreras[1], R. Rodríguez[1], A. Nuñez[1], I. Rey-Stolle[2], M. Gabás[2], M. Honojosa[2], C. Algora[2], I. García[2], X. Barrero[1], I. Lombardero[2], L. Cifuentes[2] and J. Bautista[2].

[1]Universidad Carlos III de Madrid, Spain, [2]Instituto de Energía Solar, Universidad Politécnica de Madrid, Spain.

Optimized Power-over-Fiber System to Remotely Feed Smart Nodes for Low-Power Consumption Applications

10:15-11:30 ***POSTER SESSION II (Photovoltaic, optoelectronic and photonic devices)***

V2. PHOTOVOLTAIC AND OPTOELECTRONIC/PHOTONICS DEVICES AND DISPLAYS

ID-8 C. Outes[1], E. Fernández[1], N. Seoane[2], F. Almonacid[1] and A. J. García-Loureiro[2].

[1]Universidad de Jaén, Spain, [2]Universidad de Santiago de Compostela, Spain.

Study of Recombination Effects in a Vertical-Tunnel-Junction GaAs Solar Cell

ID-11 A. A. A. Torimtubun, J. Pallares and L. F. Marsal.

Universitat Rovira i Virgili, Tarragona, Spain.

Effect of Thermal Annealing on the Performance of PTB7-Th:PC70BM-Based Ternary Organic Solar Cells

ID-13 J. Olea, S. Algaidy, D. Caudevilla, E. García-Hemme, A. del Prado, D. Pastor, R. García-Hernansanz, F. Zenteno, E. San-Andrés, G. González-Díaz, I. Mártil, D. Montero, P. Gomez, J. Gonzalo, and J. Siegel.
Universidad Complutense de Madrid, Spain.
Advances on GaP:Ti material and solar cells

ID-30 M. Fisse[1], L. López[1], L. Yedra[1], F. Peiró[1], S. Estradé[1], S. Paetel[2], R. Fonoll-Rubio[3], M. Guc[3] and V. Izquierdo-Roca[3].
[1]Universitat de Barcelona, Spain, [2]Zentrum für Sonnenenergie und Wasserstoff-Forschung, Stuttgart, Germany, [3]Institut de Recerca en Energia de Catalunya, Barcelona, Spain.
Characterization of thin CIGS solar cells by electron microscopy techniques

ID-38 G. López-Rodríguez, E. Ros, P. R. Ortega, C. Voz, J. Puigdollers and I. Martín.
Universitat Politècnica de Catalunya, Barcelona, Spain.
Thin c-Si Solar Cells Based on VOx Heterojunctions

ID-47 S. Algaidy[1], J. Olea[1], D. Caudevilla[1], E. García-Hemme[1], A. del Prado[1], D. Pastor[1], D. Montero[1], R. García-Hernansanz[1], E. San Andrés[1], G. González-Díaz[1], I. Mártil[1], J. Siegel[2], J. Gonzalo[2], M. Wang[3] and Y. Berencén[3].
[1]Universidad Complutense de Madrid, Spain, [2]IO-CSIC, Madrid, Spain, [3]Helmholtz-Zentrum Dresden-Rossendorf, Dresden, Germany.
Recrystallization of GaAs supersaturated with Ti

ID-52 L. K. Acosta, J. Ferre-Borrull and L. F. Marsal.
Universitat Rovira i Virgili, Tarragona, Spain.
Progress in Engineering Photonic Structures based on Nanoporous Anodic Alumina

ID-55 I. Torres.
CIEMAT, Madrid, Spain.
Silicon heterojunction solar cells with Graphene-modified front transparent conductive electrodes

ID-57 R. Barrio.
CIEMAT, Madrid, Spain.
Laser Fired Contacts in multicrytalline silicon solar cells

ID-61 L. F. Marsal[1] and J. G. Sánchez[2].
[1]Universitat Rovira i Virgili, Tarragona, Spain, [2]ICIQ, Tarragona, Spain.
Bulk-Heterojunction Organic Solar Cells Towards 20% of Power Conversion Efficiency

ID-64 E. García, D. Caudevilla, S. M. Algaidy, F. Pérez, R. García, J. Olea, D. Pastor, A. del Prado, E. San Andrés, I. Mártil and G. González.
Universidad Complutense de Madrid, Spain.
Unveiling the optoelectronic mechanisms ruling Ti hyperdoped Si photodiodes

ID-66 E. López-Aymerich.
Universitat de Barcelona, Spain.
Simulations and nanofabrication of photonic crystals based on silicon pillars for mechanical biosensors

ID-74 S. González-Torres.
Universitat de Barcelona, Spain.
Inkjet-printed ZnO and NiOx: layer and device characterization for optoelectronics

ID-81 R. Izquierdo-López, J. Pedrós, R. Fandan, A. Boscá and F. Calle.
Instituto de Sistemas Optoelectrónicos y Microtecnología, Dpto. de Ingeniería Electrónica, Universidad Politécnica de Madrid, Spain.
SAW-driven plasmons in graphene heterostructures for fingerprinting ultrathin polymer layers

ID-87 B. Galiana[1], R. de la Cruz[1], M. Modesto[1], C. Kanvinda-Malu[2], S. Athanasopoulos[1], E. Salas[1], E. García-Tabarés[1], B. García[1] and J. E. Muños[1].
[1]Universidad Carlos III de Madrid, Spain, [2]Universidad Rey Juan Carlos, Madrid, Spain.
Improvement of III-V solar cells by using oxides doped with rare earths

V1. SENSORS, ACTUATORS AND MICRO/NANO SYSTEMS

ID-25 C. Reig[1], F. Pardo[1], J. A. Boluda[1], F. Vegara[1], M. D. Cubells[1], J. Sanchis[1], S. Abrunhosa[2] and S. Cardoso[2].
[1]Universidad de Valencia, Spain, [2]INESC-Microsystems and Nanotechnologies, Lisbon, Portugal.
Advanced Giant Magnetoresistance (GMR) sensors for Selective-Change Driven (SCD) circuits

11:30-12:00 Meet with friends

Session Th III: Device modelling, simulation and beyond

Chairperson Oral Session: A. García-Loureiro (Universidad de Santiago de Compostela)

Chairperson Poster Session: S. Dueñas (Universidad de Valladolid)

12:00-13:15 POSTER SESSION III (Device modelling, simulation and beyond)

H2. DEVICE MODELLING AND SIMULATION

ID-3 A. E. Atamuratov[1], B. O. Jabbarova[1], M. M. Khalilloev[1], A. Yusupov[2] and A. G. J. Loureiro[3].
[1]Urgench State University, Uzbekistan, [2]Tashkent University of Information Technologies, Uzbekistan, [3]Universidad de Santiago de Compostela, Spain.
Self-heating effect in nanoscale SOI Junctionless FinFET with different geometries

ID-7 A. J. Pérez-Ávila[1], E. Pérez[2], J. B. Roldán[1] and C. Wenger[2] and F. Jiménez[1].
[1]Universidad de Granada, Spain, [2]IHP.
Multilevel memristor based matrix-vector multiplication: influence of the discretization method

ID-19 F. Pasadas[1], T. Grour[2], A. Medina-Rull[3], M. Najari[4], E. G. Marin[3], A. Toral-López[3], M. C. Pardo[3], F. J. G. Ruiz[3], A. Godoy[3], L. Elmir[2] and D. Jiménez[1].
[1]Universitat Autònoma de Barcelona, Spain, [2]GEEE, [3]Universidad de Granada, Spain, [4]Jazan University, Saudi Arabia.
Modeling of ion-sensitive FETs based on 2D-TMDs

ID-31 A. Valera.
Universidad de Jaén, Spain.
Modelling and potential of hybrid micro-scaling MJ solar cell and thermoelectric generator

ID-37 C. Santa Cruz[1], G. Vinuesa[1], O. G. Osorio[1], H. García[1], B. Sahelices[1], H. Castán[1], S. Dueñas[1], J. Jiménez[1], M. Bargalló[2] and F. Campabadal[2].
[1]Universidad de Valladolid, Spain, [2]IMB-CNM (CSIC), Barcelona, Spain.
Semiempirical Memdiode Model for Resistive Switching Devices in Dynamic Regimes

ID-40 N. Mavredakis[1], A. Pacheco[2], P. C. Feijoo[1] and D. Jiménez[1].
[1]Universitat Autònoma de Barcelona, Spain, [2]Dpto. Ingeniería Electrónica, Universitat Autònoma de Barcelona, Spain.
Analysis of traps-related effects hindering GFETs performance

ID-53 J. Cuesta-Lopez, A. Toral-Lopez, M. C. Pardo, E. G. Marin, F. G. Ruiz, F. Pasadas and A. Godoy.
Universidad de Granada, Spain.
Variability assessment of the performance of MoS2 based BioFETs

ID-65 P. C. Feijoo[1], F. Pasadas[1], A. Pacheco[2], F. Alveiro[1] and D. Jiménez[1].
[1]Universitat Autònoma de Barcelona, Spain, [2]Dpto. Ingeniería Electrónica, Universitat Autònoma de Barcelona, Spain.
Impact of Self-Heating on Small-Signal Parameters of Graphene Field-Effect Transistors over a Wide Frequency Range

ID-76 F. A. Chaves, P. C. Feijoo and D. Jiménez.
Universitat Autònoma de Barcelona, Spain.
Electrically and Chemically Doped 2D lateral pn junctions: Equilibrium and out-of-the equilibrium properties

ID-90 J. J. Santaella[1], F. M. Gómez-Campos[2], S. Rodríguez-Bolívar[2] and K. Critchley[3].
[1]VALEO, Paris, France, [2]Universidad de Granada, Spain, [3]University of Leeds, United Kingdom.
Electrical simulation of a QLED device based on quantum dots using the Transfer Hamiltonian approach

V4. NEW DEVICE CONCEPTS: QUANTUM DEVICES, NANO-DEVICES, RF, MICROWAVE AND POWER DEVICES

ID-2 G. González[1], M. Bargalló[2], F. Jiménez[1], F. Campabadal[2] and J. B. Roldán[1].
[1]Universidad de Granada, Spain, [2]IMB-CNM (CSIC), Barcelona, Spain.
RTN study of TiN/Ti/HfO2/Pt resistive switching devices based on neural network analysis

ID-10 J. G. Fernández[1], N. Seoane[1], K. Kalna[2] and A. J. García-Loureiro[1].
[1]Universidad de Santiago de Compostela, Spain, [2]Swansea University, United Kingdom.
Threshold voltage variability study in a 12 nm gate length Nanosheet FET

ID-22 M. Saludes-Tapia[1], S. Poblador[1], F. Campabadal[2], J. Suñé[1], E. Miranda[1] and M. Bargalló[2].
[1]Universitat Autònoma de Barcelona, Spain, [2]IMB-CNM (CSIC), Barcelona, Spain.
Complementary Resistive Switching in Anti-Serially Connected HfO2-based Memristors

ID-33 J. Martínez
ISOM, Universidad Politécnica de Madrid, Spain.
Towards a hybrid graphene device for Green Energy

ID-59 G. Paz[1], I. Íñiguez de la Torre[1], H. Sánchez[1], V. Hoel[2], Y. Cordier[2], T. González[1] and J. Mateos[1].
[1]Universidad de Salamanca, Spain, [2]IEMN, France.
GaN-based HEMTs operating as zero-bias microwave detectors at low temperature

ID-84 F. M. Gómez-Campos.
Universidad de Granada, Spain.
Influence of dimensionality and stoichiometry in the electronic structure of InAs quantum dot solids

15:00-15:45 INVITED TALK

Y. Chen.
Duke University, U.S.A.
Hardware/Software Co-design for AI Systems

15:45-17:00 ORAL SESSION III (Device modelling, simulation and beyond)

ID-28 **15:45-16:00**

E. Pérez-Martín[1], I. Íñiguez de la Torre[1], T. González[1], C. Gaquiere[2] and J. Mateos[1].
[1]Universidad de Salamanca, Spain, [2]IEMN, France.

Bias-dependence of surface charge at low temperature in GaN nano-diodes

ID-26 **16:00-16:15**

B. Orfao E Vale.
Universidad de Salamanca, Spain.

Technological Parameters and Edge Fringing Capacitance in GaN Schottky Barrier Diodes: Monte Carlo Simulations

ID-39 **16:15-16:30**

F. Pasadas[1], A. Pacheco[2], A. Mansouri[3], P. Kumar[4], G. Calabrese[4], K. Patel[4], A. Zurutuza[5], O. Habibpour[3], H. Zirath[3], R. Sordan[4] and D. Jiménez[1].
[1]Universitat Autònoma de Barcelona, Spain, [2]Dpto. Ingeniería Electrónica, Universitat Autònoma de Barcelona, Spain, [3]CUT, [4]POLIMI, Italy, [5]Graphenea, Gipuzkoa, Spain.

Towards the experimental demonstration of non-quasi-static effects in graphene field-effect transistors

ID-72 **16:30-16:45**

M. M. Al Chawa[1], R. Tetzlaff[2], S. Stavrinides[3], C. de Benito[4] and R. Picos[4].
[1]Technische Universität Dresden, Germany, [2]Nil, [3]International Hellenic University, Greece, [4]Universitat de les Illes Balears, Spain.

Energy Based Analysis of Reset Transition in ReRAM Memristive Devices

ID-75 **16:45-17:00**

E. Salvador[1], M.B. Gonzalez[2], F. Campabadal[2], J. Martin-Martinez[1], R. Rodriguez[1] and E. Miranda[1].
[1]Dpto. de Ingeniería Electrónica, Universitat Autònoma de Barcelona, Spain, [2]IMB-CNM (CSIC), Barcelona, Spain.

In-depth Analysis of the Statistical Distribution of RRAM Electrical Parameters Intended for Compact Modeling

11 June 2021, Friday

Session Fr IV: Sensors, actuators and biomedical devices

Chairperson Oral Session: C. Aracil (Universidad de Sevilla)

Chairperson Poster Session: C. García Núñez (University of the West of Scotland)

9:00-9:45 INVITED TALK

M. Dominguez-Pumar.
Universitat Politècnica de Catalunya, Spain.
Mars 2020: the third NASA mission with Spanish wind sensing technology in Mars

9:45-11:00 ORAL SESSION IV (Sensors, actuators and biomedical devices)

ID-62 **9:45-10:00**
M. Rovira[1], C. Fernández-Sánchez[1], S. Demuru[2], B. P. Kunnel[2], D. Briand[2] and C. Jiménez-Jorquera[1].
[1]IMB-CNM (CSIC), Barcelona, Spain, [2]EPFL, Switzerland.
Paper-based wearable patch for sweat biomonitoring

ID-50 **10:00-10:15**
M. Moreno[1], V. Parra-Monreal[2], M. Ortega-Machuca[2], J. Ramón-Azcon[2], W. Svendsen[3] and A. Romano-Rodríguez[1].
[1]Universitat de Barcelona, Spain, [2]IBEC, Barcelona, Spain, [3]Technical University of Denmark-DTU, Denmark.
Detection of cytokines in skeletal muscle tissue using optical SPR sensing platform

ID-41 **10:15-10:30**
A. Peña[1], D. Matatagui[2], C. Cruz[2], P. de la Presa[1], P. Marín[1] and C. Horrillo[2].
[1]Instituto de Magnetismo Aplicado, Madrid, [2]Instituto de Tecnologías Físicas y de la Información, CSIC, Madrid, Spain.
Study of magnetoelastic resonance for chemical sensors: Ribbons vs microwires

ID-70 **10:30-10:45**
I. Sayago[1], C. Sánchez[2], J. L. Sanjurjo[1], J. P. Santos[1], S. Ogilvie[3], H. J. Wood[3], A. Graf[3], M. Large[3], A. B. Dalton[3], R. Garriga[4] and E. Muñoz[5].
[1]ITEF-CSIC, Madrid, Spain, [2]Up Devices and Technologies, Madrid, Spain, [3]University of Sussex, United Kingdom, [4]Universidad de Zaragoza, Spain, [5]Instituto de Carboquímica ICB-CSIC, Zaragoza, Spain.
Resistive gas sensors based on MoS2 nanosheets with high response to low NO2 concentrations

ID-68 **10:45-11:00**
A. Alcacer[1], H. Ben Halima[2], A. Errachid[2] and J. Bausells[1].
[1]IMB-CNM (CSIC), Barcelona, Spain, [2]Institute of Analytical Sciences (UCBL), France.
eHealth system with ISFET-based immunosensor for heart failure biomarker detection in saliva

11:00-11:30 Meet with friends

11:30-13:15 POSTER SESSION IV (Sensors, actuators and biomedical devices)

V1. SENSORS, ACTUATORS AND MICRO/NANO SYSTEMS

ID-4 J. M. Moreno[1], M. Rodríguez[1], P. R. Ortega[2] and J. M. Quero[3].
[1]Solar MEMS Technologies S.L., Sevilla, Spain, [2]Universitat Politècnica de Catalunya, Barcelona, Spain, [3]Universidad de Sevilla, Spain.
In orbit data of miniaturized 2-axis sun sensors for attitude control applications in spacecrafts

ID-6 A. Rodríguez, D. Vega, D. Cardador and D. Segura.
Universitat Politècnica de Catalunya, Spain.
Study of the performance impact by fabrication imperfections in electrochemically etched macroporous silicon photonic crystals

ID-17 M. Tomić, I. Gràcia, E. Figueras, C. Cané and S. Vallejos.
IMB-CNM (CSIC), Barcelona, Spain.
ZnO nanorods and their modification with Au nanoparticles for UV-light activated gas sensing

ID-36 O. Ferrer.
IMB-CNM (CSIC), Barcelona, Spain.
3D Detectors for timing applications

ID-42 M. Pelayo[1], K. McAughey[2], D. Gibson[1], D. Hughes[2] and C. García[1].
[1]University of the West of Scotland, United Kingdom, [2]Novosound, Scotland, United Kingdom.
Glancing Angle Deposition of Nanostructured ZnO Thin Films for Ultrasonics

ID-44 C. Pérez-González.
Universidad de Valladolid, Spain.
Development of a potentiometric bioelectronic tongue modified with gold nanoparticles for dairy industry

ID-54 J. Gómez-Suárez, F. Meléndez, P. Arroyo, S. Rodríguez, S. Palomeque, J. I. Suárez and J. Lozano.
Universidad de Extremadura, Spain.
Detection of 2,4,6 Trichloroanisole at low concentrations by means of machine olfaction

ID-58 M. Pozo-Gómez, J. D. Aguilera-Martín, P. de la Presa, C. Cruz, P. Marín, M. C. Horrillo and D. Matatagui.
Instituto de Tecnologías Físicas y de Información, CSIC, Madrid, Spain.
Modeling and simulation of a magnonic gas sensor to detect diseases in human breath

ID-67 C. Sánchez[1], J. P. Santos[2], A. Azabal[1], S. Ruiz-Valdepeñas[1], J. Lozano[3], I. Sayago[2] and J. L. San Jurjo[2].
[1]Up Devices and Technologies, Madrid, Spain, [2]ITEF-CSIC, Madrid, Spain, [3]Universidad de Extremadura, Spain.
Automation and optimization device for the fabrication of sensors with nanomaterials

ID-71 A. Doblas.
IMB-CNM (CSIC), Barcelona, Spain.
Technology Developments on iLGAD Sensors at IMB-CNM

ID-77 D. Estrada[1], M. Dolcet[1], R. Soriano[1], J. Santander[1], M. Salleras[1], L. Fonseca[1], J. M. Sojo[2], A. Morata[2] and A. Tarancon[2].
[1]IMB-CNM (CSIC), Barcelona, Spain, [2]IREC, Ciudad Real, Spain.
Highly-packed arrangement of an all-Si based thermoelectric microgenerator

ID-82 A. Doblas.
IMB-CNM (CSIC), Barcelona, Spain.
Proton Low Gain Avalanche Detector (pLGAD) for Low Energy Particles Detection

ID-83 C. Iain Douglas, C. García Núñez, D. Gibson and M. Caffio.
University of the West of Scotland, United Kingdom.
Development of a Highly Sensitive and Flexible Graphene Foam Based Pressure Sensors

V3. BIOMEDICAL DEVICES AND LAB-ON-CHIP

ID-69 L. Lefaix[1], A. Blanquer[2], L. Bacakova[2], J. Esteve[1] and G. Murillo[1].
[1]IMB-CNM (CSIC), Barcelona, Spain, [2]Institute of Physiology of the Czech Academy of Sciences, Prague, Czech Republic.
Development of hybrid piezoelectric microdevices for bioapplications

ID-86 J. A. Fontanilla and A. Luque.
Universidad de Sevilla, Spain.
Low-cost voltage amplifier for biological signal acquisition through generic micro-electrode array

ID-88 C. Aracil, J. D. Urbano-Gámez, F. Perdigones, J. A. Fontanilla and J. M. Quero.
Universidad de Sevilla, Spain.
Towards a 3D-Printed and Autonomous Culture Platform Integrated with Commercial Microelectrode Arrays

13:15-13:30 ***CLOSING***

Chairperson: M. Nafría (UAB)

ABSTRACTS

9 June 2021

Wednesday

ORAL SESSION I

Materials: Processing and characterization

Wednesday 9

9:45-11:00

Chairperson: Á. L. Álvarez-Castillo (Universidad Rey Juan Carlos)

Overcoming the solid solubility limit of Te in Ge by ion implantation and pulsed laser melting recrystallization.

D. Caudevilla[1,*], E. García-Hemme[1], D. Pastor[1], S. Algaidy[1], J. Olea[1], E. San Andrés[1], R. García-Hernansanz[1], A. del Prado[1], G. González-Díaz[1], I. Mártil[1], F. Zenteno[1], Y. Berencén[2]

[1]Dpto. EMFTEL, Fac. CC. Físicas, Univ. Complutense de Madrid, 28040 Madrid, Spain; *danicaud@ucm.es
[2]Helmholtz-Zentrum Dresden-Rossendorf, Institute of Ion Beam Physics and Materials Research, Bautzner Landstr. 400, 01328 Dresden, Germany.

1. Introduction

Short and mid-infrared sensing based on CMOS compatible semiconductors is a technological challenge. Germanium hyperdoped with deep level donors, such as tellurium, would lead to the formation of an intermediate band within the band gap that allows Ge for sub-band gap mid-infrared photoresponse at room temperature [1]. To hyperdope Ge, a combination of non-equilibrium techniques is proposed: ion implantation followed by Pulsed Laser Melting (PLM).
To avoid implantation-induced Ge surface porosity, LN2 (77K) temperatures are typically used. In this work, we propose to use alternatively slightly higher implantation temperatures (143 K) together with an a-Si capping layer.

2. Experimental

DSP, 300 µm <100> p-Ge wafers (1 Ω·cm) were implanted with $^{130}Te^{+}$ at doses of 10^{14} cm^{-2} and 10^{16} cm^{-2} with an energy of 120 keV. To mitigate the surface implantation-induced damage produced by heavy ions at high energy, a 50-nm-thick a-Si capping layer was sputtered on top of the wafers [2] combined with ion implantation at temperatures below 143 K.
After ion implantation, the wafers were cut in 5×5 mm^2 square samples. The a-Si capping layer was selectively etched by submerging the samples in TMAH (25%) at 60ºC for 5 min. After the etching process, the samples were pulsed laser annealed with a Xe-Cl excimer laser (Coherent COMPexPRO201) at a wavelength of 308 nm, with a pulse duration of 28 ns and an energy density of 0.5 $J \cdot cm^{-2}$. All the fabrication steps were performed at Helmholtz-Zentrum Dresden-Rossendord's facilities.
The phonon spectra were determined by µ-Raman spectroscopy in the wavenumber range of 100-550 cm^{-1} using a 532-nm-Nd:YAG laser. Transmission Electron Microscopy (TEM) was performed to analyze the crystal structure, whereas Energy Dispersive X-Rays Spectroscopy (EDS) was used to characterize the material composition. We also obtained the in-depth profiles of the Te implanted samples by ToF-SIMS.

3. Results and conclusion

The tellurium in-depth profiles are shown in Fig. 1. Upon Te implantation, 72% of the implanted Te atoms were found to penetrate the Ge substrate. After etching the a-Si layer and performing PLM, Te was found to be redistributed deeper into the substrate. Nevertheless, even for the lowest dose and after PLM, we demonstrate that the Te solid solubility limit in Ge (2×10^{15} cm^{-3}, Ref. [3]) is surpassed by three orders of magnitude.
Fig. 2 shows the Raman spectra of the implanted doses before the PLM (after the a-Si capping layer etch), and after the PLM process. Even at the lowest implanted dose, the Ge substrate is amorphized. After PLM, however, the crystallinity of the samples is recovered for both implanted doses. The c-Ge vibrational mode shows a low-frequency asymmetry, which is related to a partial lack of crystallinity. The shift of the Ge-Ge peak at 300 cm^{-1} likely originates from strain, induced by the Te incorporation.
Fig. 3 and 4 show the TEM images from the two as-implanted samples with the capping layer. It is observed that the amorphous Ge:Te region becomes thicker and the interface between the a-Si capping layer and the amorphized Ge becomes more diffuse as the dose increases. Fig. 5 and 6 indicate that the crystallinity of the implanted layer is fully recovered after PLM, with no signs of extended defects. Furthermore, EDS confirms Te incorporation above the 5% into the Ge layer at the highest dose, before and after laser melting.
In this work, we demonstrated that Ge layers can be supersaturated with Te concentrations several orders of magnitude above the solid solubility limit. The resulting supersaturated Ge:Te layers are fully recrystallized without extended defects after the PLM process.

References (Times 10 bold)

[1] Gandhi, Hemi H., et al. AIP Advances 10.7 (2020).
[2] Tran, Tuan T., et al. Applied Physics Letters 109.8 (2016).
[3] Abrikosov, N. Kh. Semiconducting II–VI, IV–VI, and V–VI Compounds. Springer, 2013.

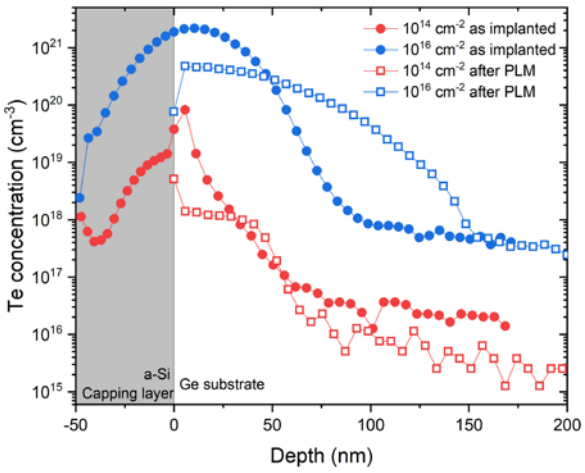

Fig.1. ToF-SIMS profiles of low- (10^{14} cm^{-2}) and high-dose (10^{16} cm^{-2}) supersaturated Ge:Te before and after PLM. The first 50 nm corresponds to the a-Si capping layer.

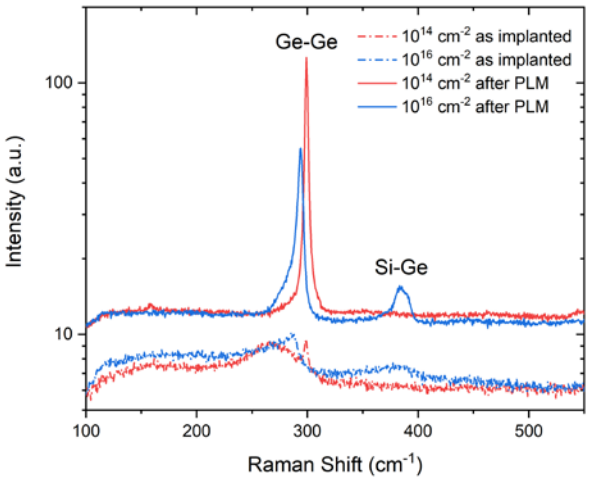

Fig.2. Raman spectra of Te-implanted Ge samples at different doses (10^{14} cm^{-2} in red and 10^{16} cm^{-2} in blue). The dashed lines correspond to the samples before PLM and the filled lines to PLM processed samples with a fluence of 0.5 J·cm^{-2}. We indicate the peaks corresponding to Ge-Ge bonding (at 300 cm^{-1}) and to Ge-Si bonding (at 380 cm^{-1}).

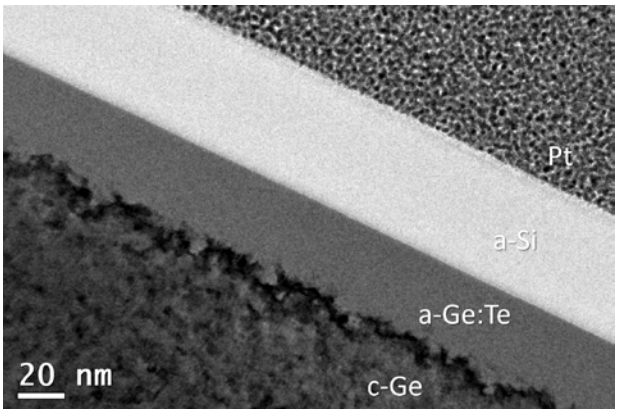

Fig.3. TEM image of a germanium substrate as implanted with Te^+ at a dose of 10^{14} cm^{-2}. From top-right to bottom-left we see the Pt from sample preparation, the a-Si capping layer, and the germanium substrate, amorphized in the first 40 nm.

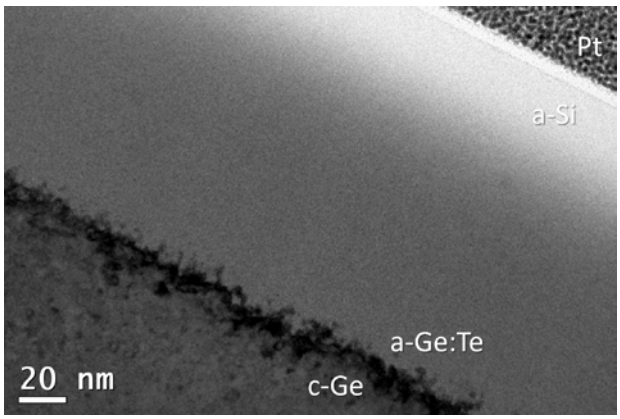

Fig.4. TEM image of a germanium substrate as implanted with Te^+ at a dose of 10^{16} cm^{-2}. From top-right we see the Pt from sample preparation and then the a-Si capping layer mixed with the amorphized Ge substrate (150 nm in total).

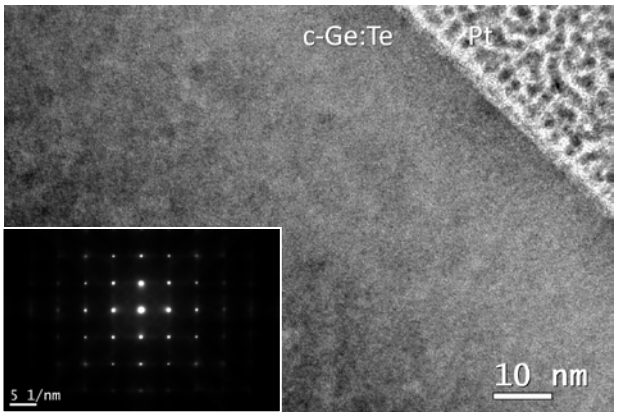

Fig.5. TEM image of the recrystallized Ge:Te implanted at a dose of 10^{14} cm^{-2}. The a-Si was removed before PLM. In the inset we can see the SAED diagram to verify the crystallinity.

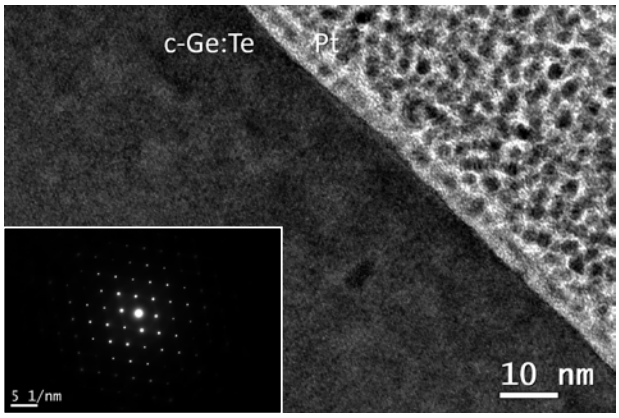

Fig.6. TEM image of the recrystallized Ge:Te implanted at a dose of 10^{16} cm^{-2}. The a-Si was removed before PLM. In the inset we can see the SAED diagram to verify the crystallinity.

Fabrication, characterization and modeling of TiN/Ti/HfO_2/W memristors: programming based on an external capacitor discharge

F. Jiménez-Molinos[1], H. García[2], M.B. González[3], S. Dueñas[2], H. Castán[2], E. Miranda[4], F. Campabadal[3], J.B. Roldán[1]

[1]Depto. Electrónica y Tecnología de Computadores. Universidad de Granada. 18071 Granada, Spain.
Email: jmolinos@ugr.es
[2]Depto. Electrónica, Universidad de Valladolid. Paseo de Belén 15, 47011 Valladolid, Spain
[3]Institut de Microelectrònica de Barcelona, IMB-CNM (CSIC), Campus UAB, 08193 Bellaterra, Spain
[4]Dept. Enginyeria Electrònica. Universitat Autònoma de Barcelona. Edifici Q. 08193 Bellaterra, Spain

1. Introduction

Memristors based on resistive switching, such as bipolar valence change memories, are key devices for the implementation of synaptic weights in neuromorphic circuits. For that task, multilevel operation is required and several programming schemes have been proposed under voltage ramps or pulsed voltage operation [1,2]. Furthermore, current pulses have also been proposed for a better control of the potentiation (set) [3]. In the latter case, hardware limitations hinder the use of short current pulses and transitions are obtained with just one applied pulse, which prevents cumulative effects linked to pulse series. To overcome this issue, in this work the control of set/reset processes by a limited amount of charge is explored. Memristors based on a TiN/Ti/HfO_2/W stack have been fabricated and characterized. The experimental data are simulated and analysed using the dynamic memdiode model.

2. Device fabrication and measurement

The devices used are TiN/Ti/HfO_2/W structures. The 10 nm-thick HfO_2 layer was grown by atomic layer deposition at 225°C using TDMAH and H_2O as precursors, and the top and bottom metal electrodes were deposited by magnetron sputtering. The bottom electrode consists of a 50 nm-W layer deposited on a 20 nm-Ti adhesion layer on a highly doped n-type silicon wafer. The top electrode is a 200 nm-TiN on a 10 nm-Ti layer acting as oxygen getter material. Electrical contact to the bottom electrode is made through the Al-metallized back of the silicon wafer. The resulting structures are square cells of 5×5 μm^2. A schematic cross-section of the active area is given in Fig. 1.

To carry out the electrical measurements, an HP 4155B semiconductor analyzer was used to measure the conductance values. As shown in Fig. 2, two relays control the capacitor charging (ϕ_1 off and ϕ_2 on) using an electrometer, and the capacitor discharge (ϕ_1 on and ϕ_2 off) through the memristor.

3. Device modelling and results

The devices have been modeled by means of the dynamic memdiode model [4]. The set of fitting parameters is the same in all the simulations performed here. Fig. 3 shows the experimental and modeled *I-V* characteristic obtained under a ramped voltage signal.

Fig. 4 shows the device final conductance (the read voltage is 0.1 V) after set programming using different capacitors previously charged with 1nC, as a function of the initial capacitor voltage. According to the device model, the current is a function of the applied voltage, V_m, and the state variable, h ($I(V_m, h)$, see Fig. 5). The trajectories on such surface, followed during the transient processes carried out for obtaining Fig. 4, are represented in Fig. 5a. Note that the transition is fast enough so that the voltage remains almost constant while the state variable h evolves; in this context, the capacitor acts also as a current limiting device. As shown in Fig. 5b, the final device state, h, does not depend on the initial one (if the latter is lower than the final value reached departing from h=0).

Reset processes have also been experimentally performed (Fig. 2) and modeled. Different capacitors were charged with 6nC and connected to the memristor afterwards. The resultant conductance at 0.1V is plotted in Fig. 6 and the simulated trajectories on the $I(V_m, h)$ surface are shown in Fig. 7.

Note that the model [4] successfully reproduces the device behavior for different operation regimes: ramped voltage excitations (Fig. 3) or transient response during the capacitor discharge process (Figs. 4 and 6).

Acknowledgements

The authors thank the support of the Spanish Ministry of Science, Innovation and Universities and the FEDER program through projects TEC2017-84321-C4-1-R, TEC2017-84321-C4-2-R, TEC2017-84321-C4-3-R, TEC2017-84321-C4-4-R.

References

[1] S. Poblador et al., Micr.Eng. vol. 187-188, p. 148, 2018.
[2] H. García et al., Micr. Eng. vol. 215, p. 110984, 2019.
[3] H. García et al., IEEE JEDS vol. 8, p. 291, 2020.
[4] E. Miranda, J. Suñé, TechRxiv preprint, 2020.

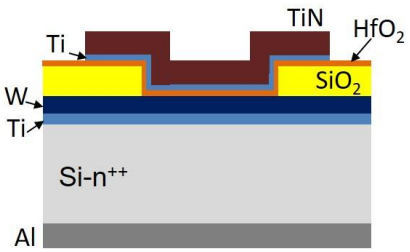

Fig.1. Device cross-section schematics.

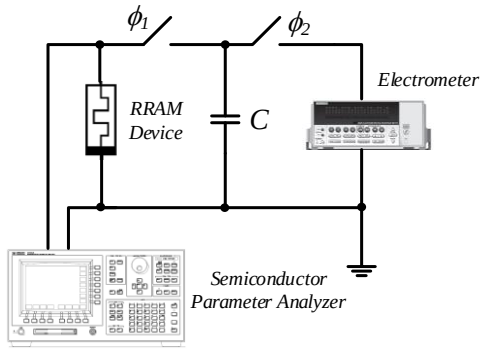

Fig.2. Measurement setup

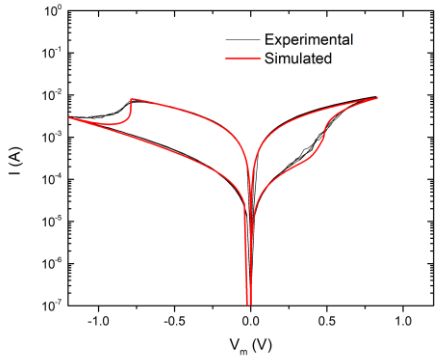

Fig.3. Experimental (black) and modeled (red) I-V curve.

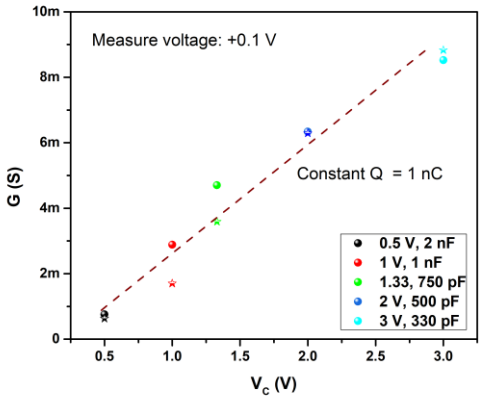

Fig.4. Resultant conductance at 0.1 V versus capacitor voltage after programming (set process). Different capacitors previously charged with 1nC where employed. Balls: experimental data; stars: simulated results. The dashed line represents the linear fitting of the experimental data.

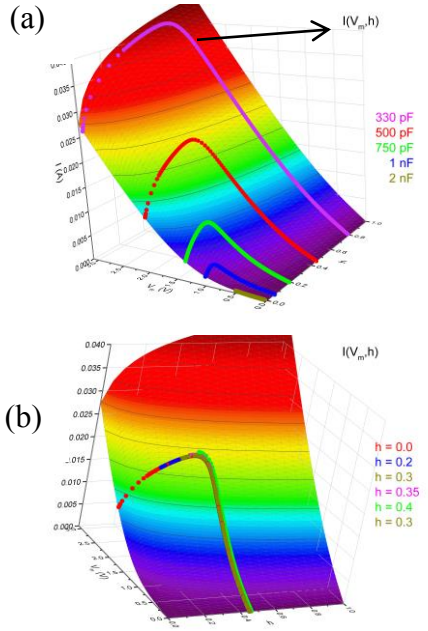

Fig.5. a) Modeled device current characteristics $I(V_m, h)$ shown in 3D surfaces. Simulated trajectories during the same programming events as those in Fig. 4 are shown. b) Simulated trajectories departing from different memristor initial states (h values) are shown (they correspond to a case of C = 500 pF).

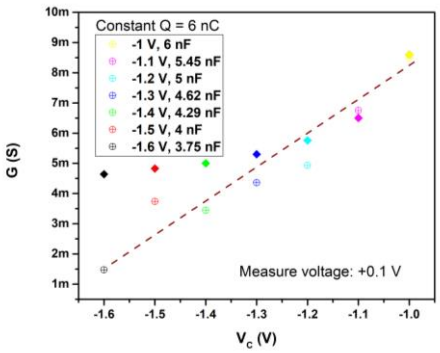

Fig.6. Conductance at 0.1 V versus capacitor voltage after a reset process for different capacitors previously charged with 6nC. Circles: experimental data; diamonds: simulated results. The dashed line represents the linear fitting of the experimental data.

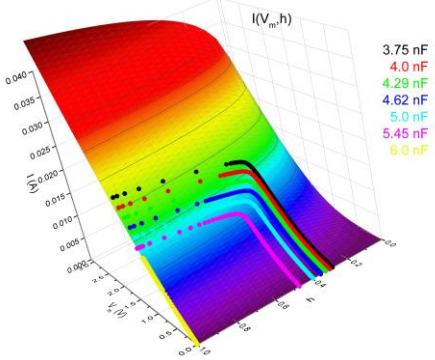

Fig.7. Simulated trajectories on the modeled $I(V_m,h)$ surface during the same reset processes as those in Fig. 6.

A complete smart approach for the RTN characterization and modelling of scaled MOSFETs

J.Martin-Martinez[1*], G. Pedreira[1], P. Saraza-Canflanca[2], J.Diaz-Fortuny[1], R. Castro[2], R. Rodriguez[1], E. Roca[2], X. Aymerich[1], F.V. Fernandez[2], M. Nafria[1].

[1]Electronic Engineering Department, Universitat Autònoma de Barcelona, 08193 Barcelona, Spain
[2]Instituto de Microelectrónica de Sevilla, IMSE-CNM, CSIC and Universidad de Sevilla, 41092 Seville, Spain
*javier.martin.martinez@uab.es

Time-Dependent Variability (TDV) has become a serious concern in advanced technology nodes due to its impact on circuit reliability. TDV includes transient effects, such as Random Telegraph Noise (RTN) [1], and aging phenomena, such as Bias Temperature Instability (BTI) and Hot-Carrier Injection (HCI) degradation [2]. Recently, it has been demonstrated that aging experiments in hundreds of devices can be parallelized, to obtain the required statistical information within a feasible experimental time [3]. This work is focused on RTN characterization, where particular challenges appear. We present here a new method that drastically reduces the testing time and also the analysis effort.

The ENDURANCE chip has been designed to perform massive time-zero and time-dependent variability characterization in a large number of devices (Fig. 1) [3]. The core of this chip is an array of transistors in which each device is connected through switches to several external lines for biasing. In this way, the devices can be either stressed, measured or switched (Fig. 2), to implement an automated Measurement-Stress-Measurement testing procedure. By correctly setting up the state of the switches, the stress phases are overlapped (Fig. 3) and consequently, the duration of the aging experiments is drastically reduced [4]. However, as shown in Fig. 3, the measurement phases never overlap, which is a drawback for the parallelization of typical RTN experiments where a continuous monitorization of the device current is needed. The result is that RTN testing time can be extremely long. However, in this paper, a new scheme for the simultaneous characterization of RTN in hundreds of devices is proposed; this scheme reduces the RTN testing time and facilitates data analysis.

RTN is observed as random and sudden changes of the transistor drain current (Fig. 4a), which have been related to the capture/emission of charges in/from the defects in the device. The new characterization scheme proposed here starts with the evaluation of $\Delta I_D = I_D(t_2) - I_D(t_1)$ for each RTN trace, where t_1 and t_2 are two instants (Fig. 4a), such that $t_2 - t_1$ is fixed to a predetermined value. The histogram in Fig. 4b shows the ΔI_D probability density function obtained from current measurements at V_{GS}=-0.6V of 784 pMOS transistors in the ENDURANCE chip, for $t_2 - t_1$ =40s. The peak around 0 is associated to the cases where either there is no active defect in the device or all the defects are at the same occupancy state at t_1 and t_2 (i.e., the same current level is measured at the two instants). The width of this peak is related to the background noise of the measurement system. The tail of the ΔI_D distribution is indicative of an I_D shift in this time interval because the defect occupancy has changed. Then, since ΔI_D is evaluated from the current at two instants, it can be easily obtained with our set up by simply applying the same voltage during the Stress and Measurement phases in our test scheme (Fig. 3), and measure the currents at two times separated by the predetermined interval ($t_2 - t_1$=40s, in this case).

The resulting data is the basis for the modelling of the RTN phenomenon. The model parameters can be extracted from the ΔI_D distributions in Fig. 4, i.e., the statistical distributions of the number of defects (N_{Def}) and the I_D shift caused by the trapping/detrapping of each defect (η). This is done following the procedure shown in the flow diagram of Fig. 5: assuming Poisson and exponential distributions for N_{Def} and η, respectively, ΔI_D distributions are generated through Monte-Carlo simulation, to determine the N_{Def} and η distributions that minimize the difference between the experimental and generated density functions (lines in Fig. 4b and 4c).

To verify the method, complete RTN traces of the same transistors have been measured (Fig. 6) and analyzed in detail (one by one) using the procedure explained in [5]. The bars in Fig 7 show the N_{Def} and η distributions obtained from this analysis, whereas the lines correspond to the distributions obtained using the new proposed scheme. The excellent agreement between both distributions indicates that the statistical distribution of N_{Def} and η can be obtained by measuring ***only two points*** of the I_D traces separated by a time interval $t_2 - t_1$ rather than the entire current trace. Consequently, RTN measurements in a set of devices can be also parallelized, with the consequent saving in testing time. As an example, in the experiment shown, it was reduced from ~9h to 118s.

In conclusion, we have demonstrated that the probability distributions of N_{Def} and η (key for RTN modelling) can be obtained by measuring the drain current only at two instants. Then, this smart analysis method, combined with the ENDURANCE chip and pipelined test scheme, provides a complete framework for the statistical characterization and analysis of the TDV mechanisms in affordable measurement times.

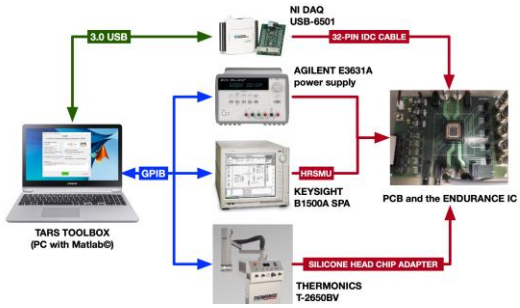

Fig.1. Experimental setup used to automate the characterization of RTN. 784 pMOS transistors with W/L=80nm/60nm from the chip ENDURANCE were measured.

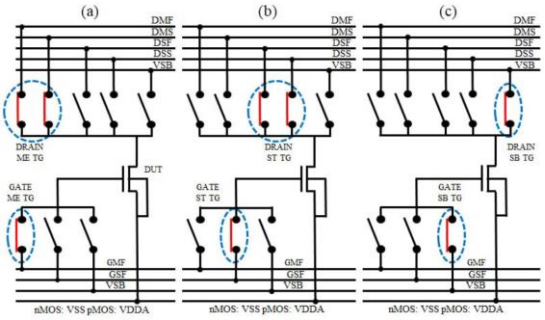

Fig.2. Schematic of the transistor connections that establish different operation modes.

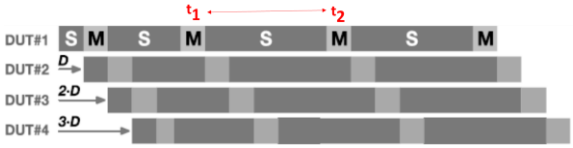

Fig. 3. Example of the stress-measurement time flow, for the case of 4 devices (*D* is a delay introduced so that the measurement phases never overlap). Our RTN characterization method is based in the I_D acquisition at two different measurement phases (M), when the stress and measurement voltages are the same. The longer the delay between the selected measurement phases, the larger the number of defects that contribute to RTN.

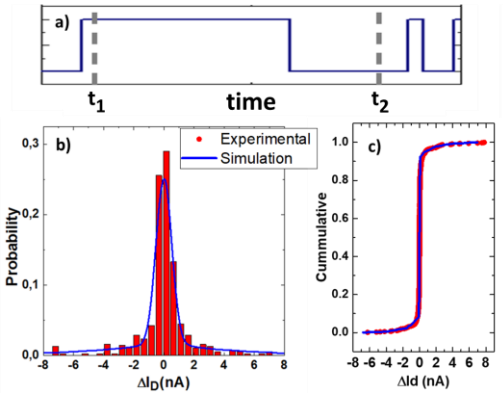

Fig. 4. a) Schematic RTN waveform, to illustrate the new method used to characterize RTN in a large number of devices. To apply this method, the current at only two instants must be measured. b) Probability and cumulative c) density functions of ΔI_D obtained when considering t_2-t_1=40s. (bars and symbols: from experimental traces. Line: obtained with our method).

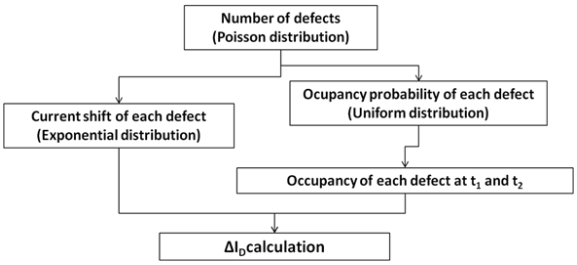

Fig. 5. Flow diagram of the procedure designed to generate one ΔI_D value.

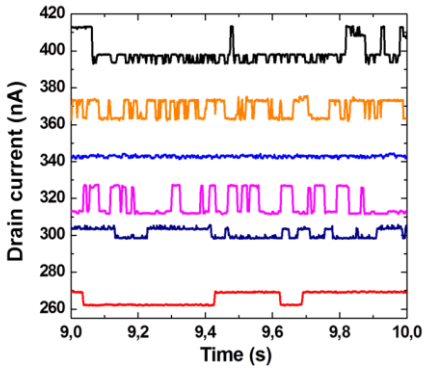

Fig.6. Some representative shots of the I_D traces (V_{GS} = 0.5V and V_{DS} = 100mV). The drain current (I_D) was registered during 40s, with a sampling time of 2ms. To better visualize the associated current levels, only 1s out of the 40s long waveforms is shown.

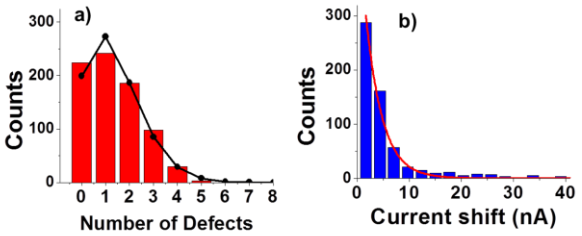

Fig. 7. N_{Def} (a) and η (b) distributions obtained from the detailed analysis of the complete set of traces (bars) [5]. Lines correspond to the Poisson and exponential distributions derived from our method.

[1] C. Liu et. al., IRPS, pp. XT.17.1-5 (2014). [2] C. Schlünder et al., IRPS, pp. 2E-4.1-8 (2017). [3] J. Diaz-Fortuny et al., IEEE JSSC, 54 (2), 476-488 (2019). [4] J. Diaz-Fortuny et al., IEEE TIM, 69 (3), 853-864 (2020). [5] J. Martin-Martinez et al., IEEE EDL, 35 (4), pp. 479-481, (2014).

This work was supported by the TEC2016-75151-C3-R and PID2019-103869RB-C3/AEI/10.13039/501100011033 projects through the Ministry of Science, Innovation and Universities (MICINN) and European Regional Development Fund (ERDF).

Massive covalent functionalization of graphene by local electric-fields: a path for multianalyte biosensors

Fernando Borrás[1], Sergio Quesada[1], A. López-García, Alicia de Andrés[2], Carmen Coya[1] Ángel Luis Álvarez[1*]

[1]Escuela Técnica Superior de Ingeniería de Telecomunicación, Universidad Rey Juan Carlos, 28933 Madrid, Spain
[2]Instituto de Ciencia de Materiales de Madrid (ICMM), Consejo Superior de Investigaciones Científicas (CSIC), Sor Juana Inés de la Cruz 3, 28049 Madrid, Spain,
*angelluis.alvarez@urjc.es

1. Abstract

Graphene is currently managed in chemical sensors mainly through 4 strategies: i) incorporation of adsorbates ii) covalent functionalization iii) electrochemical functionalization in solution, and iv) through intermediate layers of conjugated polymers that facilitate binding with substances of interest. [1]

Among those, adsorbate-adapted strategies, i.e., attached molecules without covalent bonding, is likely the most used. As a result of the charge transfer process, many adsorbed molecules have the ability of doping or changing slightly the graphene gap, and therefore, varying the optoelectronic properties. However, the result is not very robust and more susceptible to environmental hazards, although the subsequent recovery of the sensor may be more straightforward, typically by washing or heating treatments.

Covalent bonds definitely transform the sp2 to sp3 orbitals, drastically changing the graphene gap, and conferring more robustness to this union. But most important, much of the biomolecules of greatest interest such as enzymes, antibodies, peptides, aptamers, or nucleic acids, need to resort to previous functionalization with covalent bonds to be immobilized for their use in immunoassays.

Although each type of bioreceptor will behave slightly different, the general immobilization strategy lies in the chemical and spatial specificity exhibited by the bioreceptors to bind to *very specific functional groups* (considered "target molecules"). The advantage of graphene-based biosensors is the ease of functionalizing its sp2 bonds with these target groups (which may be, for instance, the C-OH hydroxyls and C-OOH carboxylic bonds that appear in graphene oxide, GO), and subsequently immobilize the bioreceptor of interest that shows chemical reactivity with them (process outlined in Figure 1).

Detection is traditionally carried out by optical or electrical methods. The optical methods are accomplished by recording the luminescence from the marker, or particularly its quenching, which is favoured by the conductive character of graphene, but does so to a much lesser extent on the insulating GO, absorption measurements (with good linearity upon concentration of the marker), FTIR (to detect specific links), or Raman and its amplified effects such as SERS. Electrical methods are performed via measurement of changes in resistance/conductivity, frequency response (impedances), or charge flow. The signal is usually amplified by integrating this layer into the channel of a FET.

In this work, we provide evidences of having functionalized a graphene layer with different non-oxygenated chemical groups (amine anions NH2-, or cations from aryldiazonium salts) in separated regions of the same sample (see Figure 2). We highlight that this was performed not in solution but in dry conditions, just modifying the composition of the atmospheric vapour. For this task, we use a home-made instrument in which electric field-assisted functionalization (either anodic or cathodic) is achieved massively, in areas of tens to thousands μm in size. This allows characterization at macroscopic-scale by techniques such as X-Ray Photoelectron Spectroscopy and optical differential interference contrast (DIC). The instrument and procedure are described in detail elsewhere [2,3]. This is the first step to develop subsequent chemical reactions to attach different biomolecules of interest in each region.

An in-depth study of the oxidation or reduction progress by means of numerical modeling will be presented in order to reveal the physical and chemical mechanisms driving the process.

References

[1] J. Plutnara, M. Pumeraa, Z. Sofer, J. Mater. Chem C, "The chemistry of CVD graphene" 6, pp. 6082-6101, 2018.
[2] AL. Alvarez, C. Coya, M. Garcia-Vélez, "Development of electrical-erosion instrument for direct write micro-patterning on large area conductive thin films", Rev. Sci. Instrum. 86, pp. 084704-09, 2015.
[3] S. J. Quesada et al., "New Concepts for Production of Scalable Single Layer Oxidized Regions by Local Anodic Oxidation of Graphene", Small, 1902817, 2019.

Figures

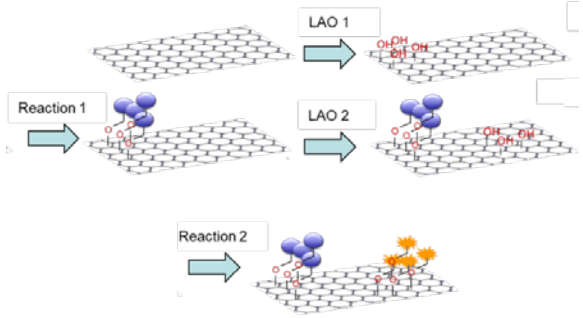

Figure 1. Procedure for immobilization of different antibodies (purple and yellow features) in graphene, when it is oxidized selectively in different regions, by local anodic oxidation (LAO). Chemical reactions will be subsequently developed on this sample to detect antigens.

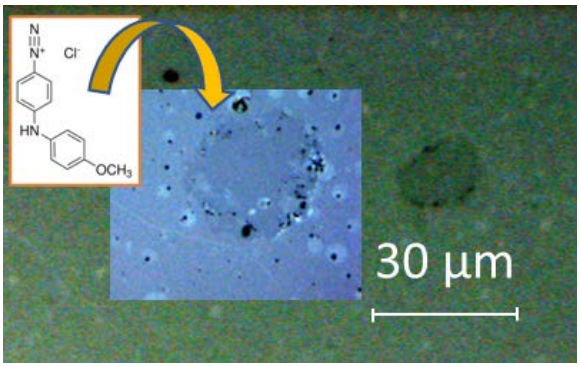

Figure 2. .DIC image of two spots on graphene. The small one (green background) was obtained at operative voltage V_0=+35V under relative humidity RH=95%, using distilled water. The big spot (blue background at same scale) was obtained under identical conditions but dissolving in the vapor a specific content of Variamine Blue B Diazonium salt. The significant increase in size is attributed to the incorporation of additional diazonium cations.

Analysis of the Characteristic Current Fluctuations in the High Resistance State of HfO_2-based Memristors

M.B. González[1*], M. Zabala[1], K. Kalam[2], A. Tamm[2], F. Jiménez-Molinos[3], J.B. Roldán[3], F. Campabadal[1]

[1]Institut de Microelectrònica de Barcelona, IMB-CNM (CSIC), 08193 Bellaterra, Spain.
[2]Institute of Physics, University of Tartu, 50411 Tartu, Estonia.
[3]Depto. Electrónica y Tecnología de Computadores. Universidad de Granada. 18071 Granada, Spain.
*Electronic mail: mireia.bargallo.gonzalez@csic.es

1. Introduction

Memristors based on resistive switching structures are being intensively investigated for a wide number of applications such as resistive random access memories, physical unclonable functions, logic circuits, and as electronic synapses in neuromorphic networks [1]. The main mechanism responsible for the resistive switching (RS) of HfO_2-based memristors consists in the formation and partial dissolution of a nanometer size oxygen deficient conductive filament (CF) in the insulating layer due to the application of an electric field and the temperature rise induced by Joule heating. Considering the CF dimensions, the presence of single traps inside or near the conductive path can strongly influence the filamentary conduction, giving rise to current fluctuations with relative larger amplitudes in the high-resistance state (HRS) than in the low-resistance state (LRS) [2]. Therefore, it is crucial to obtain a better understanding of the current fluctuation features and of the key transport mechanisms that may induce stochastic variability and reduce the device performance. In this work, the characteristic current fluctuations in the HRS of HfO_2 memristors and their associated physical mechanisms are investigated.

2. Experimental

The studied TiN/Ti/HfO_2/Pt devices have a cross-point configuration as shown in Fig. 1. They were fabricated on Si wafers with a thermally grown 200nm SiO_2 layer. First, the bottom electrode was deposited and patterned by lift-off. It consists of a stack of 100nm-thick Pt layer on a 5nm Cr. Then, a 8nm HfO_2 layer was grown in a Picosun TM R-200 ALD reactor at 200ºC using TEMAH and plasma O_2 as hafnium and oxygen precursors, respectively. The top electrode consisting of 200nm TiN and 10nm Ti, was then deposited by magnetron sputtering and patterned by photolithography and lift-off. Finally, the contact area to the bottom Pt electrode was defined by photolithography and dry etching. The resulting structures are square cells of $5\times5\mu m^2$. A top-view optical image is given in Fig. 1a, and the schematic cross-section of the MIM structures is presented in Fig.1b.

The current–time (I–t) characteristics were measured in the HRS of the devices using a Keysight B1500 semiconductor parameter analyzer equipped with a Waveform Generator and a Fast Measurement Unit.

3. Results and Discussion

The typical forming process and bipolar RS behavior of the studied devices are shown in Fig. 2 with the two resistance states in the I-V loops corresponding to a fully formed (LRS) and a partially ruptured (HRS) CF in the HfO_2 insulating layer. Fig. 3 shows an I-t trace measured at -0.2V in the HRS, in which reversible 2-levels random telegraph noise (RTN) signals are detected [3]. These fluctuations are caused by the presence of electrically active defects located in the vicinity of the conductive filament, which may alter the tunneling path and induce large stochastic current fluctuations [4]. The RTN data are analyzed with the time-lag plot technique [5], which consists in plotting the current value at a certain moment (current at $i + 1$) versus the previous value (current at i) (Fig. 4). The points in the diagonal of the plot indicate the two current levels (L_0 and L_1) (see Fig. 5a), while points outside the diagonal represent a current change associated with charge capture/emission processes. Fig. 5b shows the extraction of the capture and emission times related to the I-t trace represented in Fig. 3.

Furthermore, the presence of current instabilities at high stressing conditions has been also investigated. Fig. 6 shows typical current fluctuations observed in the HRS at high degradation levels, where RTN signals and also, irreversible current changes owing to trap density variations inside or near the CF are recognized [4], [6]. These irreversible fluctuations can be explained by oxygen vacancy generation or recombination and drift of oxygen ions, which are field-driven processes, thus influencing the shape, size, or length of the CFs and their stoichiometry.

Acknowledgements

This work was partially funded the Spanish Ministry of Science and Innovation and the ERDF program (TEC2017-84321-C4-1-R, TEC2017-84321-C4-3-R), the ERDF project “Emerging orders in quantum and nanomaterials” (TK134) and the Estonian Research Agency (PRG4, PRG753).

References
[1] Banerjee, et al., *Nanoscale*, 9, 14442-14450, 2017.
[2] Y. T. Chung, et al., in *Proc. IRPS 2014*, pp. MY.2.1-2.5.
[3] E. Simoen and C. Claeys, Random Telegraph Signals in Semiconductor Devices, IOP Publishing, 2016.
[4] M. B. González et al., *IEEE TED*, 63, 3116-3122, 2016.
[5] T. Nagumo, et al., *in Proc. IEDM 2009*, pp. 1–4.
[6] D. Veksler, et al., *in Proc. IEDM 2012*, pp. 9.6.1–9.6.4.

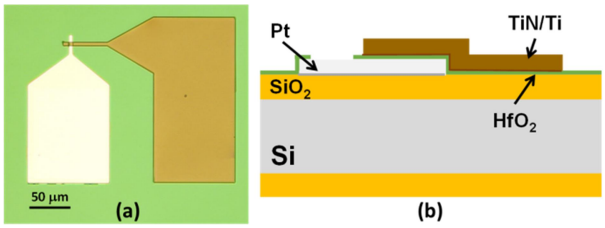

Fig.1. (a) Top-view optical image of a 5×5 µm^2 device, showing the Pt and TiN contact pads. (b) Schematics of the cross-section of the TiN/Ti-HfO_2-Pt MIM structure.

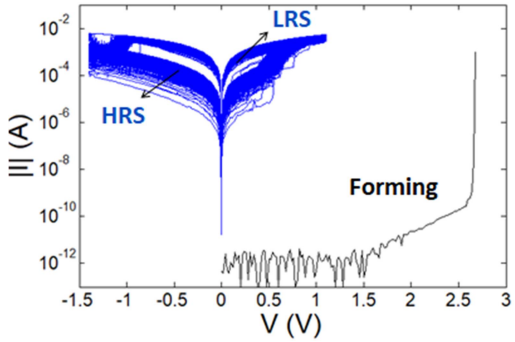

Fig.2. I-V characteristics of the forming process and the subsequent 2270 RS cycles.

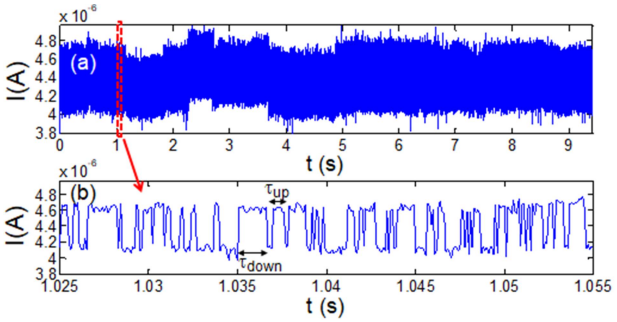

Fig.3. (a) Random telegraph noise I-t trace measured at -0.2V for more than 94000 data points with a time step of 100µs. (b) Zoomed I-t trace of the red box in (a).

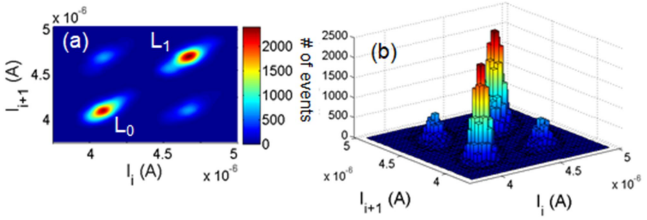

Fig.4. Time-lag plot of the I–t trace represented in Fig. 3a, (a) 2-D and (b) 3-D views.

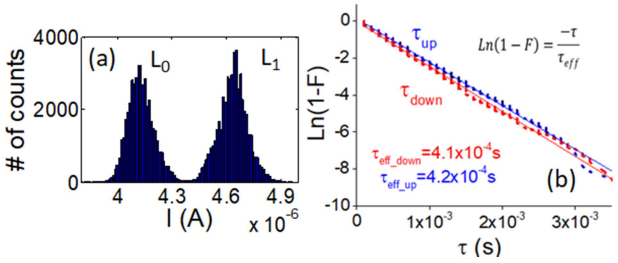

Fig.5. Histogram of the current levels of the I-t trace represented in Fig. 3a, showing two well-defined current levels (L_0, L_1) as a result of the activation and deactivation of one defect. (b) Extraction of the effective times τ_{up} and τ_{down} using the cumulative distribution function (F).

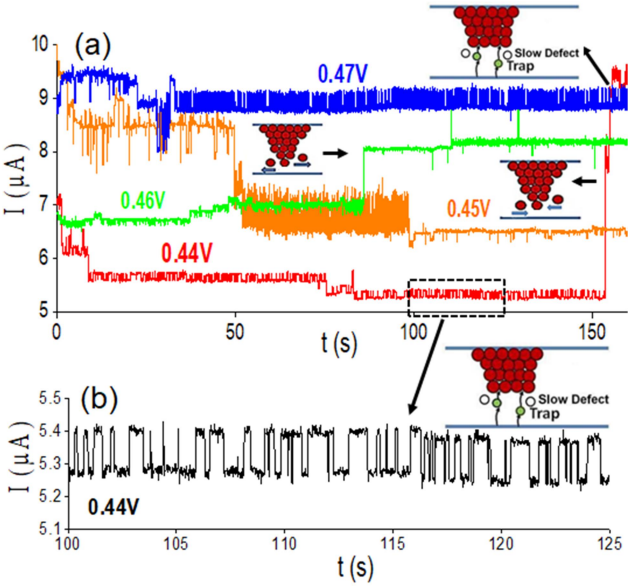

Fig.6. (a) Typical current fluctuations observed in the HRS at high degradation levels. Trap density variations inside or near the CF also occur at high stressing conditions. Reversible two level random telegraph fluctuations are also observed. (b) Zoomed I-t trace of the black box in (a).

POSTER SESSION I

Materials: Processing and characterization

Wednesday 9

11:30-13:15

Chairperson: F. Campabadal (CSIC)

Base and work vacuum pressure influence during sputtering of Al films for sun sensor applications

Gema López-Rodríguez[1], Gerard Masmitjà[1], Isidro Martín[1], José Miguel Moreno[2], Manuel Rodríguez[2], José Manuel Quero[3], Juan García[3], Pablo Ortega[1]

[1] Universitat Politècnica de Catalunya (UPC), Micro and Nanotechnologies Group, MNT, Barcelona, Spain, pablo.rafael.ortega@upc.edu
[2] Solar Mems Technologies, La Rinconada (Sevilla), Spain, jmmoreno@solar-mems.com
[3] Escuela Superior de Ingenieros, Universidad de Sevilla (US), Sevilla, Spain, quero@us.es

1. Abstract

In this work we explore the impact of the base and work sputtering vacuum pressure on aluminum film morphology. Aluminum layers were deposited on radiation-resistant coverglass substrates as blocking light material in sun sensors for satellite applications. Both, base and work vacuum pressure affect directly on the grain morphology which has a clear impact not only in the visual appearance of the deposited films changing the apparent color of the samples observed with a microscope with a non-axial white light from light blue to black, as well as the direct and diffuse reflectance of the surface. This last aspect might be crucial when the sun sensor can be integrated with other optical instruments in the same platform, in order to decrease or reinforce residual light reflections from it.

2. Introduction

Satellites and other spacecrafts require attitude control systems to ensure that solar panels, antennas and other instruments are well oriented to perform their functions properly. Sun sensors are routinely used forming part of their attitude control systems, providing a good orientation accuracy with a reasonable low cost. One easy way to measure the sun vector is using a set of photodiodes whose illumination depends on the light incidence angle. Arranging two pair of photodiodes orthogonally [1], or using a four-quadrant photodiode configuration [2] as can be seen in Fig. 1a, the sun vector in two axes can be determined. In essence, a photodiode-based sun sensor requires a light window which causes an unequal illumination onto the diodes (see Fig. 1b). This light window can be made by means of a glass metallized in the front side with an opaque metal material, typically aluminum, except in the corresponding light window. Additionally, by choosing properly the composition/dopant of the glass, it can be used as a shield against space radiation during the mission (so-called coverglass substrates [1]). In order to guarantee an excellent adherence of the metal layer with the coverglass, sputtering is the most preferred deposition technique, providing also a good thickness control and repeatability. It is well known that RF power and deposition time have a direct impact in the deposition rate and layer thickness. Less evident it is the effect of the base and work vacuum pressure during deposition in the metal layer characteristics. In this work we study the effect of these last deposition parameters on the morphology of the Al film, i.e. grain structure, which have a strong impact on the apparent color exhibited by the surface and its light reflectance (direct and diffuse). These aspects become critical issues for satellite applications where high quality standings are required.

3. Experimental and Results

Uncoated coverglass samples (Qioptiq) 4” wafers were used in the study. After clean the samples with acetone, IPA and DI water the corresponding Al layer was deposited by sputtering (300 W RF power, during 30’ using Ar as inert gas) resulting in 250 ± 25 nm thick opaque films. Work vacuum pressure was controlled adjusting the Ar content with a mass flow meter to obtain the desired value. Only the base and work vacuum pressure were set as free parameters in the study in the 1.5×10^{-6} to 2.7×10^{-5} and 10^{-3} to $2.3\cdot10^{-3}$ mbar range respectively. Optical microscope images were made using non-axial white light from a ring of LEDs (Olympus SZX10). Grain morphology and surface reflectance (total and diffuse) was determined by SEM/AFM and UV-Vis-IR spectroscopy measurements using an integrating sphere, respectively. As can be seen in Fig. 2 and table I, both background and work vacuum pressure have a strong impact in the apparent visual color appearance from light blue to black. AFM measurements reveal that surface color is correlated with the grain size of the samples (see Fig. 3) with RMS roughness from 4.8 to 9.0 nm depending on base and work vacuum pressure. Surface morphology influences also in the diffuse and total reflectance (see Fig. 4). On the one hand, samples with very small grain morphology exhibit an apparent black color due to the absence of diffuse reflectance, i.e. highly specular surface. On the other hand, large grain morphology samples have a remarkably diffuse reflectance offering an apparent light blue color and less specular surface.

References

[1] P. Ortega, G. López-Rodríguez, J. Ricart, et al. "A miniaturized two axis sun sensor for attitude control of nano-satellites," IEEE Sensors Journal, vol. 10 (10), pp. 1623-1632, October 2010.

[2] F.J. Delgado, J.M. Quero, J. García, et al. "SENSOSOL: multifov 4-quadrant high precision sun sensor for satellite attitude control," Proc. of 2013 Spanish Conference on Electron Devices (CDE-2013), Valladolid Spain, pp. 123-126, February 2013.

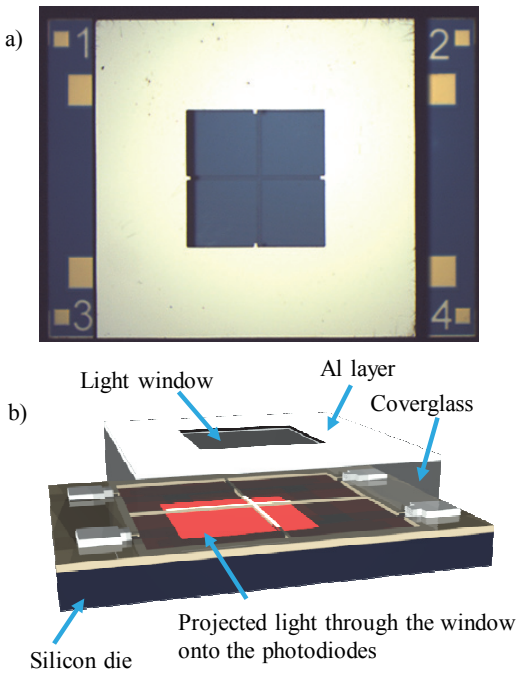

Fig.1. a) Top view of a fabricated four-quadrant sun sensor. The sputtered aluminum layer was deposited onto the coverglass and patterned using standard photolithography. b) 3D sketch of the sun sensor.

Table I. Samples processed using different base and work vacuum pressure showing the color appearance of the film (optical microscope view with axial white illumination).

Sample	Base pressure ($\times 10^{-5}$ mbar)	Work pressure ($\times 10^{-3}$ mbar)	(*)Color
#6	1.0	1.0	Dark blue
#5	1.0	1.3	Dark blue ++
#7	1.0	2.3	Black
#8	0.15	1.0	Dark Black +
#2	0.15	1.3	Dark blue +
#9	0.15	2.3	Black
#10	2.7	1.0	Light blue

(*) Color threshold that the naked eye is able to appreciate:
Dark blue + means darker than dark blue.
Dark blue ++ means darker than dark blue +

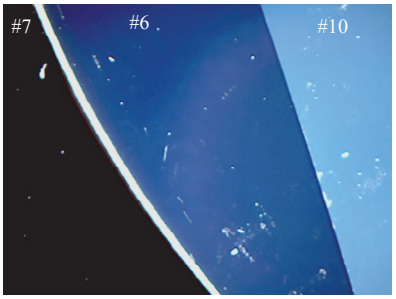

Fig.2. Apparent aspect through optical microscope (non-axial white illumination) of three representative samples processed with different base and work vacuum pressures conditions, samples #6, #7 and #10 (see Table I for details).

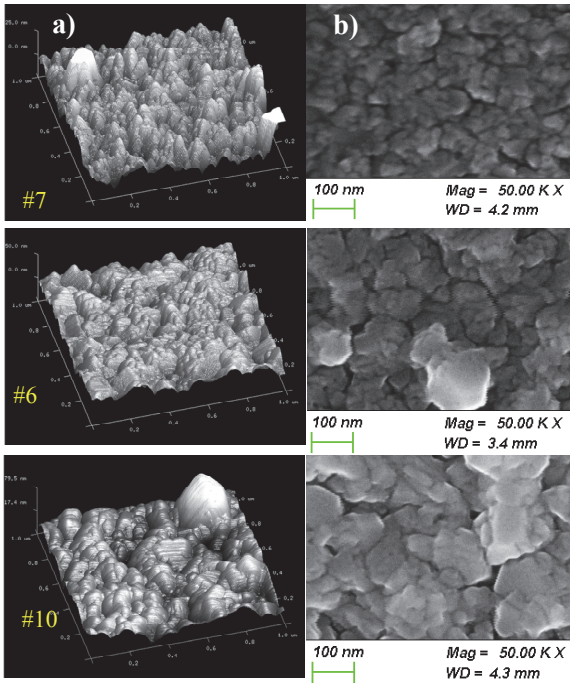

Fig.3. a) AFM and b) SEM images for samples #7, #6 and #10.

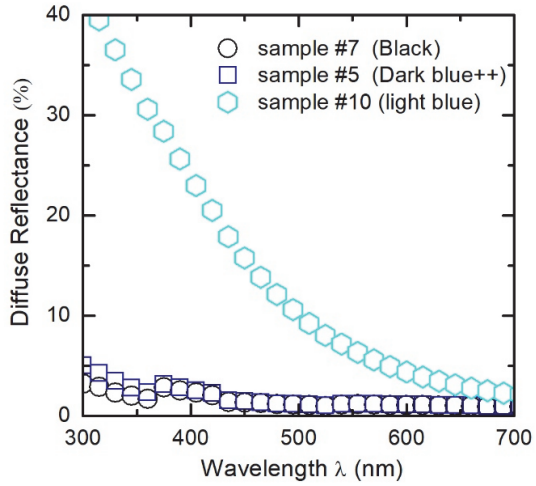

Fig.4. Diffuse reflectance in the visible part of the spectrum measured in several representative samples.

Atomic layer deposition of SnO_2 films for c-Si solar cells

Arnau Torrens, Gerard Masmitjà, Estefanía Almache, Benjamin Pusay, Eloi Ros, Gema López-Rodríguez, Isidro Martín, Cristobal Voz, Joaquim Puigdollers, Pablo Ortega

[1]Universitat Politècnica de Catalunya (UPC), Micro and Nanotechnologies Group (MNT), Barcelona, Spain, pablo.rafael.ortega@upc.edu

1. Abstract

This work explores atomic layer deposited (ALD) SnO_2 films as electron selective contacts for crystalline silicon solar cells. Technological parameters involved in the ALD process, as can be the reactant exposure time, the inert gas purge time and deposition temperature, are determined in order to have a well-controlled growth rate in a surface-saturate ALD regime. Growth rates of ~0.66 Å/cycle are achieved on samples deposited at 150 ºC after process optimization. Electron contact selectivity of SnO_2 layers was assessed by lifetime and transfer length method (TLM) measurements on c-Si(n-type) substrates. Preliminary results confirm a promising surface recombination velocities values below 100 cm/s on symmetrical c-Si(n) samples with fully-ALD $Al_2O_3/TiO_2/SnO_2$ stacks (6/20/100 cycles) deposited at 150 ºC.

2. Introduction

A solar cell consists basically of three regions as can be seen in Fig. 1: a semiconductor absorber region where photons of the incident light are converted in electron-hole pairs. Additionally, in order to separate efficiently photogenerated carriers, it is mandatory to include two selective contacts on both outer surfaces of the absorber region. These selective contacts exhibit a strong asymmetric conductivity depending on the carrier type. For instance, in an electron selective contact, holes are blocked, i.e. low hole conductivity, and electrons can flow easily thought it, i.e. high electron conductivity.

SnO_2 material as electron selective contact are already explored in thin film PV technologies using several deposition processes, as can be sputtering, spin coating and ALD [1]. Among that, ALD is a very interesting technique due to the accurate thickness control, high conformal layers and the facility to combine different films during ALD deposition to form complex contact stack structures [2], including transparent conductive oxides (TCOs) as ZnO:(i), AZO or ZTO [3].

This work is focused on develop electron selective contacts on c-Si solar cells based on thermal atomic layer deposited (ALD) SnO_2 films. The main parameters involved in the ALD process, as can be tin and water precursor duration pulses, T_{Sn} and T_w respectively, as well as the purge times (T_{purge}) and deposition temperature are determined to guarantee a self-limiting surface reacting regime characteristic of the ALD process. In order to determine the contact selective behavior, both contact resistivity and effective lifetime (τ_{eff}) will be measured using the transfer length method (TLM) and quasy-steady-state photoconductance (QSS-PC) technique respectively.

3. Experimental and results

c-Si(n) samples from <100> 4" 1-5 Ωcm FZ-wafers were used in the study. After a HF dip (1%) to remove native oxide, samples underwent the ALD stage depositing the corresponding ALD layers on both surfaces (symmetrical samples). Thermal ALD (Savannah 200 ALD system) was carried out using TDMASn and water as tin and oxidant precursors respectively. Tin precursor was heated at 65ºC and water was kept at room temperature, whereas deposition was done at 150ºC. Purge stage between reactant pulses were made under N_2 vent (20 sccm). ALD Al_2O_3/TiO_2 (6/20 cycles) stacks were deposited at the same temperature using the procedure described in [2]. Layer thicknesses and effective lifetime were measured by ellipsometry and QSS-PC technique, respectively.

As can be seen in Fig. 2, TDMASn and water pulses of 0.2 s and 0.02 s with purge times around 10 s guarantee to work in the ALD window, where the growth rate is nearly constant. By studying the layer thickness with the number of cycles (see Fig.3), we can confirm a small incubation period at the begin of deposition process of about 11 cycles and a growth rates of ~0.66 Å/cycle.

τ_{eff} measurements as-deposited and after accumulative annealings (10' under N_2 ambient) show that single SnO_2 layers do not provide any surface passivation. Nevertheless, the inclusion of a ultrathin ALD stack of Al_2O_3/TiO_2 between silicon and the SnO_2 layer improves noticeably passivation at the contact exhibiting stable τ_{eff} values over 120 µs up to 300 ºC, i.e. effective surface recombination velocities (S_{eff}) lower than 100 cm/s.

These promising results must be complemented with contact resistivity measurements, which will be reported at the conference.

Aknowledgements

This work has been supported partially by the Spanish Government through projects PID2019-109215RB-C41, TEC2017-82305-R and ENE2017-87671-C3-2-R.

References

[1] Y. Chen, Q. Meng, L. Zhang, et al. "SnO_2-based electron transporting layer materials for perovskite solar cells: a review of recent progress," Journal of Energy Chemistry, vol. 35, pp. 144-167, 2019.
[2] G. Masmitjà, P. Ortega, J. Puigdollers, et al. "Interdigitated back-contacted crystalline silicon solar cells with low-temperature dopant-free selective contacts," J. Mater. Chem. A, vol. 6, pp. 3977-3985, 2018.
[3] J. Lindahl, J. Keller, O. Donzel-Gargand, et al. "Deposition temperature induced conduction band changes in zinc tin oxide buffer layers for Cu(In,Ga)Se_2 solar cells," Solar Energy Materials & Solar Cells, vol. 144(2016), pp. 684-690, 2016.

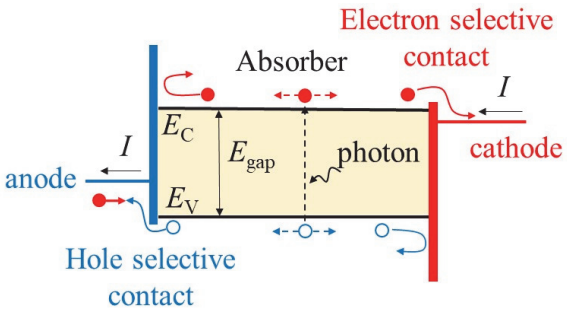

Fig.1. Basic solar cell concept based on the energy diagram of a semiconductor absorber with energy bandgap E_{gap} including two selective contacts at the outer surfaces. E_C, E_V are the conduction and valence band edges of the semiconductor, respectively.

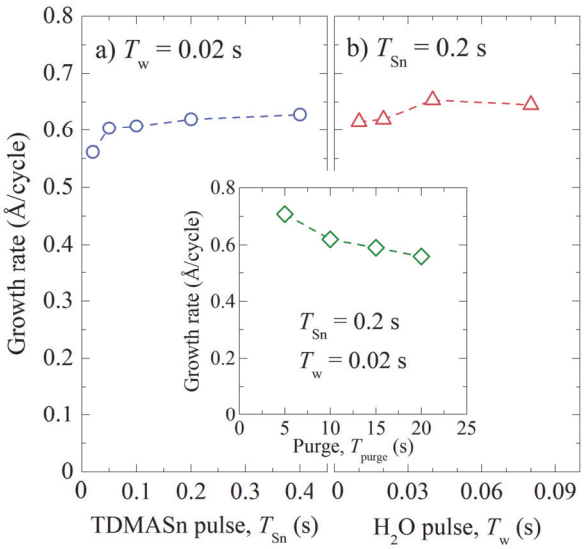

Fig.2. Growth rate as a function of a) TDMASn and b) water pulse times for a deposition temperature of 150 ºC (T_{purge} = 10 s in all cases) using 200 ALD cycles. Influence of the purge time between TDMASn and water pulses in the growth rate is shown in the inset. All lines serve as a guide to the eye.

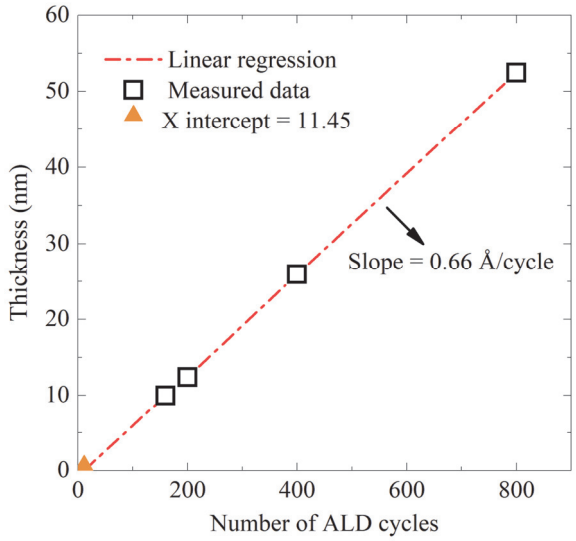

Fig.3. SnO_2 thickness vs. number of ALD cycles. TDMASn and water pulse times were of 0.2 and 0.02 s respectively with purge times of 10 s. Deposition was performed at 150 ºC.

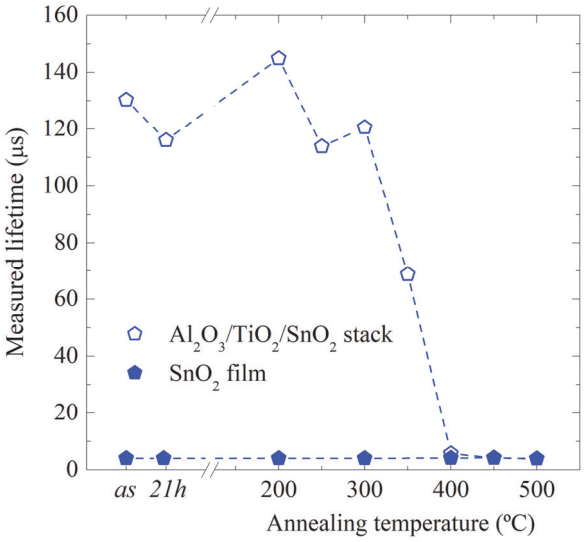

Fig.4. Effective lifetime before (as-deposited and 21 hours later) and after a post-annealing stage for samples with a single SnO_2 layer (100 cycles) and alternatively an $Al_2O_3/TiO_2/SnO_2$ (6/20/100 cycles) stack. Accumulative annealings of 10 min were made in the study. τ_{eff} values were evaluated at a carrier excess density of $\Delta n = 10^{15}$ cm^{-3}. All lines serve as a guide to the eye.

High Pressure Sputtering of materials for selective contacts in emerging photovoltaic cells

E. San Andrés[1], R. García-Hernansanz[1], G. P. Moreno[1], E. García-Hemme[1], R. Barrio[2], I. Torres[2], D. Caudevilla[1], D. Pastor[1], J. Olea[1], A. del Prado[1], S. Algaidy[1], F. Zenteno[1]

[1]Dpto. Estructura de la Materia, Física Térmica y Electrónica, Universidad Complutense de Madrid, Spain 28040.
[2]Unidad de Energía Solar Fotovoltaica, Dpto. de Energías Renovables, CIEMAT, Spain 28040.
Contact: esas@ucm.es, +0034 91 394 4533.

1. Abstract

We characterized the growth by high pressure sputtering (HPS) of materials intended for selective contacts for solar cells. We studied the deposition of ITO, MoO_x and TiO_x using pure Ar and mixed Ar/O_2 atmospheres as well as ceramic or metallic targets. We show that HPS deposition of these materials is feasible.

2. Introduction

The understanding of the physical behavior of photovoltaic cells is a topic that has evolved rapidly during the last decade. In particular, the photovoltaic community has reached the consensus that the *pn* junction electric field is not necessary for the photovoltaic effect. Now we know that an efficient solar cell only needs a good absorber sandwiched by two membrane-like structures, each one permeable to only one type of carrier (electrons or holes). These membranes are the so-called *selective contacts* (SC). [1]
At present, there is research on many materials that show this selective character when they are grown on Si. The most promising ones are MoO_x for hole SC, and TiO_x for electron SC [2]. However, these oxides typically degrade when exposed to air, so *in situ* capping is also interesting. This capping can be metallic and/or transparent.
In this article we show our results on the deposition of these materials by a non-conventional technique such as HPS. This technique is specially fitting because it can also be used for the deposition of high quality ITO and metallic films. Therefore, either a transparent conductive or metallic capping layers can be deposited sequentially in the same system, thus minimizing interfacial degradation which is critical for an efficient photovoltaic cell.

3. Experiments

We have sputtered these materials on transparent glass, quartz substrates, or on a-Si:H passivated n-Si wafers. We did not intentionally heat the substrates, thus the growth temperatures were under 80 ºC. The targets were either 2" ceramic ITO, metallic Ti or metallic Mo. The sputtering atmosphere was pure Ar or mixed Ar/O_2. We studied the effect of pressure variations (in the 0.1 mbar to 2.3 mbar range) and *rf* power (from 5 W to 50 W). The plasma was characterized by glow discharge optical spectroscopy (GDOS). The films were characterized by profilometry, ellipsometry and sheet resistance measurements.

4. Results

Fig. 1 shows the GDOS in the 200 nm – 600 nm wavelength range when the sputtering is done in pure Ar atmosphere at a pressure of 0.5 mbar. We observe that when ionized Ar is present all the relevant species (In, Sn, Mo and Ti) are extracted. For ITO no clear O signal could be detected, because O emissions in the available range are close to Ar^+ emissions. In any case, the films were transparent and with reasonable resistivity, indicating that there was enough oxygen for the oxidation of the film. To determine the optimal RF power we focused on the integrated area of relevant peaks for each material. For instance, Fig. 2 shows how Ti needs 20 W to be extracted and saturates for powers higher than 40W, as the integrated intensity of the Ti-related peaks located in the 397.5-401. nm range shows.
To fabricate the oxides, either the Ti or Mo metallic films could be oxidized, or the oxides could be directly grown by a mixed Ar/O_2 atmosphere. Fig. 3 shows that introducing O_2 produces the disappearance of the Ti and Mo peaks. However, ellipsometry shows that transparent films grow (TiO_x or MoO_x) but with a reduced growth rate.
Increasing pressure improves film uniformity for the metallic targets. However, pressure does not influence uniformity for the ceramic target. Fig. 4 shows that for the same pressure the uniformity is better for the metallic Mo target than the ceramic ITO.
Finally, we have evaluated whether HPS affects the passivation quality achieved by a very thin layer (~5 nm) of a-Si:H deposited onto a Si wafer, as it is often observed with many sputtering processes. As Fig. 5 shows, the sputtering induced damage is limited since the passivated wafer can still reach a minority carrier lifetime of ~1 ms after a mild 200ºC hot plate anneal. These results show that HPS is a promising technique for the deposition of materials for emerging solar cells.

References

[1] U.W. P. Würfel, *Physics of Solar Cells: From Basic Principles to Advanced Concepts* (Wiley-VCH, 2016)
[2] J. Bullock et al., *Efficient silicon solar cells with dopant-free asymmetric heterocontacts* Nat. Energy 15031 (2016).

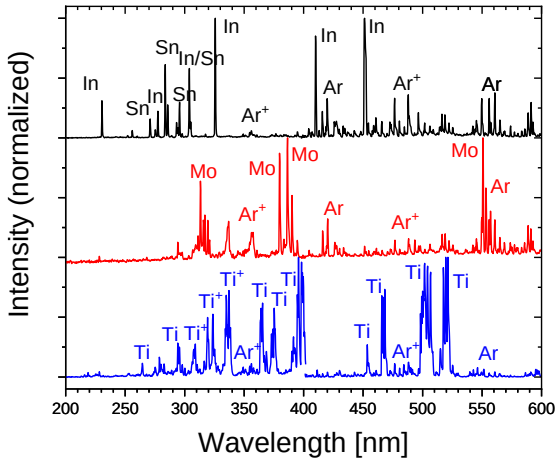

Fig.1. Normalized GDOS spectra of HPS processes in pure Ar atmosphere at a pressure of 0.5 mbar: ITO (black), Mo (red) and Ti (blue).

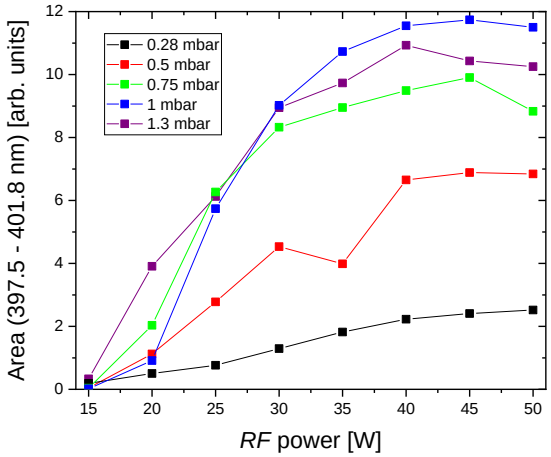

Fig.2. Integrated area of the Ti emissions in the 397.5-401.75 range as a function of RF power for several Ar pressures.

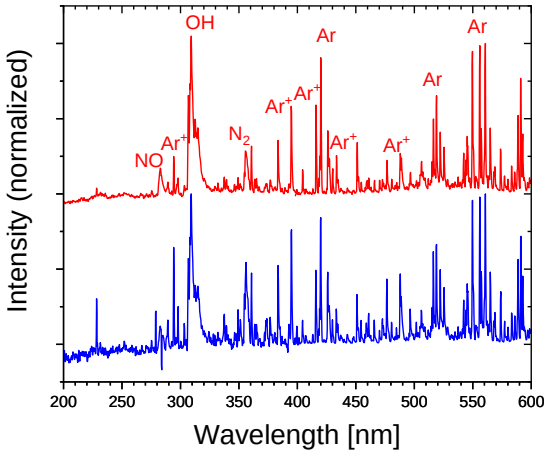

Fig.3. Normalized GDOS spectra of HPS processes in Ar/O_2 mixed at a pressure of 0.5 mbar and 40W or *rf* power: Mo 99%/1%(red) and Ti 95%/5% (blue). Unlabeled peaks are related to Ar or Ar^+ emissions. Spectra are almost identical. The only metal emission detected is the line at 387 nm from Mo, but close to the detection limit.

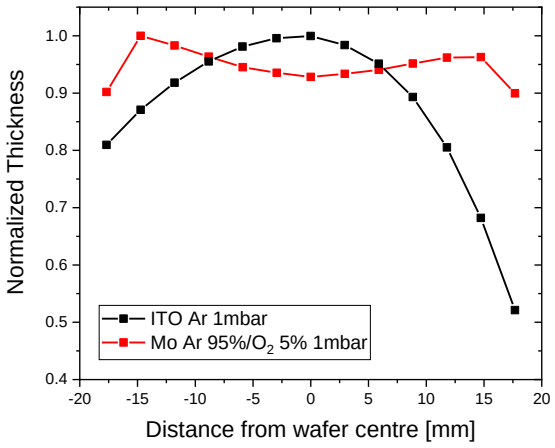

Fig.4. Normalized thickness of the deposited films as a function of distance to the 2" wafer center for a ceramic target (ITO) and a metallic target (Mo).

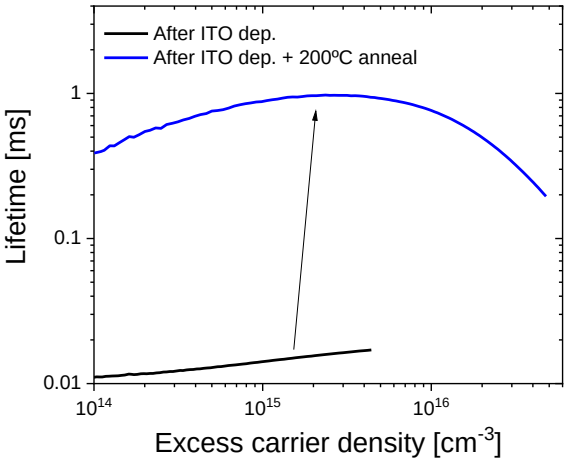

Fig.5. Minority carrier lifetime of wafer passivated by PECVD a-Si:H on both sides after ITO deposition (black), and after a hot plate anneal at 200ºC (blue), showing good interface recovery after the anneal.

Light-trapping improvement of limited-quality silicon wafers for silicon heterojunction solar cell applications

R. Barrio[1], D. Canteli[2], N. González[1], I. Torres[1], A. Márquez[2], C. Molpeceres[2], J.J. Gandía[1]

[1]CIEMAT, Unidad de Energía Solar Fotovoltaica, Dpto. de Energía, 28040-Madrid, Spain.
[2]Centro Láser, Universidad Politécnica de Madrid, 28038-Madrid, Spain.
Contact: rocio.barrio@ciemat.es.

1. Abstract

Laser-based surface texturing treatments have been investigated as a promising option for innovative low-cost concepts to improve the light absorption of silicon heterojunction solar cells manufactured from unconventional silicon wafers. A great advantage of using a laser as a processing tool is its high precision, which lead to selected and well-controlled morphologies. This is a particularly interesting feature for multicrystalline silicon wafers, where the large number of grain boundaries makes it difficult to obtain high light-trapping morphologies by other methods. The investigations described in this work include testing different patterns on the wafer surface in order to define the best morphology to improve the light absorption. A significant decrease in reflectance (R<9%) has been achieved by direct-laser texturization and has been compared with acid-chemical etching with average reflectance upper than 20%. This result suggests the enormous potential of direct laser texturization for this type of wafers, without chemical residues and its easy incorporation to manufacture low-cost silicon heterojunction solar cells.

2. Introduction

The exponential growth of photovoltaic energy in recent years was mainly driven by crystalline silicon solar cell. The roadmap of silicon solar cell development requires the introduction of passivating contacts. In this scenario, there are different kinds of silicon technology. Among them, Silicon Heterojunction solar cells (SHJ), also known as HIT, use passivating selective contacts based on thin-film amorphous silicon. SHJ hold the record for open circuit voltage at one sun of 750 mV and an efficiency greater than 26 % [1].

For this technology, one of the biggest technological challenge is to reduce the higher cost of production of the cells, while maintaining its high efficiencies. Some strategies for this could be the reduction of the silver in the contacts or the use low quality silicon wafers as multicrystalline silicon (mc-Si) instead of high-quality silicon wafers. In this last option, there are not enough developments made with mc-Si oriented for SHJ applications, due to the higher concentration of contaminants or defects from its production method, which could generate a high recombination. Therefore, a greater effort is needed in the research of this type of mc-Si wafers so that they can be employed in next SHJ solar cells

3. Methods and Results

This article describes a process to improve light-trapping by laser texturing with the goal to attain surface morphologies that improve optical confinement without inducing surface defects. It consists of generating geometric patterns of surface topography through direct- laser scribing processes applied to the mc-Si. In this regard, special attention has been paid to the analysis of the state of these surfaces, which is a critical factor for this kind of cells. A picosecond pulsed laser (Katana HP) emitting at 1064 nm was used.

Two different patterns were tested: the first consisting of a series of parallel grooves, and a second one where a subsequent series of lines was performed by scribing grooves perpendicular to the first one. Both, 15 µm and 30-µm pitches, were tested with 10-µm wide and 8-µm deep grooves. These surface textures were characterized by reflectance measurement, XPS (X-ray Photoelectron Spectroscopy), SEM (Scanning Electron Microscopy). The superficial recombination was also evaluated by implied-V_{oc} values by QSSPC (quasy-steady-state photoconductance).

Laser texturing shows a spectacular improvement in light trapping for all samples, with hemispheric reflectance weighted below 9% in some of the patterns analyzed, with respect to the results we obtained with acid-chemical texturing [2]. However, these first laser-textured surfaces have been found to be highly recombinant with respect to as-cut wafers and chemical-etching textured wafers. Therefore, laser-process parameters should be adjusted to try to reach a balance between good optical confinement and low surface recombination to be employed efficiently in low-cost SHJ solar cells with limited-quality Si-wafers.

Acknowledgements
This work was supported by the project CHENOC (ENE2016-78933-C4-3-R and ENE2016-78933-C4-4-R).

References

[1] K. Yoshikawa. *et al.* Nat. Energy **2**, (2017).
[2] R. Barrio *et al.* JOM, **72**, 608–614 (2020).

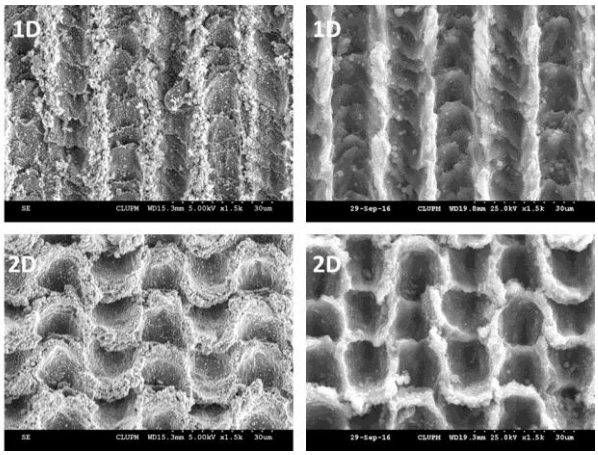

Fig 1. SEM images of laser textured mc-Si wafers with 1D parallel grooves and 2D patterns with scribing grooves perpendicular to the first one, both with 15-µm pitch, at 90 degrees and 1500-X magnification. Left-hand-side pictures correspond to samples after the texturisation process, with a SiO_2 layer on their surfaces, and right-hand-side pictures correspond to the same samples after having eliminated the oxide.

Pattern	**Pitch (µm)**	**$R_{hem,w}$ (%) 350-1100 nm [with SiO_2]**	**$R_{hem,w}$ (%) 350-1100 [without SiO_2]**
No laser	-	-	34.0
Parallel grooves	15	6.3	10.0
Perpendicular grooves	15	6.5	8.8
Parallel grooves	30	11.0	16.3
Perpendicular grooves	30	8.9	11.0

Table 1. Weighted hemispherical-reflectance of mc-Si wafers after the texturisation process by using laser with different patterns and pitches before and after the elimination of the SiO_2 layer with a 10% HF solution for 5 minutes.

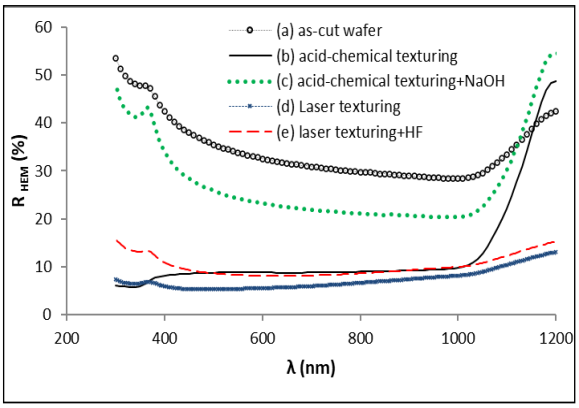

Fig. 2. Comparison of spectral hemispherical reflectance in different superficial stages of the mc-Si wafers: (a) as-cut wafer; (b) after acid-chemical texturing, (c) after removing the porous-silicon layer with NaOH grown during the acid-chemical etching (d) after laser texturing and (e) after subsequent immersion in HF to eliminate the SiO_2 layer grown during the laser processing.

Nanosecond laser assisted chemical vapor deposition process for the growth of ZnO thin films.

Sergio Sánchez[(1,2)], Isabel Ayerdi[(1,2)], Oihane Beldarrain[1], Gemma García Mandayo[(1,2)], Enrique Castaño[(1,2)], Santiago Olaizola[(1,2)].

1 CEIT-Basque Research and Technology Alliance (BRTA), Manuel Lardizabal 15, 20018 Donostia / San Sebastián, Spain.

2 Universidad de Navarra, Tecnun, Manuel Lardizabal 13, 20018 Donostia / San Sebastián, Spain

Contact name: Sergio Sánchez (ssmartin@tecnun.es).

1. Abstract

Aerosol-assisted chemical vapor deposition (AACVD) is a extensively used method for the growth of thin films. Its main advantages are that it has readily temperature requirements, it has a high deposition rate, it is cost-effective and it has safer availability of precursors compared with other conventional thin film deposition techniques, as MOCVD or ALD, [1]–[2].

Laser-Assisted Chemical Vapor Deposition (LACVD) is an innovative technique for depositing thin films by laser inducing surface chemical reactions [3]–[4]. The laser interacts with the substrate, heating it until it reaches the temperature needed to assist the chemical reaction. As the material only grows where the laser beam reaches the substrate, a good dimensional control of the deposited material is achieved. Furthermore, the use of a nanosecond laser reduces the thermal diffusion through the substrate countenancing the growth of thin films on substrates with a low melting temperature.

The standard AACVD deposition method has a high deposition rate, however, the patterning of micro- or nanostructures in the grown thin films requires several additional steps including lithographic processes. LACVD technique enables the direct patterning of the grown material, however, pulsed lasers provide low deposition rates. This is because there is no continuous temperature on the substrate but a transitory behavior. In this work, AACVD and LACVD techniques are combined in order to take advantage of their strengths while minimizing the disadvantages of each technique when used individually.

2. Experimental and results

In this work, the AACVD deposition of ZnO with the thermal assistance of a nanosecond pulsed laser is studied. A schematic diagram of the experimental set-up for the LEAACVD system is shown in Fig. 1. This setup includes a gas system to provide the carrier gas that delivers the aerosol droplets to the reaction chamber, an atomizer where the aerosol droplets are generated, a reaction chamber where the deposition takes place and a laser system to assist the AACVD process. In a first stage, the thermal effects of the nanosecond pulsed laser on the surface of the substrate have been analyzed for several pulse lengths and laser powers. The accumulation of heat in the substrate has been studied, measuring the temperature on the surface of the substrate using a thermographic camera. However, the transitory temperature peaks provoked by the pulsed laser cannot be captured by the camera. At that point, they have been studied by means of a MATLAB simulation using the 2D heat transfer equation (Fig. 2). In a second stage, ZnO thin films have been grown by AACVD and LEAACVD using zinc chloride as a chemical precursor.

To study the material deposited with this new technique and based on previous AACVD results, two sets of experiments were carried out. For the first one, a pulse duration of 200 ns and three different power values were considered; 5 W, 5,25 W and 5,5 W. For the second one, a pulse duration of 50 ns and 3 different power values were chosen: 5 W, 6 W and 7 W. It has obtained ZnO grains (Fig. 3), which is a breakthrough in order to develop this new technique.

References.

[1] M. J. Powell, D. B. Potter, R. L. Wilson, J. A. Darr, I. P. Parkin, and C. J. Carmalt, “Scaling aerosol assisted chemical vapour deposition: Exploring the relationship between growth rate and film properties,” *Mater. Des.*, vol. 129, no. January, pp. 116–124, 2017.

[2] C. E. Knapp and C. J. Carmalt, “Solution based CVD of main group materials,” *Chem. Soc. Rev.*, vol. 45, no. 4, pp. 1036–1064, 2016.

[3] C. Duty, D. Jean, and W. J. Lackey, “Laser chemical vapour deposition: materials, modelling, and process control,” *Int. Mater. Rev.*, vol. 46, no. 6, pp. 271–287, 2004.

[4] P. C. Nordine, S. C. de la Veaux, and F. T. Wallenberger, “Silicon fibers produced by high-pressure LCVD,” *Appl. Phys. A Solids Surfaces*, vol. 57, no. 1, pp. 97–100, 1993.

73.

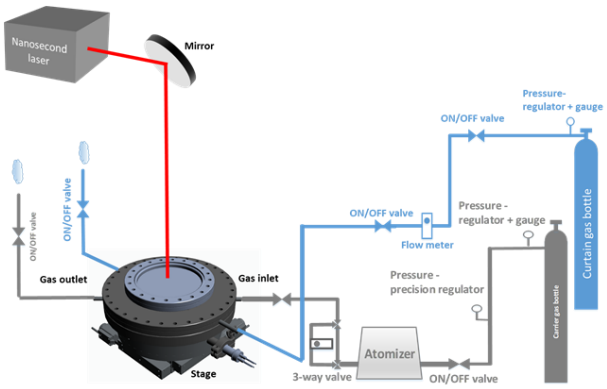

Fig.1. Schematic diagram of the setup with; nanosecond pulsed laser, reaction chamber, atomizer and gas system.

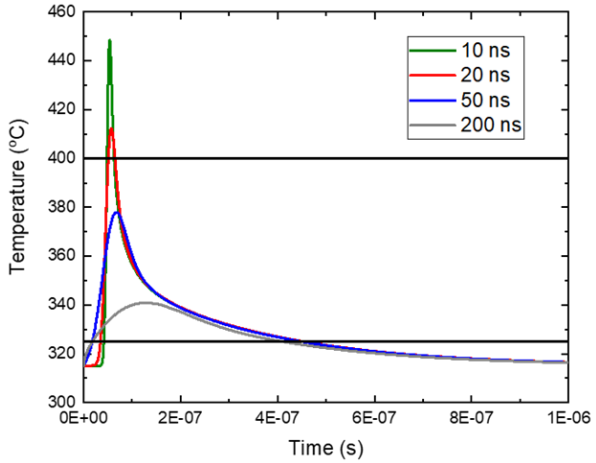

Fig.2. Temperature curves versus time when a pulse fall upon the substrate for 4 different pulse lengths; 10 ns, 20 ns, 50 ns and 200 ns. The laser power is 5 W. The flat lines demarcate the range of temperature where there is ZnO deposition.

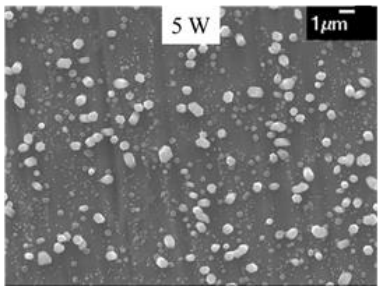

Fig.1. ZnO grains deposited with the LEAACV technique, for a laser power of 5W, a pulse duration of 200 ns, and 1 h of deposit time.

Chemical beam epitaxy of $GaP_{1-x}N_x$ for the integration of III-V solar cells and light-emitting devices on Si(001)

Karim Ben Saddik[1], Javier Grandal[2], Basilio Javier García[1]* and Sergio Fernández-Garrido[1]**

[1]Electronics and Semiconductors Group, Applied Physics Department, Universidad Autónoma de Madrid, C/ Francisco Tomás y Valiente 7, 28049 Madrid, Spain
[2]Instituto de Sistemas Optoelectrónicos y Microtecnología (ISOM), Universidad Politécnica de Madrid, Avda. Complutense 30, 28040, Madrid, Spain
*E-mail: basilio.javier.garcia@uam.es / Phone: +34 91 497 4005 / Fax: +34 91497 3969
**E-mail: sergio.fernandezg@uam.es / Phone: +34 914975 880 / Fax: +34 91497 3969

The monolithic integration of III-V semiconductor devices on Si is pursued following either metamorphic or pseudomorphic growth approaches. In the case of the metamorphic approach, the elastic strain in the III-V layers grown on Si, resulting from their different lattice parameters, is deliberately relaxed at the III-V/Si interface. This method, currently explored for the fabrication of triple-junction (Ga,In)P/GaAs/Si solar cells [1], is clearly promising, but it implies the unavoidable creation of threading dislocations, which deteriorate the quality of the materials limiting the final device performance. The pseudomorphic approach is, in contrast, much easier to implement because it is based on III-V materials lattice-matched to Si. This second approach is, however, as attractive as restrictive, since it simplifies the epitaxial growth process at the expense of severely limiting the choice of III-V compound semiconductors. Within this framework, quaternary $GaP_{1-x-y}As_yN_x$ alloys are ideal, since they can be grown lattice-matched to Si with widely tunable band gaps [2]. In particular, the ternary $GaP_{1-x}N_x$ is lattice-matched to Si with a direct band gap of 1.96 eV for x = 0.021. Therefore, $GaP_{1-x}N_x$ compounds are of interest for the fabrication of both double junction $GaP_{1-x}N_x$/Si solar cells and red-light emitting devices. Nevertheless, despite the great potential of this material, reports on $GaP_{1-x}N_x$ based devices are rather scarce yet due to the difficulties to synthesize them with a high structural perfection.

In this work, we report a comprehensive study on the growth by chemical beam epitaxy of $GaP_{1-x}N_x$ thin films on (001) oriented Si, as required for the pseudomorphic monolithic integration of III-V devices with the Si manufacturing technology. We analyze the dependence of the chemical composition on the growth parameters, specifically, on the substrate temperature and the fluxes of the group-V precursors (DMHy and TBP for N and P, respectively). The properties of the samples, grown on commercially available state-of-the-art GaP on Si(001) substrates, are investigated in-situ by reflection high-energy electron diffraction (RHEED) and ex-situ by high-resolution X-ray diffraction (HRXRD), scanning electron microscopy (SEM) and atomic force microscopy (AFM). Figure 1(a) illustrates the effect of the substrate temperature on the incorporation of N for constant fluxes. The incorporation of N follows an Arrhenius like temperature dependence with an activation energy of about 0.83 eV, attributed to the energy barrier for the thermal desorption of DMHy. Figure 1(b) shows the dependence of the N content on the flux of DMHy for a given flux of TBP at two different temperatures. Regardless of the temperature, the data reveal a linear increase of the N content with the flux of DMHy. Combining the results derived from the data shown in Figs.1(a) and 1(b), we conclude that the dependence of the N content on the substrate temperature and the flux of DMHy can be written as

$$[N] = \left(-4.8 \times 10^{-8} + \frac{BEP_{DMHy}}{1.8 \times 10^{2}\ Torr}\right) e^{\frac{0.83\ eV}{k_B T}}, \qquad (1)$$

where BEP_{DMHy} is the beam equivalent pressure of the DMHy flux in Torr units. The growth diagram shown in Fig. 2(a) visualizes the impact of both the substrate temperature and the flux of DMHy on the N content according to Eq.(1). A further analysis of the incorporation of N as a function of the flux of TBP, while keeping constant the substrate temperature and the DMHy flux [see Fig. 1(c)], demonstrates that the exponential prefactor in Eq.(1) depends on the flux of TBP. Interestingly, as also indicated in the growth diagram, we find that under certain growth conditions $GaP_{1-x}N_x$ alloys are rough [see Fig. 2(b)] and segregate into several phases characterized by different N contents. Finally, for x values of about 0.021, we demonstrate the possibility of synthesizing single-phase films with smooth surfaces, as revealed by RHEED and AFM [see Fig. 2(c)].

References

[1] Press release Fraunhofer Institut (2020)
[2] K. Ben Saddik et al. J. Appl. Phys. **126**, 105704 (2019).

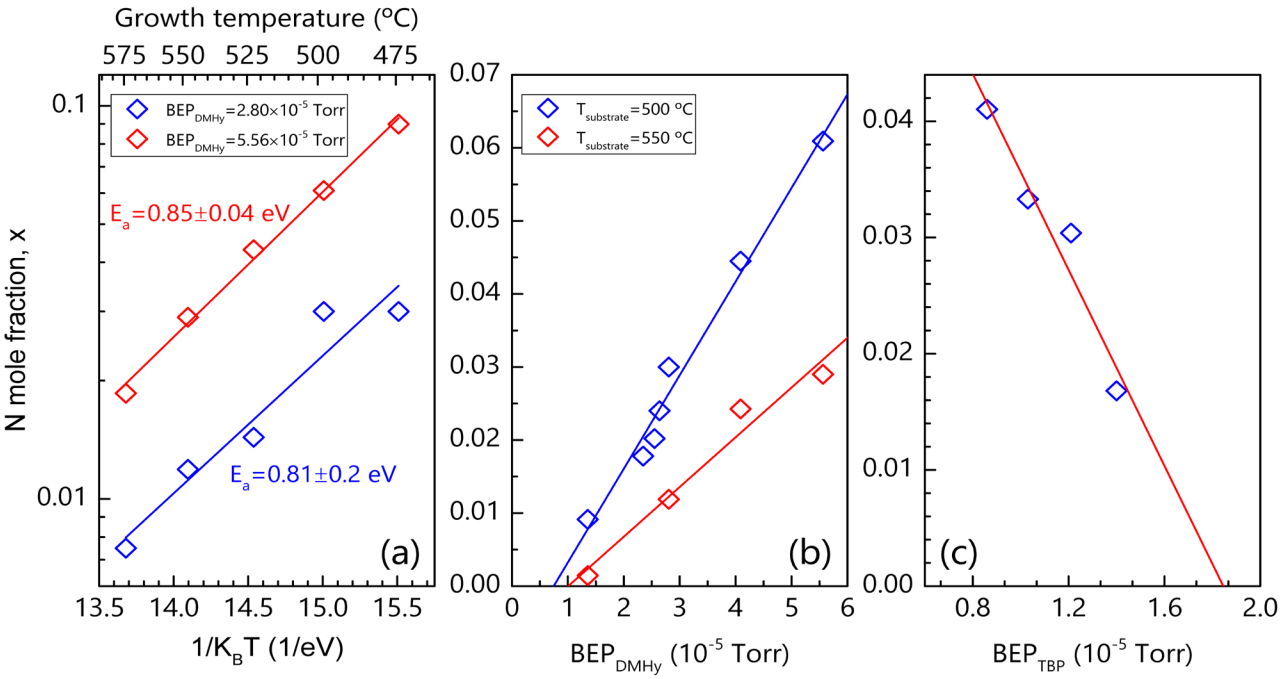

Fig. 1 (a) Arrhenius plot illustrating the temperature dependence of the N mole fraction, x, on the growth temperature for two different fluxes of DMHy (given as BEP). The solid lines are fits of Arrhenius laws to the experimental data. (b) N mole fraction as a function of the BEP of DMHy for two different growth temperatures. (c) N mole fraction as a function of the TBP BEP. The solid lines in (b) and (c) are linear fits to the experimental data.

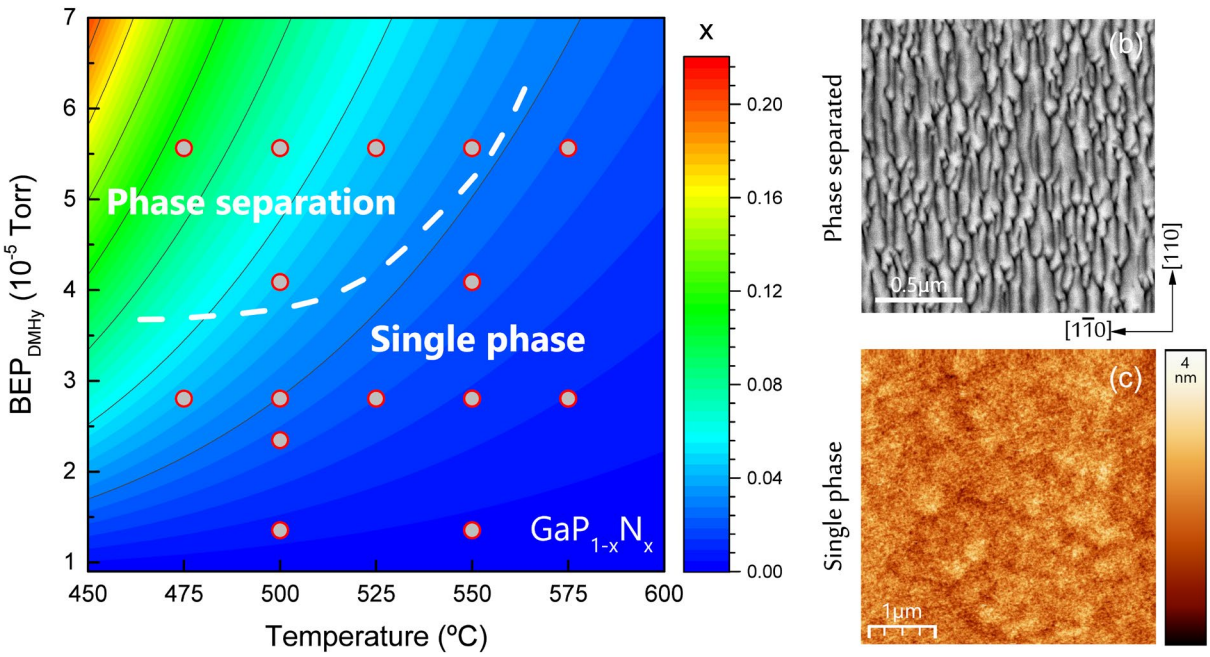

Fig. 2 (a) Growth diagram depicting, according to Eq. (1), the dependence of the incorporation of N into $GaP_{1-x}N_x$ on the growth temperature and the BEP of DMHy for a given flux of TBP. The N mole fraction, x, is displayed as a contour plot with a linear scale. The dashed line shows the boundary between the growth conditions that result in single-phase and phase-separated $GaP_{1-x}N_x$ layers, as concluded from HRXRD studies (not shown here). The solid symbols indicate the growth conditions of the samples grown for this study. (b) Exemplary plan-view scanning electron micrograph of a sample grown within the phase-separation growth regime. A pronounced roughness is observed characterized by the formation of elongated stripes along the [110] direction. (c) Exemplary 5 × 5 μm^2 atomic force micrograph of a sample grown within the single-phase regime. The root mean square roughness is 0.4 nm.

A contact resistance extraction method of 2D-FET technologies without test structures

Anibal Pacheco-Sanchez, David Jiménez
Departament d'Enginyeria Electrònica, Escola d'Enginyeria, Universitat Autònoma de Barcelona, Bellaterra 08193, Spain
AnibalUriel.Pacheco@uab.cat, David.Jimenez@uab.cat

I. Abstract

A Y-function based method (YFM) is used here to extract the contact resistance R_c of two-dimensional (2D) field-effect transistor (FET) technologies. The methodology relies on individual transfer characteristics, at a single drain-to-source voltage, of devices from a same technology with different channel lengths. In contrast to the widely used transfer length method where a global-back gated test structure is required, the YFM presented here can be applied to 2D-FETs regardless the gate architecture and it does not require neither the fabrication of dedicated test structures. Hence, it is a useful and immediate tool for device characterization and scaling studies. R_c is extracted here for graphene, phosphorene and MoS_2 devices using the proposed methodology. Extracted values are in good agreement with the ones obtained with other approaches.

II. 2D-FETs' contact resistance characterization

The contact resistance R_c associated to the physical phenomena arising from the metal-channel interface in two-dimensional (2D) field-effect transistors (FETs) is one of the major issues to overcome in the development of these emerging technologies [1], [2]. A precise and reliable R_c characterization is required towards obtaining reproducible and more transparent contacts in 2D-based technologies. One of the oftenly used approaches to obtain R_c values in 2D-FETs is the transfer length method (TLM), adopted from incumbent technologies [3] in which a fabricated test structure containing multiple back-gate transistors with different channel lengths Ls and sharing a common channel material is required. In addition to the fabrication challenges involving large area 2D layers-based structures [4], [5], the TLM-based R_c extraction has not been as immediate and accurate as expected in 2D tehcnologies due to the different physics in metal-2D junctions not included in the underlying TLM considerations [6]-[10]. Furthermore, due to the Schottky-like nature of metal-2D contacts [2], [9], [10], the associated bias-dependent R_c of 2D devices with different gate architectures [2], [11]-[14] is not properly embraced by TLM structures which, in most of the cases, are electrostatically controlled by a global back-gate (GBG), and hence, it can mislead performance projections for other device architectures. A Y-function [15] based methodology (YFM) presented elsewhere for conventional devices [16] is adapted and applied for the first time here to 2D transistors. In contrast to a YFM presented elsewhere for 2D-FETs [17], values of R_C can be extracted here for a specific V_{DS} due to the nature of the method since only one single transfer curve of a device is required to characterize a technology regardless its gate architecture -in contrast to TLM. This characterization might be useful for scaling studies, modeling and immediate technology evaluation at specific escenarios.

III. Extraction methodology

By considering a drift-diffusion approach and an inhomogeneous potential along the 2D channel, the electron drain current I_D in 2D-FETs, in terms of the external gate/drain-to-source voltages $V_{GS/DS}$, can be approximated at the linear unipolar regime as [17]

$$I_D \approx \beta V_{aux} V_{DS} \left(1 + \theta V_{aux}\right)^{-1}, \quad (1)$$

where $\beta = \mu_0 C_{ox} w_g / L$ with μ_0 as the low-field mobility, C_{ox} the oxide capacitance, w_g the gate width, $V_{aux} = V_{GS} - V_{th} - 0.5V_{DS}$ with V_{th} as the charge threshold voltage [15] and $\theta = \theta_{ch} + \theta_c$ the extrinsic mobility degradation coefficient with θ_{ch} as the intrinsic mobility degradation due to vertical fields and $\theta_c = \beta R_C$ [15], [18]. From Eq. (1), the product of the total device resistance $R_{tot} = V_{DS}/I_D$ and the Y-function ($Y = I_D/\sqrt{g_m} = \sqrt{V_{DS}\beta}\left(V_{GS} - V_{th} - 0.5V_{DS}\right)$, with the transconductance g_m) can be expressed as

$$R_{tot} Y = \sqrt{V_{DS}\beta^{-1}} + \theta\beta^{-1} Y, \quad (2)$$

which is valid for low- and high-lateral fields in contrast to other approaches where the charge control relation is limited to low V_{DS}, i.e., $|V_{GS} - V_{th}| \gg 0.5|V_{DS}|$ [16], [19]. Notice that neglecting θ_{ch}, as oftenly done in previous reports of 2D-FETs [19], [20], can mislead the extracted R_C values in YFMs as demonstrated elsewhere [17]. The factor $\theta\beta^{-1}$ is obtained from the slope Eq. (2) plotted versus Y. Similarly, the intercept and slope of Y plotted versus V_{GS}, at a given V_{DS}, yield V_{th} and β, respectively. By using the definition of θ, R_c is extracted from the intercept at 0 of the $\theta\beta^{-1}$ versus β^{-1} plot built from devices with different L for a specific V_{DS}. This methodology is valid for p-type FETs as well by considering hole transport in Eq. (1). In the case of graphene (G) FETs, the underlying transport equation of the method should be modified in order to take into account the corresponding charge control, i.e., the Dirac voltage $V_{Dirac} = V_{GS}|_{\min I_D}$ rather than V_{th} should be used in Eq. (1) [21].

IV. Results

The YFM presented here has been applied to fabricated 2D-FET technologies [8], [22]-[24]. The step-by-step procedure (cf. Section III) can be visualized in Fig. 1 where R_c of a GBG GFET technology [8] has been extracted. Extracted values of a top-gate (TG) GFET technology [22], a TG MoS_2FET technology [23] and a TG BPFET technology [24] are reported in Table I. Eq. (1), calculated using the extracted parameters including R_c shows a good agreement with the experimental data for some of the technologies evaluated here as shown in Figs. 1(a) and Fig. 2.

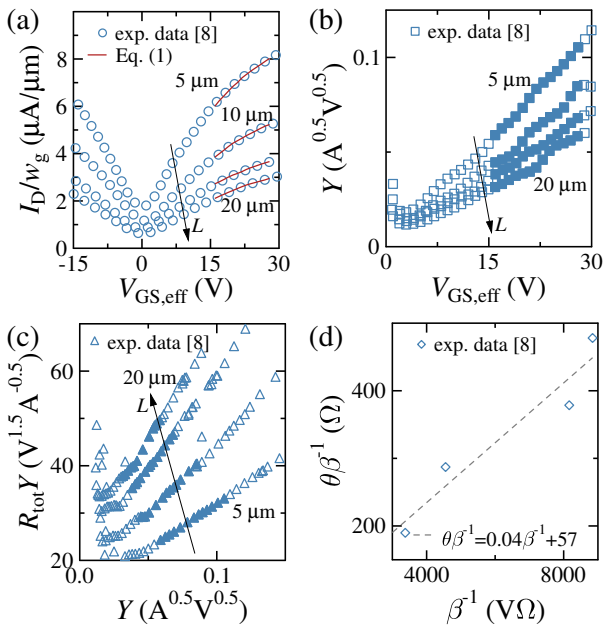

Fig. 1. R_c extraction methodology applied to a GBG GFET technology presented in [8] with gate width of 20 µm and channel lengths of 5 µm, 10 µm, 15 µm and 20 µm. (a) Transfer characteristics, (b) Y-function versus V_{GS} plots used to extract V_{th} and β, (c) $R_{tot}Y$ versus Y plots used to extract $\theta\beta^{-1}$ and (d) $\theta\beta^{-1}$ versus β^{-1} plot used to extract R_c. Empty markers represent experimenal data, filled markers represent experimental data within the bias region where the extraction method has been applied. Solid lines in (a) represent Eq. (1) results by using the extracted parameters. Dashed line in (d) represents a linear extrapolation where the intercept at 0 corresponds to R_c. $V_{DS} = 0.05$ V for all data. $V_{GS,eff} = V_{GS} - V_{Dirac}$ for this case.

TABLE I
CONTACT RESISTIVITY VALUES EXTRACTED OF FABRICATED 2D-FET TECHNOLOGIES WITH DIFFERENT METHODS INCLUDING THE ONE PRESENTED HERE. THE DEVICE CHANNEL LENGTHS AND GATE ARCHITECTURES OF EACH TECHNOLOGY ARE INDICATED.

[ref.]	w_g (µm)	L (µm)	gate architecture	$R_c \cdot w_g$ (kΩ · µm) YFM here / other method
GFET				
[8]	20	5, 10, 15, 20	GBG	1.14 / ∼1 (TLM)
[22]	3.4	0.1, 0.3, 1, 2	TG	0.27 / –
MoS_2FET				
[23]	1	4, 8, 16	TG	51.73 / –
BPFET				
[24]	–	0.35, 0.85, 1.85, 3.85	TG	4.22 / ∼4.4 (TLM)

ACKNOWLEDGEMENTS

This work has received funding from the European Union's Horizon 2020 research and innovation programme under grant agreements No GrapheneCore2 785219 and No GrapheneCore3 881603, from Ministerio de Ciencia, Innovación y Universidades under grant agreement RTI2018-097876-B-C21(MCIU/AEI/FEDER, UE). This article has been partially funded by the European Regional Development Funds (ERDF) allocated to the Programa Operatiu FEDER de Catalunya 2014-2020, with the support of the Secretaria d'Universitats i Recerca of the Departament d'Empresa i Coneixement of the Generalitat de Catalunya for emerging technology clusters to carry out valorization and transfer of research results. Reference of the GraphCAT project: 001-P-001702.

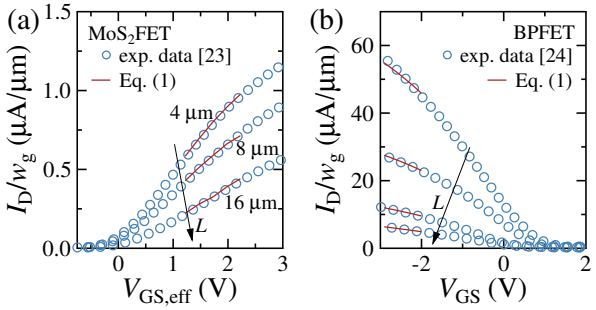

Fig. 2. Transfer characteristics of top-gate devices with different channel lengths of fabricated 2D-FET technologies: markers represent experimental data and lines the drain current (Eq. (1)) calculated with the extracted parameters using the YFM presented here. (a) TG MoS_2FET technology reported in [23]. $V_{DS} = 0.2$ V and $V_{GS,eff} = V_{GS} - V_{th}$. (b) TG BPFET technology reported in [24] with $L = 0.35$ µm, 0.85 µm, 1.85 µm and 3.85 µm. $V_{DS} = 1$ V.

REFERENCES

[1] F. Giubileo, A. Di Bartolomeo, *Prog. Surf. Sci.*, 92, 2017. DOI: 10.1016/j.progsurf.2017.05.002
[2] Z. Cheng et al., *IEEE T. Electron Dev.*, 65 (10), 2018. DOI: 10.1109/TED.2018.2865642
[3] D. Schroder, Wiley-IEEE Press, 2016. DOI: 10.1002/0471749095
[4] D. Neumaier et al., *Nat. Mater.*, 18, 2019. DOI: 10.1038/s41563-019-0359-7
[5] W. Choi et al., *Mater. Today*, 20(3), 2017. DOI: 10.1016/j.mattod.2016.10.002
[6] S. Venica et al., *IEEE T. Electron Dev.*, 65(4), 2018. DOI: 10.1109/TED.2018.2802946
[7] F. Driussi et al., *IEEE T. Semiconduct. M.*, 33(2), 2020. DOI: 10.1109/TSM.2020.2981199
[8] A. Gahoi et al., *Adv. Electron. Mater.*, 6, 2020. DOI: 10.1002/aelm.202000386
[9] Y, Xu et al., *ACS Nano*, 10(5), 2016. DOI: 10.1021/acsnano.6b01842
[10] S. B. Mitta et al., *2D Mater.*, 8, 2021. DOI: 10.1088/2053-1583/abc187
[11] J, Kang et al., *Phys. Rev. X*, 4, 2014. DOI: 10.1103/PhysRevX.4.031005
[12] F. A. Chaves et al., *2D Mater.*, 2, 2015. DOI: 10.1088/2053-1583/2/2/025006
[13] S. K. Lee et al., *Semicond. Sci. Tech.*, 34, 2019. DOI: 10.1088/2053-1583/aba449
[14] H. Liu et al., *IEEE Electron Dev. Lett.*, 35(7), 2014. DOI: 10.1109/LED.2014.2323951
[15] G. Ghibaudo, *Electron. Lett.*, 24(9), 1988. DOI: 10.1049/el:19880369
[16] R. Trevisoli et al., *IEEE T. Electron Dev.*, 64(7), 2017. DOI: 10.1109/TED.2017.2704928
[17] A. Pacheco-Sanchez, D. Jiménez, *Electron. Lett.*, 56(18), 2020. DOI: 10.1049/el.2020.1502
[18] C. Hao et al., *Solid-State Electron.*, 28(10), 1985. DOI: 10.1016/0038-1101(85)90034-6
[19] H.-Y. Chang et al., *Appl. Phys. Lett.*, 104, 2014. DOI: 10.1063/1.4868536
[20] J. Na et al., *Appl. Phys. Lett.*, 104, 2014. DOI: 10.1063/1.4878839
[21] A. Pacheco-Sanchez, et al., *Solid-State Electron.*, 172, 2020. DOI: 10.1016/j.sse.2020.107882
[22] J. Bai et al., *Nano Lett.*, 11(6), 2011. DOI: 10.1021/nl201331x
[23] D. Wu et al., Mater. Express, 6(2), 2016. DOI: 10.1166/mex.2016.1289
[24] J. Miao et al., *ACS Nano*, 9(9), 2015. DOI: 10.1021/acsnano.5b04036

Gamma Radiation Effects on HfO_2-based RRAM Devices

M. Maestro-Izquierdo[1], M. B. González[1], P. Martín-Holgado[2], Y. Morilla[2], and F. Campabadal[1]

[1]Institut de Microelectrònica de Barcelona, IMB-CNM (CSIC), Carrer dels Til·lers, s/n. Campus UAB, 08193 Bellaterra, Spain. e-mail: francesca.campabadal@csic.es
[2]Centro Nacional de Aceleradores. Avda. Thomas A. Edison 7, 41092 Sevilla, Spain.

1. Introduction

Resistive random access memories (RRAMs) are emerging non-volatile memories based on the resistive switching (RS) phenomenon, which consists in the switching of the device between two different resistance states: the high resistance state (HRS) and the low resistance state (LRS). In HfO_2-based RRAMs, RS is attributed to the formation and partial disruption of an oxygen-deficient conductive filament in the HfO_2 layer between two metal electrodes [1]. In view of the promising features of these devices, they are of interest in electronics for space applications, so the radiation hardness of them should be assessed. As for gamma-ray radiation, devices have been reported to withstand up to a total dose in the order of Mrad(Si) although data retention worsened [2]. In this work, we study the effect of gamma radiation on the RS characteristics of TiN/Ti/HfO_2/W devices, by comparing the results before and after irradiation of unbiased devices, up to a total dose of 22 Mrad(Si). Data retention, in turn, has been assessed by in-situ measuring the device resistance while under radiation exposure.

2. Experimental Procedure

The studied TiN/Ti/10nm-HfO_2/W RRAM devices have a cross-point configuration as shown in Fig. 1. A detailed description of the fabrication process flow and of their RS characteristics can be found in [3]. For the electrical characterization of the RS performance, before and after irradiation, an Agilent B1505A semiconductor parameter analyzer was used, while, for measurements during irradiation, a custom socked board and an ArcOne platform was employed (Fig. 2). Gamma radiation experiments were carried out in the RadLab facility of the CNA, equipped with a gamma irradiator, containing a source of ^{60}Co (Fig. 2b), and the instrumentation to remotely monitor the dose rate and the accumulated dose.

The experimental procedure consisted in first assessing the RS current-voltage (I-V) characteristics of the devices prior to irradiation, by cyclically applying negative and positive voltage sweeps (Fig. 3) 40 times (40 RS cycles). Next, the devices were placed in the socket board (Fig. 2a) with all terminals short-circuited and exposed to the gamma source with a dose rate of 24.1 krad(Si)/h. After a certain time under radiation exposure, the devices were removed from the irradiation room, the measurement of 20 RS cycles was done and the devices were placed back to the irradiation. This procedure was repeated 8 times until a cumulative dose of 22.1 Mrad(Si) was reached (see Table 1). After this, the evaluation of data retention during irradiation was performed by continuously monitoring the resistance of the devices using the ArcOne platform.

3. Results

Fig. 4 shows an example of the RS measurements before and after irradiation with a total cumulative dose of 22.1 Mrad(Si). In order to analyze the effect of the gamma irradiation, after each irradiation step, the RS parameters were extracted from 20 RS I-V curves, and their values compared to those of the non-irradiated devices. In Fig. 5a the results for the transition voltages in one device are plotted showing that, after each irradiation step, the extracted values are within the cycle-to-cycle variability limits of the fresh device. With respect to the device resistances, as shown in Fig. 5b, no significant difference in the LRS is observed whereas for HRS a small decrease in the mean value after a total cumulative dose of 22.1 Mrad(Si) is obtained, although with a large enough window between LRS and HRS.

As for data retention assessment, 4 devices were first driven to the LRS and then exposed to radiation and their resistance measured at +0.1V during exposure. The same procedure was followed for devices driven to the HRS. The obtained results are shown in Fig. 6 clearly indicating excellent data retention in the case of LRS for a total dose up to 7.9 Mrad(Si). In the HRS, although some instabilities existed that led to variations in the device resistance and even a sudden decrease at some point during radiation exposure, in none of the devices a switch to the LRS was registered, so data retention was also good in the HRS up to a cumulative dose of 7.9 Mrad(Si).

Acknowledgements

The authors thank Alter Technology for the use of their instrumentation. The support of the Spanish Ministry of Science and Innovation and the FEDER program through projects TEC2017-84321-C4-1-R and ESP2015-68245-C4-4-P, is acknowledged.

References

[1] D. Ielmini, *Semicond. Sci. Technol.* vol. 31, 063002, 2016.
[2] R. Fang et al., *Appl. Phys. Lett.* vol. 104, 183507, 2014.
[3] S. Poblador et al., *Microelectron. Eng.* vol. 187-188, pp. 148-153, 2018.

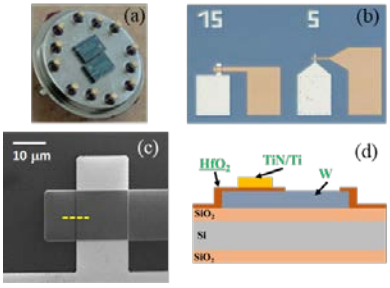

Fig.1. (a) Wire-bonded packaged chips. (b) Optical image of 15×15 µm^2 and 5×5 µm^2 devices. (c) SEM micrograph and (d) schematic cross-sectional view at the yellow dashed line in (c).

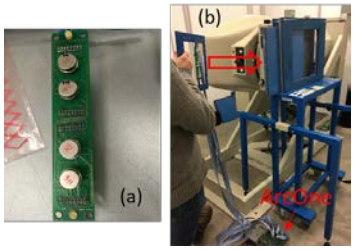

Fig.2. (a) Package socked board and (b) gamma irradiator with a ^{60}Co source and irradiation set-up, with the ArcOne characterization platform.

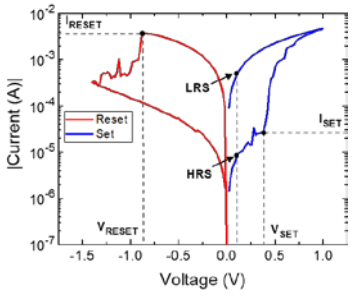

Fig.3. I-V characteristics of a RS cycle. The voltage wss applied to the TiN electrode while the W electrode was grounded. The characteristic RS parameters are indicated.

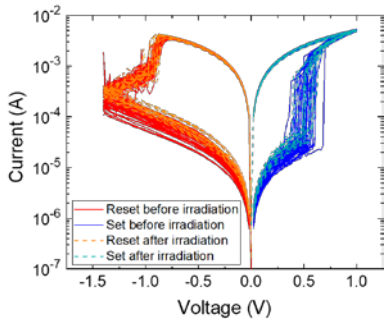

Fig.4. RS I-V curves before and after gamma irradiation with a total cumulative dose of 22.1 Mrad(Si).

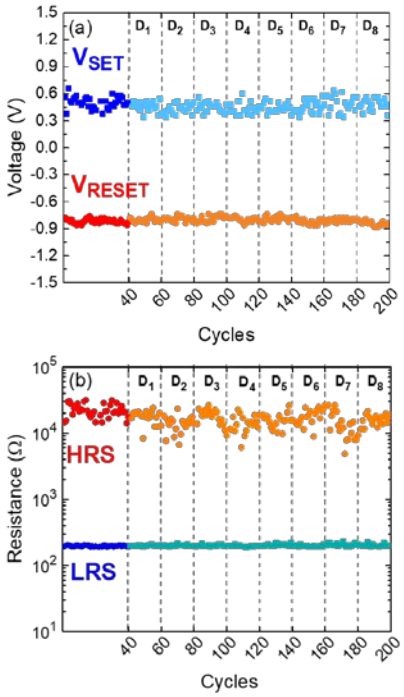

Fig.5. (a) Switching voltages and (b) resistance values, at +0.1 V for each resistance state, extracted from RS I-V curves before (first 40 cycles) and after each gamma irradiation step with a cumulative dose of D_i (see Table 1).

Step	1	2	3	4	5	6	7	8
D_i (Mrad)	0.3	0.8	1.8	4.8	10.4	12.1	17.6	22.1

Table 1. Cumulative dose after each gamma irradiation step.

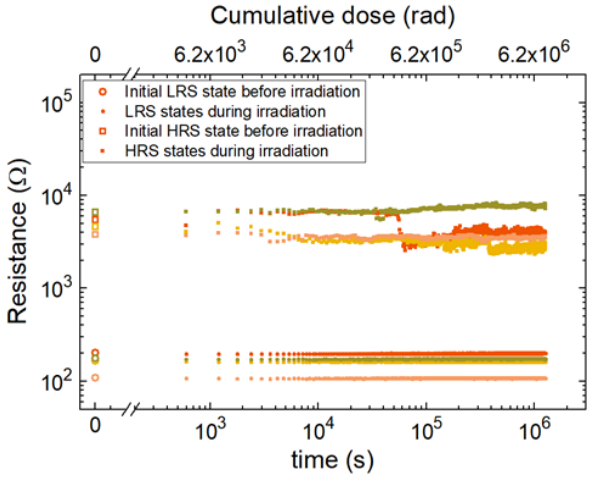

Fig. 6. Retention characteristics of 4 devices biased at +0.1 V during irradiation. In-situ measurements were performed during exposure to gamma radiation at a dose rate of 22.2 krad/h.

Advances in the development of high efficiency III-V multijunction solar cells on Ge|Si virtual substrates

Víctor Orejuela[1], Iván García[1*], Clara Sánchez[1], Manuel Hinojosa[1], Shabnam Dadgostar[2]
Monalisa Ghosh[3], Pere Roca i Cabarrocas[3], Ignacio Rey-Stolle[1]

[1]Instituto de Energía Solar, Universidad Politécnica de Madrid, 28040 Madrid, Spain
[2]GdS Optronlab, Universidad de Valladolid, 47011 Valladolid, Spain
[3]LPICM-CNRS, Ecole Polytechnique, 91128, Palaiseau, France
*igarcia@ies.upm.es

1. Abstract

Virtual substrates based on Ge layers directly deposited on Si have become a promising route to realize the long-sought high-efficiency III-V multijunction solar cells on silicon substrates. We investigate two alternatives of Ge|Si templates, which differ in the deposition technique (CVD vs low-temperature RT-PECVD) and the thickness of the Ge layer (μm vs nm scale). The design of the whole multijunction cell is dictated by the Ge|Si template used. We analyze the theoretical potential of these virtual substrates and show the first experimental steps toward the achievement of cost-effective triple-junction solar cells on Si.

2. Introduction

The implementation of already demonstrated high efficiency III-V solar cells on Ge|Si virtual substrates is one major advantage compared to other approaches to develop III-V solar cells on Si-based on graded buffers. To this end, two different Ge|Si template fabrication approaches are being assessed at IES-UPM.

Firstly, with CVD-deposited Ge layers in the thickness range of 2-5 μm, multijunction solar cells with an active Ge bottom junction can be obtained. The Si substrate does not play a photovoltaic role in this case. By embedding a porous layer, the Si substrate can be removed to obtain lightweight and flexible solar cells.

Secondly, the use of Ge layers in the range of a few tens of nm, deposited by RF-PECVD on Si, is an alternative route. In this case, the Si substrate can function as the bottom subcell. The thin Ge helps preventing the formation of cracks, which is one of the main challenges in this technology. However, the parasitic light absorption within the Ge layer must be considered when designing the solar cell structure.

In this work we discuss the potential of each approach from the perspective of performance and technological challenges, and we show experimental prototype solar cells.

3. Results

We have demonstrated previously GaInP/GaInAs/Ge triple-junction solar cells on Ge|Si substrates [1] (Fig. 1). The active Ge junction is shown to produce the required photocurrent for thicknesses as low as 3 μm, even considering a high Ge/Si interface recombination velocity (Fig. 2). Promising minority carrier collection efficiencies are measured, except in the GaInAs middle cell (Fig. 3). The formation of cracks during cooldown, after the epitaxial deposition of the structure, affects the minority carrier properties, mainly the lifetime, which also cause low voltages. We are currently developing designs that prevent the formation of cracks by thinning the III-V structure at the cost of a slight efficiency drop.

The alternative Ge|Si virtual substrates based on an ultra-thin Ge layer help prevent the formation of cracks. In this case the Ge layer does not play a photovoltaic role. Our calculations show that efficiencies approaching 35% at 1 sun AM1.5G can be attained with a GaInP/GaInAs/Si triple-junction solar cell. The design of the upper subcells for current matching depends on the Ge layer thickness (Fig. 4), which also affects the overall efficiency. Our first implementations using unoptimized Ge|Si templates show functional devices with promising carrier collection efficiencies in the Si bottom cell (Fig. 5).

Both approaches will benefit from the ongoing development of Ge|Si virtual substrates with lower defect densities. An extended discussion of results will be presented at the time of the conference.

References

[1] I. García *et al.*, "Ge virtual substrates for high efficiency III-V solar cells: applications, potential and challenges," in *46th IEEE PVSC*, Chicago, USA, 2019, pp. 1444–1451, doi: 10.1109/PVSC40753.2019.89.

[2] R. Cariou, R. Ruggeri, X. Tan, G. Mannino, J. Nassar, and P. Roca i Cabarrocas, "Structural properties of relaxed thin film germanium layers grown by low temperature RF-PECVD epitaxy on Si and Ge (100) substrates," *AIP Adv.*, vol. 4, no. 7, p. 077103, Jul. 2014, doi: 10.1063/1.4886774.

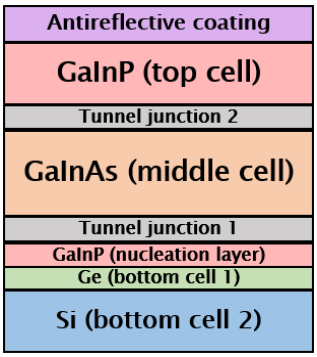

Figure 1. General structure of the triple-junction solar cells studied. "Bottom cell 1" indicates that this layer is the bottom cell for the first set of experimental devices (thicker Ge layer) and "bottom cell 2", for the other set (thinner Ge layer).

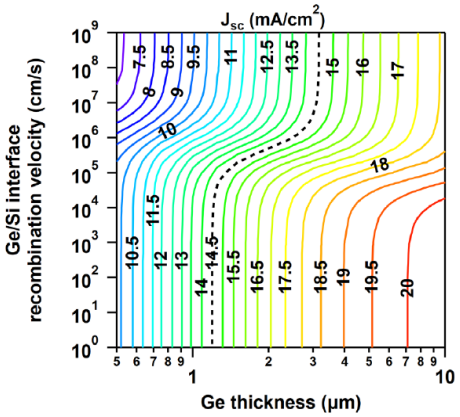

Figure 2. Calculated contour plots of the Ge subcell J_{sc} vs the Ge/Si interface recombination velocity and the Ge thickness. The black dashed contours correspond to a J_{sc} of 14.5 mA·cm^{-2} required for current matching in a triple-junction cell. The cells are modelled with an optimum anti-reflection coating and the solar spectrum used is the AM1.5d-G173.

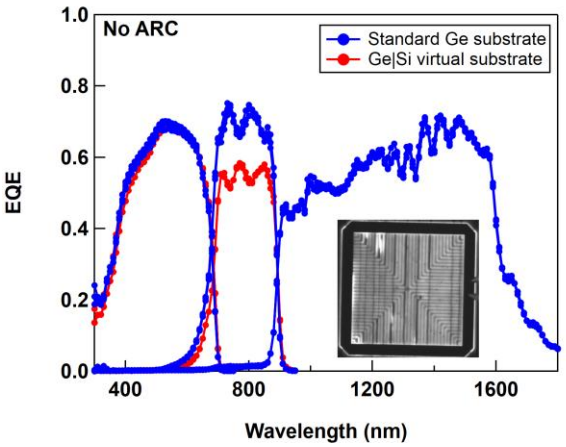

Figure 3. EQE of GaInP/GaInAs/Ge triple-junction solar cells grown on Ge|Si templates with 5 μm thick Ge layers fabricated by CVD. The inset shows an electroluminescence map which evidences the formation of cracks in these cells.

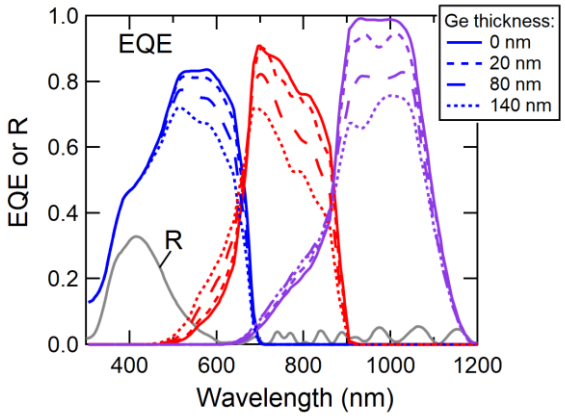

Figure 4. Calculated EQE of triple-junction solar cells on Ge|Si optimized for highest efficiency by current matching, for different thicknesses of the Ge layer. Thicker Ge layers parasitically absorb more light in the Si bottom cell energy range, requiring thinning the upper subcells to achieve current matching, but producing an overall efficiency loss.

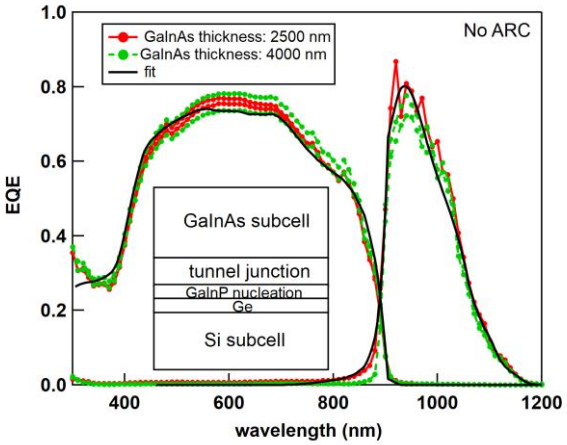

Figure 5. EQE of GaInAs/Ge|Si dual-junction solar cells grown on Ge|Si templates with 20 nm thick Ge layers fabricated by RF-PECVD. A close fit to the data is obtained, and the fitting parameters show good diffusion lengths in the Si subcell. Better Ge|Si templates are being fabricated to attain good quality also in the GaInAs subcells, which is limited in these solar cells by the quality of the original Si substrates used for these prototypes.

Coalescence, crystallographic orientation and luminescence of ZnO nanowires grown on Si(001) by chemical vapour transport

S. Fernández-Garrido[1*], C. Pisador[1], J. Lähnemann[2], S. Lazić[3], A. Ruiz[4], A. Redondo-Cubero[1]

[1]Grupo de Electrónica y Semiconductores, Dpto. Física Aplicada, Universidad Autónoma de Madrid, C/ Francisco Tomás y Valiente 7, 28049 Madrid, Spain
[2]Paul-Drude-Institut für Festkörperelektronik, Leibniz-Institut im Forschungsverbund Berlin e.V., Hausvogteiplatz 5–7, 10117 Berlin, Germany
[3]Universidad Autónoma de Madrid (UAM), Instituto Universitario de Ciencia de Materiales 'Nicolás Cabrera' (INC) and Condensed Matter Physics Center (IFIMAC), Departamento de Física de Materiales, 28049, Madrid, Spain
[4]Instituto de Ciencia de Materiales de Madrid, CSIC, C/ Sor Juana Inés de la Cruz 3, Cantoblanco, 28049, Madrid, Spain
*E-mail: sergio.fernandezg@uam.es / Phone: +34 914975 880 / Fax: +34 91497 3969

The synthesis of semiconductors as nanowires (NWs) instead of epitaxial films provides new degrees of freedom for the design of opto- and electronic devices as well as the possibility of combining otherwise incompatible materials [1]. Among the wide variety of semiconductors that can be grown as NWs, ZnO and GaN stand out. In the particular case of ZnO, the synthesis of this compound as NWs is the subject of worldwide research because of their multiple potential applications, including the development of photocatalytic water splitting cells, piezoelectric nanogenerators, gas and biological sensors, ultraviolet detectors, electrochromic displays, field effect transistors, and light emitters [2]. The catalyst-free self-assembled formation of ZnO NWs is as attractive as popular because it is the simplest method to obtain nanostructures with a structural perfection comparable to that of bulk materials. However, this growth approach also has inherent limitations and drawbacks. Besides the poor degree of control over the NW radius and areal density, a non-negligible fraction of NWs typically merge during growth forming coalesced NW aggregates. As a result of the mutual misorientation of coalesced NWs, the coalescence process can potentially deteriorate the structural quality of the NWs by the creation of dislocated tilt and twist boundaries at the coalescence joints. So far, no attempts were made to unambiguously quantify the coalescence degree or to systematically correlate this effect with the structural perfection and luminescence properties of ZnO NW ensembles.

Here, we present a comprehensive characterization of self-assembled ZnO NWs grown by chemical vapour transport on Si(001), as desired for the monolithic integration of ZnO devices with the complementary metal oxide semiconductor (CMOS) technology. The examination of NW ensembles by scanning electron microscopy (SEM) reveals that a non-negligible fraction of NWs merge together forming coalesced aggregates during growth (Fig. 1). We show that the coalescence degree can be unambiguously quantified by a statistical analysis of the cross-sectional shape of the NWs (Fig. 2). The examination of the structural properties by X-ray diffraction (XRD) evidences that the NWs crystallize in the wurtzite phase, elongate along the *c*-axis, and are randomly oriented in plane. The luminescence of the ZnO NWs, investigated by photoluminescence (PL) and cathodoluminescence (CL) spectroscopy, is characterized by two bands, the near-band-edge emission and the characteristic defect-related green luminescence of ZnO. The correlation of scanning electron micrographs and monochromatic cathodoluminescence intensity maps reveals that: (i) coalescence joints act as a source of non-radiative recombination, and (ii) the luminescence of ZnO NWs is inhomogeneously distributed at the single NW level. Specifically, the near-band-edge emission arises from the NW cores, while the defect-related green luminescence originates from the volume close to the NW sidewalls (Fig. 3). Two-dimensional simulations of the optical guided modes supported by ZnO NWs (Fig.4) allow us to exclude waveguiding effects as the underlying reason for the luminescence inhomogeneities. We thus attribute this observation to the formation of a core–shell structure in which the shell is characterized by a high concentration of green-emitting radiative point defects as compared to the core.

References

[1] R. Yan et al., Nat. Photonics **3**, 569 (2009).
[2] G.-C. Yi et al., Semicond. Sci. Technol. **20**, S22 (2005).

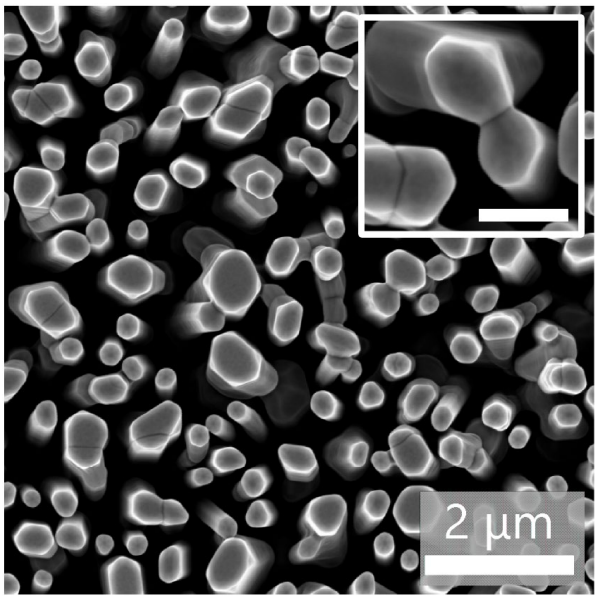

Fig. 1. Plan-view scanning electron micrograph of a representative ZnO NW ensemble. The inset shows a magnified plan-view scanning electron micrograph illustrating the formation of different types of coalesced NW aggregates. The scale bar in the inset represents 0.5 µm.

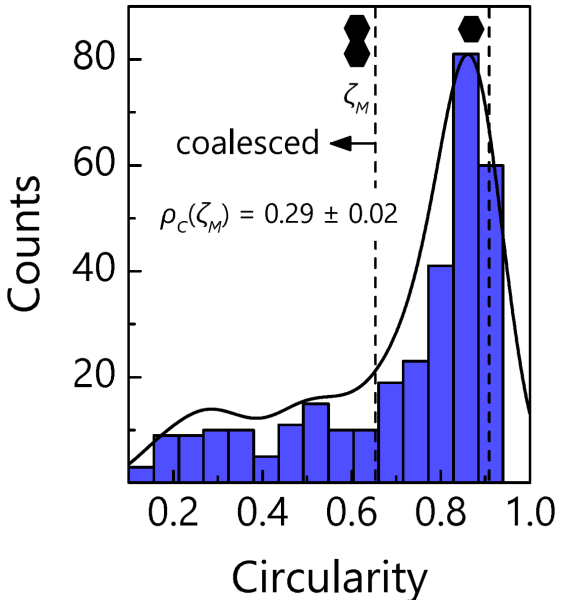

Fig. 2. Circularity histogram corresponding to the analysis of the cross-sectional shape of the NWs of the ensemble shown in Fig. 1. The circularity is defined as $C = 4\pi A/P^2$, where A and P are the NW cross-sectional area and perimeter, respectively. The solid line is a kernel density estimation. The vertical dashed lines indicate the circularity of the geometrical shapes shown close to them. The coalescence degree ρ_C (i.e., the ratio between coalesced NWs and the total number of objects) obtained using the criterion of a minimum circularity for uncoalesced NWs of $\zeta_M = 0.653$ is provided in the figure.

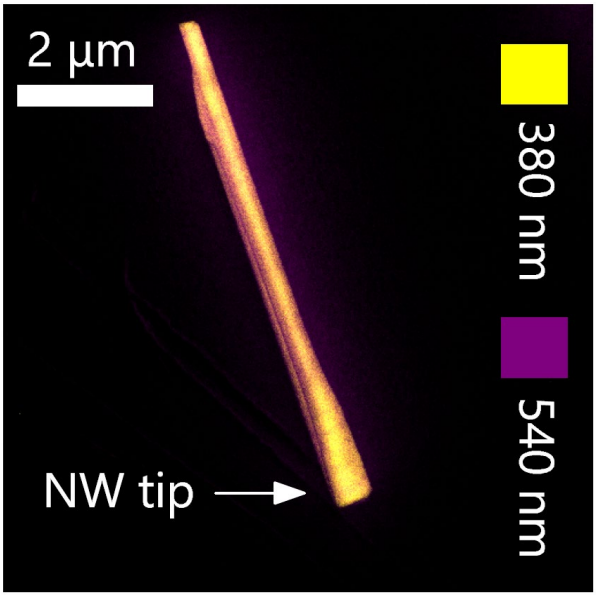

Fig. 3. Superimposed scanning electron micrograph and false-colour CL intensity maps at 380 (yellow) and 540 nm (purple) for a single ZnO NW mechanically transferred onto a Si wafer. Even though the near-band-edge emission (380 nm) is stronger close to the NW tip, it is generated in the core of the NW along its entire length. On the contrary, the green luminescence (540 nm) primarily arises from the volume close to the NW sidewall facets.

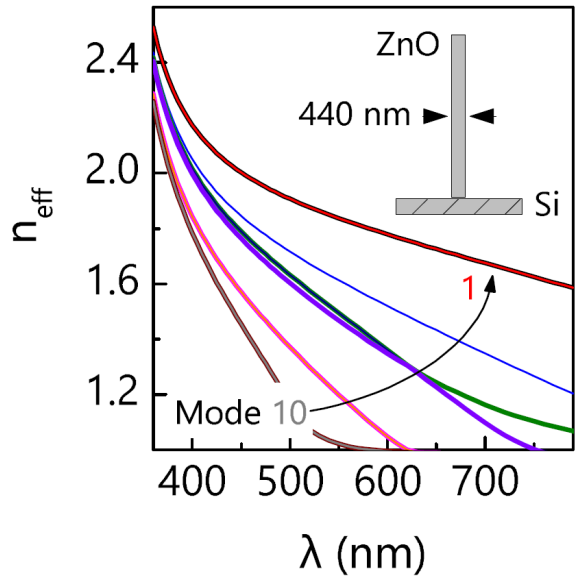

Fig. 4. Simulated effective refractive index for the first ten guided modes as a function of the light wavelength for a NW with a radius of 220 nm, i. e., the mean NW radius of the ensemble shown in Fig. 1. The inset illustrates the simulated structure, a single upright NW surrounded by air on a Si wafer. The simulation was performed using the software Lumerical FEEM, a finite element Maxwell equation solver based on the eigenmode method.

Analysis of metal gate workfunction fluctuations on MOSFETs variability using KPFM characterization and device simulation tools.

A. Ruiz[1], N. Seoane[2], S. Claramunt[1], A. García-Loureiro[2], M. Porti[1], M. Nafria[1]

[1]Electronic Engineering Department, Universitat Autònoma de Barcelona, Barcelona 08193, Spain
[2]CITIUS, Universidade de Santiago de Compostela, Santiago de Compostela 15782, Spain
Electronic address: ana.ruiz@uab.cat

1. Abstract

2D workfunction (WF) maps of a TiN layer were measured with Kelvin Probe Force Microscope (KPFM) with nanometer spatial resolution. These data were then introduced into a device simulator to analyze the effect of the polycristallization-related TiN metal gate WF fluctuations on the MOSFET electrical variability. The impact of the spatial distribution of such fluctuations was also investigated.

2. Introduction

Metal gates in recent technological nodes, due to their polycrystallinity, contain grains with different sizes and orientations. Therefore, workfunction fluctuations (WFs) are observed, which lead to threshold voltage variability between devices. Some works have analysed the impact of such WF fluctuations on the variability of MOSFETs. However, they use statistical models with assumptions that cannot represent the actual situation in a device. In this work, the impact of polycrystalline metal gates on the electrical characteristics of MOSFETs is investigated from KPFM data, which allows obtaining simultaneously topographical and WF fluctuations 2D maps at the nanoscale [1].

3. Experimental results

Fig. 1a shows a 520 nm x 240 nm topographical map of a 100 nm thick TiN layer deposited on a HfO2/Si substrate. It shows a granular structure, where the Grains (Gs) are surrounded by grain boundaries (GBs, depressions). Fig. 1b shows the measured WF map at the same surface region, and Fig. 2a shows a pixel to pixel correlation between the topographical and WF maps. Note that GBs tend to show lower WFs (WF < 4.1 eV) than nanocrystals.

From Fig. 1a, the Gs have been identified and the TiN granular pattern has been represented in Fig. 1c, where the GBs have been neglected. Gs with different maximum WF values are measured as shown in Fig. 2b, which corresponds to a 2D-histogram that relates the maximum WF and the maximum height of each grain in Fig. 1c. Note that although a continuous distribution of maximum WFs is measured, WFs are mostly concentrated at ~4.3 eV and, with smaller frequency, around ~4.5 eV, suggesting two predominant WFs values. This result is compatible with the presence of two grain orientations in the TiN layer ([111] and [200]) [2] whose WFs are separated by 200 mV, as confirmed by XRD analysis (Fig. 3). In addition, Fig. 2b indicates a much higher number of nanocrystals with low WF than with high WF.

Note that the data obtained from KPFM provide new information on the properties of the polycrystalline TiN layer, not considered in previous works. Besides the presence of nanocrystals with a continuous distribution of WFs (not only two discrete values), GBs with lower WF are also detected, which could also affect the variability of devices. Therefore, all these features should be taken into account when studying the WF fluctuations as a MOSFET variability source.

4. Simulations

To investigate the MOSFET variability related to the WF fluctuations linked to the polycrystallinity of the TiN layer, different WF distributions representing the metal gate of a MOSFET were considered. The maps shown in Fig. 1 have been divided to generate 100 non-overlapping 50 nm x 50 nm WF gate profiles. Next, these profiles were introduced into a 3D in-house-built drift-diffusion device simulator [3] as metal gate, to evaluate the device electrical characteristics of MOSFETs with a gate area of 50 x 50 nm^2. Two cases have been analyzed: (i) the actual WF distribution (Fig. 1b, experimental) (with GBs and a continuous distribution of WF for the Gs), and (ii) an approximated WF distribution, with two discrete values of the WF and without GBs, as in Fig. 1d. Note that the last is the customary approach when considering this kind of MOSFET variability source. To generate the approximated WF map (Fig. 1d), the grain pattern in Fig. 1c is the starting point. We generated an artificial WF map where GBs have been neglected and, for the Gs in Fig. 1c, two discrete and constant values, corresponding to the [111] and [200] orientations, were only considered. We have assigned 4.30 eV to the nanocrystals with WF lower than 4.4 eV and 4.5 eV to those with higher values, leading to WF maps as that shown in Fig. 1d. The MOSFET

characteristics for devices with GBs and continuous WFs distributions (Fig. 1b) and without GBs and discrete WFs distributions (Fig. 1.d) have been compared. Fig. 4 shows the off-current (I_{OFF}) and threshold voltage (V_T) distributions obtained for these two cases. Note that, the approximation (i. e., without GBs and with the discrete WF distribution), leads to a ~10% and ~18% reduction in σV_T and $\sigma \log(I_{OFF})$, respectively, and to larger mean values of the distributions (~0.12 V in the case of V_T).

The effect of the spatial location of the Gs in the MOSFET gate area has also been evaluated. As an example, Fig. 5 shows the impact that a single grain (with <WF>=4.3 eV) has on the V_T of the device, when located at different positions along the channel. The grain (inside the square in Fig. 5) was moved from the source end (X=0 nm) to the drain end (X=50 nm) to capture this effect. A device with a uniform gate with WF=4.3 eV was simulated as a reference, showing V_T=0.762 V. Fig. 5 indicates that, when compared to the reference value, different changes in V_T are produced, which depend on the position of the grain along the channel. Larger deviations from the uniform case are measured when the metal inhomogeneity is located close to the source.

5. Conclusion

The impact of the WF fluctuations of polycrystalline metal gates on the MOSFET variability has been analysed. The presence of GBs and the WF continuous distribution of the Gs need to be considered to obtain more realistic information. Moreover, the device characteristics and variability are also affected by the spatial distribution of such fluctuations.

This work has been partially supported by the Spanish AEI, Xunta de Galicia and ERDF (TEC2016-75151-C3-1-R, PID2019-103869RB-C32, RYC-2017-23312, PID2019-104834GB-I00, ED431F 2020/008).

References

[1] V. Iglesias et al., *Appl. Phys. Lett.*, 99, 10, Sep. 2011.
[2] K. Shubhakar et al, *Appl. Phys. Lett.*, 98. 2011.
[3] A. J. Garcia-Loureiro et al, *IEEE Trans. Comput. Des. Integr. Circuits Syst.*, 30, 6, 841–851, 2011.

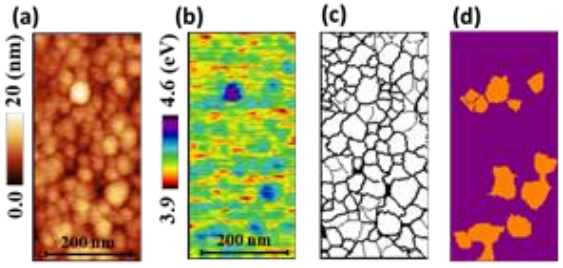

Fig.1. Topography (a) and WF (b) maps obtained with KPFM on a TiN layer. Binary mask (c) of the grains identified in (a) and generated WF map (d) from the binary mask. Orange corresponds to 4.5eV and purple to 4.3eV WFs values.

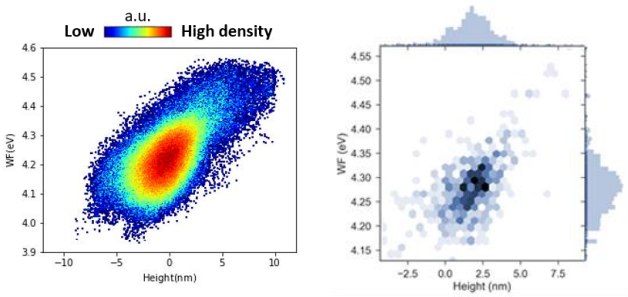

Fig.2. (a) Relationship between the WF and topography map, pixel by pixel. The general trend is that depressed areas show lower WF. (b) 2D-histogram showing the maximum WF vs maximum height of the grains, obtained from Fig. 1c. In the X axis, the height of each grain is determined with respect to the mean value of the topographical image (Fig. 1a).

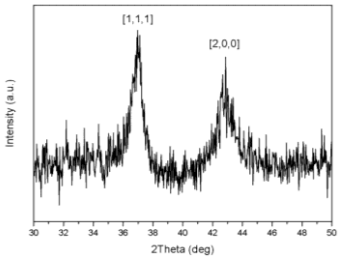

Fig. 3. XRD spectrum of the TiN layer, showing the [1,1,1] and [2,0,0] orientations of TiN.

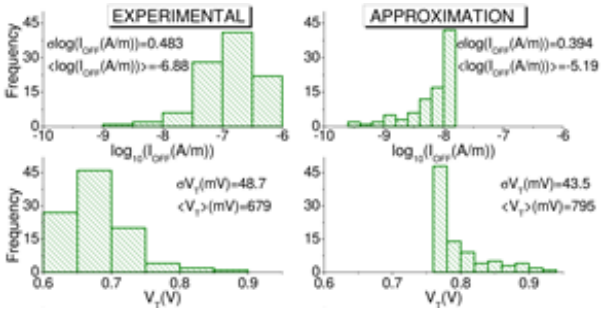

Fig.4. Distributions of I_{OFF} and V_T related to WF fluctuations in 50nmx50nm Si MOSFETs (at a drain bias of 50 mV) when considering the experimental, ie., GBs and a continuous WF distribution, (left column) and an approximated discrete (right column) WF distribution without GBs (Fig. 1b and 1d respectively). The mean value (< >) and standard deviation (σ) of the statistical ensembles are also indicated.

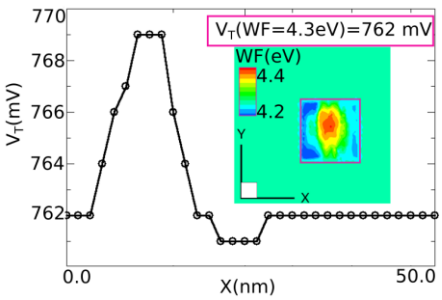

Fig.5. V_T spatial sensitivity to the TiN grain WF (in the square) when its position is swept along the channel (see green rectangle) of the MOSFET. The rest of the device gate has a constant WF=4.3 eV. V_T was evaluated at V_D=50 mV.

Luminescence of $GaP_{1-x}N_x$ grown by chemical beam epitaxy: correlation with growth conditions

Karim Ben Saddik[1], Jonas Lähnemann[2], Miguel Pérez-Cerdán[1], María Ángela Pampillón[1], Javier Grandal[3], Basilio Javier García[1]* and Sergio Fernández-Garrido[1]**

[1]Electronics and Semiconductors Group, Applied Physics Department, Universidad Autónoma de Madrid, C/ Francisco Tomás y Valiente 7, 28049 Madrid, Spain
[2]Paul-Drude-Institut für Festkörperelektronik, Leibniz-Institut im Forschungsverbund Berlin e.V., Hausvogteiplatz 5–7, 10117 Berlin, Germany
[3]Instituto de Sistemas Optoelectrónicos y Microtecnología (ISOM), Universidad Politécnica de Madrid, Avda. Complutense 30, 28040, Madrid, Spain
*E-mail: basilio.javier.garcia@uam.es / Phone: +34 91 497 4005 / Fax: +34 91497 3969
**E-mail: sergio.fernandezg@uam.es / Phone: +34 914975 880 / Fax: +34 91497 3969

The incorporation of small amounts of N into GaP induces an indirect-to-direct band gap transition, as described by the band anticrossing (BAC) model [1]. In addition, for a N mole fraction x of 0.021, the ternary compound $GaP_{1-x}N_x$ has the same lattice parameter as Si, which paves the way for the monolithic pseudomorphic integration of III-V optoelectronic devices with the widespread and highly scalable Si manufacturing technology.

In this work, we analyze the correlation between the luminescence of $GaP_{1-x}N_x$ alloys grown on GaP/Si(001) substrates by chemical beam epitaxy (CBE) with both the growth parameters and the sample morphology. Figure 1 presents a growth diagram that describes the dependence of the chemical composition of $GaP_{1-x}N_x$ alloys grown by CBE on both the substrate temperature and the flux of the N precursor (DMHy), when keeping constant the remaining parameters. The N content increases linearly with the flux of DMHy and decreases exponentially with the substrate temperature. Importantly, the combination of low substrate temperatures and high DMHy fluxes enhances the incorporation of N but results in samples with phase separation and rough surface morphologies. Figure 2(a) shows the photoluminescence (PL) spectra at 12 K of $GaP_{1-x}N_x$ layers grown at 500 °C with increasing fluxes of DMHy. The luminescence is red-shifted from about 2.1 to 1.87 eV as the N content increases from 0.009 to 0.044, a shift well described by the BAC model [1]. Figure 2(b) summarizes the influence of the growth temperature on the PL for a given flux of DMHy. As the growth temperature is increased from 475 to 575 °C, the N content decreases and the PL intensity steadily increases. Interestingly, the overall comparison of the two series of samples reveals that the highest PL intensity is obtained for the sample with x = 0.018, i.e., the one with the closest lattice match to the Si substrate. To elucidate whether the enhancement of the PL intensity is exclusively due to a reduction in the lattice-mismatch, we compare in Fig. 2(c) the low temperature PL spectra of two samples grown with comparable N contents (x = 0.008) within the same growth regime, but at two different temperatures, namely, 500 and 575 °C. The sample prepared at 575 °C exhibits an integrated PL intensity which is 3.5 times larger than that of the sample grown at 500 °C. We thus conclude that higher substrate temperatures may hinder the creation of non-radiative point defects. To assess the spatial distribution of the luminescence as well as to correlate its properties with the sample morphology, the samples are simultaneously investigated by cathodoluminescence (CL) spectroscopy and scanning electron microcopy. As an example, Figs. 3(a) and 3(b) present maps of the peak emission wavelength of spatially resolved CL spectra for two different samples with x = 0.06 and 0.03, respectively. As can be seen, we detect spatial fluctuations in the emission wavelength that become more pronounced as the N content is increased. Based on the present study, we conclude that: (i) samples with comparable mean compositions exhibit different luminescence properties depending on how they are grown, and (ii) even though low substrate temperatures and DMHy fluxes facilitate the homogenous incorporation of N while preserving a smooth surface morphology, high substrate temperatures enhance the luminescence efficiency. Therefore, it would be of high interest to explore the effect of rapid thermal annealing processes on the luminescence properties of $GaP_{1-x}N_x$ alloys grown by CBE. Those studies are underway.

References

[1] W. Shan et al. Appl. Phys. Lett. **76**, 3251 (2000).

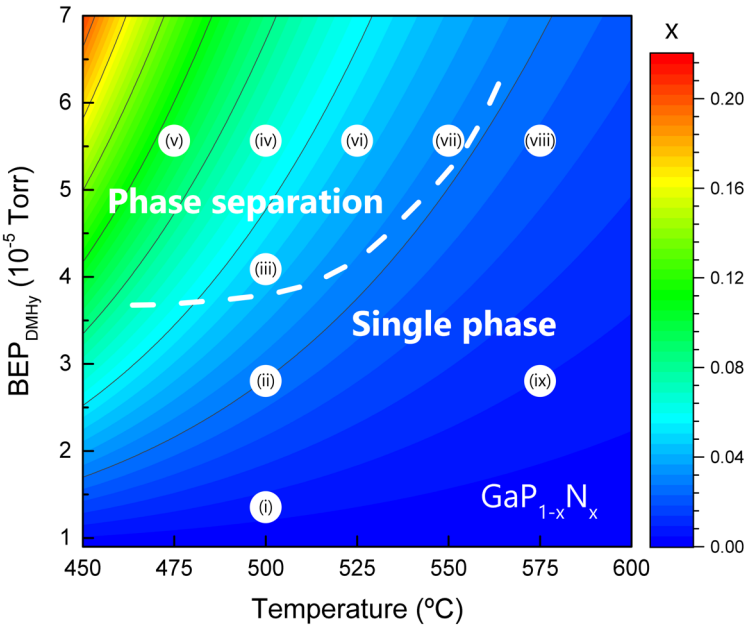

Fig. 1 Growth diagram depicting the dependence of the incorporation of N into $GaP_{1-x}N_x$ on the growth temperature and the beam equivalent pressure (BEP) of DMHy, which is directly proportional to its flux. The N mole fraction is displayed as a contour plot with a linear scale. The diagram holds for given BEP values of the Ga and P precursors (TEGa and TBP, respectively). The dashed line shows the boundary between the growth conditions that result in single phase and phase-separated $GaP_{1-x}N_x$ layers. The labels (i)–(ix) indicate the growth conditions of the samples investigated within the framework of this study. These labels are also used in Figs. 2 and 3.

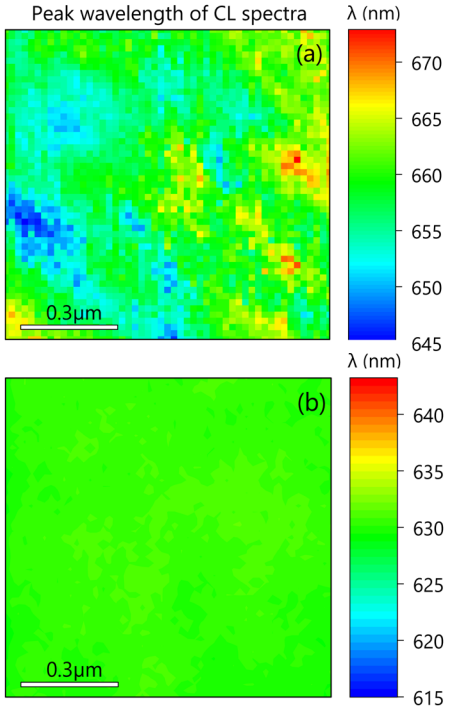

Fig. 3 1×1 μm² spatially-resolved CL maps at 30 K of the emission wavelength of two $GaP_{1-x}N_x$ layers with (a) x = 0.06 and (b) x = 0.03. These samples are those labelled as (iv) and (ii), respectively, in Fig.1. The peak emission wavelength is obtained from a Gaussian fit to the near-band-edge emission in a hyperspectral CL map.

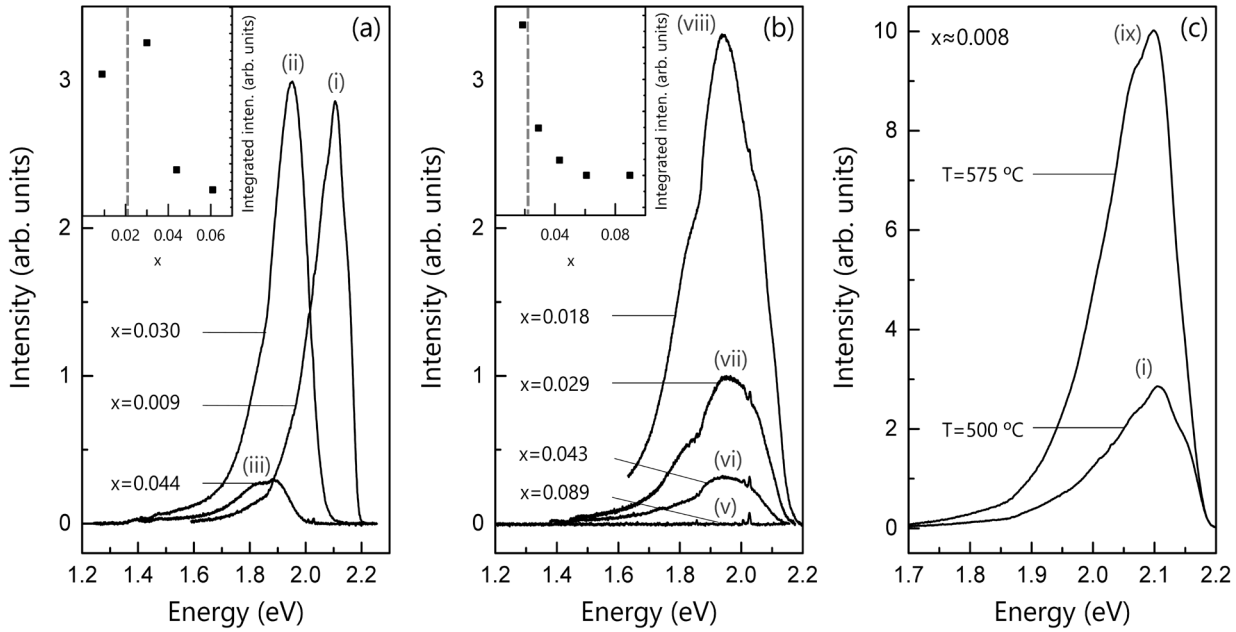

Fig. 2 Low-temperature (12 K) PL spectra of $GaP_{1-x}N_x$ layers grown (a) at 500 ºC with different fluxes of DMHy, the N mole fraction increases from 0.009 to 0.044 as the DMHy flux is varied from 1.4×10^{-5} to 5.6×10^{-5} Torr, and (b) using a BEP of DMHy of 2.8×10^{-5} Torr at increasing substrate temperatures from 475 to 575 ºC, which results in decreasing N mole fractions from 0.089 to 0.018. The insets show the integrated intensity of the PL spectra (including additional samples) as a function of the N mole fraction. The vertical dashed lines indicate the N mole fraction for which the $GaP_{1-x}N_x$ alloy is lattice matched to Si, i.e., x = 0.021. (c) Low-temperature (12 K) PL spectra of two $GaP_{1-x}N_x$ layers with approximately the same N mole fraction (x ≈ 0.008) but grown at different substrate temperatures, as indicated in the figure. The intensity scales in (a)–(c) are directly comparable. The labels (i)–(ix) can be used to identify the growth conditions of the different samples using Fig. 1.

Effects of Surface Treatments on the Performance of CdZnTeSe Radiation Detectors

Authors: L. Martínez-Herraiz[1], E. Ruiz[2], A. F. Braña[2], J.L. Plaza[1].

1. Crystal Growth Laboratory, Material Science Department, Universidad Autónoma de Madrid, Spain.

2. Electronics and Semiconductors Group, Applied Physics Department, Universidad Autónoma de Madrid, Spain.

Author e-mail: lidia.martinezh@estudiante.uam.es

1. Abstract

Room temperature detectors for X-ray and gamma-ray radiation are of great interest in a wide range of fields, such as medical and astrophysical space imaging, safety systems in nuclear power industry and high energy physics installations, renewable energy (solar cells), photodiodes, photoconductors, infrared windows and homeland security **[1,2]**.

The requirements that a suitable material for X-ray and gamma detection at room temperature have to fulfill are the following:

High atomic number, high density, high resistance and a wide band-gap. These properties ensure that a large area of the bulk material is active in allowing the charge generation, as well as carrying generated charge throughout detector material to metallic contacts, and finally, to readout electronics as shown in **figure 1**.

Despite the efforts made over decades in the development of CdTe and CdZnTe as X-ray and gamma radiation detectors at room temperature, their mass production is not possible. This is due to the fact that these materials present high concentrations of Te secondary phases and lack of homogenization as a result of Zn segregation, therefore reducing detector performance. Recent publications **[3]** propose the addition of Se (CdZnTeSe), as a solution for the reduction of secondary phases of Te and Zn segregation.

But even when a high quality crystal is available, unwanted chemical impurities and lattice imperfections, are introduced during crystal manufacturing processes (slicing, lapping, polishing and surface treatment), which causes donor and acceptor states **[4]**. These levels behave as recombination centers, which results in the deterioration of the spectral sensitivity of the device.

In the present study, information is provided on contact formation after crystal surface polishing grade and its influence on device performance.

Experimental studies of CdZnTeSe grown by the Vertical Gradient Freeze (VGF) method. After metallic contacts of Au, with planar geometry guard diode **figure 2**, was deposited by thermal evaporation. The differences in polishing processes on the device performance will be studied. In this way devices fabricated on samples polished with different alumina powder grain sizes (1 μm and 0.03 μm) will be analyzed.

The methodological approach taken in this study is a mixed methodology based on electrical and morphological characterization of the contacts. As follows, an important diode parameter, as barrier height (ϕ_{Bo}), is obtained from I-V plots **figure 3** using Thermionic Emission Theory **[1]**. Those curves also provided leakage currents and sensor breakdown voltages.

Moreover, surface topography and contact thicknesses were obtained with Atomic Force Microscopy (AFM) measurements. Electrostatic mode (EFM), derived from AFM estimations, is sensitive to the electrostatic force between sample and tip. That force is often due to surface local potential, is directly related to semiconductor-metal work function **[5]**. Barriers height obtained oscillate between 0.9 to 0.6 eV. Although barrier height has never been measured for Au-CdZnTeSe, these values are too close to CdZnTe data **[6]**.

References

[1] C. D. Balbasi, et al., *Appl. Phys.* A, ***126***, 614 (2020).
[2] S. K. Chaudhuri, et al, *IEEE Electron Device Lett.*, ***41***, 9 (2020).
[3] U. N. Roy, et al., *Nature Sci. Rep.*, **9**, 1620 (2019).
[4] O. Sik, et al., *Phys. Scr.*, **2013**, T157 (*2013).*
[5] J. F. Bresse,et al., *Microchim. Acta*, ***132,*** 449–455 (2000).
[6] S.Bell, et al., *Appl. Surf. Sci.*,**427**, 1257-1270 (2018).

2. Figures Appendix

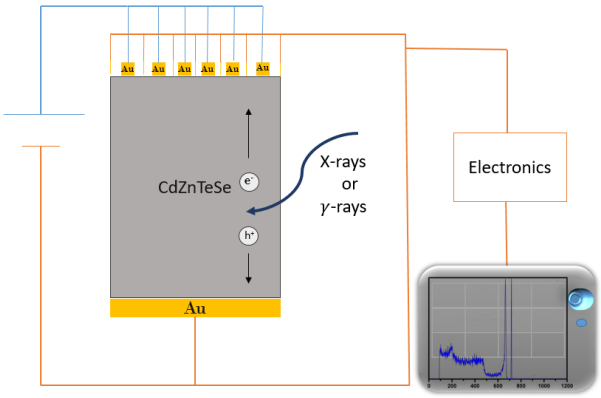

Fig.1. Simple schematic of the performance of a CdZnTeSe nuclear sensor.

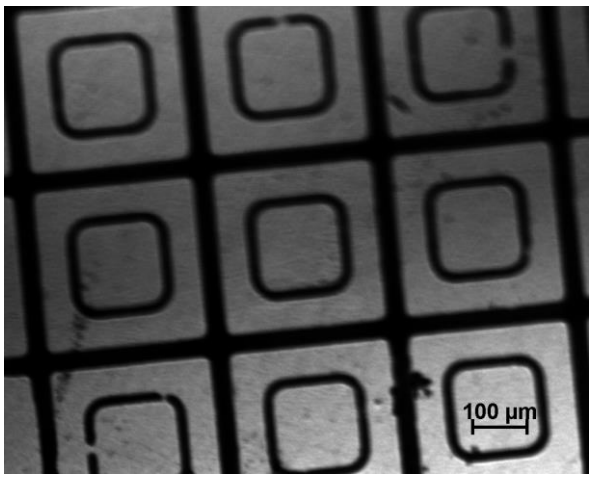

Fig.2. Guard diode configuration used in CdZnTeSe sensors.

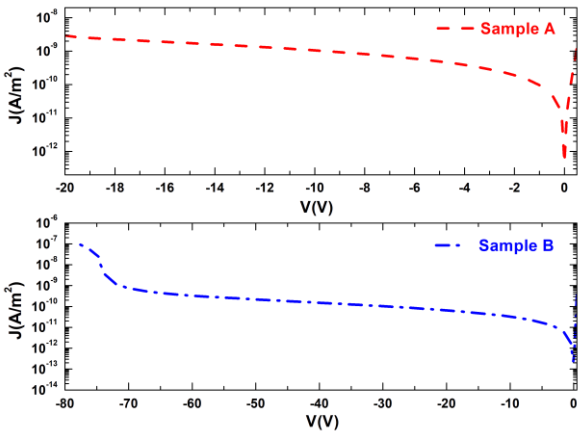

Fig.3. Current of the CdZnTeSe detectors versus applied voltage. a) The surface of sample A was treated by polishing with 1 µm particle size alumina suspension and b) sample B was treated by polishing with 0.3 µm particle size alumina suspension.

10 June 2021

Thursday

ORAL SESSION II

Photovoltaic, optoelectronic and photonic devices

Thursday 10

9:00-10:15

Chairperson: J. R. Ramos-Barrado (Universidad de Málaga)

High-efficiency *intrinsic*-Vertical-Tunnel-Junction multi-band-gap concentrator solar cells up to 15,000 suns

A. García-Loureiro[1,2*], E. F. Fernández[3**], N. Seoane[1], P. Rodrigo[3], E. Comesaña[2] and F. Almonacid[3]

[1] Centro Singular de Investigación en Tecnoloxías de Información, University of Santiago de Compostela, Spain
[2] Departamento de Electrónica e Computación, University of Santiago de Compostela, Spain
[3] Centro de Estudios Avanzados en Ciencias de la Tierra, Energía y Medio Ambiente, University of Jaén, Spain

Corresponding author: *antonio.garcia.loureiro@usc.es; **eduardo.fernandez@ujaen.es

Abstract

Ultra-high concentrator photovoltaic (UHCPV) technology, usually referred to systems with concentrations above 2000 suns, has been signaled as a promising research avenue for achieving CPV systems with higher efficiencies and lower cost [1]. This can be explained considering that the theoretical efficiency (η) of solar cells tends to grow with concentration while the amount of expensive semiconductor material is strongly reduced. Despite this potential, significant efforts are still needed to overcome several technological challenges, namely: a) solar cells with efficiencies peaking at UH levels, b) high-efficiency optical designs able to reach UH and c) cooling strategies tailored to remove, or even exploit, the heat waste. This work is focused on proposing a solution to the first concern. Multi-junction (MJ) cells have demonstrated impressive efficiencies (η) above 45% for concentrations (Cratio) within 100-1000 suns. The most critical limiting factor of horizontal MJ cells for increasing η with Cratio is related to the huge series resistance (Rs) losses produced at UH light intensities. This is due to the unavoidable trade-off between the shadowing of the front metallic contact and the Rs, as well as by the Rs of the different semiconductor layers of the stack. In this sense, big efforts are being conducted by the community for understanding the IV dynamics and developing MJ cells with a high performance at UH levels [2, 3, 4]. Despite of this, to the date, the peak of efficiency of standard MJ solar cells seems to be limited to concentrations factors below 1000 suns, no matter how the front-grid pattern is designed or how much the area of the cell is reduced [4]. Therefore, it is not possible to completely exploit the theoretical increase of η with Cratio and the cost reduction capacity of UHCPV systems.

In this work, we investigate the main features of the so-called intrinsic-Vertical-Tunnel-Junction (i-VTJ) multi-band-gap (MBG) solar cell recently presented by the authors [6, 7]. Figure 1 shows the fundamental unit of the proposed structure, which consists of two identical subcells connected in series using a highly doped tunnel junction (TJ). In addition, an intrinsic semiconductor layer (i-layer) is included between the pn junctions. This layer reduces the recombination rate and allows the width to be increased. In addition, η is enhanced since the electrical field, responsible for charge carrier separation, covers most of the illumination area. Figure 2 shows the impact of the thickness of the i-layer on the Voc and FF for various materials. In addition, Figure 3 shows a scheme (left) of a i-VTJ made up of GaAs/Si/Ge and the efficiency (right) of various materials up to 15,000 suns. As can be seen, the solar cells achieve outstanding η at UH levels, > 40% at 15,000 suns for 2BG and 3BG i-VTJ cells. The ability of the proposed structure to lower the cost of CPV are shown in figure 4. The key features, and potential, of the device will be presented at the conference and final manuscript. Other better band-gap combinations with potential efficiencies above 60% at UH levels will be also discussed.

References

[1] C. Algora and I. Rey-Stolle, Next Generation of Photovoltaics, pp. 23-60., Springer, 2012.
[2] M. Ochoa, E. Barrigón, L. Barrutia, I. García, I. Rey-Stolle and C. Algora, "Limiting factors on the semiconductor structure of III–V multijunction solar cells for ultra-high concentration (1000–5000 suns)," Progress in Photovoltaics: Research and Applications, vol. 24, no. 10, p. 1332, 2016.
[3] B. Paquette, A. Boucherif, V. Aimez and R. Arès, "Novel multijunction solar cell design for low cost, high concentration systems," Progress in Photovoltaics: Research and Applications, vol. 24, no. 2, p. 150, 2016.
[4] A. Braun, B. Hirsch, A. Vossier, E. Katz and J. Gordon, "Temperature dynamics of multijunction concentrator solar cells up to ultra-high irradiance," Progress in Photovoltaics: Research and Applications, vol. 21, no. 2, pp. 202-208, 2013.
[5] A. Vossier, B. Hirsch, E. Katz and J. Gordon, "On the ultra-miniaturization of concentrator solar cells," Solar Energy Materials and Solar Cells, vol. 95, no. 4, pp. 1188-1192, 2011.
[6] N. Seoane, E. F. Fernández, F. Almonacid and A. García-Loureiro, "Ultra-efficient intrinsic-Vertical-Tunnel-Junction (i-VTJ) structures for next-generation concentrator solar cells," Progress in Photovoltaics: Research and Applications, vol. in press, 2020.

[7] E. F. Fernandez, N. Seoane, F. Almonacid and A. Garcia-Loureiro, "Vertical-Tunnel-Junction (VTJ) Solar Cell for Ultra-High Light Concentrations (>2000 Suns)," IEEE Electron Device Letters, vol. 40, no. 1, p. 44, 2019.

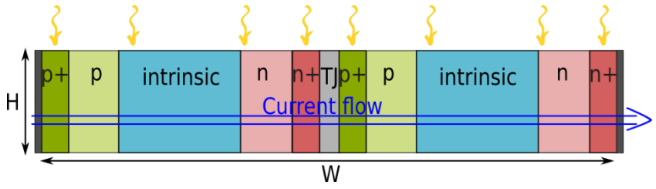

Fig. 1. Scheme of the fundamental unit of the *i*-VTJ solar cell (H = height and W = width).

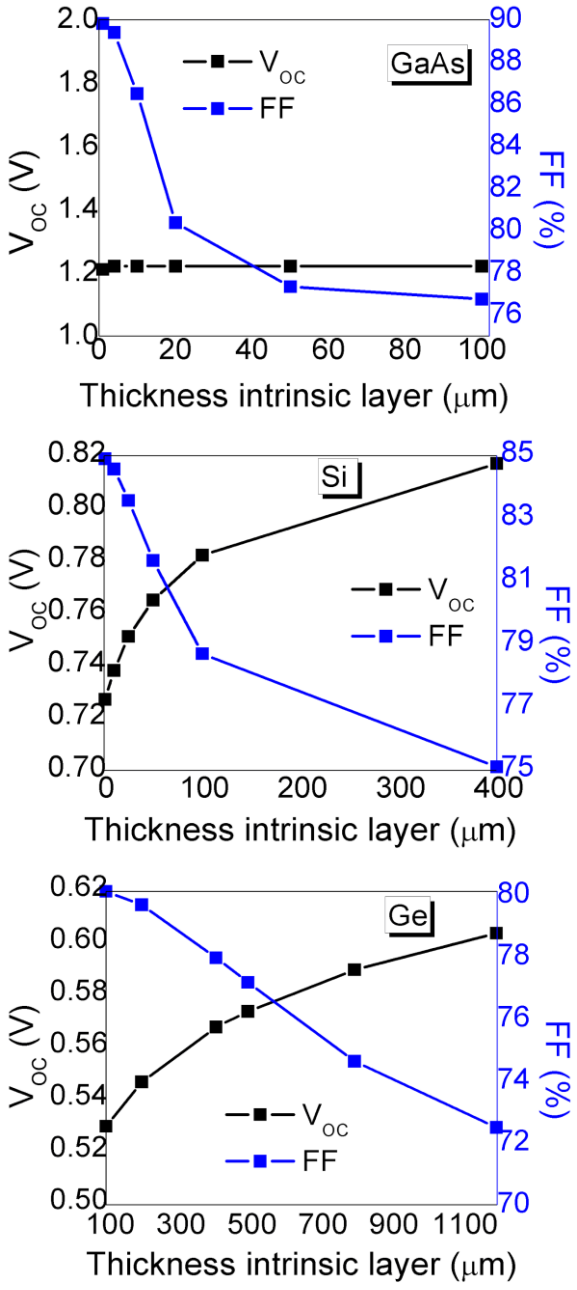

Fig. 2. Variation of open-circuit voltage (V_{oc}) and fill factor (FF) with the thickness of the intrinsic layer at 10000 suns.

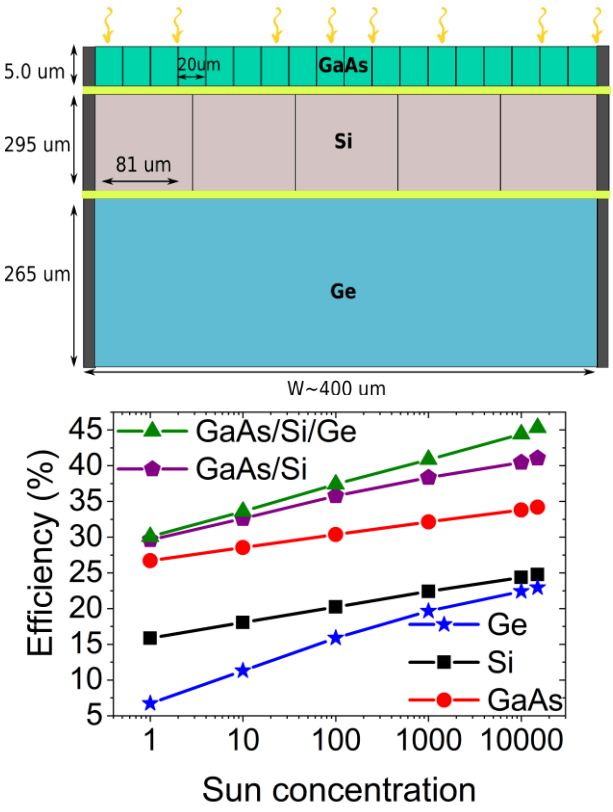

Fig. 3. Scheme (top) of a 3BG i-VTJ solar cell for a concentration of 10,000 suns, and efficiency versus concentration (bottom) for GaAs, Si, GaAs/Si and GaAs/Si/Ge *i*-VTJ solar cells up to 15,000 suns.

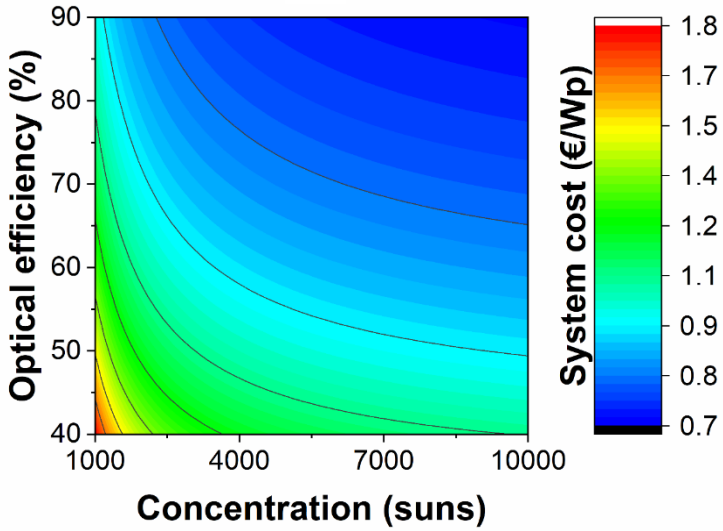

Fig. 4. Contour plot of expected system cost per Watt-peak (Wp) as a function of the sun concentration and system optical efficiency (Generator cost = 130 €/m^2, BOS cost = 0.34 €/Wp and cell cost = 12 €/cm^2).

Influence of Spray Pyrolysis Deposition Technique on the Performance and stability of Polymer Solar Cells

Enas Moustafa, Josep Pallarès and Lluis F. Marsal*

Department of Electric, Electronic, Engineering and Automatic, Universitat Rovira i Virgili, 43007, Tarragona, Spain.

E-mail: enas.moustafa@urv.cat, josep.pallares@urv.cat, lluis.marsal@urv.cat.

1. Abstract

In this research work, noteworthy progress has been achieved to fabricate inverted polymer solar cells (iPSCs) using spray pyrolysis technique to deposit a thin film of ZnO as interfacial layer. A standard iPSCs fabricated by spin coating (SC) technique has been used as reference cells. It has been observed that the performance of the iPSCs fabricated by ZnO-SP were quite similar to the reference samples fabricated by the ZnO-SC technique. In addition, Higher stability has been observed for the ZnO-SP devices more than the ZnO-SC ones. Hence, this promising spray pyrolysis technique might be a breakthrough forward step for commercializing the inverted polymer solar cell based on mass production scale.

2. Introduction

Polymer solar cells have been extensively investigated as promising solar cells due to their flexibility, low fabrication cost, lightweight and being capable of engaging with other electronic applications [1]. The deposition technique of the layers is an important factor which should be mentioned because it influences the interfaces between the layers and the film surface morphology. Spray pyrolysis technique (SP) is widely used for thin film deposition which matches the industrial mass production not only lab-scale. Moreover, it is a low cost, facile technique that does not require any vacuum or complicated conditions [2].

3. Device fabrication

In this work, Spray pyrolysis (SP) and spin coating (SC) techniques have been used to prepare a thin film of ZnO as Electron transporting layer (ETL) in the fabricated devices. The structure of the iPSCs is ITO/ZnO /PTB7-Th: $PC_{70}BM$/V_2O_5/Ag. The ZnO precursor solution has been synthesized by sol gel method [3]. For the spin coating technique, the ZnO solution spun over the pre-cleaned ITO substrate at 3000 rpm for 30 s, then kept for 1 h to be annealed at 200 ºC [3]. For the spray pyrolysis technique, the synthesized solution was diluted with ethanol by 1:6 v/v. It has been deposited over the pre-heated ITO at 350 ºC and the sprayed films left to anneal for 1 h [4]. The active polymer blend was prepared by dissolving 25 mg/ml of PTB7-Th:$PC_{70}BM$ 1:1.5 w/w in chlorobenzene with 3 % DIO. Then the blend filtered and spun over the ZnO layer without heat treatment. Finally, V_2O_5 and Ag films were thermally evaporated.

4. Results and discussions

A performance comparison has been carried out between the iPSCs used the SP and SC techniques to deposit ZnO-ETL. Fig.1. (a) illustrates the current density-voltage performance curve (J-V) under AM1.5 illumination. Table 1. shows the detailed performance parameters of the fabricated devices. From the obtained results it can be noticed that all the fabricated cells have the same V_{OC}. It is worth mentioning that the generated J_{SC} for the iPSCs fabricated by the ZnO sprayed using SP technique was higher than the ones deposited by SC technique. Fig.1. (b) displays the J-V characteristic curves of the iPSCs under dark. It has showed that a higher leakage current appeared for the iPSCs fabricated by the ZnO-SP technique. Fig.1. (c) shows the impedance spectroscopy (IS) of the T_{80} (devices reached 80% from the initial value) of degraded ZnO-SC and ZnO-SP iPSCs with bias voltage at Voc. It can be noticed that a typical semicircle behaviour of Nyquist plot has been obtained for the degraded ZnO-SP devices but, some deviation from the typical shape appeared for the ZnO-SC iPSCs. This observed behaviour might be attributed to the degradation over time. In addition, it is worth mentioning that the created impeded traps in the ZnO-SC devices were more than that produced in the ZnO-SP iPSCs. Which proof the higher stability of devices fabricated by ZnO-SP than that of the ZnO-SC ones.

References

[1] S. K. Hau, H. L. Yip and A. K. Jen, “A Review on the Development of the Inverted Polymer Solar Cell Architecture,” Polymer Reviews J, vol. 50, pp. 474–510, Nov. 2010.

[2] A. Tecaru, A. I. Danciu, V. Muşat, E. Fortunatoa and E. Elangovan, “Zinc Oxide Thin Films Prepared by Spray Pyrolysis,” Optoelectronics and Advanced Materials J, vol. 12, pp. 1889 – 1893, Sep. 2010.

[3] J. G. Sánchez, V. S. Balderrama, S. I. Garduño, E. Osorio, A. Viterisi, M. Estrada, J. F-Borrull, J. Pallarès and L. F. Marsal, “Impact of Inkjet Printed Zno Electron Transport Layer on The Characteristics of Polymer Solar Cells,” RSC advanced, vol. 8, pp. 13094–13102, Mar. 2018.

[4] E.Moustafa, J. G. Sánchez, L. F. Marsal and J. Pallarès, “High Efficiency Inverted Polymer Solar Cells Fabricated Based On ZnO-ETL Utilizing Spray Pyrolysis Technique,” EUPVSEC, pp. 1-4, April. 2020.

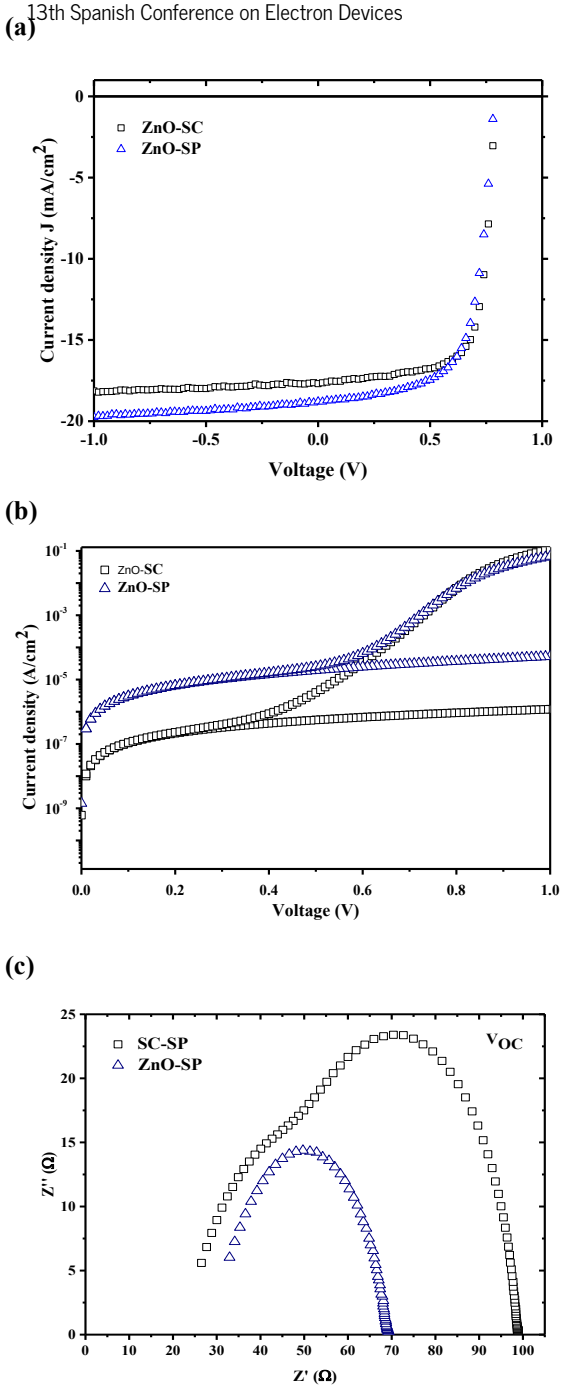

Fig.1. J-V characteristic curves of ZnO-SC and ZnO-SP fabricated iPSCs a) under illumination conditions AM 1.5 and b) at dark condition (Symbols for experimental data and the lines for the fitting), (c) The IS at V_{OC} under 1.5 AM illumination of the ZnO-SC and ZnO-SP degraded iPSCs.

Samples	**V_{OC} (V)**	**J_{SC} mA/cm²**	**FF**	**PCE %**	**R_S Ω.cm²**	**R_P Ω.cm²**
ZnO-SC	0.79	17.84	0.69	10.00	1.48	989
ZnO-SP	0.78	18.62	0.67	9.68	2.49	973

Table 1. Solar Cells Performance parameters for the iPSCs Fabricated by SC and SP Techniques.

Flexible and transparent supercapacitors based on ZnO nanowires

Elena Navarrete-Astorga[1], Jorge Rodríguez-Moreno[1], M. Cruz López-Escalante[1], Juan J. Peinado-Pérez[1], Francisco Martín[1], Enrique A. Dalchiele[2], José Ramón Ramos-Barrado[1]

[1]Universidad de Málaga, Departamentos de Física Aplicada I & Ingeniería Química, Laboratorio de Materiales y Superficies (Unidad Asociada al CSIC), E29071 Málaga, Spain
[2]Instituto de Física, Facultad de Ingeniería, Herrera y Reissig 565, C.C. 30, 11000 Montevideo, Uruguay

1. Introduction

The development of flexible and optically transparent devices are the consequence of the emerging proliferation in portable intelligent electronic devices, such as panels, displays or phones for example [1], [2]. Advances in flexible transparent power sources such as Li-ion batteries or supercapacitors are important for the market demands and they are expected to have high optical transparency and a good energy storage, also under deformation conditions.

In this work we present a flexible and optically transparent supercapacitor based on ZnO nanowires, which have a good transmittance and its capacitance is now the subject to improve.

2. Materials and experimental

Thin transparent and flexible ITO/PET sheets from Sigma-Aldrich were used as substrates for the electrodes. ZnO nanowires (ZnO NW) were electrochemically grown by the use of an AUTOLAB potentiostat, from a solution of 1mM Zn acetate and 0.1 M Na acetate, from Sigma-Aldrich. The grown was carried out under 70 ºC by the use of a thermal bath, and oxygen was bubbled during the chronoamperometry process, set during 5, 15, 30 and 60 minutes. Once the electrodes were made, a polymeric electrolyte were synthesized by our previous publication [3]. To make the symmetric supercapacitors, two electrodes (grown during the same time) were dipped into the electrolyte solution and then stack together to form the supercapacitor. Charge-discharge curves were carried out with a Biologic Potentiostat, and cyclic voltammetries were obtained by a Potentiostat from Autolab. Transmittance spectra were obtained from a VARIAN spectrophotometer.

3. Results and discussion

Charge-discharge curves carried out at ±1µA showed a potential peak of 0.5 V for the samples grown during 5, 15 and 60 min, and 0.25 V for the sample grown during 30 min. Under deformation conditions, the potential peak was the same. Fig. 1 shows the charge-discharge curves for the 15 min sample in a plane and bending position.

Cyclic voltammetries were carried out for all the samples at different scan rates of 25, 50, 75 and 100 mV s^{-1}, setting a potential window between -1 and 0.5 V. From these measurements, the specific values of capacitance, energy and power were calculated. These values were improved at higher scan rates, as we expected. Best values were obtained for the supercapacitor made with two electrodes grown during 30 min, obtaining a specific capacitance of 5.6 µF cm^{-2}, an energy of 6.3 µJ cm^{-2} and a power of 0.4 µJ s^{-1} cm^{-2}, at a scan rate of 100 mV s^{-1}.

Optical transmittance spectra were obtained (Fig. 2), showing values from 48.3 to 75.4 % at 550 nm, which is the wavelength which the photopic eye sensitivity function has maximum sensitivity. The best value was for the supercapacitor made with two electrodes grown during 5 min, as expected. A picture of the samples is shown in Fig. 3.

References

[1] J. Li, Q. Jiang, N. Yuan, and J. Tang, “A Review on Flexible and Transparent Energy Storage System,” *Materials (Basel).*, vol. 11, no. 11, p. 2280, 2018, doi: 10.3390/ma11112280.

[2] W. Zhao, M. Jiang, W. Wang, S. Liu, W. Huang, and Q. Zhao, “Flexible Transparent Supercapacitors: Materials and Devices,” *Adv. Funct. Mater.*, vol. n/a, no. n/a, p. 2009136, Dec. 2020, doi: https://doi.org/10.1002/adfm.202009136.

[3] J. Rodríguez-Moreno, E. Navarrete-Astorga, E. A. Dalchiele, L. Sánchez, J. R. Ramos-Barrado, and F. Martín, “Polyvinylpyrrolidone-LiClO4 solid polymer electrolyte and its application in transparent thin film supercapacitors,” *J. Power Sources*, vol. 237, pp. 270–276, 2013, doi: 10.1016/j.jpowsour.2013.03.043.

Acknowledgements

The authors are grateful to Programa Operativo FEDER Andalucía of Spain for the financial support received through the project UMA18/FEDERJA039.

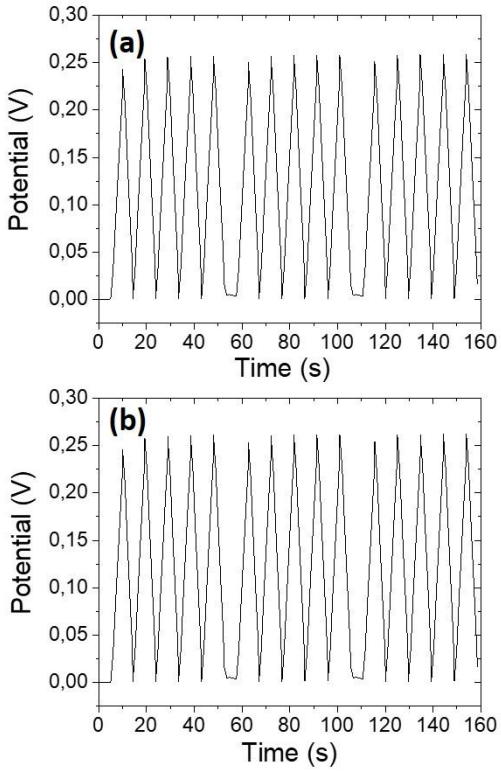

Fig.1. Charge-discharge curves for the symmetric supercapacitor made from two electrodes grown during 30 min (a) plane position (b) bending position.

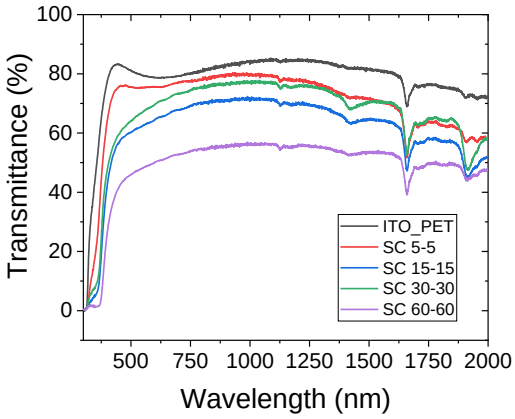

Fig.2. Optical transmittance for the symmetric supercapacitors made from electrodes grown during 5, 15, 30 and 60 minutes.

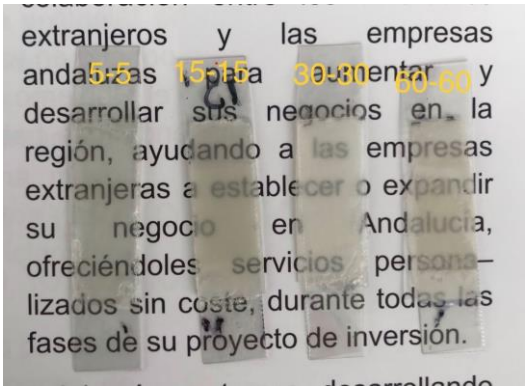

Fig.3. Photo of the four flexible supercapacitors where the transmittance can be appreciated.

Influence of graphene on hybrid perovskites-based solar cells performance

Carlos Redondo-Obispo[1,3], Teresa S Ripolles[1], Esteban Climent-Pascual[2], Alicia de Andrés[3], Ángel Luis Álvarez[1] and Carmen Coya[1*]

[1]Escuela Técnica Superior de Ingeniería de Telecomunicación (ETSIT), Universidad Rey Juan Carlos, 28933 Madrid, Spain
[2] Escuela Técnica Superior de Ingeniería Industrial, Universidad Politécnica de Madrid, C/ José Gutiérrez Abascal 2, 28006 Madrid, Spain.
[3]Instituto de Ciencia de Materiales de Madrid (ICMM), Consejo Superior de Investigaciones Científicas (CSIC), Sor Juana Inés de la Cruz 3, 28049 Madrid, Spain,
*carmen.coya@urjc.es

1. Abstract

Novel and disruptive applications can be provided by the synergy between different types of materials with different functionalities that could not be achievable by other means. The excellent properties that hybrid perovskites provide on one hand, and those of graphene on the other, can envision great enhancement of devices properties. This work focuses on photovoltaic applications, where hybrid perovskites solar cells (PSCs) have already demonstrated outstanding power conversion efficiencies (PCEs), reaching a certified 25.5% efficiency of photovoltaic devices for 3D Pb-based perovskites in a record time.[1] The incorporation-*doping*- of graphene (G) and graphene-related materials (GRM) in the PSC devices is a promising route toward applications and improvements in performance and, very important for its commercial launch, stability.[2,3,4] Carbon-based materials, including carbon nanotubes (CNTs), graphite and graphene and its derivatives, have proven to be helpful due to their stability, reasonable cost, and easy manufacturing on an industrial scale.

PSCs have surpassed CIGs and CdTe, but using low-temperature and *cost-effective methods*, revolutionizing existing technologies with simple layered-structured devices: i.e. transparent electrode/hole transport layer(HTL)/active layer/electron transport layer(ETL)/metal contact (Figure 1). The different active layers are deposited by solution processed methods. Most of the advances in the performance of PSCs have resulted from improvements in device architecture and material composition.

In this work, we study and compare the effect of the incorporation of pristine graphene flakes in a) the active layer (perovskite precursor solution $MAPbI_3$ ($MA = CH_3\text{-}NH_3^+$)) and b) in the PEDOT:PSS HTL layer, resulting in different effects both, in the intrinsic properties of the active layer and in the device properties. Extremely low graphene content in the HTL layer results in increased PCEs of the solar cell devices (figure 2a), and higher crystallinity, shown by X-ray diffraction analysis (XRD), of the $MAPbI_3$ active layer (figure 2c). [3] When graphene is added into the photoactive $MAPbI_3$ layer, the lowest amount of graphene leads to a photovoltaic improvement, while a detrimental effect is observed for higher concentrations (Figure 2d,f).

In-depth studies of structural properties (XRD), optical (absorption and photoluminescence emission) studies and device characterization by impedance spectroscopy will be presented in this work aimed to understand the physical and chemical mechanisms produced by the addition of graphene and its relationship with final device properties. Preliminary studies show great potential for developing the pathway for these cost-effective materials.

References

[1] A.K. Jena, A. Kulkarni, T. Miyasaka, Halide perovskite photovoltaics: background, status, and future prospects, Chem. Rev. 119 (5) (2019) 3036–3103.
[2] M. Hadadian, J-H. Smått and J-P. Correa-Baena. The role of carbon-based materials in enhancing the stability of perovskite solar cells Energy Environ. Sci., 2020,13, 1377-1407
[3] J. Zhang, J. Fan, B. Cheng, J. Yu, W. Ho. Graphene-Based Materials in Planar Perovskite Solar Cells. Solar RRL 2020, 4 (11), 2000502.
[4]C. Redondo-Obispo, T. S. Ripolles, S. Cortijo-Campos, A. L. Álvarez, E. Climent-Pascual, A. de Andrés, C.Coya. Enhanced stability and efficiency in inverted perovskite solar cells through graphene doping of PEDOT:PSS hole transport layer. Materials and Designs 191 (2020) 108587.

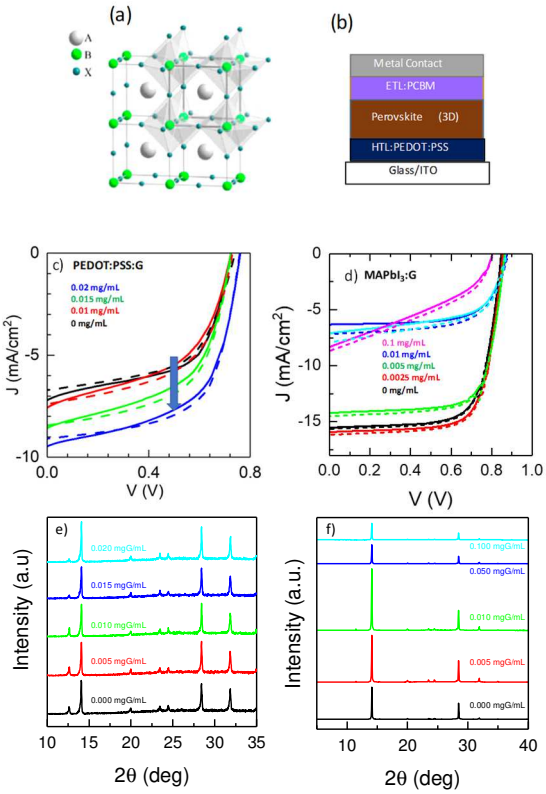

Figure 2. a) Schematic representation of the tetragonal unit cell of an ABX_3 perovskite, and b) inverted structure of a perovskite solar cell. c) Current-voltage performances under 1 sun illumination for the solar cells with graphene-doped PEDOT:PSS as HTLs and d) with graphene flakes into $MAPbI_3$ solution, in forward sweep (solid lines) and reverse sweep (dashed lines). (The blue arrow indicates the direction graphene increases). e) XRD patterns of the pristine $MAPbI_3$ films on graphene-doped PEDOT:PSS layers and, f) graphene-doped $MAPbI_3$ films on glass.

Optimized Power-over-Fiber System to Remotely Feed Smart Nodes for Low-Power Consumption Applications

J. D. López-Cardona[1], M. Delgado[2], R. Altuna[1], I. García[2], A. Nuñez-Cascarejo[1], M. Hinojosa[2], P. C. Lallana[1], I. Lombardero[2], A. Fresno[1], L. Cifuentes[2], X. Barrero[1], J. Bautista[2], R. Rodríguez[1], M. Gabás[2], D. S. Montero*[,1], I. Rey-Stolle[2], C. Algora[2], C. Vázquez[1]

[1] Electronics Technology Dpt., Universidad Carlos III of Madrid, 28911 Leganés (Madrid), Spain.
[2] Instituto de Energía Solar, Universidad Politécnica de Madrid, 28040 Madrid, Spain.
* Corresponding author: dsmontero@ing.uc3m.es

1. Abstract

We report an optimized Power-over-Fiber (PoF) solution to remotely feeding smart sensors and control electronics suitable for low-power consumption demand applications. A customized photovoltaic laser power converter is developed and characterized to maximize the PoF system efficiency. The system is successfully tested, capable of feeding a smart remote node consuming 15.5 mW.

2. Introduction

Optical-fiber-linked power-by-light systems, known as Power-over-Fiber (PoF), consist of a high-power laser (HPL), a transmission line (optical fiber), and a photovoltaic laser power converter (PLPC). The latter is responsible for transforming the received optical power into electricity thus driving an electronic circuit directly or by means of an intermediate signal conditioning stage. The main advantages of deploying PoF systems include galvanic insulation between the two fiber ends, lack of electromagnetic noise, savings in copper cable weight, and no need for external batteries or public power lines. These optically powered remote units are envisaged in application fields such as Internet-of-Things (IoT) [1], avionics, automotive, domotics, etc. However, limitations of overall system performance mostly depend on the efficiencies of the HPL, optical fiber and, mainly, the PLPC [2].

In this work, an optimized PoF solution to remotely feed smart nodes with low-power demands is presented and experimentally tested. Our PoF system design outperforms in efficiency compared to other PoF systems reported elsewhere as well as to current state-of-the-art commercially available systems.

3. PV Converter and Experimental Setup

A customized GaAs PLPC with HP-SMA connector was fabricated (Fig.1). We fabricated the semiconductor structure of the converter by MOVPE on GaAs substrates. The device has an area of 0.1 cm^2 to optimize the light transfer to the converter and is manufactured using photolithography, metal deposition, liftoff, wet etch, and deposition of antireflective layers. The converters are encapsulated in TO-8 packages.

Fig. 2 shows a schematic of the PoF system developed. The system includes a HPL of 1.5W@2.2A (maximum) with a central wavelength of 808nm and a 4m-long 200µm core diameter silica optical fiber connected to the smart remote node, although reaching longer distances would be feasible. The remote node hardware consists of two boards (Main and Communication boards). It includes an energy management unit with the capability of tracking the maximum power point (MPPT) of the PLPC. This smart node also embeds a bidirectional optical communications link from/to the central office powered by PoF and allows power on demand depending on the remote node status.

4. Results

For an input optical power of 0.482 W our PLPC shows the maximum conversion factor of 56.5%@808nm. Fig. 3 shows the PLPC I-V curves at different optical power inputs. We successfully tested different operation modes for the bidirectional optical communications link at the remote node while being powered by PoF: remotely turning the node into sleep mode, data transmission and data reception for node control and status. Remote node power demand was also measured being 15.5mW (5.5mA, 3V) provided by the PV cell. Fig. 4 shows a picture of the experimental setup for PoF testing purposes.

References

[1] J. D. López-Cardona, D. S. Montero, C. Vázquez, "Smart Remote Nodes Fed by Power Over Fiber in Internet of Things Applications", IEEE Sensors J, 19 (17), pp. 7328-7334, 2019

[2] J.D. López-Cardona et al., “Remote Optical Powering using Fiber Optics in Hazardous Environments,” J. Lightwave Technol., vol. 36(3), pp. 748-754, 2018.

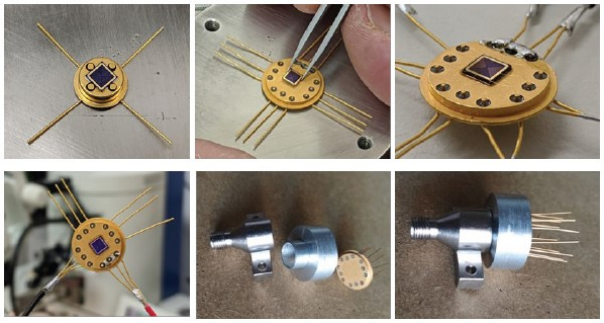

Fig.1 Pictures of the customized PLPC onto a TO-8 with HP-SMA connector to optical fiber.

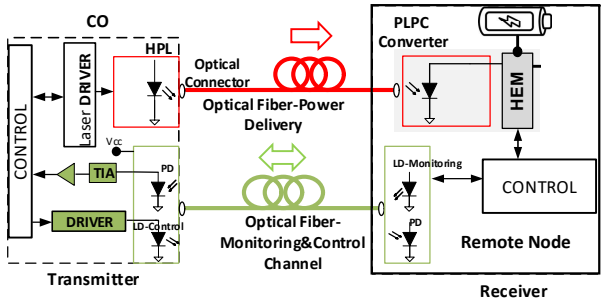

Fig.2 Schematic of different building blocks of the PoF system and the remote node. HEM: Hardware Energy Management.

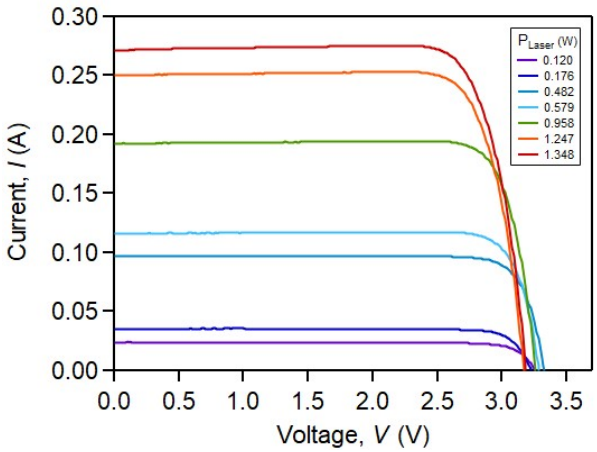

Fig.3 Measured I-V curve of the customized PV cell for different values of the input optical power at 808nm.

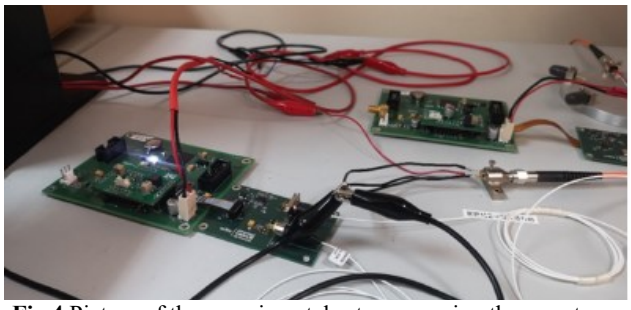

Fig.4 Picture of the experimental setup powering the remote node via PoF.

POSTER SESSION II

Photovoltaic, optoelectronic and photonic devices

Thursday 10

10:15-11:30

Chairperson: J. Pallares (Universitat Rovira i Virgili)

Study of Recombination Effects in a Vertical-Tunnel-Junction GaAs Solar Cell

Celia Outes[1*], Eduardo F. Fernández[1], Natalia Seoane[2], Florencia Almonacid[1], Antonio J. García-Loureiro[2]

[1]Centro de Estudios Avanzados en Ciencias de la Tierra, Energía y Medio Ambiente, University of Jaén, Spain
[2]Centro Singular de Investigación en Tecnoloxías Intelixentes, University of Santiago de Compostela, Spain

Corresponding autor: * coutes@ujaen.es

Abstract

Concentrator photovoltaics (CPV) has reached the highest efficiencies (η) among all the photovoltaic (PV) technologies [1]. Also, these systems have demonstrated a noteworthy capacity to produce high energy levels and to reduce the cost of electricity [2]. Ultra-high (UH) CPV with concentration ratio (C_{ratio}) above 1000 suns is considered one of the most promising areas to obtain high η and low-cost new generation CPV systems [3]. This is due to the theoretical η of solar cells increases with C_{ratio} and the amount of semiconductor material is drastically reduced. Despite the potential of the UHCPV systems, several goals need to be reached in order to improve the technology: solar cells with η peaking at UH levels (e.g. decreasing the series resistance losses (R_S)) [4], optical designs able to reach UH levels [5] and thermal mechanisms able to exploit the UH heat waste [6].

This work is focused on the study of recombination effects in a GaAs-based vertical-tunnel-junction (VTJ) solar cell that was first introduced in [7] and later optimised in [8]. It is composed by two identical GaAs subcells joined by a tunnel junction (TJ) with the anode and cathode placed laterally (see scheme and the main dimensions in Fig. 1). The p^+ and n^+-layers are doped with $5{\cdot}10^{19}$ cm^{-3}, the p and n-layers with $1{\cdot}10^{15}$ cm^{-3} and the n^{++}/p^{++} layers in the TJ with $7{\cdot}10^{19}$ cm^{-3}. With this structure is possible to increase the area of the cell exposed to the light by connecting multiple VTJs via TJs. This configuration reduces the R_S losses of the multi-junction horizontal structures, so the η increases linearly with C_{ratio}, even up to 10000 suns [7].

Fig. 2 presents the Auger, Shockley-Read-Hall (SRH), radiative and total recombination (TR) rates under 100 (a) and 10000 suns (b). These values were obtained along the width of the device at 3 µm of the vertical direction from the incident light surface (see Fig. 1) at the open-circuit voltage (V_{OC}) operation point. Results show that for 100 suns radiative is the dominant mechanism in the p-layers, being the 63.5% of the total rate, and in the n-layers SRH dominates, being the 52.8%. On the other hand, for 10000 suns (Fig. 2 (b)), radiative is the dominant recombination, being the 64.75% of the total rate in the p-layers and the 76.4% in the n-layers. It is important to note that Auger is the least recombination effect for both C_{ratio}, and its maximum values can be found in the more doped layers. Fig. 3 shows the IV curves for TR, without recombinations (NR) and for each recombination at 100 (a) and 10000 suns (b). These figures show that the short-circuit current (I_{SC}) is almost constant independently of the mechanism considered for both low and UH C_{ratio}. On the other hand, the figures also show that Auger and SRH do not affect the characteristic IV curve, while radiative decreases the V_{OC} for both C_{ratio}. Fig. 4 (a) shows the IV curves for 100 and 10000 suns for TR. These curves show that I_{SC}, V_{OC} and η increases with C_{ratio}, being η at 10000 suns 3.3% larger than at 100 suns. Finally, Fig. 4 (b) presents the comparison of the η between 100 and 10000 suns for TR, NR and for each recombination. This figure shows that for all cases η increases at least 3% with C_{ratio} and is not limited by either of the recombination mechanisms. In addition, the results show that radiative affects η the most at UHC_{ratio}, since for Auger and SRH η is ~33.0% and for radiative ~32.0%. A detailed investigation of these results will be provided at the conference.

References

[1] J. F. Geisz *et al.* doi: 10.1038/s41560-020-0598-5.
[2] E. F. Fernández *et al.* doi: 10.1016/j.energy.2016.03.060.
[3] C. Algora *et al.* doi: 10.1007/978-3-642-23369-2_2
[4] M. Ochoa *et al.* doi: 10.1002/pip.2791.
[5] J. P. Ferrer-Rodríguez *et al.* doi: 10.1364/OL.41.001985.
[6] A. Valera *et al.* doi: 10.1016/j.solener.2019.02.013.
[7] E. F. Fernandez *et al.* doi: 10.1109/LED.2018.2880240.
[8] C. Outes *et al.* doi: 10.1016/j.solener.2020.04.029.

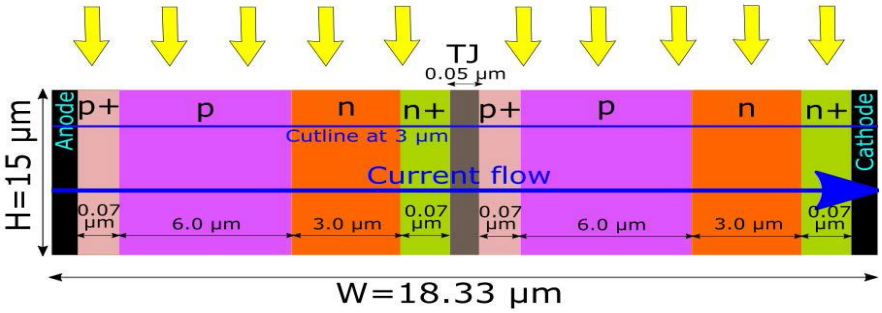

Fig. 1. 2D scheme of the Vertical-Tunnel-Junction (VTJ) including the main dimensions of the structure (H=height and W=width).

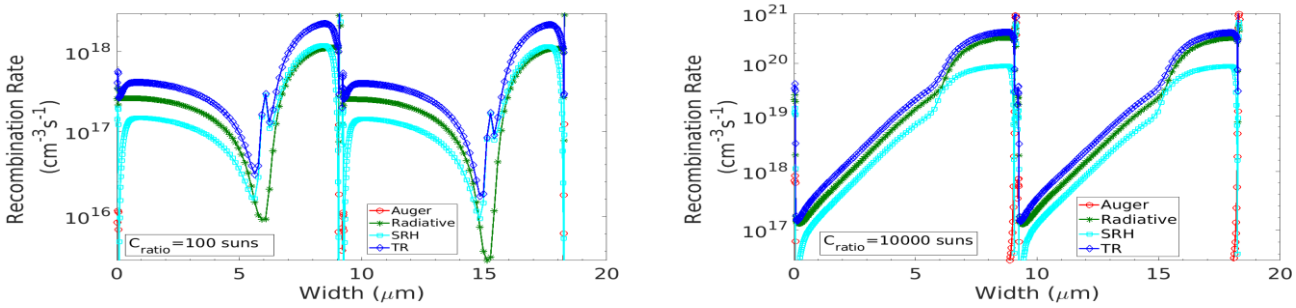

(a) **(b)**

Fig. 2. Recombination rates obtained for Auger, radiative and Shockley-Read-Hall (SRH) and the total recombination (TR) for a cutline along the width of the device structure at 3 µm o the vertical direction from the incident light surface under 100 (a) and 10000 (b) suns at the V_{OC} operation point.

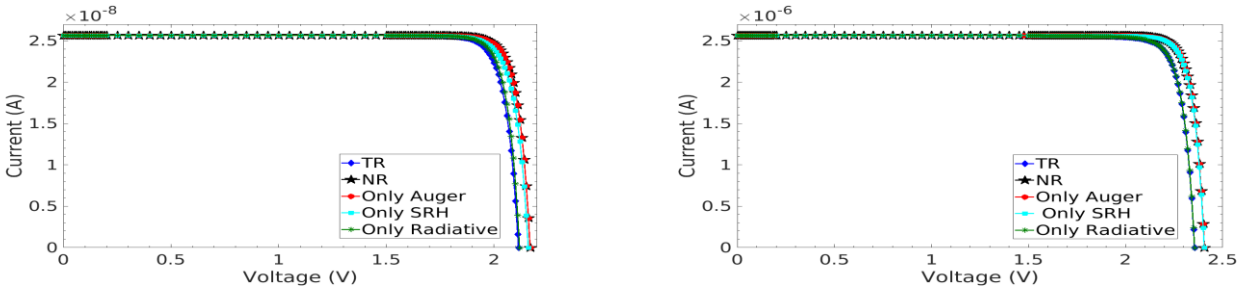

(a) **(b)**

Fig. 3. IV curves for the total recombination (TR), without recombinations (NR) and for Auger, Shockley-Read-Hall (SRH) and radiative at 100 suns (a) and 10000 suns (b).

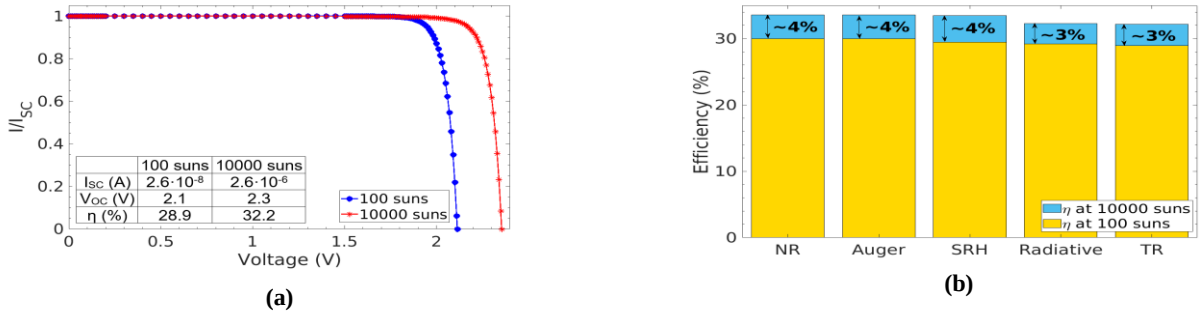

(a) **(b)**

Fig. 4. (a) IV curves for 100 and 10000 suns for the total recombinations (TR). (b) **C**omparison of the efficiency between 100 and 10000 suns concentration for the VTJ solar cell for TR, without recombinations (NR) and for Auger, Shockley-Read-Hall (SRH) and radiative.

Effect of Thermal Annealing on the Performance of PTB7-Th:$PC_{70}BM$-Based Ternary Organic Solar Cells

Alfonsina A. A. Torimtubun[a], Jorge Follana-Berná[b], Josep Pallarès[*a], Ángela Sastre-Santos[*b], and Lluis F. Marsal[*a]

[a]Department of Electric, Electronic and Automatic Control, Universitat Rovira i Virgili, 43007 Tarragona, Spain.
[b]Área de Química Orgánica, Instituto de Bioingeniería, Universidad Miguel Hernández de Elche, 03202 Elche, Spain.
E-mail: lluis.marsal@urv.cat

1. Abstract

Molecular design and device engineering are two important strategies to improve the performance of organic solar cells (OSC). In this study, we investigate the influence of the thermal annealing treatment on the performance of ternary OSC based on PTB7-Th:$PC_{70}BM$ bulk heterojunction incorporating a newly designed solution-processable phthalocyanine-based third component, $CuPcF_{48}$. The addition of $CuPcF_{48}$ has shown to improve the power conversion efficiency (PCE) of up to 3% in ternary OSC compared to binary OSC through molecular design strategy. On the contrary, a drop in PCE for both binary and ternary OSC upon thermal annealing was observed. The result suggest that the device engineering strategy by thermal annealing treatment may not suitable for the device improvement of PTB7-Th:$PC_{70}BM$-based blend.

2. Introduction

Organic solar cells (OSC) have been receiving more attention due to their low-cost, light weight, facile processing and flexibility for large area devices.[1] In recent years, a great effort has been made on material synthesis, device engineering and theoretical modelling to optimize the performance of bulk heterojunction OSC.[2], [3] Up to now, the power conversion efficiency (PCE) of such cells can exceed 17% in both single junction and tandem cells.[4] Ternary OSC could combine the merit of binary and tandem cells to improve device performance. Another strategy is thermal annealing (TA), which is an important method for regulating the morphology of bulk heterojunction OSC, and has become an essential option for optimizing the device efficiency and performance.[5] Strategy such as thermal annealing or ternary system has been used in OSC to obtain its best device performance by our group.[6], [7] In this work, we examine the effect of thermal annealing on device performance for a new solution-processable small molecule, $CuPcF_{48}$, in binary and ternary bulk heterojunction systems.

3. Results and Discussion

Since the ternary system and thermal annealing can both help to improve the device performance and efficiency, it is thus attractive to investigate the influence of TA on the device performance of binary and ternary systems. The binary and ternary device were fabricated using inverted structure of ITO/PFN/Active layer/V_2O_5/Ag with the optimal conditions of a donor/acceptor (D/A) weight ratio of 1:1.5, the solvent chlorobenzene 97% (v/v) and DIO additive 3%. A 3% weight ratio of $CuPcF_{48}$ added to the total D/A=1:1.5 and thermal annealing with at 100°C for 5 min were used as the variable conditions. Current density-voltage (J-V) curves of all devices is displayed in Fig. 1. The relevant photovoltaic parameters under AM 1.5G illumination are listed in Table 1. The binary PTB7-Th:$PC_{70}BM$ device shows a PCE of 8.83%. With the addition of $CuPcF_{48}$, the increase in short-circuit current density (J_{SC}) was observed from 16.34 mA cm^{-2} for binary device to 16.81 mA cm^{-2} for ternary device. This trend is observed for both devices with and without thermal annealing, leading to 3% enhancement of PCE. On the other hand, the thermal annealing treatment can lead to the decrease of J_{SC} and FF simultaneously for both binary and ternary system, leading to the poor device performance. This latter results suggest that the thermal annealing may not suitable for the device improvement of PTB7-Th:$PC_{70}BM$-based blend.

4. Conclusion

Devices based on a newly solution-processable small molecule $CuPcF_{48}$ as a third component in PTB7-Th:$PC_{70}BM$ bulk heterojunction ternary system have been investigated. The addition of $CuPcF_{48}$ has shown to improve the PCE of up to 3% in ternary OSC compared to binary OSC through molecular design strategy. On the contrary, a drop in PCE for both binary and ternary OSC upon thermal annealing was observed. The result suggest that the device engineering strategy by thermal annealing treatment is not suitable for the device improvement of PTB7-Th:$PC_{70}BM$-based blend.

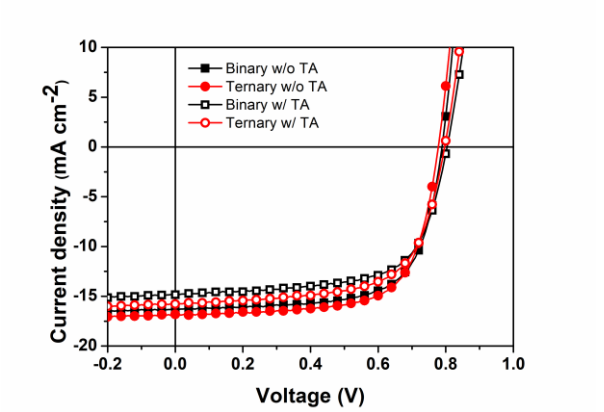

Fig.1. Current density-voltage (J-V) characteristics of binary and ternary devices with and without thermal annealing treatment.

Table 1. Device parameters for binary and ternary OSC with and without thermal annealing treatment.

System	TA	J_{SC} [mA·cm^{-2}]	V_{OC} [V]	FF [%]	PCE [%]
Binary	-	16.34	0.79	68.41	8.83
	TA	14.77	0.80	65.47	7.78
Ternary	-	16.81	0.78	69.09	9.06
	TA	16.18	0.79	64.86	8.37

References

[1] B. Zhao *et al.*, "Flexible polymer solar cells with power conversion efficiency of 8.7%," *J. Mater. Chem. C*, vol. 2, no. 26, pp. 5077–5082, 2014, doi: 10.1039/c3tc32520b.

[2] A. A. A. Torimtubun, J. G. Sánchez, J. Pallarès, and L. F. Marsal, "A cathode interface engineering approach for the comprehensive study of indoor performance enhancement in organic photovoltaics," *Sustain. Energy Fuels*, vol. 4, pp. 3378–3387, 2020, doi: 10.1039/d0se00353k.

[3] V. S. Balderrama *et al.*, "High-efficiency organic solar cells based on a halide salt and polyfluorene polymer with a high alignment-level of the cathode selective contact," *J. Mater. Chem. A*, vol. 6, no. 45, pp. 22534–22544, 2018, doi: 10.1039/c8ta05778h.

[4] Q. Liu *et al.*, "18 % Efficiency organic solar cells," *Sci. Bull.*, vol. 65, no. 4, pp. 272–275, 2020, doi: 10.1016/j.scib.2020.01.001.

[5] W. Zhang *et al.*, "Effect of post-thermal annealing on the performance and charge photogeneration dynamics of PffBT4T-2OD/PC71BM solar cells," *Polymers (Basel).*, vol. 11, no. 3, 2019, doi: 10.3390/polym11030408.

[6] J. G. Sanchez, A. A. A. Torimtubun, V. S. Balderrama, M. Estrada, J. Pallares, and L. F. Marsal, "Effects of Annealing Temperature on the Performance of Organic Solar Cells Based on Polymer: Non-Fullerene Using V2O5 as HTL," *IEEE J. Electron Devices Soc.*, vol. 8, no. October 2019, pp. 421–428, 2020, doi: 10.1109/JEDS.2020.2964634.

[7] A. A. A. Torimtubun, J. Follana-Berná, Á. Sastre-Santos, J. Pallarès, and L. F. Marsal, "The Role of Fluorinated Phthalocyanines as Non-Fullerene Acceptors in Ternary Organic Solar Cells," *Solar RRL*, 2020, submitted.

Advances on GaP:Ti material and solar cells

J. Olea,[1] S. Algaidy,[1] D. Caudevilla,[1] E. García-Hemme,[1] A. del Prado,[1] D. Pastor,[1] R. García-Hernansanz,[1] F. Zenteno,[1] E. San-Andrés,[1] G. González-Díaz,[1] I. Mártil,[1] D. Montero,[1] P. Gomez,[2] J. Gonzalo,[2] and J. Siegel.[2]

[1]Dpto. EMFTEL, Fac. CC. Físicas, Univ. Complutense de Madrid, 28040, Madrid, Spain. 913944441 oleaariz@ucm.es
[2]Laser Processing Group, Instituto de Optica, IO-CSIC, Serrano 121, 28006, Madrid, Spain. j.gonzalo@io.cfmac.csic.es

1. Introduction

Supersaturated GaP based solar cells could reach very high efficiencies [1]. From previous works, we observed a strong sheet photoconductance at energies below the GaP bandgap. We also concluded that the Pulsed-Laser Annealing (PLA) process produced a passivating surface oxide film. This passivation is extremely important for optoelectronic devices. In this work, we further our understanding of the optoelectronic properties of GaP:Ti fabricated by ion implantation and PLA.

2. Experimental

DSP 400 µm (100) n-GaP samples (0.064 Ωcm) were used for Transmittance (T) and Reflectance (R) measurements. SSP 450 µm (100) undoped n-GaP samples (0.65 – 2.6 Ωcm) were used for the rest of the measurements. Samples were $^{48}Ti^{+}$ implanted at 7º in a Varian CF3000 model refurbished by IBS at 32 keV with 8×10^{14} and 2×10^{15} cm^{-2} doses and subsequently PLA processed in air with an ArF excimer laser (193 nm, 20 ns pulse) as in Refs. [1, 2]. The PLA energy density used was in the 0.38 – 0.52 J/cm^2 range. T+R measurements were obtained using a UV/Vis/NIR Perkin-Elmer Lambda 1050 spectrophotometer at CIEMAT facilities. Results were used to obtain the absorption coefficient and the refractive index by the method described in Ref. [3]. Some 1×1 cm^2 samples were back and front contacted with an Au/Au:Ge (88:12) stack. Dark I-V measurements were conducted with an Agilent 2400 SMU and External Quantum Efficiency (EQE) measurements were obtained by means of a SRS830 DSP lock-in amplifier, illuminating with a UV-Vis-NIR Horiba iHR320 spectrophotometer with a 250 W halogen lamp, calibrated by a Si S2281 photodiode. X-ray Photoelectron Spectroscopy (XPS) measurements were performed to analyze the surface of GaP and a 5 – 10 s NH_4OH etch (see Ref. [4]) was conducted to eliminate the surface oxide produced by the PLA process. A Fisons MT500 spectrometer operated at 300 W at CENIM-CSIC facilities was used for XPS characterization.

3. Results and discussion

The obtained refractive index for GaP:Ti samples presented in Fig. 1 is higher than the one of the bare substrate, and there is a clear trend with the dose. On the other hand, Fig. 2 shows that the obtained absorption coefficient of the GaP:Ti semiconductor material is very high in the Vis-IR range, with values over 10^4 cm^{-1}. This result suggests that this material can be of interest for optoelectronic applications and in particular for photovoltaic devices.

The measured dark I-V curve shown in Fig. 3 was fitted with the classic diode model, yielding the following results for the best sample: $I_0 = 4.00\times10^{-14}$ A, n = 1.50, $R_{sh} = 4.33\times10^8$ Ω, and $R_s = 4.73\times10^3$ Ω. EQE results presented in Fig. 4 show a very clear response at energies below the GaP bandgap, due to the introduction of Ti through implantation. However, the EQE values are very low, most likely due to the high series resistance. We suggest that the thin (~5 nm) passivating amorphous oxide at the GaP surface, already discussed in Ref. [2], is increasing the front contact resistance (see Fig. 5).

In order to eliminate this surface oxide and fabricate an intimate contact with GaP, we analyzed the NH_4OH etch by XPS (Fig. 6) and concluded that it can be easily removed. New samples are being fabricated to study the influence of this recipe on the optoelectronic properties of GaP:Ti/GaP devices.

References

[1] J. Olea et al., “Strong subbandgap photoconductivity in GaP implanted with Ti”, Prog. Photovolt. Res. Appl., vol. 26, pp. 214-222, 2018.
[2] J. Olea et al., “On the properties of GaP supersaturated with Ti”, J. Alloys Comp., vol. 820, 153358, 2020.
[3] N. Maley, “Critical investigation of the infrared-transmission-data analysis of hydrogenated amorphous silicon alloys”, Phys. Rev. B, vol. 46, pp. 2078-2085, 1992.
[4] H. Morota and S Adachi, “Properties of GaP(001) surfaces chemically treated in NH4OH solution”, J. Appl. Phys., vol. 100, 054904, 2006.

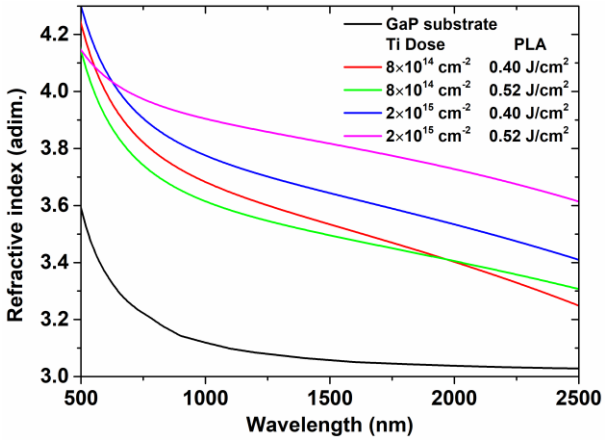

Fig.1. Refractive index of several GaP:Ti layers after the PLA process. The refractive index of the reference substrate is also depicted.

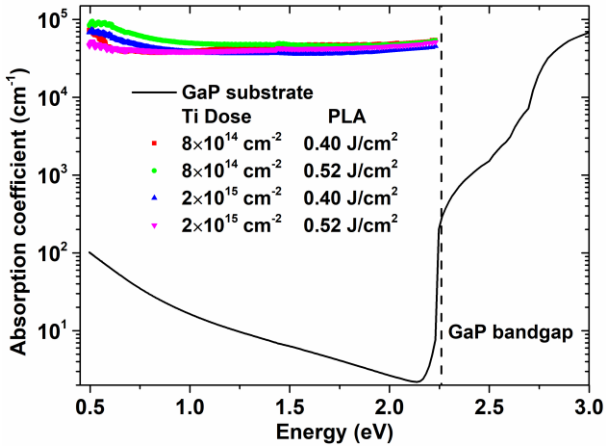

Fig.2. Absorption coefficient of GaP:Ti layers after the PLA process, compared to the one of the reference GaP substrate. The dashed line marks the GaP bandgap at 2.26 eV. The substrate shows free carriers absorption at energies below the bandgap.

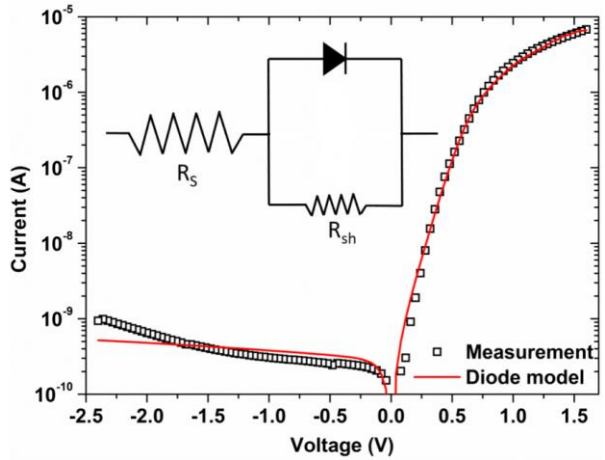

Fig.3. Measured and fitted IV curves of one of the GaP:Ti/GaP devices. The circuit model used is shown in the figure.

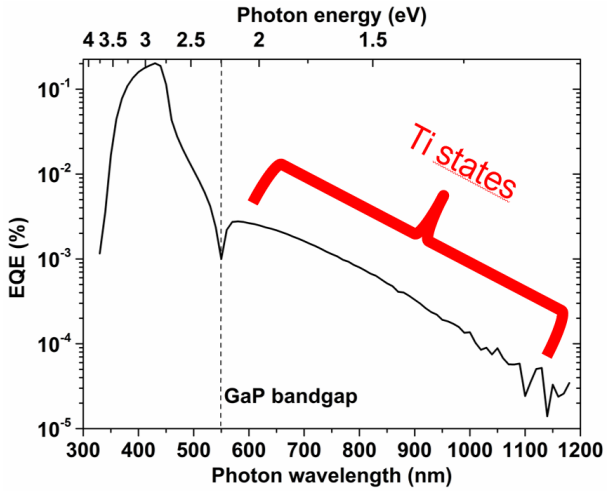

Fig.4. EQE of one of the GaP:Ti/GaP devices. The bandgap is marked at 2.26 eV. The EQE values are very low, possibly due to the high series resistance of the device. EQE at energies below the GaP bandgap is originated by the Ti deep states.

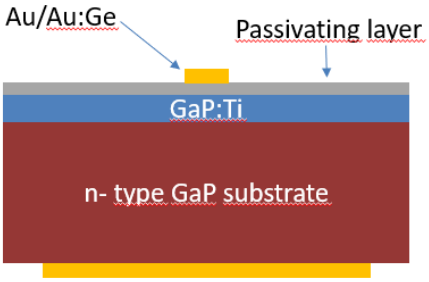

Fig.5. Structure of the GaP:Ti/GaP devices. The back contact covers the whole surface while the front contact is smaller. The thin (~5 nm) passivating surface oxide layer described in Ref. [2] and produced by the PLA process is also under the front contact.

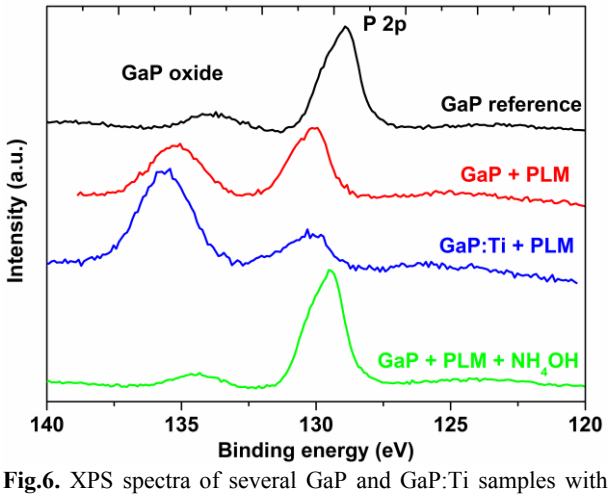

Fig.6. XPS spectra of several GaP and GaP:Ti samples with and without PLA process. The spectra show the P 2p band and a band attributed to the surface oxide layer. The NH_4OH short etch (5 – 10 s) removes this layer opening the possibility of creating an intimate contact to the GaP:Ti surface.

Characterization of thin CIGS solar cells by electron microscopy techniques

M. Fisse (mfisse@ub.edu)[1], L. López-Conesa[1,2], L. Yedra[1], F. Peiró[1,3], S, Estradé[1,3], S. Paetel[4], R. Fonoll-Rubio[5], M. Guc[5] and V. Izquierdo-Roca[5]

[1]LENS-MIND, Departament d'Enginyeria Electrònica i Biomèdica, Universitat de Barcelona, 08028, Barcelona, Spain
[2]CCiTUB, Centres Científics i Tecnológics de la UB, Universitat de Barcelona, 08028, Barcelona, Spain
[3]Institute of Nanoscience and Nanotechnology (IN2UB), Universitat de Barcelona, 08028, Barcelona, Spain
[4]Zentrum für Sonnenenergie- und Wasserstoff-Forschung, Baden-Württemberg (ZSW), Meitnerstr. 1, 70563 Stuttgart, Germany.
[5]Catalonia Institute for Energy Research (IREC), Jardins de les Dones de Negre 1, 08930 Sant Adrià de Besòs-Barcelona, Spain.

1. Abstract

Cu(In,Ga)Se_2 (CIGS) solar cells have proven to be a competitive technology on the thin film photovoltaic devices. This compound offers a good alternative to silicon monocrystalline devices since characterized CIGS solar cells have achieved efficiencies as high as 23,35% [1]. Since the obtention of these promising results, there have been lots of studies centered on the composition and the best possible treatments to improve these values, for example [2] and [3]. Heavy alkali-based post-deposition treatments (PDT) have proven to maximize the efficiency of the CIGS solar cells [4]. The next step on the study of CIGS thin film photovoltaic devices is to manage to properly transfer these processes from cells (laboratory) to a pre-industrial module level.

In this work, we deal with the structural and chemical analysis of thin film solar cells grown in a pre-industrial inline-system for the CIGS deposition. The devices consist in a stack of Mo\MoSe\CIGS\CdS\i-ZnO\ZAO grown on soda-lime glass (SLG) (see Fig. 1) and show good electro-optical properties with efficiencies up to 18.0% without antireflective coating.
Conventional and advanced microscopy techniques were applied using JEM-2100 and JEM-2010 electron microscopes, equipped with X-ray detector from (Oxford Instruments) and energy filter (Gatan) respectively. Besides atomic resolution phase contrast imaging (HRTEM) and Selected Area Electron Diffraction (SAED), Electron Energy-Loss Spectrometry (EELS) in both low-loss and core loss regimes, was also applied for the analysis of composition dependent plasmon peak shift and composition quantification respectively. These observations were also supported by Energy Dispersive X-Ray analysis (EDX). Additionally, phase and grain orientation maps were obtained by precession assisted electron diffraction (PED) using the Astar system from Nanomegas. Diffraction patterns were collected in STEM mode using a nanoprobe electron beam that is precessed to minimize the dynamical effects and improve the pattern quality. Once the acquisition is done, the diffraction patterns are indexed automatically using a template matching [5]. This technique allows us to study the changes in phase or orientation of different grains.

First, to evaluate the crystalline quality of the CIGS layer, a non-complete CIGS device, annealed at 520ºC, consisting only in Mo\MoSe\CIGS layers was observed in planar-view (PV orientation). For the preparation of a thin foil a mechanical procedure was done (polishing using different sized papers until a 1µm grain) followed by a final ion beam thinning. The observation of this sample allowed us to study the grain boundaries and orientations and the structure of the CIGS, which space group is $I\bar{4}2d$ (see Fig.2 and Fig.3).

For the study of a whole device, a set of complete samples was prepared. These samples were treated by RbF-PDT at different source temperatures: 300ºC (no RbF treatment), 490ºC, 520ºC and 540ºC. The [Cu]/([Ga]+[In]) (CGI) ratio was always kept constant. A focused ion beam (FIB) was used in order to obtain lamellas thin enough to be observable by TEM in cross section (XS) geometry. As in the PV sample, all the above referred electron microscopy techniques were applied.

The FIB used allowed us to get an overview of these samples and showed that the interface between the Mo and the CIGS layer seem to be very weak (see Fig. 4), causing the sample to break apart when using mechanical procedures instead of FIB to thin the specimen to electrotransparency. The performed observations showed that, despite the CGI ratio remains constant through the vast majority of the CIGS layer, it raises in the Mo\CIGS

interface. The [Ga]/([Ga]+[In]) (GGIn) ratio was also studied and the EDX data revealed that, despite it remains constant on the upper half of the CIGS layer, it raises from the half to the Mo\CIGS interface. A change on the CIGS plasmon peaks was also observed, concomitant with a change in the mean free path suggesting a variation of Ga/In ratios along the structure. All these observations are complemented by Raman and PL spectroscopies performed on very same samples.

References

[1] Press-Release of Solar Frontier 17/01/2019: Solar Frontier Achieves World Record Thin-Film Solar Cell Efficiency of 23.35%.

[2] T. Maeda, W. Gong and T.Wada, "Crystallographic and optical properties and band structures of $CuInSe_2$, $CuIn_3Se_5$ and $CuIn_5Se_8$ phases in Cu-poor Cu_2Se-In_2Se_3 pseudo-binary system", Japanese Journal of Applied Physics, 2016, **55** 04ES15.

[3] L. Kronik, L. Burstein, M. Leivbovitch, Y. Saphira, D. Gal, E. Moons, J. Beier, G. Hodes, D. Cahen, D. Hariskos, R. Klenk, and H.-W. Schock, "Band diagram of the polycrystalline CdS/Cu(In,Ga)Se_2 heterojunction", American Institute of Physichs, 4th September 1995, **67** (10).

[4] T. Kodalle, T. Bertram, R. Schlatmann and C.-A. Kaufmann, "Effectiveness of an RbF Post Desposition Treatment of CIGS Solar Cells in Dependence on the Cu Content of the Absorber Layer", IEEE Journal of Photovoltaics, VOL. 9, NO.6, NOVEMBER 2016.

[5] A.-D. Darbal, M. Gemmi, J. Portillo, E. Rauch and S. Nicolopoulos. "Nanoscale Automated Phase and Orientation Mapping in the TEM". Microscopy Today, 2012 November, doi:10.1017/S1551929512000818

Fig. 1. CIGS device structure.

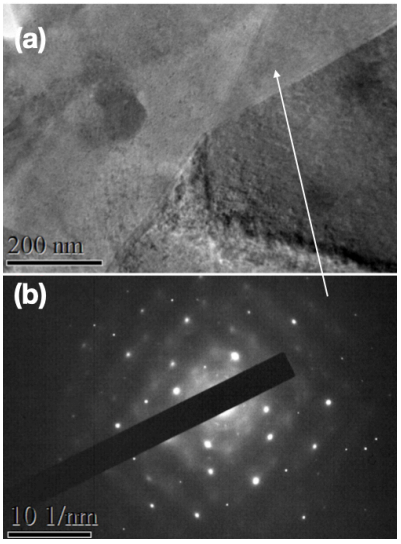

Fig. 2. (a) Different grains observation from the PV sample. **(b)** SAED performed on the selected grain in **(a)**.

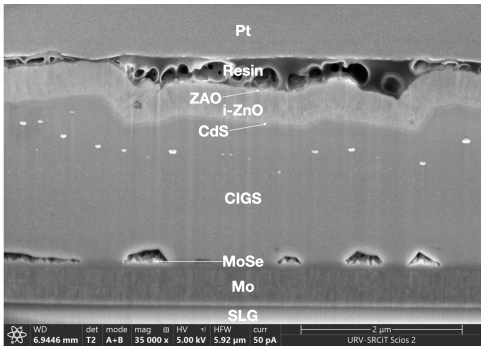

Fig. 3. Cross-section view of the sample annealed at 490ºC. Resin and Pt are additional layers grown to protect the surface during the preparation of the thin lamella by FIB.

Thin c-Si Solar Cells Based on VO_x Heterojunctions

Gema López-Rodriguez, Eloi Ros, Pablo Ortega, Cristóbal Voz, Joaquim Puigdollers, Isidro Martín

Universitat Politècnica de Catalunya (UPC), Micro and Nanotechnologies Group, MNT, Barcelona, Spain,
gema.lopez@upc.edu

1. Abstract

Previous results in our research group have demonstrated good efficiencies of solar cells fabricated on conventional thick c-Si substrates using Vanadium Oxide (VO_x) as hole selective contacts. In this work, we report on the adaptation of this technology on thin (≤ 40 µm) c-Si substrates. First solar cells are finished on 40 µm-thick substrates demonstrating the viability of the technology. Efficiencies are limited by high series resistance related to the device geometry that will be reviewed in future devices. In addition, detailed modelling of the optical properties of the device demonstrates important penalties in short-circuit current density due to the flat surface of the fabricated devices. Texturized PDMS films are placed on top of the solar cell to reduce optical losses leading to significant improvement in that parameter. Fabrication of 20 µm-thick solar cells with revised technology is underway.

2. Introduction

Crystalline silicon (c-Si) photovoltaic technology is always looking for more efficient and environmentally-friendly solutions to be attractive in front of conventional energy sources. Among many other efforts, the reduction of wafer thickness is one of the general trends and research activities have demonstrated that excellent efficiencies can be obtained with devices well below 50 µm [1].

Fabricating c-Si solar cells on thin substrates introduces the requirement of low temperature processing. For this reason, most of the fabricated devices are based on silicon heterojunction technologies [2-4]. That technology needs toxic and/or flammable dopant gas precursors to define the selective contacts on the absorber. As an alternative, Transition Metal Oxides have demonstrated excellent properties as hole transport layers keeping a low temperature approach [5].

In this work, we report on c-Si solar cells fabricated on thin (≤ 40 µm) substrates with hole selective contacts based on thermally evaporated Vanadium Oxide (VO_x). The work is adapting a similar technology developed by our research group on conventional thick substrates where laser processed phosphorus silicon carbide ($SiC_x(n)$) films were used as electron selective contacts [6]. Up to now, we have finished 40 µm-thick devices whose results are included in this abstract. However, we are currently fabricating 20 µm-thick devices and the obtained results will be presented at the conference.

3. Experimental and Results

Solar cells are fabricated using a N-type 1-5 Ωcm 40±4 µm-thick substrates. In figure 1.(a) we show a cross-section of the fabricated devices following the technology reported in [6]. Apart from the substrate thickness, the main difference to devices reported in [6] is that substrate is glued onto 700 µm-thick Schott Borofloat 33 glass using transparent epoxy EPO-TEK 302-3M and permitting the patterning of the rear surface in an Interdigitated Back Contacted (IBC) structure. We define 1x1 cm^2 solar cells with two different distances between fingers or pitch (*p*) of 550 and 850 µm.

Solar cells were measured under standard illuminated conditions (AM1.5g, 100 mW/cm^2, 25 ºC) leading to curves shown in figure 1.(b). Photovoltaic figures are also shown in the inset table where efficiencies of 10.5 % and 10.4 % are obtained for the samples with 550 and 850 µm pitch respectively. Short-circuit current density (J_{sc}) and open-circuit voltage (V_{oc}) values are comparable for both devices suggesting that recombination and optical properties are very similar for both devices, while the low *FF* values are the responsible for limiting efficiency. In order to evaluate the effect of the series resistance, *suns*-V_{oc} measurements are carried out and the *pseudoJ-V* curves are calculated and plotted in figure 1.(b) for direct comparison. In addition, pseudo Fill Factor (*pFF*) values are also obtained leading to values beyond 80.0 % demonstrating the good quality of the VO_x/c-Si heterojunction. By comparing *FF* and *pFF* a value for the series resistance can be calculated [7] leading to 4.7 Ωcm^2 and 5.8 Ωcm^2 for samples with short and long pitch. This result indicates that the geometry of the cell plays a significant role in the high resistance values of the fabricated devices and will be revised in future runs.

Finally, in Figure 2 we show EQE curve for sample with longer pitch. Using optical raytracing simulator, we are able to reproduce the absorptance of silicon substrate. By doing so, the expected EQE with perfect carrier collection, i.e. no electrical losses, is also plotted in Figure 2. This curve is very close to the experimental one indicating that non-absorbed photons are responsible for the main J_{sc} losses. In order to minimize them, we introduce a texturized PDMS film that improves optical properties of the cells, as reported in [8]. By doing so, J_{sc} is improved to 28.4 mA/cm^2 for both samples leading to 11.1 %and 10.7 % of efficiency for short and long pitches.

Acknowledgments

This work has been supported partially by the Spanish Government through projects PID2019-109215RB-C41, TEC2017-82305-R and ENE2017-87671-C3-2-R

References

[1] M.M. Moslehi *et al.* "World-record 20.6% efficiency 156 mm x 156 mm full-squaresolar cells using low-cost kerfless ultrathin epitaxial silicon & poroussilicon lift-off technology for industry-leading high-performance smartPV modules", PV Asia Pacific Conference, 2012.

[2] H. Sai *et al.*, "Impact of silicon wafer thickness on photovoltaic performance of crystalline silicon heterojunction solar cells", Japanese Journal of Applied Physics 57, 08RB10 (2018).

[3] C. T. Trinh *et al.* "Potential of interdigitated back-contact silicon heterojunction solar cells for liquid phase crystallized silicon on glass with efficiency above 14%", Solar Energy Materials and Solar Cells 174, pp. 187-195 (2018).

[4] H. Sivaramakrishnan Radhakrishna *et al.*, "Heterojunction IBC solar cells on thin (< 50 µm) epitaxial Si foils produced from kerfless layer transfer process", Proceedings of 33rd EUPVSEC, Amsterdam, Netherlands, 2017, pp. 740-744.

[5] L. G. Gerling *et al.*, "Transition metal oxides as hole-selective contacts in silicon heterojunctions solar cells", Solar Energy Materials and Solar Cells 145, pp. 109-115(2016).

[6] G. Masmitjà *et al.*, "V_2O_x-based hole-selective contacts for c-Si interdigitated back-contacted solar cells", Jounral of Materials Chemistry A 5, pp. 9182-9189 (2017).

[7] M.A. Green, "Solar cells: Operating principles, technology and system applications" (USA:Prentice-Hall Inc., Englewood Cliffs, NJ, 1982) pp. 97.

[8] A. Rosell et al. "Textured PDMS films applied to thin crystalline silicon solar cells", IEEE J. Photovolt. 10, 351–357 (2020).

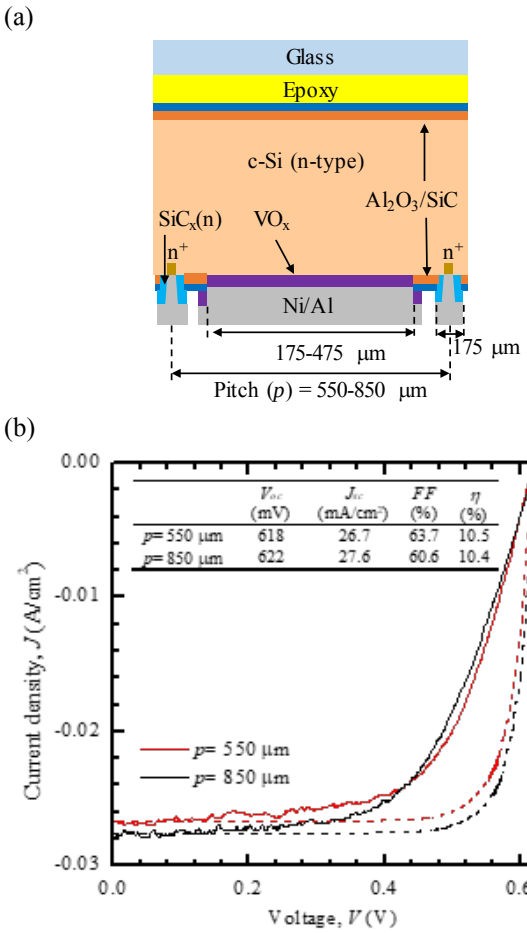

Fig.1. (a) Cross-section of the fabricated devices. (b) Illuminated *J-V* curves under standard conditions and *pseudoJ-V* curves obtained from *suns-*V_{oc} measurements.

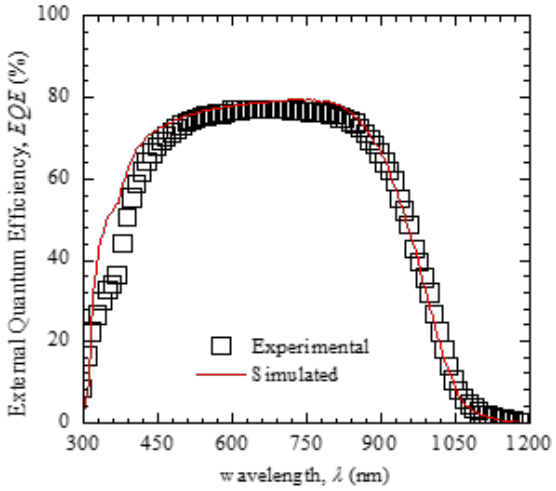

Fig.2. External Quantum Efficiency of the cell with *p*= 850 µm together with simulation without electrical losses).

Recrystallization of GaAs supersaturated with Ti

S. Algaidy,[1*] J. Olea,[1] D. Caudevilla,[1] E. García-Hemme,[1] A. del Prado,[1] D. Pastor,[1] D. Montero,[1] R. García-Hernansanz,[1] E. San Andrés,[1] G. González-Díaz,[1] I. Mártil,[1] J. Siegel,[2] J. Gonzalo,[2] M. Wang[3] and Y. Berencén[3]

[1]Dpto. EMFTEL, Fac. CC. Físicas, Univ. Complutense de Madrid, 28040, Spain. *sarialga@ucm.es
[2]Laser Processing Group, Instituto de Optica, IO-CSIC, Serrano 121, 28006, Madrid, Spain.
[3]Helmholtz-Zentrum Dresden-Rossendorf, Institute of Ion Beam Physics and Materials Research, Bautzner Landstr. 400, 01328 Dresden, Germany.

1. Introduction

The evolution of semiconductor materials plays an important role in improving current technologies. GaAs is one of the most used materials in the field. Improving the properties of GaAs would have a great impact in developing better optoelectronic devices and photovoltaic cells [1]. In this work, we study the supersaturation of GaAs with Ti, aiming to introduce deep levels within the bandgap, which would allow photon absorption below the bandgap energy. For this purpose, a Ti concentration well above the solid solubility limit is required. We obtained a supersaturated GaAs:Ti by ion implantation followed by pulsed laser melting with a very good recovery of the crystalline quality[2,3].

2. Experimental

Undoped semi-insulator GaAs (SI-GaAs) grown in the <100> direction, single-side polished, 350 μm thick with a resistivity of $5.5x10^8$ Ω cm at room temperature and a mobility of 5000 cm^2/Vs was implanted in a VARIAN CF3000 ion implanter by the polished surface with a $^{48}Ti^+$ dose of $2x10^{15}$ cm^{-2} at an energy of 32 keV. The implantation was performed using a 7° tilt angle, to prevent channelling.

The implanted samples were irradiated with an ArF excimer laser in air (λ = 193 nm, 20 ns full width half maximum). The beam size of the laser projected onto the sample surface had a dimension of 1x1 mm^2 to lead to an energy density in the 0.30-0.65 J/cm^2 range.
The measurement of Ti concentration after ion implantation was obtained using time of flight secondary ion mass spectroscopy (ToF-SIMS) performed with an Ion-TOF model. The area of interest chosen for the SIMS process was within the pulses irradiated by the PLM. The sputtering beam was a 300 μm x 300 μm spot size.

Raman scattering spectra were analysed using an Olympus BXFM microscope equipped with coupled charge detector model AndoriDus DU-420 peltier cooled. The scattered light was recorded at room temperature in an unpolarized backscattering configuration using a laser of wavelength (532nm), with an optical power of 22mW. The spatial resolution was set to 0.9nm. To analyze the crystal quality of the implanted samples, cross -section Transmission Electron Microscopy (XTEM) was used. Lamellas of samples were fabricated using Focused Ion Beam Scanning Electron Microscopy (FIB-SEM), with a Helios Nanolab 650 system. Structural properties were then analysed by obtaining TEM images in a JEOL JEM 3000F microscope operating at 300kV.

3. Results and discussion

The structural results of the GaAs:Ti samples are shown in figure 1, 2 and 3. Figure 1 confirms the presence of Ti within the lattice of GaAs. ToF-SIMS shows a different concentration of Ti with respect to depth, with the variation of the PLM energy fluence used. With the lowest PLM energy density, the Ti is being pushed more to the surface of the sample and accumulates near the surface. For higher energies, the Ti profile goes deeper in the sample. Which could be related to the Ti diffusion over the whole liquid phase during PLM. Furthermore, it's worth mentioning that there were no Ti losses during the PLM process. Figure 2 shows a Raman spectrum of the samples along with the as-implanted sample. It confirms the amorphization of the sample after ion implantation and the recovery of the crystalline structure after applying PLM. Figure 3 shows a cross-section view of four of the samples using TEM technique. A bubble-like behaviour at lower PLM energy can be observed. A better recrystallization of the films is found as the PLM energy density is increased. Furthermore, no extended defects were observed, such as (cellular breakdown, stacking faults, etc)

References

[1] J. Olea et al., "Strong subbandgap photoconductivity in GaP implanted with Ti", Prog. Photovolt. Res. Appl., vol. 26, pp. 214-222, 2018.
[2] Palacios, P et al., 2006. Energetics of formation of Ti Ga 3 As 4 and Ti Ga 3 P 4 intermediate band materials. *The Journal of chemical physics*, *124*(1), p.014711. (IB)
[3] Kim, Tet al., 2010. Heat flow model for pulsed laser melting and rapid solidification of ion implanted GaAs. *Journal of Applied Physics*, *108*(1), p.013508.

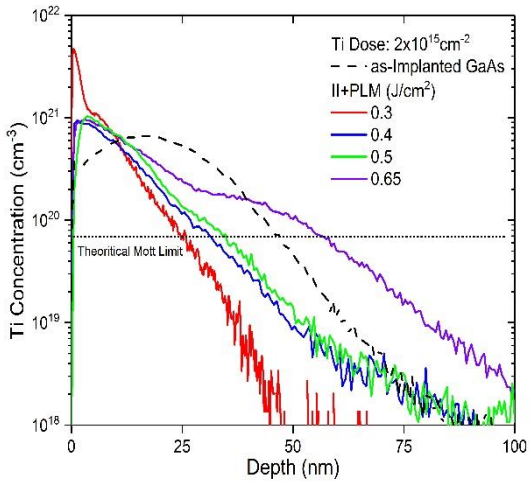

Figure 1. ToF-SIMS of GaAs:Ti for the as-implanted and samples subjected to PLM at different energies.

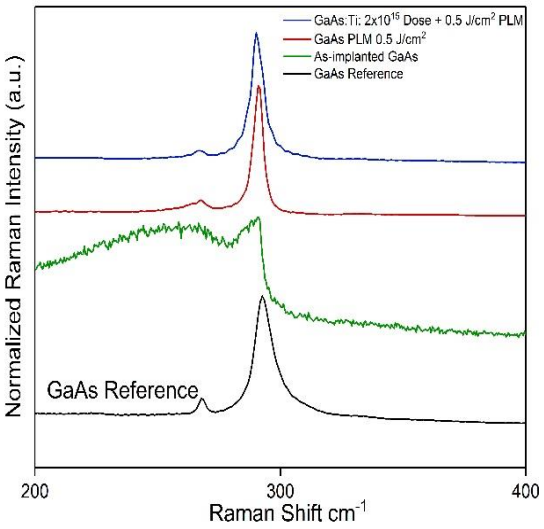

Figure 2. Raman spectra of GaAs reference along with the as-implanted, PLM processed and implanted + PLM.

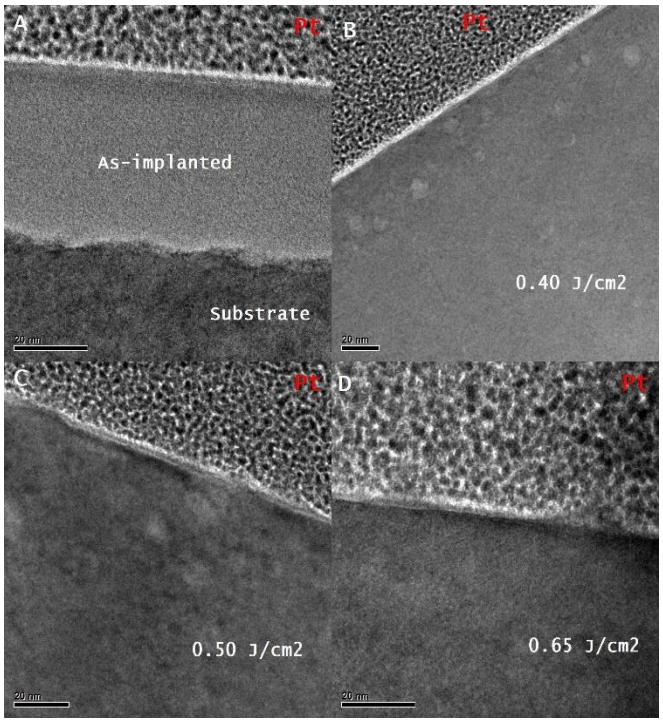

Figure 3. TEM images of GaAs:Ti. A) as-implanted sample. B) GaAs:Ti using 0.4 J/cm^2 PLM energy. C) GaAs:Ti annealed using 0.5 J/cm^2 PLM energy. D) GaAs:Ti annealed using 0.65 J/cm^2 PLM energy.

Progress in Engineering Photonic Structures based on Nanoporous Anodic Alumina

Laura K. Acosta, Josep Ferré-Borrull and Lluis F. Marsal*

*Departament d'Enginyeria Electrònica, Elèctrica i Automàtica, Universitat Rovira i Virgili, Avinguda Països Catalans 26, 43007 Tarragona, Spain. *Corresponding author e-mail address: lluis.marsal@urv.cat*

1. Abstract

Nanoporous Anodic Alumina Photonic Structures (NAA-PS) are obtained by electrochemical anodization of aluminum in the appropriate conditions and by means of continuously varying anodization current. NAA-PS presents excellent optical properties to enable their application in several fields such as chemical and optical biosensing, drug delivery, photocatalysis, optical encoding and others. Motivated for this excellent properties in this work, we present the recent advances of different photonic structures with different anodization approaches (sinusoidal and Gaussian) based on multiple periodic structures in overlapped and stacked configuration. Our work provides new existing opportunities to integrate these unique PC structures into photonic sensors and other platform materials for light-based technologies.

2. Introduction

Photonic Structures (PSs) are optical materials with allowed and forbidden photonic bands that modify the movement of photons when these travel across the structure. These light–matter interactions can be tuned with accuracy by engineering the PC's structure, which features regularly distributed regions of high and low refractive index in one, two, or three spatial dimensions [1-2]. PSs can be produced with different architectures and materials to get versatile light control across the extensive range of spectral regions for specific applications, including photonic encoding, chemical sensing and biosensing and photocatalysis [3,6]. Since the pioneering works nanoporous anodic alumina (NAA) has long been observed as an ideal base material for developing nanoporous PSs due to its cylindrical nanopores with well-defined and highly controllable geometric properties. NAA is formed by electrochemical oxidation of aluminum, a cost-effective and fully scalable process compatible with conventional micro- and nanofabrication. [7-8]

3. Methods and Results

Materials

High purity Aluminium foils (thickness 0.5 mm and purity 99.99%), Ethanol (C_2H_5OH), perchloric acid ($HClO_4$), oxalic acid ($H_2C_2O_4$), hydrochloric acid (HCl), copper chloride ($CuCl_2$) were purchased from Sigma-Aldrich. Double deionized water (DI) (18.6 MΩ) was used for all the solutions unless other specified.

Fabrication and results

First Al substrates were degreased in acetone, cleaned with ethanol and DI water and finally dried under a stream of air. Before the anodization, Al substrates were electropolished in a mixture of ethanol and perchloric acid 4:1 at 20 V and 5ºC for 5 min. During the electropolishing step the stirring direction was alternated every 60 s. After the electropolishing the samples were cleaned with ethanol and DI water and dried under a stream of air [7]. Then, the anodization was carried out in $H_2C_2O_4$ 0.3 M at 5ºC applying a periodic gaussian [9] and sinusoidal [10] current profile with several design parameters like offset current (I_0), current amplitude (I_1), Period (T) and number of periods (N). Multiple periodic currents are applied sequentially instead of simultaneously. In this work, we present different photonic structures in different configurations (overlapped and stacked) on the same structure. This permits to use a higher current contrast and using electrolytes with different composition. We also present different anodization approaches. Figure 1a shows the sinusoidal current profile of PS-NAA in stack configuration. Figure 1b shows the sum of sinusoidal waves of PS- NAA (overlapped configuration) and figure 1c shows the periodic gaussian current profile of PS-NAA. Figure 2a shows the reflection spectrum of PS-NAA in stack configuration. Figure 2b shows the reflection spectrum of PS-NAA in overlapped configuration and Figure 2c shows the refection spectrum of a single PS-NAA fabricated with gaussian pulse anodization.

4. Conclusions

Photonic structures based on nanoporous anodic alumina present excellent optical properties through the whole spectral regions, from UV to IR. In this work, we presented new anodization approaches to produce new photonic structures. The findings provide new exciting opportunities to integrate these unique PC structures into photonic sensors and other platform materials for light-based technologies.

Acknowledgments

This work was supported by the Spanish Ministerio de Ciencia, Innovación y Universidades (MICINN/FEDER) RTI2018-094040-B-I00, by the Agency for Management of University and Research Grants (AGAUR) ref 2017-SGR-1527.

References

[1] Santos, A. ,. J. Mater. Chem. C. 2017, 5 (23), 5581−5599
[2] G. Macias, L.P. Hernández-Eguía, J. Ferré-Borrull, J. Pallares, L.F. Marsal, ACS Appl. Mater. Interfaces, 5 (2013) 8093.
[3] Lim, S. Y.; Law, C. S.; Markovic, M.; Kirby, J. K.; Abell, A. D. Santos A. ACS Appl. Mater. Interfaces 2018, 10 (28), 24124−24136.
[4] Liu, L.; Lim, S. Y.; Law, C. S.; Jin, B.; Abell, A. D.; Ni, G.; Santos, A. J. Mater. Chem. A 2019, 7 (39), 22514−22529.
[5] G. Macias, L.P. Hernández-Eguía, J. Ferré-Borrull, J. Pallares, L.F. Marsal, ACS Appl. Mater. Interfaces, 5 (2013) 8093. [5] J. Ferré-Borrull, J. Pallarès, G. Macias, L.F. Marsal, Materials, 2014, 7, 5225-5253.
[6] G. Macias, J. Ferré-Borrull, J. Pallares, L.F. Marsal, Nanoscale research letters, 9 (2014) p. 315
[7] A. Santos, J.H. Yoo, C. Vashisth, T. Kumeria, Y. Wang, D. Losic, Nanoscale, 8 (2016) 1360.
[8] J. Ferre-Borrull, J. Pallares, Macías G, L.F. Marsal, Materials, 7, 5225 (2014).
[9] Laura K. Acosta, Francesc Bertó-Roselló, E. Xifre-Perez, Cheryl Suwen Law, Abel Santos, J. Ferré-Borrull. L.F. Marsal, Materials. ACS Appl. Mater. Interfaces, 12, 19778-19787 (2020).
[10] Laura K. Acosta, Francesc Bertó-Roselló, E. Xifre-Perez, Abel Santos, J. Ferre-Borrull, L.F. Marsal. ACS Appl. Mater. Interfaces, 11, (2019). 3360-3371

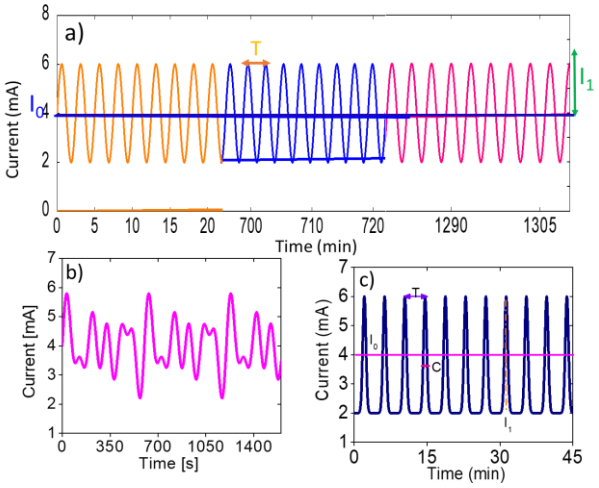

Figure 1. Anodization Current profiles of PS-NAA. (a) sinusoidal profile in stack configuration. (b) sinusoidal profile in overlapped configuration. (c) single Gaussian current profile.

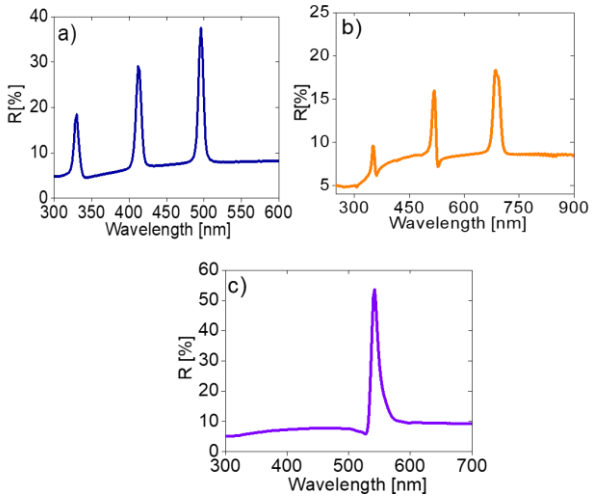

Figure 2. Reflection spectra of PS-NAA. (a) stack configuration. (b) overlapped configuration and (c) gaussian anodization.

Silicon heterojunction solar cells with Graphene-modified front transparent conductive electrodes

I. Torres[1], S. Fernández[1], R. Barrio[1], N. González[1], J. J. Gandía[1], M. De la Cruz[1], I. Rucandio[1], A. Molinero[1], J. Martínez[2], M. Fernández[3], E. Taboada[3], I. Arnedo[3,4]

[1] CIEMAT, Avda. Complutense 40, Madrid 28040, Spain.
[2] ISOM, Universidad Politécnica de Madrid, Ciudad Universitaria, Madrid, Spain.
[3] das-Nano, Polígono Industrial Talluntxe, Calle M-10, Tajonar, Navarra 31192, Spain
[4] Dpto. Ingeniería Eléctrica, Electrónica y de Comunicación, Universidad Pública de Navarra, Pamplona 31006, Spain
Contact: Ignacio.torres@ciemat.es. Telephone: +34 918466531

1. Introduction

Optoelectronic devices featuring a transparent conductive oxide in its structure such as photovoltaic solar cells may benefit from an improved electrical conduction of the oxide film. Unfortunately, a meaningful reduction in the film' electrical resistivity is generally accompanied by a decrease in the film' optical transparency. The combination of highly transparent and highly conductive 2D materials such as graphene with transparent conductive oxides in a hybrid structure could be an interesting approach to circumvent this limitation [1].

In this work, we explore the benefits of combining multiple sheets of CVD deposited graphene with ITO to be used as the transparent conductive electrode (TCE) in silicon heterojunction solar cells. Graphene sheets have the potential to further decrease the TCE sheet resistance below the ITO value, but it also reduces the optical transparency with each additional graphene sheet added. To evaluate the combined effect, we fabricated several heterojunction solar cells (see Fig. 1) with between one and three graphene sheets transferred and measured their performance.

2. Experimental

Silicon heterojunction solar cells were fabricated using double side polished CZ n-Si wafers following a standard process. The back contact consisted of a fully metallized area. On the front side, an 80 nm ITO film was sputtered from an In_2O_3:SnO_2 (90/10 wt.%) target using a DC sputtering system. Following ITO deposition, one, two or three CVD-grown monolayer graphene sheets were transferred onto the ITO surface. Lastly, the devices were completed with the deposition of a Ti+Ag metal grid on top of the TCE.

The characterization of the solar cells was carried out by means of its current-voltage characteristics measured under calibrated illumination and through quantum efficiency and Suns-Voc measurements. Additionally, the improvements in the surface conductivity were assessed through Laser Beam Induced Current (LBIC) measurements and through reflection-mode terahertz time-domain spectroscopy (THz-TDS), a novel technique which allows us to obtain surface mappings that resembles the electrical conductance.

3. Results

Fig. 2 and Fig. 3 show the measured IV characteristics and internal quantum efficiency of the fabricated solar cells and Table 1 displays the main solar cell parameters extracted. As can be seen, the cells' excellent V_{oc} is not affected by the addition of the graphene monolayers but the FF and I_{sc} values evolve as expected: with each additional layer I_{sc} loses around 5 mA while FF improves short of 1%. The losses in I_{sc} are perfectly illustrated by the internal quantum efficiency as shown in Fig. 3. On the other hand, the improvements in FF can be associated with an improved series resistance thanks to an enhanced TCE sheet resistance as concluded from LBIC and THz-TDS measurements (see Fig. 4 and Fig 5). These confronted effects affect the device efficiency oppositely and thus, while the addition of one monolayer of graphene showed a net improvement in efficiency [2], in the case of two and three sheets the loss in I_{sc} outmatches the gain in FF, preventing further efficiency improvements.

References

[1] S. Fernández et al., "Advanced Graphene-Based Transparent Conductive Electrodes for Photovoltaic Applications", Micromachines (Basel), vol. 10 (6), pp. 402-412, 2019.

[2] I. Torres et al., "Graphene-Based Transparent Electrode Incorporated into Silicon Heterojunction Solar Cell Technology". 37th European Photovoltaic Solar Energy Conference and Exhibition, pp.478-481, 2020.

Acknowledgment:

This research was funded by the Spanish government under project DIGRAFEN, grant numbers ENE2017-88065-C2-2-R and ENE2017-88065-C2-1-R

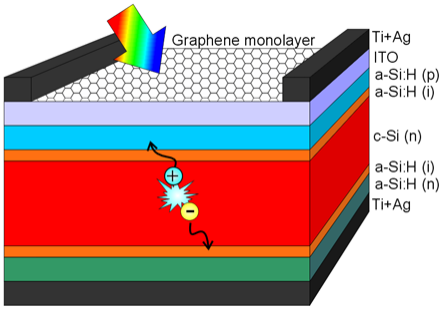

Fig. 1: Sketch of the solar cells investigated in this study. The top contact consists in 80 nm ITO with either one, two or three graphene monolayers.

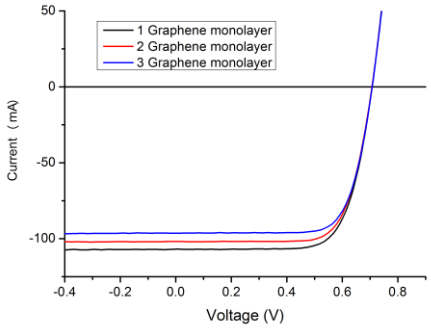

Fig. 2: Current-Voltage characteristics under illumination of the cells under study.

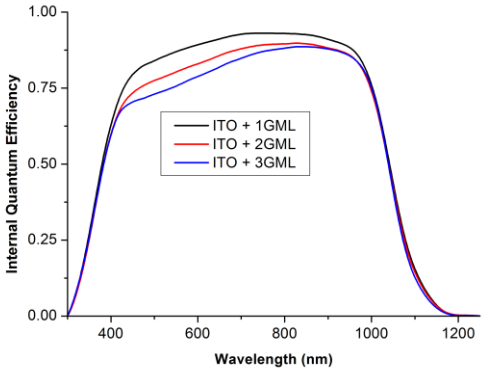

Fig. 3: Internal quantum efficiency of the cells under study.

Id	Isc (mA)	Voc (mV)	FF (%)	Eff (%)
1 GML	106.89	707	72.6	15.67
2 GML	101.81	707	73.5	15.11
3 GML	96.36	707	74.6	14.52

Table 1: Main solar cell parameters extracted from the current-voltage characteristics of the solar cells under illumination. The acronym GML stands for graphene monolayer.

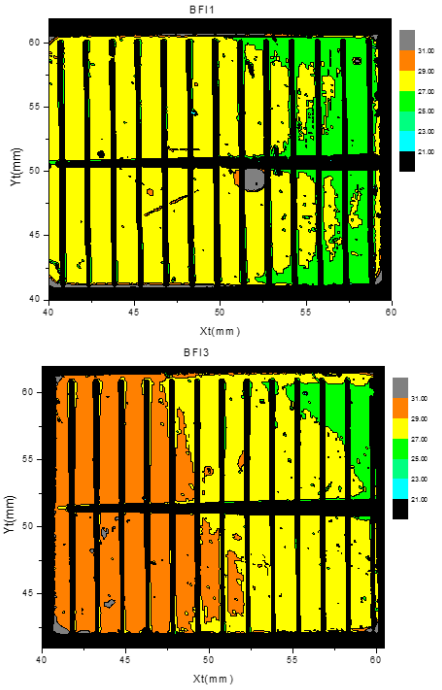

Fig. 4: LBIC maps of the cells with 1 GML (Top) and 3 GML (bottom).

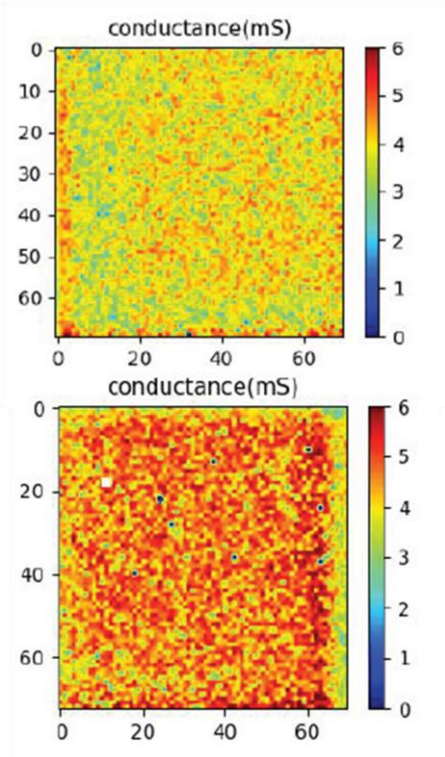

Fig. 5: THZ-TDS plots of the cells with 1 GML (Top) and 3 GML (bottom)

Laser Fired Contacts in multicrytalline silicon solar cells

R. Barrio[1], D. Canteli[2], [1], I. Torres[1], S. Fernández[1], M. De la Cruz[1], C. Molpeceres[2], J.J. Gandía[1]

[1]CIEMAT, Unidad de Energía Solar Fotovoltaica, 28040-Madrid, Spain.
[2]Centro Láser, Universidad Politécnica de Madrid, 28038-Madrid, Spain.
Contact: rocio.barrio@ciemat.es.

1. Abstract

The roadmap for the development of silicon solar cells requires the introduction of passivating contacts to obtain higher efficiencies as well as to reduce the cost of production to be industrially implemented. In this context, Laser Fired Contacts (LFC) on p-type silicon wafers have been shown to be an effective technique to improve efficiencies [1], due to their ability to reduce recombination losses on the back surface of crystalline silicon solar cells. These studies have mainly been focused on high quality monocrystalline silicon wafers and there are not enough developments made with multicrystalline silicon (mc-Si) wafers. Therefore, in this work, we present the optimization of the LFC process on p-type mc-Si and its application in two types of silicon devices: diffusion and heterojunction solar cells. These rear contacts have led to improved efficiencies for both types of solar cells over similar devices with thermalized aluminum rear contacts and without back passivation. These results illustrate the enormous potential of these localized laser-contacts created for mc-Si solar cells, perfectly compatible with a lower cost industrial production.

2. Introduction

Solar photovoltaic energy is still dominated by monocrystalline and multi-crystalline silicon due to its good efficiencies, stability, and the market confidence. For silicon technology, one of the major technological challenges is to reduce the high cost of production of the cells, while maintaining high efficiencies. Some strategies could be the reduction of the wafer thickness and the use of low-quality silicon wafers, as mc-Si, instead of high-quality monocrystalline silicon wafers. Due to the high carrier recombination in mc-Si associated to a high concentration of contaminants and defects, LFC is particularly interesting. This is because part of the carrier lifetime degradation in mc-Si absorbents is caused by the high processing temperatures during the annealing of conventional metal contacts and antireflective coatings. Furthermore, to include a passivation back layer between the rear surface aluminum electrode layer and the mc-Si wafer could improve the performance of the devices considerably.

3. Methods and characterization

The studies described in this work with p type mc-Si wafers include: i) the optimization of amorphous silicon rear passivation layer, grown by plasma-enhanced chemical vapor deposition; ii) The optimization of laser-parameters, based on the applied power in the range 0.1-0.4W (laser fluence-range: 1.41-5.76 J/cm^2) and the fraction of contacted area (Fc ≈ 0.2-5%) and iii) the application of these LFC in diffusion solar cells (Diff.) and in silicon heterojunction solar cells (SHJ).

The LFCs were characterized electrically, estimating their specific contact resistance according to [2], and morphologically through images taken using a confocal microscope. The superficial recombination of passivated mc-Si wafers after was evaluated by minority carriers effective lifetimes and implied-V_{oc} values. Finally, silicon solar cells were characterized by current density-voltage (JV) characteristics under illumination calibrated and by Internal Quantum Efficiency (IQE).

4. Results

LFC laser conditions were optimized for mc-Si wafers obtaining a specific contact resistance r_c<0.2 mΩ·cm^2. LFCs under different pulse energies and pitches were tested in diffusion silicon solar cell. The efficiencies obtained were ranged between 12.8% and 14.9% depending on the LFC conditions. Regarding the SHJ solar cells with LFC, the maximum efficiency obtained was 11.2%. A priori, we would expect better efficiencies in SHJ cells than in diffusion ones. According to IQE, it is necessary a better adjustment of the frontal emitters on mc-Si for SHJ. Furthermore, the mc-Si wafers used for the difussion solar cells had the bulk previously passivated thus providing a quality improvement over the wafers used for the SHJ solar cells. For both types of cells, efficiencies were superior to similar solar cells with Al-thermalized rear contacts (Eff ≈ 8.3 %). In view of this result, LFC could be considered as a promising technique to improve the performance of mc-Si solar cells.

Acknowledgements
This work was supported by the project CHENOC (ENE2016-78933-C4-3-R and ENE2016-78933-C4-4-R)

References

[1].E. SchneiderÏchner. *et al. Prog. Photovoltaics Res. Appl.* 10, 29–34 (2002).
[2] P. Ortega. *et al. Prog. Photovoltaics Res. Appl.* 20(2):173 - 180 (2012).

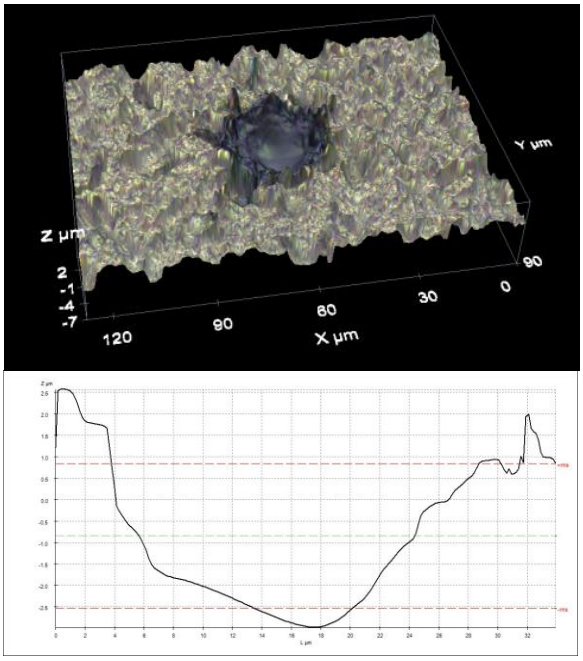

Fig. 1. Micrograph and depth-profiles of LFC obtained using a confocal microscope. These images were employed to analyse the morphology of the laser-contacts and to estimate the diameter of the craters to calculate the fraction of contacted area and then the specific contact resistance. The used laser system was a diode-pump solid-state laser (Explorer ONE laser source from Spectra Physics) emitting at 532 nm with a pulse duration of 15 ns. In particular, the image of this crater in Fig. 1 corresponds to a laser fluence of 5.76 J/cm^2 (BGL-cell) (contact diameter ~ 26 µm and crater depth >3 µm).

ID	Laser Fluence (J/cm^2)	Pitch (µm)	F_C (%)	Jsc (mA/cm^2)	Voc (mV)	FF	Eff (%)
BGJ	2.93	200	0,4	32,4	597	0,76	14,8
BGN	4.29	200	1,1	32,8	588	0,70	13,5
BGO	5.76	200	1,5	33,1	600	0,75	14,9
BGM	2.93	300	0,2	32,2	590	0,67	12,8
BGK	4.29	300	0,5	32,3	592	0,71	13,6
BGL	5.76	300	0,7	32,7	597	0,74	14,3
PV2		-	-	32,5	527	0,54	8,3

Table 1. Cell-performance parameters of diffusion silicon solar cells made with mc-Si as a function of laser conditions: Laser Fluence and distance between contacts (pitch). The grey-shaded row corresponds to the diffusion solar cell with Al-thermalized back contact.

ID	Laser Fluence (J/cm^2)	Pitch (µm)	F_C (%)	Jsc (mA/cm^2)	Voc (mV)	FF	Eff (%)
BID	2.93	200	0,7	25,9	576	0,51	7,6
BIC	4.29	200	1,2	31,7	580	0,64	11,8
BIE	2.93	300	0,3	26,1	567	0,64	9,4
BII	5.76	300	0,7	28,9	533	0,62	9,9
BIN	-	-	-	26,4	540	0,58	8,3

Table 2. Cell-performance parameters of SHJ solar cells with p-type mc-Si absorbents as a function of laser conditions: Laser Fluence and distance between contacts (pitch). The grey-shaded row corresponds to the SHJ with Al-thermalized back contact.

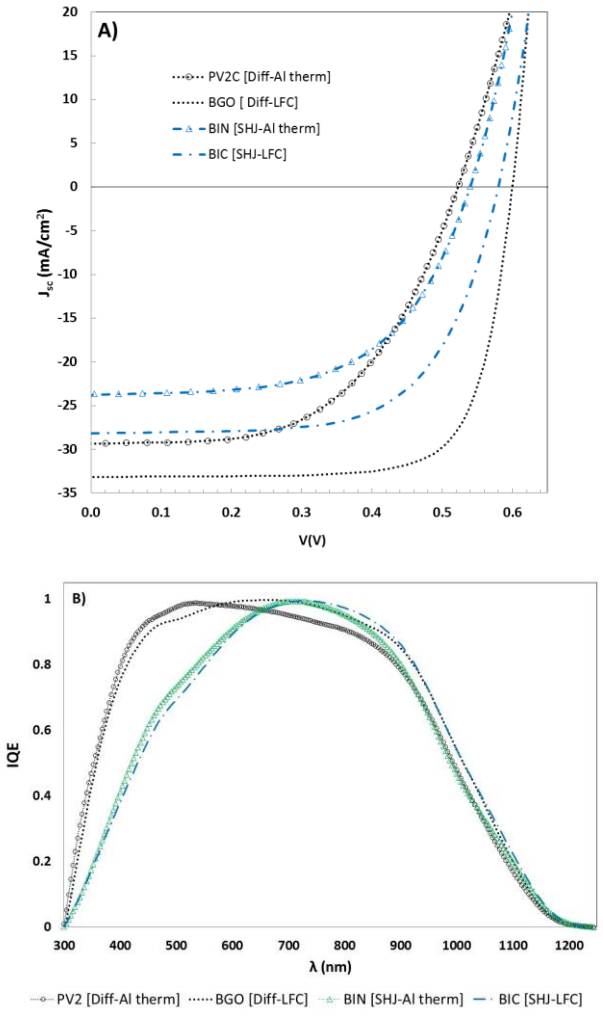

Fig. 2. A) JV characteristics and B) normalized-IQE curves, of diffusion (Diff.) and silicon heterojunction (SHJ) solar cells with mc-Si wafers, both structures with LFC (BGO & BIC) and with Al-thermalized back contacts (PV2C & BIN).

Bulk-Heterojunction Organic Solar Cells Towards 20% of Power Conversion Efficiency

J. G. Sánchez[1], J. Pallarès[2], E. Palomares*[1,3] and L. F. Marsal*[2]

[1]Institute of Chemical Research of Catalonia-The Barcelona Institute of Science and Technology (ICIQ-BIST), Av. Països Catalans, 16, E-43007 Tarragona, Spain. E-mail: epalomares@iciq.es
[2]Departament d'Enginyeria Electrònica Elèctrica i Automàtica Universitat Rovira i Virgili Av. Països Catalans 26, 43007 Tarragona, Spain, e-mail: lluis.marsal@urv.cat
[3]ICREA, Passeig Lluís Companys 23, Barcelona, E-08010, Spain.

1. Abstract

Bulk-heterojunction organic solar cells (BHJ-OSCs) are in the spotlight of the photovoltaics field because they are close to reaching the efficiency milestone of 20%. In this work, we present the evolution of the efficiency of our BHJ-OSCs and the challenges we have overcome to achieve high-efficiency devices. Moreover, we show our recent advances in BHJ-OSCs in comparison to that on the state-of-the-art.

2. Introduction

Bulk-heterojunction organic solar cells (BHJ-OSCs) are considered a promising photovoltaic technology because of their manufacturing low -cost, lightweight, and the possibility to fabricate large effective-area and flexible devices. Since BHJ-OSC was first reported [1], research on these devices focused on the role of the interpenetrating network of separate phases between donor and acceptor materials. The development of several donor polymers (such as P3HT, PCPDTBT and the PTB-family), and fullerene-based acceptors (e.g., $PC_{60}BM$, $PC_{70}BM$ and ICBA) allowed obtaining BHJ-OSCs with power conversion efficiencies (PCE) between 3.5% and 10% [2-4]. However, the PCE of the devices was limited to 10% mainly to the weak light absorption in the visible region absorption, and the low stability of the fullerene acceptors. To overcome those problems, small-new molecule acceptors, so-called non-fullerene acceptors (NFAs), were developed. The BHJ-OSCs based on new NFAs (such as ITIC, IDIC and Y families) blended with novel donor polymers (mainly PBDB-T family) have reached PCE from 11% to the highest reported 18.2% [5-7]. Herein, we presented the fabrication and characterization of several BHJ-OSCs based on polymer:fullerene, and polymer:NFA. Moreover, we demonstrated the important role of the electron transporting layer (ETL) and hole transporting layers (HTL) for charge extraction.

3. Experimental and Results

The BHJ-OSCs with different donor and acceptor materials were fabricated with the conventional and inverted structures: ITO/HTL/active layer/ETL/ cathode and ITO/ETL/active layer/HTL/anode, respectively. The materials used as HTL were PEDOT:PSS, molybdenum oxide, and vanadium oxide, whereas PFN, PDINO, titanium oxide, and zinc oxide were used as ETLs. The fabricated devices were characterized by current density vs. voltage measurements under AM 1.5 simulated illumination and dark using a solar simulator, external quantum efficiency measurements, and by impedance spectroscopy measurements under AM 1.5 illumination with a frequency sweep.

Fig. 1 shows conventional and inverted structures used to fabricating BHJ-OSCs based on different donor/acceptor systems. Fig. 2 shows the efficiency progress of our BHJ-OSCs over the last 10 years. The efficiency increases as we replaced the polymer donor material (e. g. P3HT, PTB1, PTB7, PTB7-Th) in the polymer:$PC_{70}BM$ system [8-12] and the ETL and HTL interlayers. Recently, we achieved efficiency over 14% and 17% of efficiency by using last-generation polymer donor (PBDBT-2F) and non-fullerene acceptors (BTP-4F and BTP-4Cl). It is important to highlight the optimization and characterization work carried out to achieve those efficiencies over the years [13-20]. The efficiency timeline of BHJ-OSCs in literature is also depicted in Fig. 2.

Acknowledgements

L.F.M. and J.P. thank the Spanish Ministerio de Ciencia, Innovación y Universidades (MICINN/FEDER) RTI2018-094040-B-I00, and the Agency for Management of University and Research Grants (AGAUR) ref 2017-SGR-1527 and the Catalan Institution for Research and Advanced Studies. J.G.S. and E.P. thank MINECO (projects CTQ2013- 47183 and CTQ 2017-89814-P). L.F.M and E.P. thankful to ICREA Academia Award for economical support.

References

[1] G. Yu, J. Gao, J. C. Hummelen, F. Wudi, A. J. Heeger "Polymer Photovoltaic Cells: Enhanced Efficiencies via a

Network of Internal Donor-Acceptor Heterojunctions," Science, vol. 270, pp. 1789–1791, 1995.
[2] P. Schilinsky, C. Waldauf, and C. J. Brabec, "Recombination and loss analysis in polythiophene based bulk heterojunction photodetectors," Appl. Phys. Lett., vol. 81, no. 20, pp. 3885–3887, 2002.
[3] Y. Liang et al., "For the bright future-bulk heterojunction polymer solar cells with power conversion efficiency of 7.4%," Adv. Mater., vol. 22, no. 20, pp. 135–138, 2010.
[4] Z. He et al., "Single-junction polymer solar cells with high efficiency and photovoltage," Nat. Photonics, vol. 9, no. 3, pp. 174–179, 2015.
[5] W. Zhao et al., "Fullerene-Free Polymer Solar Cells with over 11% Efficiency and Excellent Thermal Stability," Adv. Mater., pp. 4734–4739, 2016.
[6] Z. Li et al., "Donor polymer design enables efficient non-fullerene organic solar cells," Nat. Commun., vol. 7, no. 9, pp. 1–9, 2016.
[7] Q. Liu et al., "18% Efficiency organic solar cells," Sci. Bull., vol. 65, pp. 272–275, 2020.
[8] V. S. Balderrama et al., "Microelectronics Reliability Correlation between P3HT inter-chain structure and Jsc of P3HT:PC[70]BM blends for solar cells," Microelectron. Reliab., vol. 53, pp. 560–564, 2013.
[9] V. S. Balderrama et al., "Degradation of electrical properties of PTB1:PCBM solar cells under different environments," Sol. Energy Mater. Sol. Cells, vol. 125, pp. 155–163, 2014.
[10] R. C. I. Mackenzie et al., "Loss Mechanisms in High Efficiency Polymer Solar Cells," Adv. Energy Mater., vol. 6, 2016.
[11] J. G. Sánchez et al., "Stability study of high efficiency polymer solar cells using TiOx as electron transport layer," Sol. Energy, vol. 150, pp. 147–155, 2017.
[12] V. S. Balderrama, et al., "High-efficiency organic solar cells based on a halide salt and polyfluorene polymer with a high alignment-level of the cathode selective contact," J. Mater. Chem. A, vol. 6, pp. 22534–22544, 2018.
[13] V. S. Balderrama et al., "Microelectronics Reliability Influence of P3HT:PCBM blend preparation on the active layer morphology and cell degradation," Microelectron. Reliab., vol. 51, pp. 597–601, 2011.
[14] V. S. Balderrama et al., "Charge Carrier Concentration in PTB1, PTB7, and PCBM Layers Used in High-Efficiency Solar Cells," IEEE J. Photovoltaics, vol. 5, no. 4, pp. 1093–1099, 2015.
[15] P. Han, et al., "Improving the Efficiency of PTB1:PCBM Bulk Heterojunction Solar Cells by Polymer Blend Solution Aging," IEEE J. Photovoltaics, vol. 5, no. 3, pp. 889–896, 2015.
[16] V. S. Balderrama et al., "Organic Solar Cells Toward the Fabrication Under," IEEE J. Photovoltaics, vol. 6, no. 2, pp. 491–497, 2016.
[17] E. Osorio et al., "Degradation Analysis of Encapsulated and Nonencapsulated TiO2/PTB7:PC70BM/V2O5 Solar Cells under Ambient Conditions via Impedance Spectroscopy," ACS Omega, vol. 2, no. 7, pp. 3091–3097, 2017.
[18] J. G. Sánchez et al., "Impact of inkjet printed ZnO electron transport layer on the characteristics of polymer solar cells" RSC Adv., vol. 8, pp. 13094–13102, 2018.
[19] A. A. A. Torimtubun et al., "Sustainable Energy & Fuels A cathode interface engineering approach for the comprehensive study of indoor performance enhancement in organic photovoltaics" Sustain. Energy Fuels, vol. 4, pp. 3378–3387, 2020.
[20] J. G. Sánchez et al., "Effects of Annealing Temperature on the Performance of Organic Solar Cells Based on Polymer: Non-Fullerene Using V2O5 as HTL," IEEE J. Electron Devices Soc., vol. 7, pp. 421–428, 2020.

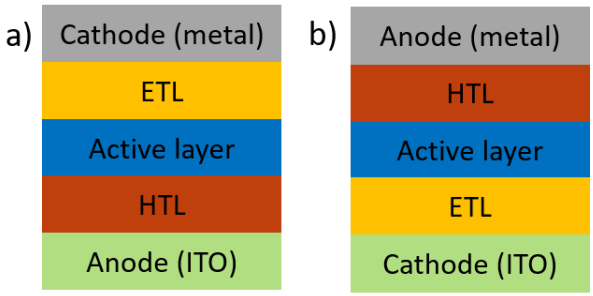

Fig. 1 Conventional (a) and inverted (b) structures used to fabricate BHJ-OSCs.

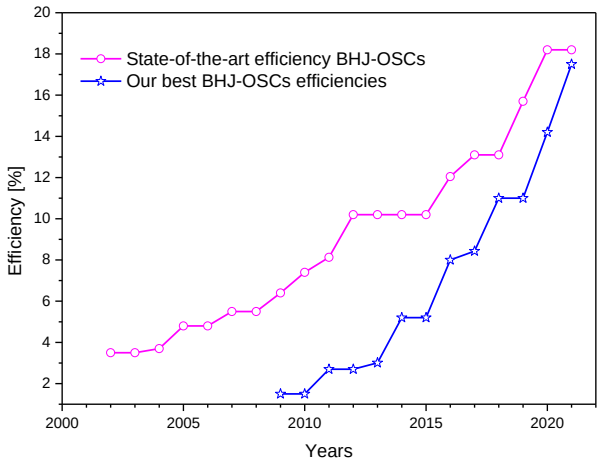

Fig. 2 Timeline of the progress of BHJ-OSCs efficiency.

Unveiling the optoelectronic mechanisms ruling Ti hyperdoped Si photodiodes

E. García-Hemme, D. Caudevilla, S. Algaidy, F. Zenteno, R. García-Hernansanz, J. Olea, D. Pastor, A. del Prado, E. San-Andrés, I. Mártil, G. González-Díaz.

Dpto. EMFTEL, Fac. CC. Físicas, Univ. Complutense de Madrid, 28040, Spain. 913944533 eric.garcia@ucm.es

1. Introduction

Si hyperdoped with deep levels impurities is being actively studied as a potential CMOS compatible infrared photodetector due to its promising optoelectronic properties.[1] Unfortunately, competitive commercial devices have not yet been obtained, mainly due to its low sub-bandgap EQE. To overcome this disadvantage, a deeper understanding of the optoelectronic mechanisms is mandatory. In this work we present a structural and optoelectronic analysis, and we discuss the origin of the optoelectronic mechanisms observed in Ti hyperdoped Si / p-Si junction photodiodes.

2. Experimental

Square-shaped samples 1×1 cm^2 in size of p-type (111) Si with a thickness of 300 µm (ρ~150-300 Ωcm at room temperature) were $^{48}Ti^+$ implanted at 7º in a Varian CF3000 model refurbished by IBS at 32 keV with 2×10^{15} cm^{-2} dose and subsequently pulsed laser melted processed in air with an a KrF excimer laser (248 nm, 20 ns pulse). See Fig. 1 a) for a schematic of the manufacturing route. ToF-SIMS measurements were carried out in a ToF-SIMS V model, with a 25 keV pulsed Bi^{3+} beam at 45° incidence. A 10.5 kV voltage was used to extract the secondary ions and their time of flight from the sample to the detector was measured with a reflection mass spectrometer. TEM images were taken with a Jeol JEM 3000F microscope operated at an accelerating voltage of 300 kV. Atomic number contrast images were recorded in the high-angle annular dark-field scanning transmission electron microscopy (HAADF-STEM) mode. Energy-dispersive X-ray spectroscopy (EDX) measurements were done with an OXFORD INCA system attached to the JEM 3000F microscope. Photodiodes were manufactured by depositing a comb-shaped metallic electrode on top of the hyperdoped layer and a full metallization on the p-Si back side. Back-side ohmic contact is ensured thanks to a p++ layer obtained by $^{11}B^+$ ion implantation and subsequent rapid thermal annealing. Temperature-dependent measurements were carried by placing the manufactured photodiodes inside a He closed-cycle Janis cryostat with a ZnSe window. Dark current-voltage measurements were performed with a Keithley SCS-4200 instrument. For spectral EQE measurements, the samples were illuminated using a TMc300 Bentham monochromator with a Globar (SiC) bar as infrared source. Measurements were carried out with a SR830 digital signal processing lock-in amplifier.

3. Results and discussion

Fig. 2 a) presents the Ti depth profile. A Ti concentration far above the solid solubility limit in Si (4×10^{14} cm^{-3}) has been obtained in the Ti hyperdoped-Si layer. Fig. 2 b) shows a representative HAADF STEM micrograph obtained in the Si [001] axis. A brighter layer is observed at a depth in agreement with the largest Ti concentration peak observed in the ToF-SIMS depth profile. TEM image shown in Fig. 2 c) demonstrates that the entire Ti hyperdoped-Si layer is monocrystalline, without the presence of any extended defects. Fig. 2 d) presents the EDXS map of the elements for the indicated region (red correspond to Si, blue to Ti). EDXS detection limit is around 1 atomic % concentration. According to the compositional map, there is a laterally uniform Ti distribution of 7 nm depth (Ti concentration higher than 1 atomic %) within the recrystallized Si layer. Fig. 3 presents the temperature dependent I-V measurements. Data were satisfactorily fitted to the double diode model. From the fittings we concluded that the main transport mechanism is due to recombination processes in the depletion region, while a tunneling process is identified at low temperatures and low bias. Fig. 4 shows the temperature dependent spectral EQE. The photoresponse extends in the sub-bandgap region down to 0.4 eV photon energy for the lower temperature. An abrupt increase of the sub-bandgap photoresponse appears as the temperature decreases. By means of numerical semiconductor device simulations, we satisfactorily correlated the dark transport mechanisms to the temperature behaviour of the spectral EQE. We identified the tunneling current as the responsible for the abrupt increase of the EQE. This work paves the route for new device optimization strategies.

References

[1] W. Mao et al., Adv. Opt. Mat., in press, DOI: 10.1002/adom.202001546.

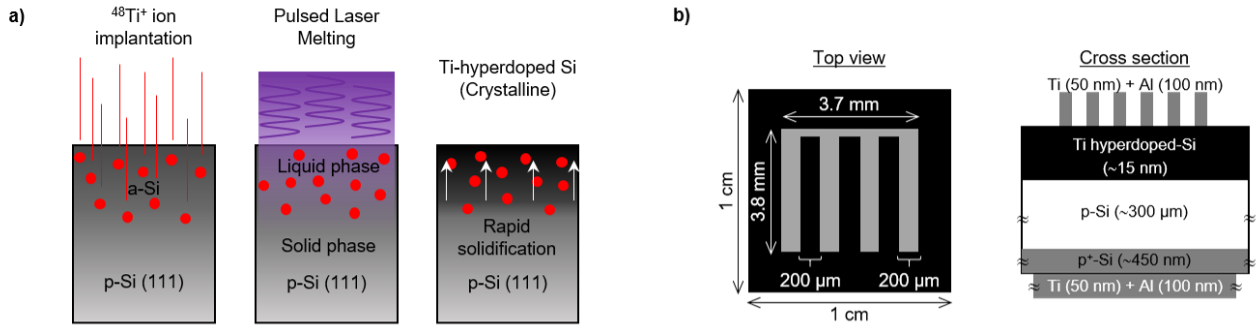

Fig.1. a) Schematic of the fabrication route for the Ti hyperdoped-Si material. Ion implantation introduces the required high concentration of Ti. Pulsed Laser Melting is used to melt the implanted layer. A rapid solidification process takes place, recovering the single-crystalline structure while maintaining a hyperdoped Si:Ti layer. **b)** Top and cross section schematic views of the photodiode geometry (dimensions not at scale).

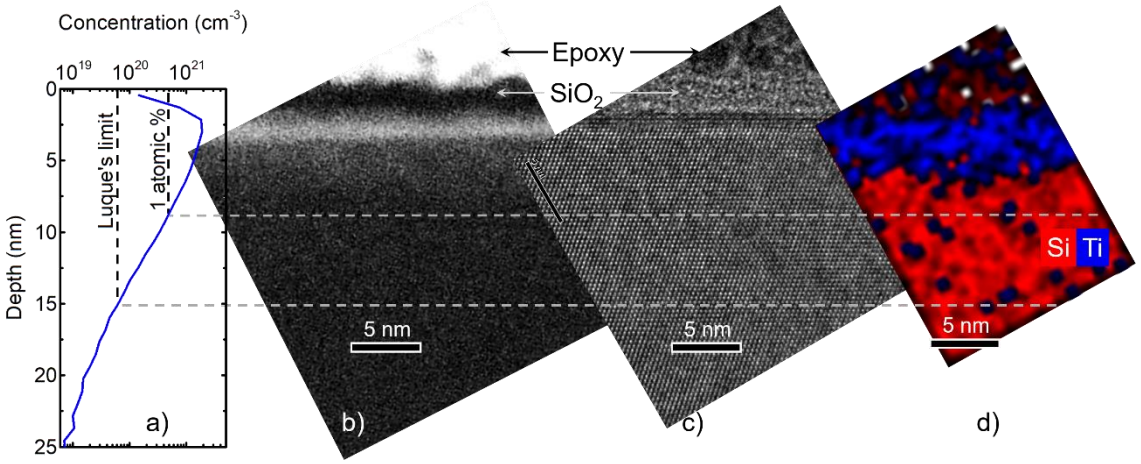

Fig.2. a) ToF-SIMS measurements showing the Ti concentration depth profile. 1 % atomic concentration and theoretical concentration to obtain an impurity band are marked as references. **b)** Atomic number contrast image recorded in HAADF-STEM mode. Brighter contrast observed near the surface corresponds to elements with a higher atomic number (Ti) with respect to the darker contrast obtained in the substrate (Si). **c)** High-resolution TEM image confirms the monocrystalline structure of the Ti hyperdoped-Si layer. **d)** Qualitative chemical map obtained from EDXS measurements indicating Si (red) and Ti (blue) presence.

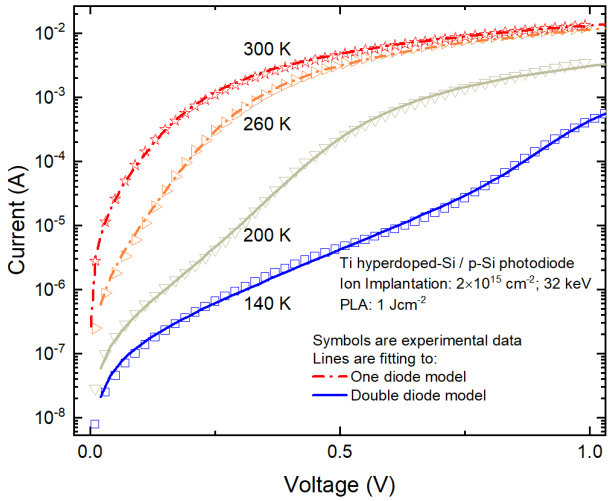

Fig.3. Temperature-dependent IV curve (open symbols) together with fit curves to the double diode model.

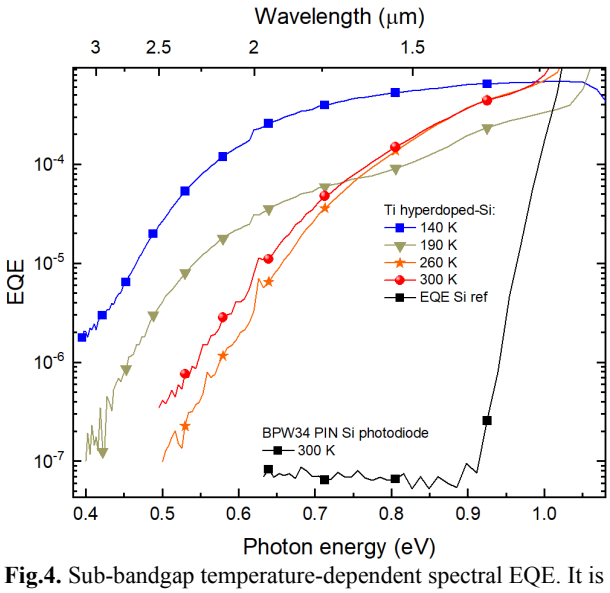

Fig.4. Sub-bandgap temperature-dependent spectral EQE. It is noteworthy the abrupt increase of the photoresponse for temperature below 240 K.

Simulations and nanofabrication of photonic crystals based on silicon pillars for mechanical biosensors

Elena López-Aymerich[1,2*], Maria Dimaki[3], Winnie E. Svendsen[3], Sergi Hernández[1,2], Daniel Navarro-Urrios[1,2,4], Mauricio Moreno[1,2], Florenci Serras[5], Albert Romano-Rodríguez[1,2]

1 Institute of Nanoscience and Nanotechnology, Universitat de Barcelona, Barcelona, Spain
2 MIND-Department of Electronics and Biomedical Engineering, Universitat de Barcelona, Barcelona, Spain
3 Department of Biotechnology and Biomedicine, Technical University of Denmark, Kongens Lyngby, Denmark
4 Catalan Institute of Nanoscience and Nanotechnology, CSIC and The Barcelona Institute of Science and Technology, Campus UAB, Bellaterra, Spain
5 Department of Genetics, Microbiology and Statistics and Institute of Biomedicine, Universitat de Barcelona, Barcelona, Spain
*corresponding author, E-mail: elenalopez@ub.edu

1. Abstract

Photonic crystals (PC) have been on the scope of nanophotonics since their first reference in 1987 [1]. Since this pioneering work, most of the configurations of PC studied and reported have been based on slabs with a regular pattern of holes in them, due to the simplicity of their fabrication. In this work, however, we present a new configuration of 2D PC slabs using pillars instead [2]. The main goal of our project is to use these PC as a biological sensor of lateral mechanical stresses in tissues. The simulations presented here consider PCs in aqueous environment and the introduction of line and point defects in them. Results of advanced nanofabrication are shown as well in this work.

2. PC and waveguide band diagrams

The periodic distribution of dielectric materials in PCs create bands that determine those light frequencies allowed and banned to be transmitted through the PC depending on the crystallographic direction. Photonic band gaps (PBG) are opened when a range of frequencies is banned for all crystallographic directions [3]. In our work we consider a PC with triangular symmetry with a pitch of 500nm and 100nm-radii pillars. The resulting band diagram is shown in **Fig.1.** The PBG is opened between the 1.31μm and 1.89μm. This frequency range matches the 2nd water transmission window, making the structure suitable for biological purposes.

In **Fig.2.** the result of the projected band diagram is shown corresponding to a waveguide (WG) created removing one line of pillars in the 2D simulations. These results are in agreement of the results obtained using simulations of the transmission and reflection spectra (**Fig.3.**) and with literature [4]. These results will be compared with the experimental measurements of the transmission and reflection spectra.

3. Nanofabrication

High aspect ratio silicon pillars have been fabricated on silicon-on-insulator (SOI) substrates thanks to the use of advanced nanofabrication technologies.

The fabrication consists of several steps, including advanced electron beam lithography (EBL) and anisotropic dry etching process using reactive ion etching (RIE). The EBL process consists of AR-P6200.09 photoresist spinning, followed by thermal aluminium deposition. E-beam exposure is carried out using a 100kV electron beam writer JEOL JBX-9500FSZ. The aluminium layer and the exposed resist are removed using TMAH and AR 600-546 remover, respectively. After that, a 20 nm-thick e-beam deposited aluminium layer is used for the final lift-off step for the pattern transfer. Remover 1165 is used for dissolving the remaining photoresist and removing the aluminium on top of it, leaving only the aluminium directly deposited on the sample's surface. The RIE step uses a combination of SF_6:C_4F_8 chemistries resulting on an anisotropic etch of the uncoated silicon. Results of this nanofabrication process can be observed in **Fig.4.**, where a PC with a linear defect (WG) and a point defect (cavity).

References

[1] E. Yablonovitch, "Photonic Crystals," J. Mod. Opt., vol. 41, pp.173-194, March 2007.
[2] S.G. Johnson, S. Fan, P.R. Villeneuve, and J.D. Joannopoulos, "Guided modes in photonic crystal slabs," Phys. Rev. B, vol. 60, pp. 5751-5758, August 1999.
[3] J.D. Joannopoulos, S.G. Johnson, and J.N. Winn, Photonic Crystals: Molding the Flow of Light, 2nd ed., Princeton Univeristy Press, 2008.
[4] S.G. Johnson, P.R. Villeneuve, S. Fan, and J.D. Joannopoulos, "Linear waveguides in photonic-crystal slabs," Phys. Rev. B, vol. 62, pp. 8212-8221, September 2000.

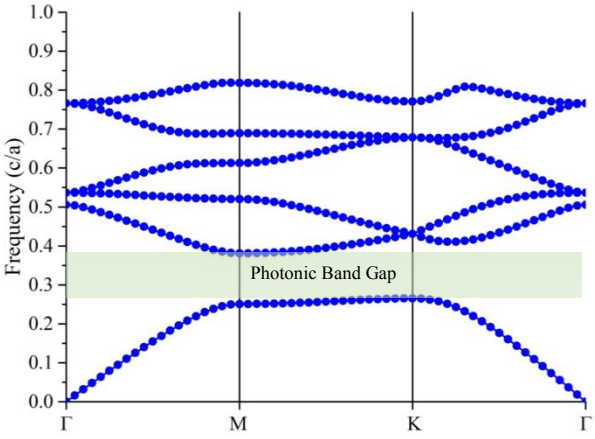

Fig.1. Band diagram of a 2D PC with 500nm pitch and 100nm radii for a light TM polarization.

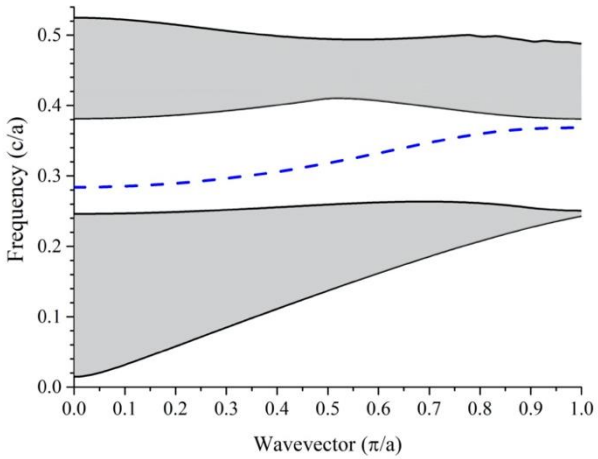

Fig.2. Projected band diagram of a 2D PC with a row of pillars missing. It can be observed when one mode is inserted within the PBG (blue discontinuous line).

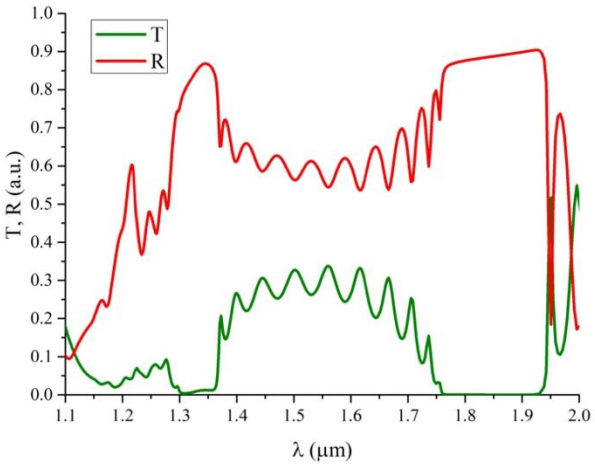

Fig.3. Transmission and reflection spectra of a 2D PC with a missing row of pillars. Both the effects of the PBG and the WG can be observed in this graph and in accordance with the previous figures.

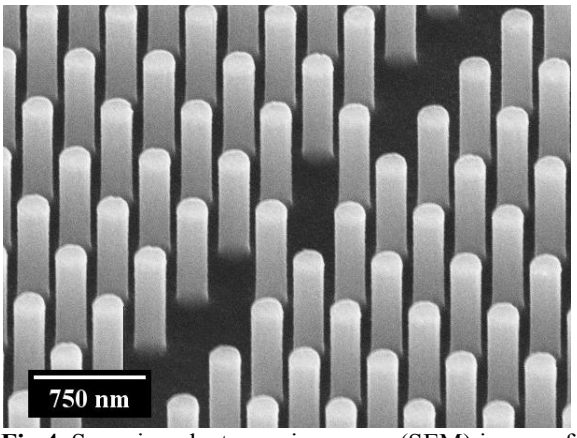

Fig.4. Scanning electron microscope (SEM) image of one of the nanofabricated samples. A PC with 500nm pitch and 100nm radii pillars is shown. In addition, a WG and a cavity can be observed in the image.

Inkjet-printed ZnO and NiOx: layer and device characterization for optoelectronics

S. González-Torres,[1] J.L. Frieiro,[1] G. Vescio,[1] A. Fernández,[1] M. Oszajca,[2] N. Lüchinger,[2] M. Rossier,[2] A. Hauser,[2] F. Linardi,[2] S. Hernández,[1] A. Cirera,[1] B. Garrido[1]

[1] MIND-IN2UB, Departament of Electronics and Biomedical Engineering, Universitat de Barcelona, Martí i Franquès 1, 08028 Barcelona (Spain)
[2] Avantama AG, Laubisruetistrasse 50, Staefa 8712, Switzerland

1. Introduction

Conventional device fabrication involves several physical and chemical thin film deposition techniques, which generally require high vacuum and high temperature processes. Furthermore, for device fabrication, these technologies require masking and several photolithography steps to achieve patterned deposition. In response to this, innovative device fabrication approaches have gained great attention. Technologies such as screen printing and inkjet printing (IJP) are being adapted to the deposition of functional materials. Functional inks can be prepared to deposit layers of a multitude of materials, as precursor inks or nanoparticle colloidal suspensions.[1]

IJP is a very interesting technology, as it is digital in nature (i.e. purely additive), it allows great control of process parameters, and is ideal for fast prototyping while maintaining the potential for scalability [1]. Thus, research in IJP of electronic devices can leverage the maturity and high throughput of current industrial processes for mass scale and cost-effective production of electronic devices. Despite the great potential of IJP, up until now, printing techniques have generally been used sporadically, e.g. for contacts or the active layer only, and generally limited to organic materials.

In this context, in this work we introduce the use of IJP for fabricating fully functional devices. We present first the formulation, printing, and characterization of thin layers of semiconducting n and p materials, ZnO and NiO_x, respectively. Afterwards we introduce the making and device characterization of a heterojunction diode with a final device structure of Pt/ZnO/NiO_x/C. Such heterostructures can be implemented for UV light photodetection and transparent UV solar cells [2].

2. Experiential details

A variety of morphological measurements including FE-SEM and profilometry demonstrate the absence of pinholes or cracks in our layers. Figures 1a and 1b are SEM images of ZnO and NiO_x printed layers, respectively, where this fact can be observed. On the other hand, XPS and PL indicate excellent compositional and structural properties. Optical measurements show light transmission above 70% in the visible spectrum. Electrical measurements of the single metal oxide layers and heterojunctions have also been performed, exhibiting ohmic and diode-like rectifying behaviors as expected for each device structure fabricated.

3. Electrical model and results

Single-layer devices show ohmic behavior, as can be seen in Figure 1c and 1d for ZnO and NiO_x, with resistivities of 5 Ω·m and 10 Ω·m, respectively. In addition, heterojunction devices display excellent current rectification behavior, with a current ratio between forward and reverse polarizations > 10^2.

$$I - \frac{(V - IR_s)}{R_p} = I_s e^{e(V-IR_s)/(n_{ideal}kT)} \quad (1)$$

By means of a two-resistance model (formula (1)), we have estimated the reverse saturation current (I_s = 10^{-15} A), the ideality factor (n = 4.4) and the equivalent series resistance R_s = 4×10^{-4} Ω of our heterojunction. The parallel resistance term can be neglected, as it has been estimated to be $R_p > 10^8$ Ω, from the first derivative dV/dI around 0V. The resulting fitting of these parameters can be seen in Figure 1e, along with the experimental data obtained.

4. Conclusion

In this work, high quality IJP ZnO and NiOx layers are presented. A variety of morphological, structural, electrical, and optical measurements have been performed to determine the proper deposition parameters and the properties of one-layer and heterojunction devices.

Although preliminary, our results indicate the suitability of these inkjet-printed layers for applications including UV light photodetection, and as charge transport materials for LEDs.

References

[1] Z. Zhan et al., "Inkjet-printed optoelectronics," Nanoscale, 2017, 9, 965-993.

[2] M. Patel et al., "Excitonic metal oxide heterojunction (NiO/ZnO) solar cells for all-transparent module integration," Solar Energy Materials and Solar Cells, 2017, 170, 246-253

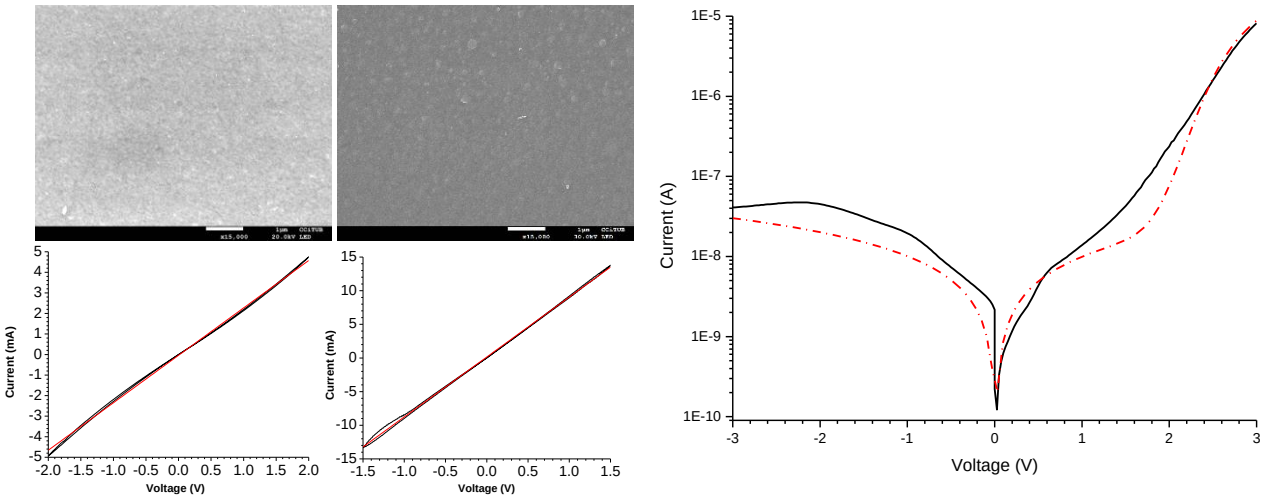

Fig.1. a) and b) SEM images of ZnO and NiOx thin layers showing high quality layers with no cracks or pinholes for both materials. **c) and d)** I-V measurements of ZnO and NiOx. Measurement in black, linear fitting in red. Both materials appear to have ohmic behavior. **e)** I-V measurements of P-N device (black line) and fit (red dotted line) according to formula (1).

SAW-driven plasmons in graphene heterostructures for fingerprinting ultrathin polymer layers

Raúl Izquierdo-López, Jorge Pedrós, Rajveer Fandan, Alberto Boscá, and Fernando Calle

Instituto de Sistemas Optoelectrónicos y Microtecnología & Departamento de Ingeniería Electrónica, E.T.S.I. de Telecomunicación, Universidad Politécnica de Madrid, Av. Complutense 30, Madrid 28040, Spain.
Contact: raul.izquierdo@upm.es

1. Surface-Enhanced InfraRed Absorption (SEIRA) Spectroscopy

The study of the optical properties of materials in the mid IR is of great importance for identifying complex compounds, determining both their composition and structure, since the vibrations of the main functional groups lie in this region of the spectrum. This set of chemical resonances is known as the IR fingerprint of the material as the position of the absorption peaks identifies unambiguously the compound. Moreover, valuable information about its conformation can be extracted from the relative heights and areas of these peaks.

However, the large mismatch between the wavelength of light ($\lambda \sim \mu m$) and the size of the molecules ($d \sim nm$) hinders the acquisition of experimental spectra due to the low absorption cross-section, which results in weak signals. In order to strengthen the interaction of the electromagnetic radiation with matter at the nanometer scale, surface plasmon polaritons (SPPs) have been proposed as a way of confining the electric field, decreasing the mode volume and therefore intensifying the light absorption [1-3]. This is known as surface-enhanced infrared absorption (SEIRA) spectroscopy.

2. Graphene Surface Plasmon Polaritons

SPPs are electromagnetic waves confined to the surface of a conducting material. Graphene is an excellent platform for generating SPPs in the mid IR, due to their increased lifetime and strong confinement ratio as compared to metals. In addition, graphene plasmons can hybridize with the optically active phonons of the substrate, forming surface plasmon-phonon polaritons (SPPPs). Furthermore, the Fermi level (E_F) in graphene can be adjusted through a gate voltage to dynamically tune the frequency of the SPPPs. Due to the reduced wavelength of SPPPs compared to that of free photons, a mechanism is needed to provide the momentum difference. A surface acoustic wave (SAW) can be used to create a virtual dynamic diffraction grating that ensures the momentum match [4,5].

Here, a transfer matrix method [6] has been used to simulate the interaction of ultrathin polymer layers with the SPPPs generated in graphene heterostructures on piezoelectric substrates by means of SAW resonators, proving their outstanding sensing capabilities in the mid IR. Figure 1 shows the dispersion of the SPPPs in a graphene/graphene/AlN/graphene/AlN heterostructure. The two graphene layers stacked at the top permit to reach large E_F values that are further tuned using the bottom graphene layer as a gate. In this way, the proposed heterostructure allows to easily cover the whole spectral region containing the vibrational resonances of most polymers. In particular, Figure 2 shows the sensing performance of this heterostructure when covered with a 2 nm-thick layer of two different polymers, 4,4′-bis(N-carbazolyl)-1,1′-biphenyl (CBP) and polyimide (PI). Besides a frequency shift and a drop in intensity, a Fano-type interference dip appears in the peaks corresponding to the SPPP when tuned at the frequency of the molecular vibrations of the respective polymers., allowing us to fingerprint them.

References

[1] F. Liu and E. Cubukcu, “Tunable omnidirectional strong light-matter interactions mediated by graphene surface plasmons”, Phys. Rev. B 88 (2013) 115439.
[2] Y. Li et al., “Graphene Plasmon Enhanced Vibrational Sensing of Surface-Adsorbed Layers” Nano Lett. 14 (2014) 1573.
[3] M. Autore et al., “Boron nitride nanoresonators for phonon-enhanced molecular vibrational spectroscopy at the strong coupling limit”, Light Sci. Appl. 7 (2018) 17172.
[4] J. Schiefele et al., “Coupling Light into Graphene Plasmons through Surface Acoustic Waves”, Phys. Rev. Lett. 111 (2013) 237405.
[5] R. Fandan et al., “Acoustically-driven surface and hyperbolic plasmon-phonon polaritons in graphene/h-BN heterostructures on piezoelectric substrates”, J. Phys. D: Appl. Phys. 51 (2018) 204004.
[6] T. Zhan et al., “Transfer matrix method for optics in graphene layers” J. Phys.: Condens. Matter 25 (2013) 215301.

Acknowlegdments

This work has received funding from the Comunidad de Madrid through project NMAT2D-CM (P2018/NMT-4511).

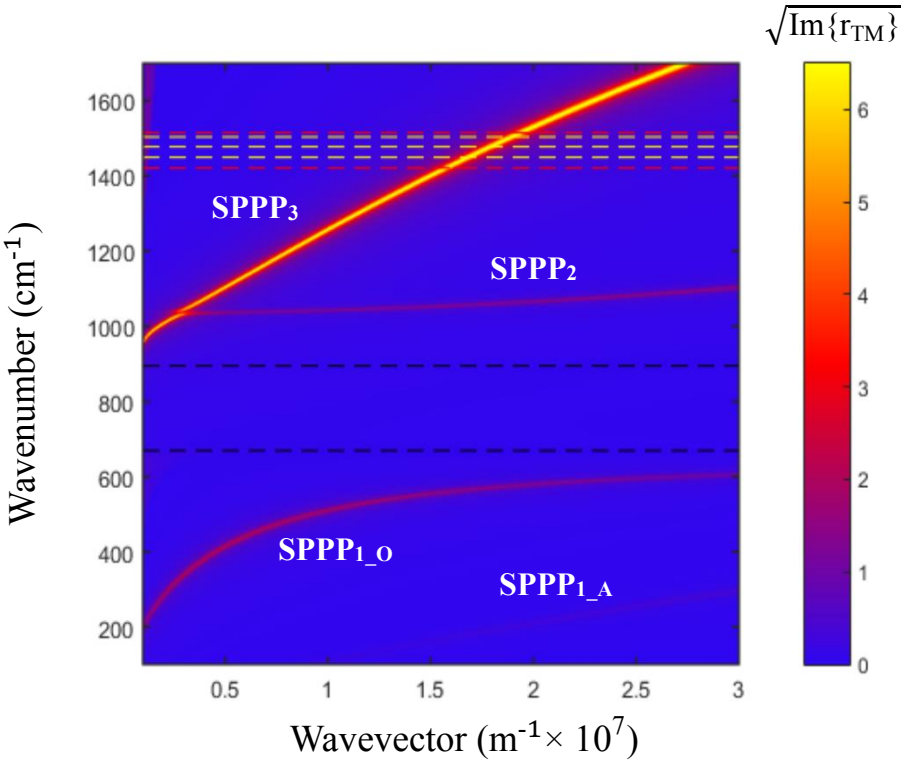

Fig.1. Dispersion of the surface plasmon-phonon polaritons ($SPPP_i$) in a graphene/graphene/AlN/graphene/AlN heterostructure. The $SPPP_1$ mode has two branches, optical (O) and acoustic (A). The black dashed lines indicate the reststrahlen band of AlN, whereas the red and yellow dashed lines correspond to the vibrational resonances of PI and CBP, respectively, shown in Figure 2.

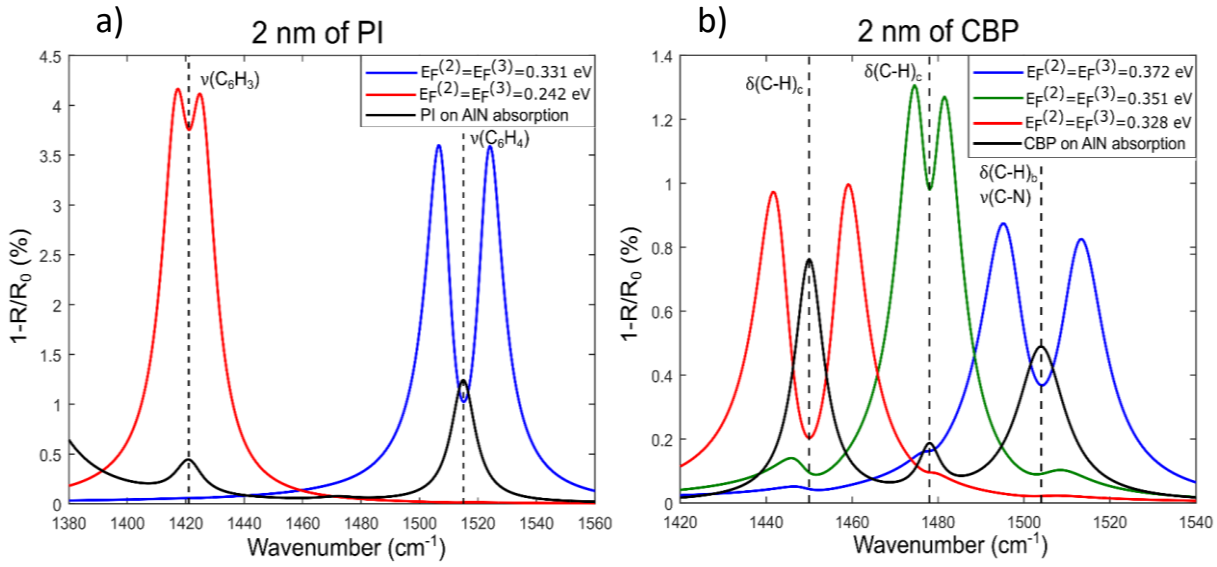

Fig.2. Extinction spectra of a graphene/graphene/AlN/graphene/AlN heterostructure covered by a 2 nm-thick layer of **(a)** PI and **(b)** CBP. The SAW wavelengths are 314 and 250 nm, respectively. The black curves show the absorption of the bare polymer (AlN is transparent in this range), while the coloured curves refer to the signal of the $SPPP_3$-polymer coupled system for different Fermi levels E_F of the top graphene sheets ($E_F^{(2)} = E_F^{(3)}$), whereas $E_F^{(1)} = 0.4$ eV for the bottom graphene sheet in all cases. The dashed vertical lines correspond to the frequencies of the vibrational resonances of the polymers, which coincide with the absorption peaks of the bare polymer and the Fano-type dips in the signal of the $SPPP_3$-polymer coupled system.

Improvement of III-V solar cells by using oxides doped with rare earths

Beatriz Galiana Blanco*[1], Rosa de la Cruz[1], Miguel Modesto Tardío[1], Clement Kanyinda-Malu[2], Stavros Athanasopoulos[1], Eduardo Salas[1], Elisa García-Tabarés Valdivieso[1], Gracia Belén Perea[1], Juan Enrique Muñoz Santiuste[1]

[1]Departamento de Física, Universidad Carlos III de Madrid, Avda. Universidad 30, 28911 Leganés (Madrid), Spain
[2]Departamento de Economía Financiera y Contabilidad II, Área de Matemáticas y Estadística, Universidad Rey Juan Carlos, Madrid, Spain

* bgaliana@fis.uc3m.es

Abstract

Nowadays, Si solar cells have reached a World record efficiency of 26.3 % which corresponds to a 91% of its theoretical limit [1], while GaAs monojunction solar cells has also saturated the efficiency improvement in the last decade [2]. On the other hand, multijunction solar cells have to deal with the current matching limitation, which implies that the subcell with the lowest photocurrent determines the current of the complete device. Consequently, although the research on the improvement of the device architecture is a hot topic, in this work we focus on the use of oxides doped with rare earths to tune the resultant spectrum that the solar cell is going to transform into photocurrent. Mainly, the proposal is based on the mechanisms of photon recycling that present this material system. They can be up-conversion (UC) that consists of the addition of two low infrared photons (IR) to emit a visible energy photon (Vis), or down-conversion (DC) when a photon of high energy (UV) is split into two lower energy (Vis). In both cases, the idea is to recycle the photons with energy lower than the bandgap of the solar cell that are not absorbed, and those of high energy that generates thermalization losses.

The initial oxide under study is La_3NbO_7 doped with Er layer whose preliminary optical luminescence measurements are gathered in Figure 1 and 2 for two different excitation wavelengths, 488 nm and 980 nm that correspond to down-conversion and up-conversion mechanisms, respectively, for different Er concentrations.

With that data, we propose, on a first stage, to study the improvement of conventional GaAs and $GaInP_2$ monojunction solar cells. Their spectral response, SR; are gathered in Figure 1. The GaInP data belongs to the double junction (GaInP/GaAs) solar cell word record [3]. In a second stage, the calculus will be extended to other III-V materials to determine the optimum relation between bandgap energy of the solar cell and photon emission energy of the oxides doped with rare earths. In a third stage, the modelling of multijunction solar cells will be carried out.

For the initial theoretical approximation, the generated photocurrent of the device, *I*, is calculated by integrating the spectral response of the device, SR(λ), with a "modified" solar spectrum by Eq.1, where A is the area of the device and E(λ) is the incident spectrum.

$$I = A \int_{\lambda_{min}}^{\lambda_{max}} E(\lambda)\, SR(\lambda)\, d\lambda$$

The spectrum E(λ) is tricked by increasing the spectral irradiance at which the oxides doped with rare earths reissue the photons converted

from the exited wavelengths according to the optical data of Figures 2 and 3. The efficiency improvement is determined assuming that the open circuit voltage as well as the fill factor are not modified.

Three cases are going to be analyzed: i) the oxide is introduced at the top of the device by using nanoparticles (DC process), ii) The oxide is deposited as at the bottom of the device (UC process) and iii) both, bottom and top. Additionally the calculus will be carried out for AM1.5G and AM0 solar spectra.

Preliminary calculations performed show promising results in the improvement of the efficiency of solar cells. More detail calculations are ongoing taking into account the quantitative luminescence emission level.

Other oxides doped with rare earths are also on-going.

References

[1] https://isfh.de/en/26-1-record-efficiency-for-p-type-crystalline-si-solar-cells/

[2] https://www.energy.gov/eere/solar/downloads/research-cell-efficiency-records

[3] I.GarcíaI. Rey-Stolle,, B.Galiana, C.Algora, Applied Physic Letters, 94 (2009) 053509

Acknowledgments

The authors acknowledge financial support of the Spanish Ministry of Science, Innovation and Universities (MICINN) through the Spanish project RTI2018-101020-B-100.

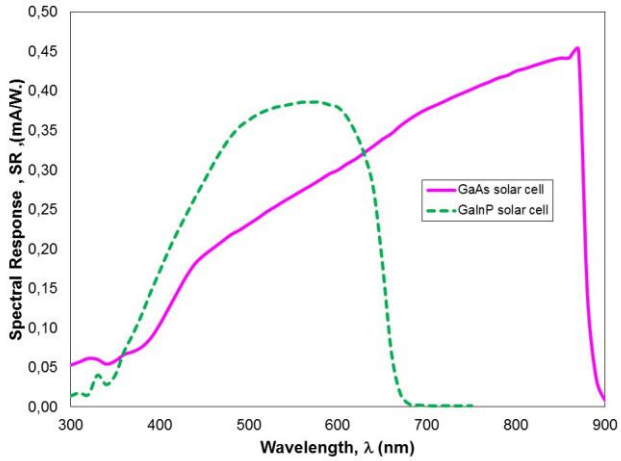

Fig.1. Spectral response of a GaAs and GaInP solar cell [3]

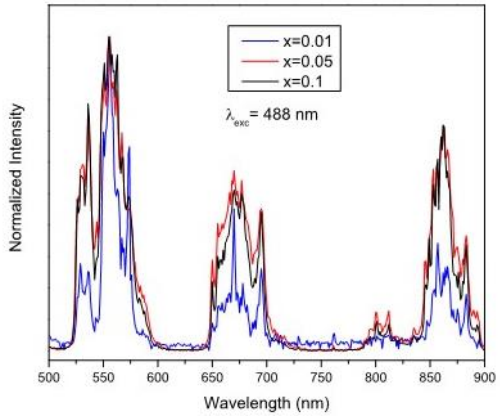

Fig.2. Luminescence spectra of La_3NbO_7 doped with Er (x=1% x=5% x=10%) between 500 and 900 nm for excitation at 488nm

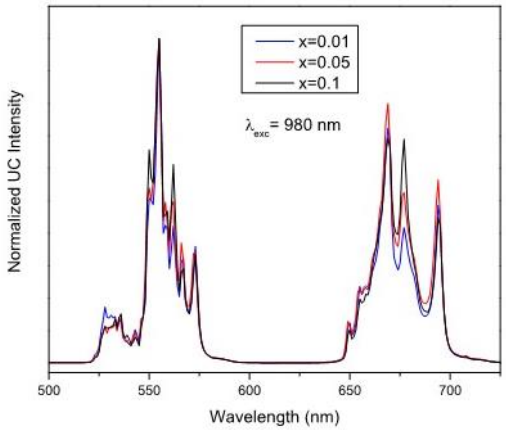

Fig.3. Luminescence spectra of La_3NbO_7 doped with Er (x=1% x=5% x=10%) between 500 and 750 nm for excitation at 980 nm

Advanced Giant Magnetoresistance (GMR) sensors for Selective-Change Driven (SCD) circuits

C. Reig[1], F. Pardo[2], J.A. Boluda[2], F. Vegara[2], M.D. Cubells[1], J. Sanchis[1], S. Abrunhosa[3], S. Cardoso[3]

[1]Department of Electronic Engineering, Universitat de València (Burjassot, Spain)
[2]Department of Computer Science, Universitat de València (Burjassot, Spain)
[3]INESC-NM (Lisbon, Portugal)

Abstract

Nowadays, bio-inspiration is driving novel sensors designs, beyond vision sensors. By taking advantage of their compatibility with standard CMOS technologies, the integration of giant magneto-resistance (GMR) based magnetic sensors within such event-driven approaches is proposed. With this aim, several topologies of such GMR sensors are designed, fabricated and characterized.

1. Introduction

Sensor arrays are key devices when getting an image, understood as a bi-dimensional distribution of a magnitude, is required. Conventional readout interfaces systematically scan every sensing element (pixel), by following a frame-based scheme. Being flexible and powerful, this approach usually demands many computing resources, which is unacceptable in applications where high speed is required. In many instances, this frame-based scheme can be reformulated into an event-driven paradigm, by considering bio-inspired approaches [1]. Vision sensors, for example, followed this path, leading to neuromorphic (or retinomorphic) vision sensors, which try to mimic the full human visual process, based on events. Implementation of event-driven vision sensors on standard CMOS technologies was demonstrated some time ago [2]. Since then, the concept has evolved, resulting in different interpretations of the bio-inspiration approach [3] and its application to fields beyond vision sensors [4]. A representative realization of event-driven vision sensors is the selective-change driven (SCD) approach [5]. An SCD sensor delivers, under requirement, the illumination level and the address of the pixel with the highest change since the last reading. Recently, preliminary simulation results have demonstrated the potential use of the SCD approach to resistive sensors, by exchanging the conventional photodiode in each pixel by a resistive sensing element, and properly re-arranging the associated analog acquisition/conditioning circuits [6]. Taking advantage of the compatibility of giant magneto-resistance (GMR) based magnetic sensors with standard CMOS technologies, elemental GMR sensors were considered to be included in such SCD schemes [7]. In this work, the use of advanced (single resistors, voltage dividers and bridges) GMR sensors is proposed.

2. Sensor design

Spin-valve structures (patterned in 3×200 µm^2, ~ 1 kΩ nominal resistance) have been considered for the GMR sensors design. The microfabrication process was carried out at the clean-room facilities of the INES-MN, as described in [7]. Two more lithographic steps are required in order provide the proper performance of the sensors (voltage dividers and full bridges), as well as including integrated current strips for characterization purposes. Three topologies have been assayed, as depicted in Fig. 2: single elements, resistance dividers and Wheatstone bridges. The CMOS design is out of the scope of this article.

3. Preliminary results

Sensors as described above have been fabricated and encapsulated, as shown in Fig. 3. Preliminary results regarding the resistance response as a function of the applied magnetic field and driven current are plotted in Fig. 4, for the single resistor configuration. Nominal resistance were about (1.1±0.1) kΩ.

Acknowledgments

This work was supported by projects TEC2015-66947-R (Spanish Ministry of Economy and Competitiveness) and PID2019-105556GB-C32 (Spanish Ministry of Science and Innovation).

References

[1] A. Osseiran, A. Rassau. Neuromorphic engineering - A paradigm shift for future IM technologies. *IEEE Instrum. Meas. Mag.* 22 (**2019**) 4–9.
[2] M. Mahowald. VLSI analogs of neuronal visual processing: a synthesis of form and function. *PhD Dissertation* (1992)
[3] C. Posch *et al.* Retinomorphic event-based vision sensors: bioinspired cameras with spiking output. *Proceedings of the IEEE* 102 (**2014**) 1470-1484
[4] J. Lazzaro *et al*. Silicon auditory processors as computer peripherals. *IEEE Trans. Neural Networks* 4 (**1993**) 523-528.
[5] J.A. Boluda et al. Selective Change Driven Imaging: A Biomimetic Visual Sensing Strategy. Sensors 11 (2011) 11000-11020.
[6] C. Reig *et al*. Address Event Representation (AER) approach to resistive sensor arrays. *MIC-Sensors Conf.*, Valencia (Spain, **2020**)
[7] J. Gómez *et al*. Elemental Giant Magnetoresistance (GMR) Sensors for neuromorphical applications. *SensorDevices Conference*, Valencia (Spain, **2020**)

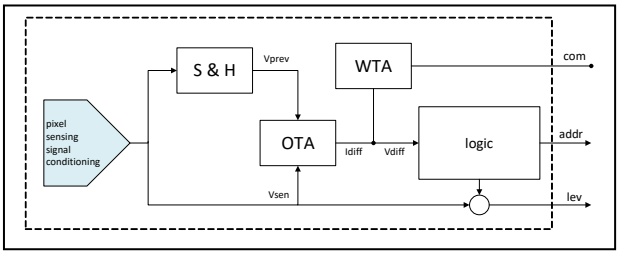

Fig. 1. General scheme of a SCD cell (S&H: sample&hold; OTA: Operational Trans-Amplifier; WTA: Winner-Take-All circuit; logic: digital/addressing circuit)

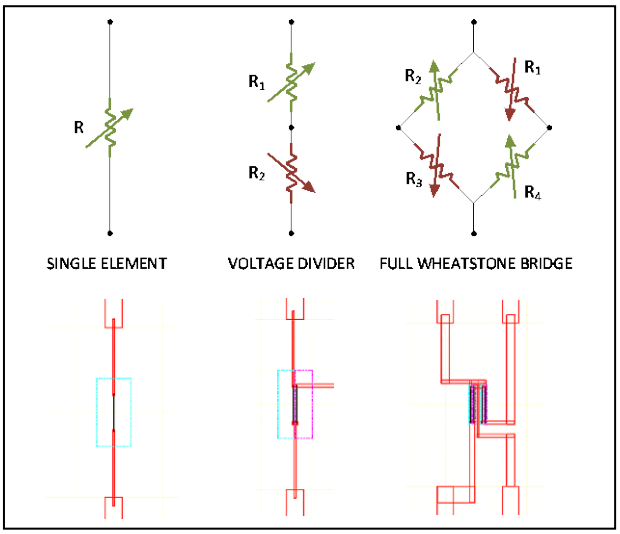

Fig. 2. Sensor topologies with the associated photolithographic masks

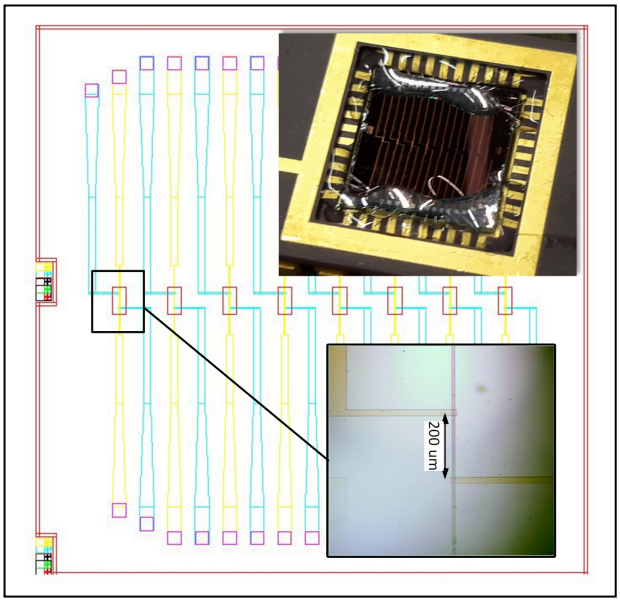

Fig. 3. Produced sensors

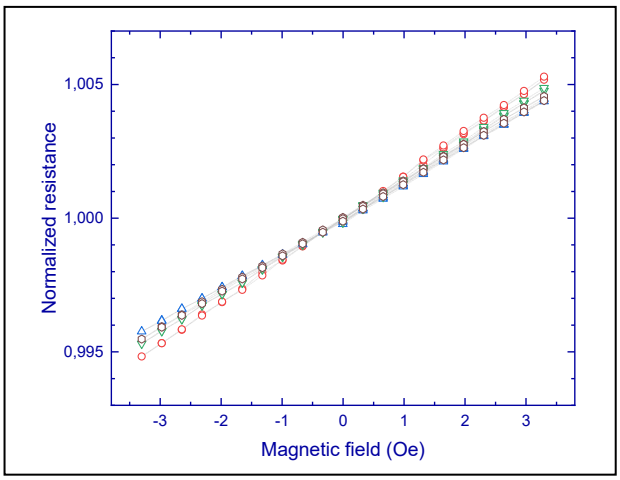

Fig. 4. Results

POSTER SESSION III

Device modelling, simulation and beyond

Thursday 10

12:00-13:15

Chairperson: S. Dueñas (Universidad de Valladolid)

Self-heating effect in nanoscale SOI Junctionless FinFET with different geometries

A.E.Atamuratov[1], B.O. Jabbarova[1], M.M. Khalilloev[1], A. Yusupov[2], A.G.J. Loureiro[3]

[1]Urgench State University (Uzbekistan), [2]Tashkent University of Information Technologies (Uzbekistan), [3]University of Santiago de Compostela (Spain).
atabek.atamuratov@urdu.uz, antonio.garcia.loureiro@usc.es

1. Abstract

In this work we study the self-heating effect (SHE) in nanoscale Silicon on Insulator Junctionless (SOI JL) FinFET transistor with fin cross section in rectangular, trapeze and triangle form. The lattice temperature dependence on the channel length as well as on buried oxide thickness is considered. It is shown that for considered transistor structure the lattice temperature in the middle of the channel is lower than at lateral sides, near source and drain. Also, we have found at the same conditions the lattice temperature depends on shape of channel cross section too.

2. Introduction

For decreasing the short channel effects SOI technology and multigate FinFET structure were proposed. However, the low heat conductivity of buried oxide induces SHE in the channel and decreasing the drain current. In this work SHE in SOI JL FinFET with different geometries is analyzed.

2. Simulation procedure, results and discussion

We have studied a SOI JL FinFET with a 0.9 nm of equivalent thickness of HfO_2 gate oxide, and the width of SiO_2 buried oxide (BOX) is W_{box} =69.4 nm. The thickness of the BOX varies between 10 and 150 nm and the length of TiN gate between 10 and 40 nm. Another main values are: the thickness of the Si channel T_{Si} =9 nm, width in the base W_{finb} = 22 nm and width in the channel top W_{fint} depend on the channel shape, which for considered trapeze cross section is 10 nm, and is zero for triangle cross section (Fig.1).

The device simulations were carried out using Advanced Sentaurus TCAD. For device simulation, along with default carrier transport model, mobility degradation models such as doping dependence to account impurity scattering effect, high field saturation to account velocity saturation effect and transverse field to account degradation at interfaces were considered. To account self-heating, a thermodynamic model for carrier transport, SRH (temperature dependent), models were included. Density gradient quantization model and mobility degradation due to high-k materials were also taken into consideration. Fig. 2 shows the very good fitting of transfer characteristics of designed SOI JL FinFET with that presented in Ref. [1].

Simulation results shows, SHE in the nanoscale SOI JL FinFET induces substantial decreasing of the drain current. On the lattice temperature distribution along the device length it is seen that at the middle of the length (in the channel) the temperature is lower than in lateral parts, near source and drain (fig 3). It is connected with different materials which surround middle (gate oxide) and lateral parts (air). Besides it, in the middle part along device length, in bottom and top of the fin the temperature is lower than in the middle of fin in vertical direction. It can be explained by more fast heat transfer at bottom and top silicon-oxide border. However, temperature dependence on position which is seen in the vertical direction at lateral parts is connected with more heat transfer through back oxide (bottom part of fin) than through air (top part of fin). Small decreasing of temperature at device edges is connected with heat transfer through contacts.

Fig. 4 shows that lattice temperature is increased linearly with increasing the gate length. It is due to contribution of field normal component connected with gate voltage to electron kinetic energy. At increasing the gate length the number of electrons in the channel covered by normal field is increased.

Lattice temperature dependence on the buried oxide thickness is shown in the Fig. 5. The lattice temperature is linearly increased with an increase in buried oxide thickness. It is agreed with model suggested in ref [2].

References

[1] S.Barraud, M.Berthomé, R.Coquand, M.Cassé, T. Ernst, M.-P.Samson, P. Perreau, K. K. Bourdelle, O.Faynot, and T. Poiroux, IEEE Electron Device Letters. **33**, 9, 1225-1227, (2012).

[2] L.J. McDaid, S. Hall, P.H. Mellor, W. Eccleston, J.C. Alderman, Physical origin of negative differential resistance in SOI transistors, Electron. Lett. 25 (13) (1989), 827–828

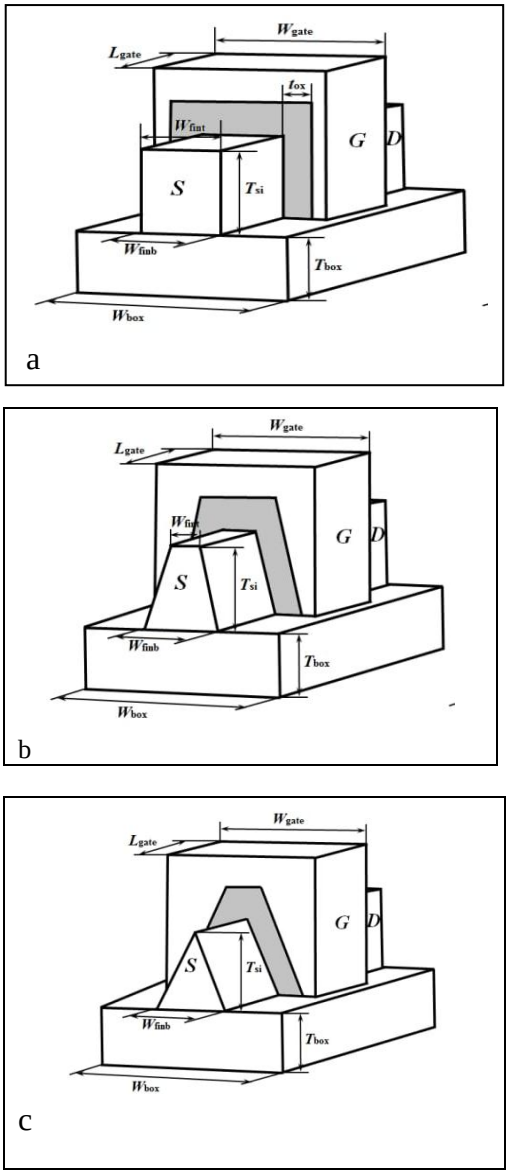

Fig.1. Simulated SOI JL FinFET with different channel cross section shape: a-rectangular, b-trapeze, c-triangle.

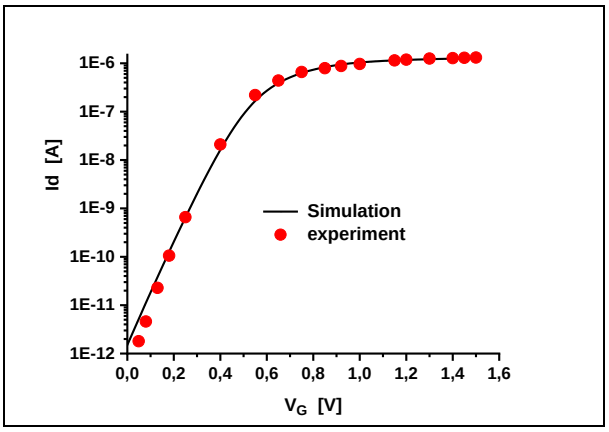

Fig.2. I_d-V_g dependence for simulated and experimental device

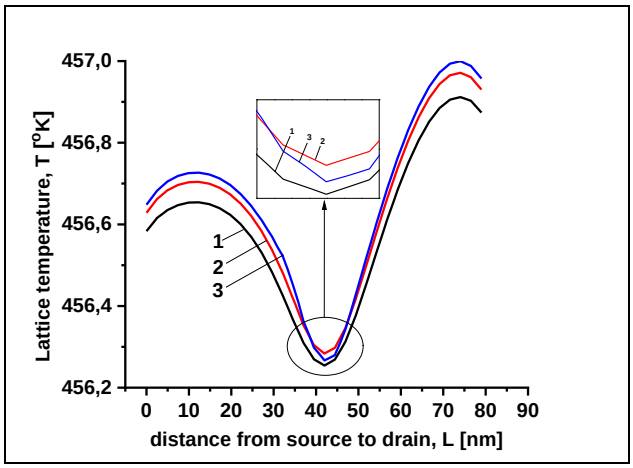

Fig.3. Lattice temperature distribution along device with rectangular cross section at bottom (1), middle (2) and top (3) of the fin

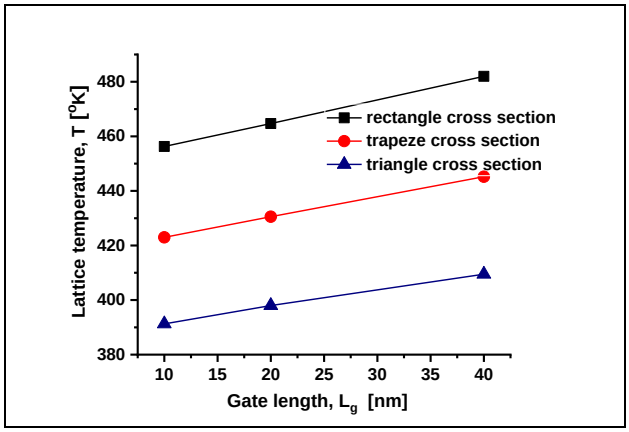

Fig.4. Lattice temperature dependence on the gate length for transistor with different cross section. T_{box}=145 nm

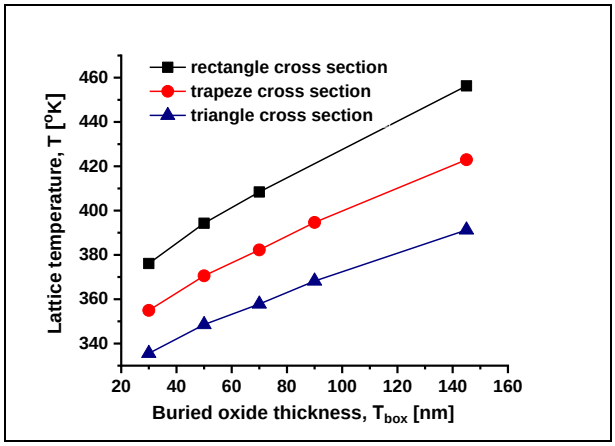

Fig.5. Lattice temperature dependence on the buried oxide thickness. L_g=10 nm

Multilevel memristor based matrix-vector multiplication: influence of the discretization method

Antonio J. Pérez-Ávila[1], Eduardo Pérez[2], Juan B. Roldán[1], Christian Wenger[2], Francisco Jiménez-Molinos[1]

[1] Dept. de Electrónica y Tecnología de Computadores, Universidad de Granada, Spain
[2] IHP-Leibniz-Institut für innovative Mikroelektronik, Frankfurt (Oder), Germany
[4] BTU Cottbus-Senftenberg, Cottbus, Germany

1. Abstract

A study about the use of memristors with discrete multilevel capability for the implementation of matrix-vector multiplication is presented. We focus our analysis on the role of the discretization method employed to translate the matrix coefficients into the memristor device conduction levels.

2. Model and weight representation

Memristors based on resistive switching are currently subjected to intense attention as promising candidates to implement analogue artificial synapses in hardware neural networks (NNs) [1]. By means of memristor crossbar arrays, the matrix-vector multiplication (MVM) operation (the core function in NN inference tasks) can be easily carried out as sketched in Figure 1.

While the exact mathematical *j* output is given by:

$$v_{out,j} = \sum_{i}^{inputs} w_{i,j} \cdot v_{in,i},$$

(where $w_{i,j}$ and $v_{in,i}$ are the matrix and input vector coefficients, respectively), the circuit implementation output is:

$$v_{out,j} = R_{norm} \sum_{i}^{inputs} \left(I_{i,j}^{+} - I_{i,j}^{-}\right)$$

Note that in order to get positive and negative weights, two memristor branches (*positive* and *negative*) are connected to each input. In the above equation, $I_{i,j}^{+}$ and $I_{i,j}^{-}$ indicate the currents through the positive and negative memristor, respectively. A discretization of the original coefficients ($w_{i,j}$) must be performed because the discrete and small set of different available memristor conduction states. We have used Al-doped HfO_2 memristors fabricated at IHP (Germany). After programming, four different states can be reached for each memristor (HRS, LRS1, LRS2, LRS3). The conductance in each state is subjected to variability and is modeled according to ref. [2]. The summer circuit includes a normalization resistor (R_{norm}) which allows the memristor pair implement a discrete weight:

$$w_{i,j,disc} = R_{norm} \cdot g_{i,j}$$

where $g_{i,j}$ accounts for the join conductance of both memristors with no dependence on the input voltage in this data scenario (the I-V memristor dependence is linear in the operation voltage range). Seven different states or conductance values of $g_{i,j}$ can be obtained (S0...S6, see Table 1). The problem of weight discretization and its corresponding implementation (selection of the state pairs to represent the weights) is faced following three different approaches: uniform (Figure 2a), uniform CDF (Figure 2b and ref. [2]) and non-uniform (Figure 2c). R_{norm} is selected as the value that minimizes the Mean Square Error (MSE), given by:

$$\epsilon(R_{norm}) = \frac{1}{N}\sum_{i,j}^{N} \left| w_{i,j} - R_{norm} \cdot g_{i,j} \right|^2$$

In contrast with the first two methods, the non-uniform one requires a value of R_{norm} to establish the discretization ranges of the weights (S0,…,S6) because they are linked to the actual pair conductances (Fig. 2c).

3. Results and discussion

These methods are tested under several weight distributions; in particular, uniform [-0.5, 0.5] and normal N(0,1). Table 2 compares the results of each method for each weight distribution, as well as the square root of the MSE. Figure 3 shows the best R_{norm} for every case (in terms of MSE minimization).

Several combinations of memristors states have been also tested (see Figure 4 and Table 1). All the possible combinations are shown in Figure 4. The result of trying these combinations using a non-uniform method (in terms of mean error per weight) is shown in Figure 5. The best combinations are Comb4 and Comb6 for uniform and Gaussian distributed weights, respectively.

Furthermore, the model proposed in [2] allows us to test the memristor conductance variability.

4. Conclusions

An analysis of different discretization methods for the implementation of matrix coefficients has been performed by means of multilevel memristors. They have been tested under different weight distributions and conductance level combinations.

Acknowledgment

The authors thank the financial support by the German Research Foundation (DFG) in the frame of research group FOR2093 and by the government of Andalusia (Spain) and the FEDER program through project A.TIC.117.UGR18.

References

[1] D. Ielmini, P. Wong, Nature electronics, vol. 1, p. 333, 2018.

[2] Antonio J. Pérez-Ávila et al, in XXXV Conference on Design of Circuits and Integrated Systems (DCIS), 2020.

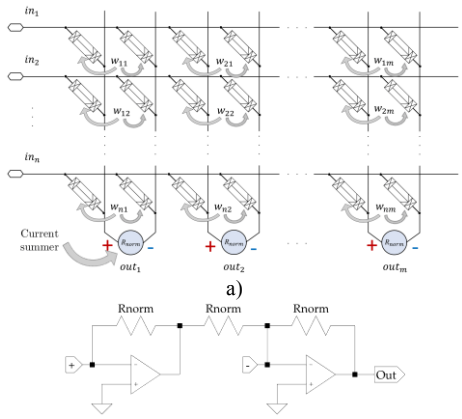

a)

b)

Fig.1. In matrix-vector multiplication, every input (in_i) is weighted by w_{ij} and that is its contribution to output (out_j). In the circuit implementation, every weight is represented by two memristors, one adding current and another subtracting it (a). The currents from every memristor are added up in the summer (b), via the I-V normalization resistance (R_{norm}).

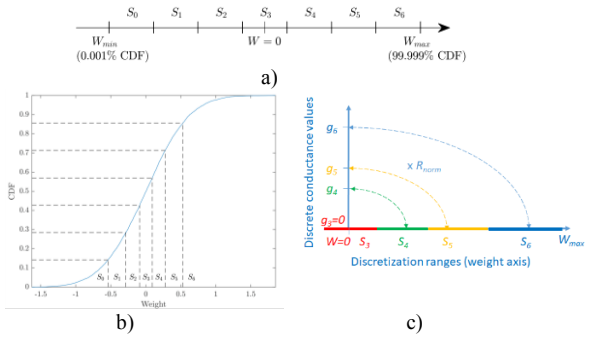

a)

b) c)

Fig.2. a) Uniform discretization method. The weights are grouped in seven uniform intervals, each of them represented by a discrete value of $g_{i,j}$. b) CDF uniform discretization method example (bottom) for a normal distribution N(0,1). Weights are grouped in seven states given by setting uniform intervals in terms of the CDF *y-axis*. This latter method assures that the most common weights values are better discretized. c) The discretization ranges are defined in terms of the available pair conductances by means of the normalization resistor (non-uniform discretization).

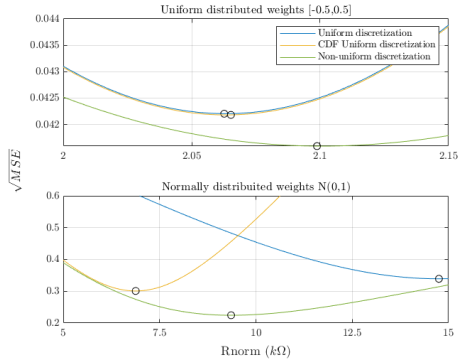

Fig.3. Mean error per weight vs R_{norm} for each discretization method. The point of minimum error is selected as the optimized value of R_{norm}.

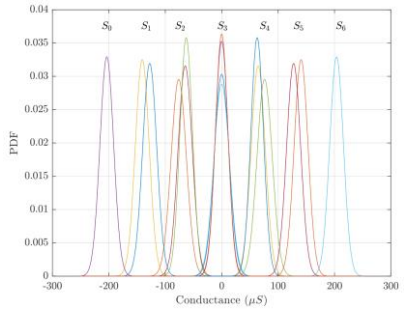

Fig.4. Resulting states of different two memristor combinations, one adding and another subtracting current from the current adder (the line color corresponds to the state implementation detailed in Table 1). Variability of each memristor conductive level is taken into account in order to determine the join conductance (the corresponding probability distribution function is shown).

		S0	S1	S2	S3	S4	S5	S6
Comb1	M+	0	0	0	3	1	2	3
	M-	3	2	1	3	0	0	0
Comb2	M+	0	1	0	3	1	3	3
	M-	3	3	1	3	0	1	0
Comb3	M+	0	0	1	3	2	2	3
	M-	3	2	2	3	1	0	0
Comb4	M+	0	1	1	3	2	3	3
	M-	3	3	2	3	1	1	0
Comb5	M+	0	0	2	3	3	2	3
	M-	3	2	3	3	2	0	0
Comb6	M+	0	1	2	3	3	3	3
	M-	3	3	3	3	2	1	0

Table 1. These are the tested combinations, which is understood as the set of states of the positive and negative memristor for every conduction state of the memristors pair. S3 is taken as (3,3) because the mean is the same than those of others combinations (0) and it shows the lowest deviation.

Method\W distri.	Uniform [-0.5,0.5]	N(0,1)
Uniform	0.04227	0.38885
CDF uniform	0.04224	0.29863
Non-uniform	0.04163	0.22323

Table 2. The square root of the MSE is shown for each method and for uniformly (between -0.5 and 0.5) and normally distributed weights (null mean and unitary deviation). Comb 1, from Table 1, has been used.

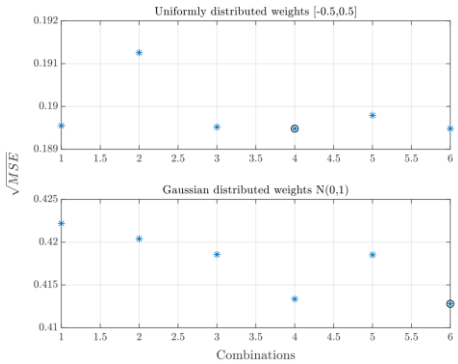

Fig.5. Square root of MSE for the non-uniform discretization method when the weights are distributed uniformly (-0.5, 0.5) and normally N(0,1), as a function of the state combinations shown in Table 1. Minimum error combinations are circled.

Modeling of ion-sensitive FETs based on 2D-TMDs

Francisco Pasadas[1,*], Tarek El Grour[2], Alberto Medina-Rull[3], Montassar Najari[4], Enrique G. Marin[3], Alejandro Toral-Lopez[3], M. Carmen Pardo[3], Francisco G. Ruiz[3], Andrés Godoy[3], Lassaad El-Mir[2] and David Jiménez[1]

[1]Departament d'Enginyeria Electrònica, Escola d'Enginyeria, Universitat Autònoma de Barcelona, Bellaterra (Barcelona), Spain.
[2]LAPHYMNE Laboratory, Gabes University, Gabes, Tunisia.
[3]PEARL Laboratory, Dpto. Electrónica y Tecnología de Computadores, Fac. Ciencias, Universidad de Granada, Granada, Spain.
[4]The Innovation and Entrepreneurship Centre, Jazan University, Jazan, Saudi Arabia.
[*] Email: francisco.pasadas@uab.es

1. Abstract

Field-effect transistors (FETs) based on transition metal dichalcogenides (TMDs) are receiving significant attention due to their ability to perform label-free electrical detection of biological species such as proteins, DNA, and other biomolecules. Their use as ion-sensitive FETs (ISFETs) has also been widely demonstrated, showing excellent detection capabilities and, in the particular case of pH, a high-stability sensing with near-ideal pH voltage sensitivity, close to the Nernst limit (around 59.2 mV/ pH at room temperature). In this work, we have combined a verified compact model of 2D-semiconductor FETs developed by some of the authors [1] with the modeling of the solid-liquid interface through the Site-Binding model and the Gouy-Chapman-Stern approach in order to achieve a comprehensive description of 2D-ISFETs.

2. Electrostatics and transport model

Figure 1a shows the cross-section of a 2D-ISFET whose structure consists of a FET where the top-gate metal is substituted by an electrolyte solution with a reference electrode immersed in it. In addition to the induced charge in the electrolyte, the electrostatic modulation of the carrier concentration in the 2D sheet is achieved via the reference electrode (V_{gs}) and a bottom gate contact (V_{bs}) coupled through a bottom dielectric. The top oxide acts as a barrier, guaranteeing an unambiguous field-effect transduction mechanism through the electrostatic control of the channel and passivating the source and drain electrodes so that ions cannot be adsorbed by these metals. The one-dimensional electrostatics along a vertical cut of the 2D-ISFET can be described using the equivalent capacitive circuit, shown in Fig. 1b. The ISFET operation is founded on the interaction between the surface charge density (N_s), generated at the top oxide-electrolyte interface due to the chemical reactions associated to the presence of ions, and the free charge carriers inside the semiconductor. This interaction is governed by the Site-Binding model [2]. In addition, the Gouy-Chapman approach is considered in terms of the formation of a double layer capacitance, C_{DL}, while a depleted region right at the solid-liquid interface is modeled through the Stern capacitance, C_{Stern} [3]. Considering the above elements, the pH variations in the bulk electrolyte are related to Ψ_0 that depends on N_s, pH, C_{DL} and C_{Stern}.

In the diffusive transport regime associated to channel lengths longer than the mean free path, an explicit expression for accurately computing the drain current of a TMD-FET is used leveraging the model reported by some of the authors in [1], [4].

3. Results

The model outcome is compared against experimental measurements of a MoS_2-FET-based pH sensor fabricated on 270 nm SiO_2/Si substrate and 30 nm of HfO_2 as gate dielectric [5]. Table 1 collects the input model parameters and Fig. 2a shows the transfer characteristics at three different pH values (pH = 3, 4, 5). Figure 2b shows the change in current and the threshold voltage (V_t) with pH. The shift of V_t due to pH found is 59 mV/pH, a value close to the Nernst limit. Finally, Table 2 collects the current sensitivity, $S_{pH\text{-}I}$, at the different transistor operation regions.

Acknowledgements

This work is supported in part by the Spanish Government under the projects TEC2015-67462-C2-1-R, TEC2017-89955-P, RTI2018-097876-B-C21; grants IJCI-2017-32297, FPU16/04043; by EC H2020 WASP 825213 and GrapheneCore3 881603; and by the European Regional Development Funds (ERDF) allocated to the Programa Operatiu FEDER de Catalunya 2014-2020, with the support of the Secretaria d'Universitats i Recerca of the Departament d'Empresa i Coneixement of the Generalitat de Catalunya for emerging technology clusters to carry out valorization and transfer of research results. Reference of the GraphCAT project: 001-P-001702.

References

[1] F. Pasadas et al. DOI: 10.1038/s41699-019-0130-6.
[2] D. E. Yates et al. DOI: 10.1039/F19747001807.
[3] Ajay et al. DOI: 10.1109/TED.2017.2668520.
[4] E. G. Marin et al. DOI: 10.1109/TED.2018.2797172.
[5] D. Sarkar, et al. DOI: 10.1021/nn5009148.

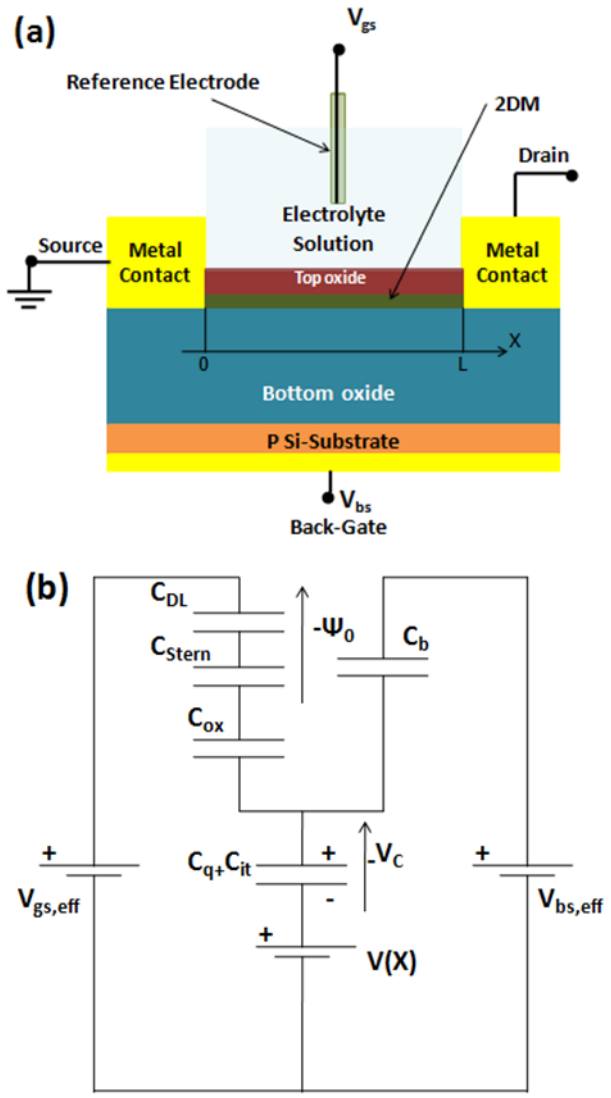

Fig. 1. a) Cross-section of a 2D-ISFET. b) Equivalent capacitive circuit.

L (μm)	5	t_{ox} (nm)	30
W (μm)	20	ε_{ox}	25
V_{gs0} (V)	0.58	t_b (nm)	270
V_{bs0} (V)	0	ε_b	3.9
C_{stern} (μF/cm^2)	20	μ_0 (cm^2/Vs)	200
		N_s (cm^{-2})	$4 \cdot 10^{14}$

Table 1. 2D-ISFET model parameters. A thorough explanation about the meaning of the input parameters can be found in [1].

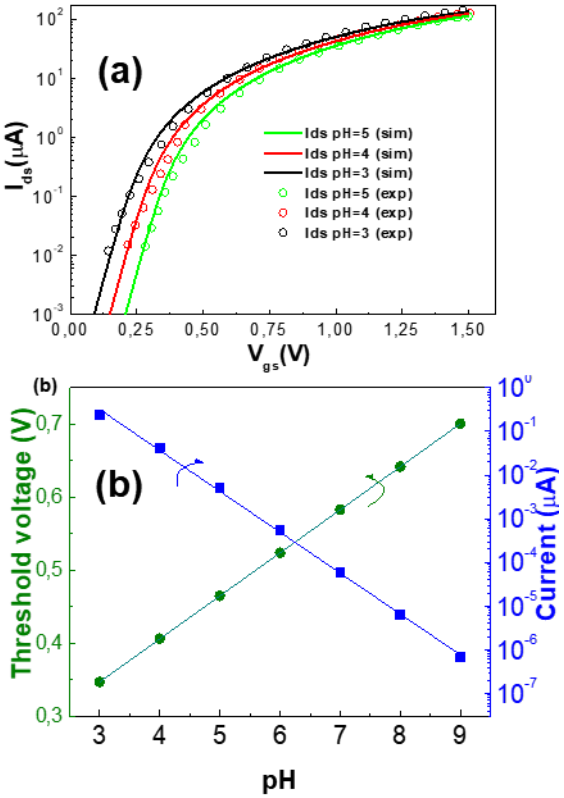

Fig. 2. a) Transfer characteristics at different pH values (3, 4 and 5) in logarithmic scale (V_{ds} = 1V). Symbols represent the measurements from [5] and solid lines are the theoretical predictions. b) Threshold voltage and drain current variation with pH (voltage sensitivity of 59 mV/pH).

ISFET operation region	V_{gs} (V)	$S_{pH\text{-}I}$ model	[5] $S_{pH\text{-}I}$ measured
Subthreshold	0.25	730	713
Saturation	0.62	47	53
Linear	1.25	14	13

Table 2. Current sensitivity for a change of pH from 4 to 5 at the different transistor operation regions.

Modelling and potential of hybrid micro-scaling MJ solar cell and thermoelectric generator

Álvaro Valera, Pedro M. Rodrigo, Florencia Almonacid and Eduardo F. Fernández

Center for Advanced Studies in Earth Science, Energy and Environment (CEACTEMA), Photovoltaic Technology Research Group (PVTech-UJA), Las Lagunillas Campus, University of Jaén (UJA), Jaén 23071, Spain.

1. Abstract

The efficiency of photovoltaic (PV) systems can be improved by the hybridization with thermoelectric generators, which allows part of the waste heat generated in the solar cells to be transformed to electricity. Concentrator photovoltaic (CPV) systems are more suitable than non-concentrating PV systems for this hybridization because of the small temperature coefficients of multi-junction (MJ) solar cells and the high temperature gradient achievable from solar cell to heat-sink [1]. Furthermore, there is theoretical evidence that increasing the concentration factor favors the hybridization [2]. The use of micro-scaling system reduces the thermal requirements being reliable the use of passive cooling at ultra-high concentration level (>2,000x) [3]. Most of the previously published studies are based on one-dimensional heat transfer analysis working under medium (10-100) and high (100-2,000) concentration levels. Currently, there are very few studies on the three-dimensional (3D) investigation by Finite Element Method (FEM) to design and optimize hybrid concentrator photovoltaic-thermoelectric generator (CPV-TEG) systems [4]. This paper presents a detailed 3D numerical model by FEM, validated on previous work [4], to investigate the potential of novel hybrid CPV-TEG receiver at UH levels of concentration up to 4,000x.

The structure of the receiver is presented in Figure 1, while the model parameters are shown in Table 1. The semiconductor physical properties have been defined by polynomial functions from real data of a commercial TEG module GM200-49-45-25. A detailed description of the CPV and CPV-TEG receiver dimensions and TE physical properties are presented in previous works [4], [5]. A heat transfer model for solids combined with electric current model was selected for modelling Peltier-Seebeck-Thomson effects (Figure 2 and 3). The solar cell efficiency is modelled assuming the impact of temperature rise by incorporating the temperature coefficient of real solar cells. TEG electrical performance is obtained from numeric solution of the modelling (V_{TEG}, I_{TEG}, Q_{hot}). Heat-sink of the system has been modelled by the absolute thermal resistance of passive cooling systems. The overall efficiency of the hybrid system is calculated by:

$$\eta_{CPV\_TEG} = \eta_{opt}\left[\eta_{cell} + \eta_{TEG}\left(1 + \eta_{cell}\right)\right]$$

Where η_{opt} is the optical efficiency of the concentrator, η_{cell} is the solar cell efficiency and, η_{TEG} is the TEG efficiency. A comparison of the hybrid CPV-TEG system performance to the same CPV system operating alone has been carried out. Figure 4 shows that micro CPV-TEG systems can reach an efficiency of 33.6 % versus the 31.6 % achievable with a CPV-alone system, working under 4,000 suns. This means a relative efficiency improvement (REI_{TMM}) of 6.2% (Figure 5). In Figure 6, it can be seen the solar cell operates at a temperature of 150 ºC in the CPV-TEG system at 4,000 suns, while the maximum cell temperature in the CPV-alone system is 51.75 ºC. CPV-TEG hybridization at micro-scales for enhancing the efficiency is suitable especially under ultra-high concentration levels because the TEG module can provide more power than the solar cell power loss caused by its temperature increase. However, the development of low temperature coefficient MJ solar cells, TE material with high ZT figure-of-merit and, optical systems able to reach ultra-high level of geometric concentration is required.

References

[1] Rodrigo PM, Valera A, Fernández EF, Almonacid FM. Performance and economic limits of passively cooled hybrid thermoelectric generator-concentrator photovoltaic modules. Appl Energy 2019;238:1150–62. https://doi.org/10.1016/J.APENERGY.2019.01.132.

[2] Rezania A, Rosendahl LA. Feasibility and parametric evaluation of hybrid concentrated photovoltaic-thermoelectric system. Appl Energy 2017;187:380–9. https://doi.org/10.1016/j.apenergy.2016.11.064.

[3] Valera A, Fernández EF, Rodrigo PM, Almonacid F. Feasibility of flat-plate heat-sinks using microscale solar cells up to 10,000 suns concentrations. Sol Energy 2019;181. https://doi.org/10.1016/j.solener.2019.02.013.

[4] Álvaro Valera, Pedro M. Rodrigo, Florencia Almonacid, Eduardo F. Fernández. Efficiency improvement of passively cooled micro-scale hybrid CPV-TEG systems at ultra-high concentration levels. Energy Conversion and Management. (UNDER REVIEW).

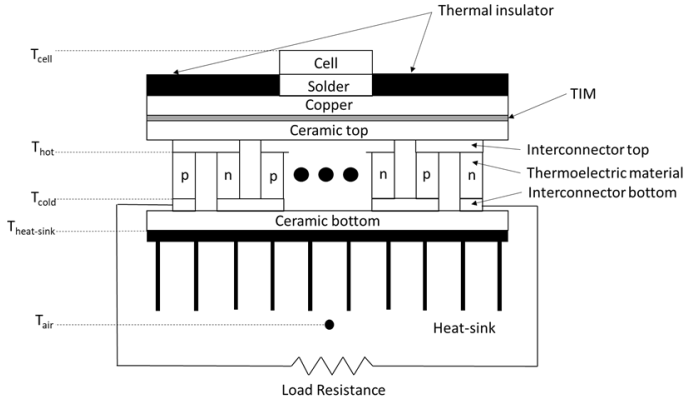

Fig.1. Structure of passively cooled CPV-TEG receiver [2].

Table 1. Parameters for the modelling.

Parameter	*CPV-TEG*	*CPV-only*	*Unit*
DNI	900	900	W/m2
Ambient temperature	20	20	ºC
Optical efficiency	80	80	%
Cell Ref efficiency	40	40	%
Cell area	0.5 x 0.5	0.5 x 0.5	mm×mm
TEG area	1.8 x 1.8	-	mm×mm
N legs	16	-	-
Fill Factor	0.5	-	-
Leg height	1	-	mm
Figure of merit	~2.4	-	-
Temperature Coefficient	-0.05	-0.05	%/K
Cooling Th Resistance	5	5	K/W

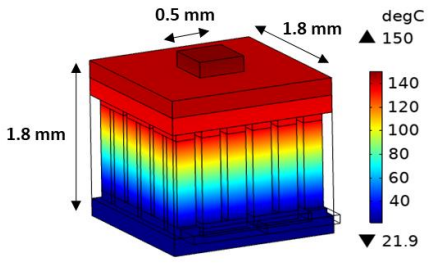

Fig.2. Temperature field solution of the simulation

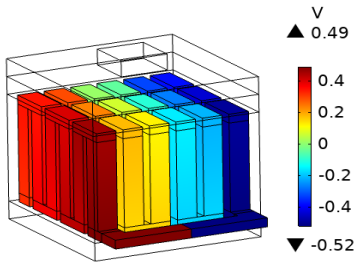

Fig.3. Potential field solution of the simulation

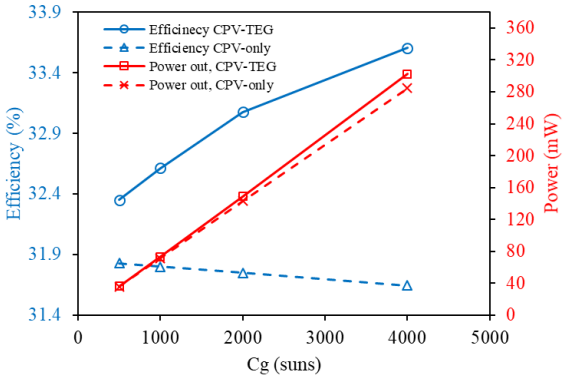

Fig.4. Efficiency and power generation of the systems as a function of the geometrical concentration.

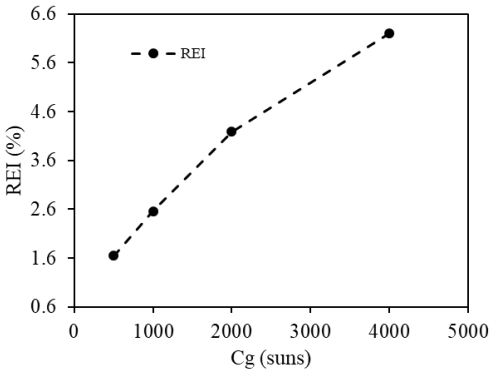

Fig.5. REI of the CPV-TEG system as a function of the geometrical concentration.

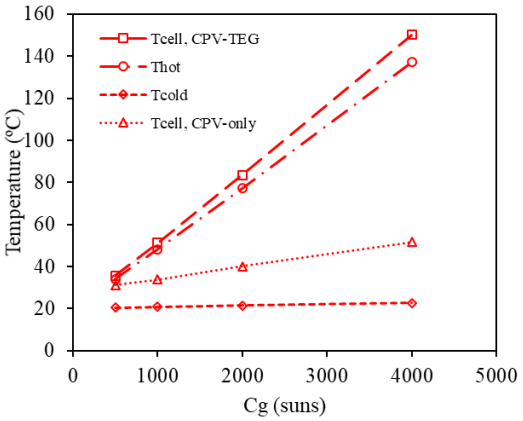

Fig.6. Average temperature as a function of geometric concentration.

Semiempirical Memdiode Model for Resistive Switching Devices in Dynamic Regimes

C. Santa Cruz[1], G. Vinuesa[1], Ó. G. Ossorio[1], H.García[1], B.Sahelices[1], H. Castán[1], S. Dueñas[1], J. Jiménez[2], M.B. González[2], and F. Campabadal[2]

[1]*Department of Electronics, University of Valladolid. 47011 Valladolid (Spain)*
[2]*Dept. Física de la Materia Condensada, University of Valladolid 47011, Valladolid (Spain)*
[3]*Institut de Microelectrònica de Barcelona, IMB-CNM (CSIC), Campus UAB, 08193 Bellaterra, (Spain)*

**Corresponding author, e-mail: sduenas@ele.uva.es*

1. Abstract

A semiempirical memdiode model (SEMM) of resistive switching devices is proposed. This model is based on the introduction of time dependencies in the parameters of the quasi-static memdiode model (QMM), as well as on the empirically observed asymmetries between the reset and set transitions. The model considerably improves the prediction of the electrical response of resistive switching devices to arbitrary input stimuli.

2. Introduction

Memristors were first defined by Chua [1] as devices in which there is a linear relationship between charge and magnetic flux. The most typical structure of a resistive switching memristor consists of a metal-insulator-metal (MIM) structure in which the resistance of the insulator depends on its recent history. Their ability to store information makes them especially interesting for many analog and digital applications such as neuromorphic and bioinspired circuits, medical diagnostics, non-volatile memories, signal processing and control systems. To achieve all of this, it is necessary to get a model which could be included in circuit simulators. The QMM model [2] is one of the most reputed in this category. In this work we introduce some modifications to this model based on experimental observations on the dynamics of set and reset transitions that allow the QMM model to be extended to arbitrary and non-stationary stimuli.

4. Experimental, results and discussion

The memristors used in this work were TiN/Ti/HfO_2/W MIM capacitors. Atomic layer deposition technique was used to grow the HfO_2 layer at 225 ºC using TDMAH and water as hafnium and oxygen precursors, respectively. Electrical characterization was carried out by using a Keythley 4200SCS mainframe.

Figures 1 and 2 show experiments in which monotonically increasing and decreasing sinusoidal voltage waveforms were applied and the currents through the memristor were recorded. Figures 3 and 4 show the best fitting obtained when using the QMM model. We observe that this model fits well the current response for positive voltage values (that is, for set transitions). However, for the reset transition (negative voltages) the QMM model fails. That indicates that some time dependencies occurring during the reset transitions are not included in the QMM model due to its quasi-stationary nature. The proposed SEMM model mainly includes changes in two parameters of the QMM model: the filament dilution speed, η^-, and the reset transition voltage, V^- [2]. Linear dependencies of these terms with the initial state, λ_0, ($\alpha + \beta(1 - \lambda_0)$), provide improved fittings. Figures 5 and 6 show that the SEMM model noticeably improves the fitting for the reset transitions. Figure 7 shows in more detail how the SEMM model fits well both current-time and current-voltage dependencies of reset transition loops. The observed asymmetries and the different time dependencies of set and reset transitions can be related to the different physical mechanisms involved in them. As we described in Ref. 3, the set transition is described by an Erlang distribution which is compatible with a percolation process, whereas the reset one fits to a sigmoidal function and can be related to an autocatalytic oxidation reaction. The first process is very fast, while the second one is considerably slower. Because of that, the quasi-static model cannot adequately describe the reset transitions.

Acknowledgements

This work was funded by the Spanish Ministry of Science, Innovation and Universities grant TEC2017-84321-C4-2-R and TEC2017-84321-C4-1-R, with support of Feder funds.

References

[1] L.O. Chua, Memristor. The Missing Circuit Element, IEEE Trans. on Circuit Theory, Vol.18, No.5, pp.507-519, 1971.
[2] E. Miranda, Compact Model for the Major and Minor Hysteretic IV Loops in Nonlinear Memristive Devices, IEEE Trans. Nanotechnol., Vol.14, No.5, pp.787–789, 2015.
[3] S. Dueñas, H. Castán, O. G. Ossorio, and H. García, Dynamics of set and reset processes on resistive switching memories, Microelectron. Eng., Vol. 216, p. 111032, 2019.

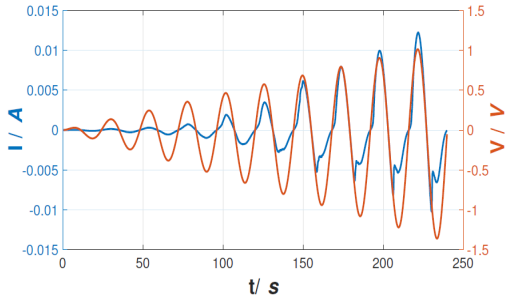

Fig. 1. First experiment: memristor response to a monotonically increasing sinusoidal voltage.

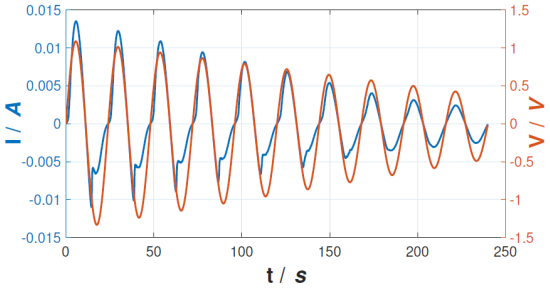

Fig. 2. Second experiment: memristor response to a monotonically decreasing sinusoidal voltage.

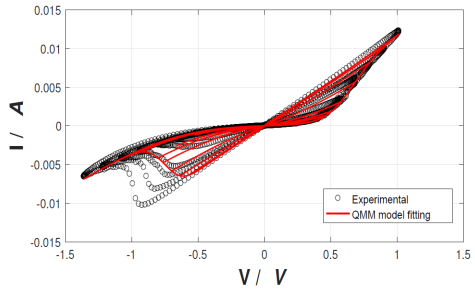

Fig. 3. QMM fitting of the experimental data of the first experiment (Fig.1)

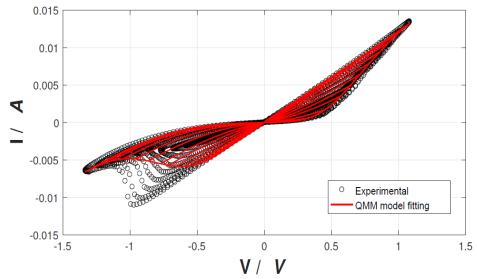

Fig.4. QMM fitting of the experimental data of the second experiment (Fig. 2).

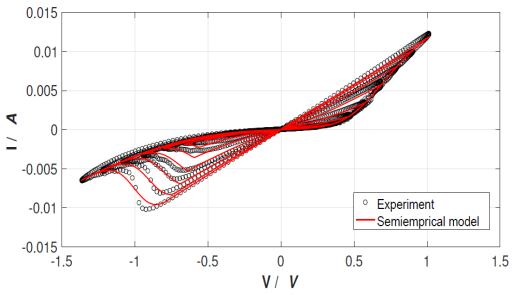

Fig. 5. Semiempirical fitting of the experimental data in Fig. 1.

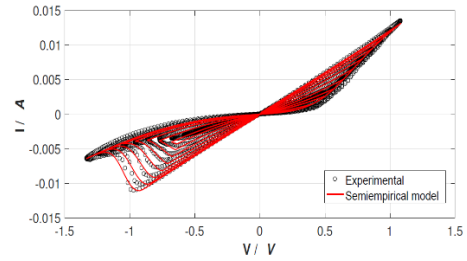

Fig. 6. Semiempirical fitting of the experimental data in Fig. 2.

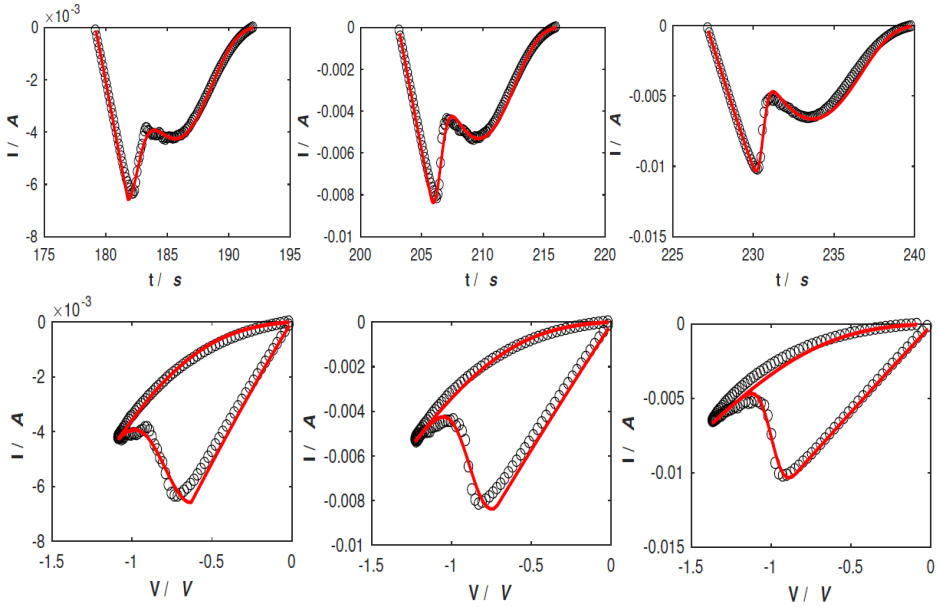

Fig. 7. Semiempirical model fitting of I-t characteristics (upper panel) and I/V loops (lower panel) of several reset transition cycles.

Analysis of traps-related effects hindering GFETs performance

Anibal Pacheco-Sanchez†*, Nikolaos Mavredakis†*, Pedro C. Feijoo, David Jiménez

Departament d'Enginyeria Electrònica, Escola d'Enginyeria, Universitat Autònoma de Barcelona, Bellaterra 08193, Spain.

† These authors contributed equally to this work
* AnibalUriel.Pacheco@uab.cat, Nikolaos.Mavredakis@uab.cat

1. Abstract

The effect of traps on DC and high-frequency behavior of a short channel single-layer GFET is discussed thoroughly in the present work. A recently proposed analytical compact model [1] is accurately validated with trap-affected and trap-reduced data. Important high-frequency figures of merit (FoM) are also derived from the model, and show a strong trap dependence through the operating point of the device [2]. These FoMs not only present gate voltage V_{GS} shifts, but also, they exhibit magnitude alterations due to traps impact.

2. Devices and Measurements

A GFET with gate width w_g=12x2 µm (2 is the number of fingers) and length 300 nm [1], [3] is measured in the present work. Staircase and opposing-pulse measurement techniques are used in sequent forward and backward sweeps. Data from the first technique are strongly affected by traps while the second leads to an almost hysteresis-free performance [1], [2].

3. Results and Discussion

The main contribution of traps to the drain current I_D of the GFET under test is a Dirac voltage V_{Dirac} shift as presented in Fig. 1 for forward and backward staircase sweeps while this shift is trivial in the opposing case. Fig. 1a, 1b illustrate I_D at low and high drain voltage V_{DS} respectively while Fig. 2a shows the corresponding extrinsic transconductance g_m. The proposed model fits precisely the data at both plots for p-type region where we focus in this study. The specific model parameters for this GFET technology [3] can be found elsewhere [1]. It is also apparent from Fig. 1c that the model predicts correctly the measured V_{Dirac} variations for both forward and backward staircase sweeps while the extension of the model at higher V_{DS} reveals that V_{Dirac} of the later trap-affected sweeps coincides for V_{DS}=0.65 V. This is also clear from the simulated I_D, g_m at this specific V_{DS}, since no hysteresis window is observed in the staircase sweeps as shown in Fig. 1b. and Fig. 2a. While one could consider biasing the device at this V_{DS} assuming traps impact is neutralized, the fact that V_{Dirac} in the opposing technique is different clearly indicates that traps are still present. Thus, this work aims to give insight into the device behavior at the specific bias point. Simulated intrinsic transconductance $g_{m,i}$ and output conductance $g_{d,i}$ are illustrated in Fig. 2b, 2c, respectively at V_{DS}= 0.65 V; due to a similar trap density at this unique V_{DS} for both forward and backward staircase sweeps [1], $g_{m,i}$ is the same at every V_{GS} while $g_{d,i}$ is identical only at V_{GS}=V_{Dirac}≈1.1 V for these two sweeps, proving that $g_{d,i}$ amplitude is also affected by traps apart from its V_{GS} fluctuations. This has a direct impact on intrinsic gain $G=g_{m,i}/g_{d,i}$ shown in Fig. 3a as well as on cut-off and maximum oscillation frequencies f_t, f_{max} in Fig. 3b, 3c, respectively. Thus, G magnitude is not the same for non-opposing sweeps which is more clear in Fig. 3a inset where G is shown vs. effective gate voltage $V_{Geff}=V_{GS}-V_{Dirac}$ and the same occurs for extrinsic f_t, f_{max} which directly depend on $g_{d,i}$ [1]. On the other hand, intrinsic f_t does not depend on $g_{d,i}$ [1] and thus, it is identical for forward and backward staircase sweeps for every V_{GS}. In general, the illustration of the opposing case for all the FoMs under study clearly demonstrates the trap-induced deviation of the bias point at the staircase measurements while the dependence on $g_{d,i}$ also causes differences on the magnitude of these FoMs. Finally, if G is extended at n-type region near Dirac point where the IV model is still acceptable (see Fig. 1b), $g_{m,i}$ is further increased while $g_{d,i}$ is further reduced resulting in an acceptable value of G close to unity.

Acknowledgements

This work was funded by the European Union's Horizon 2020 research and innovation program under Grant Agreement No. GrapheneCore2 785219 and No. GrapheneCore3 881603. We also acknowledge financial support by Spanish government under the projects TEC2015-67462-C2-1-R, RTI2018-097876-B-C21 (MCIU/AEI/FEDER, UE) and project 001-P-001702-GraphCat: Communitat Emergent de grafè a Catalunya, co-funded by FEDER within the framework of Programa Operatiu FEDER de Catalunya 2014-2020.

References

[1] A. Pacheco et al., IEEE Trans. on Elect. Dev., vol. 67, no. 12, pp. 5790-5796, 2020. DOI: 10.1109/TED.2020.3029542.
[2] M. Haferlach et al., IEEE Trans. on Nanot., vol. 15, no. 4, pp. 619-626, 2016. DOI: 10.1109/TNANO.2016.2564925.
[3] W. Wei et al., IEEE Trans. on Elect. Dev., vol. 62, no. 9, pp. 2769-2773, 2015 DOI: 10.1109/TED.2015.2459657.

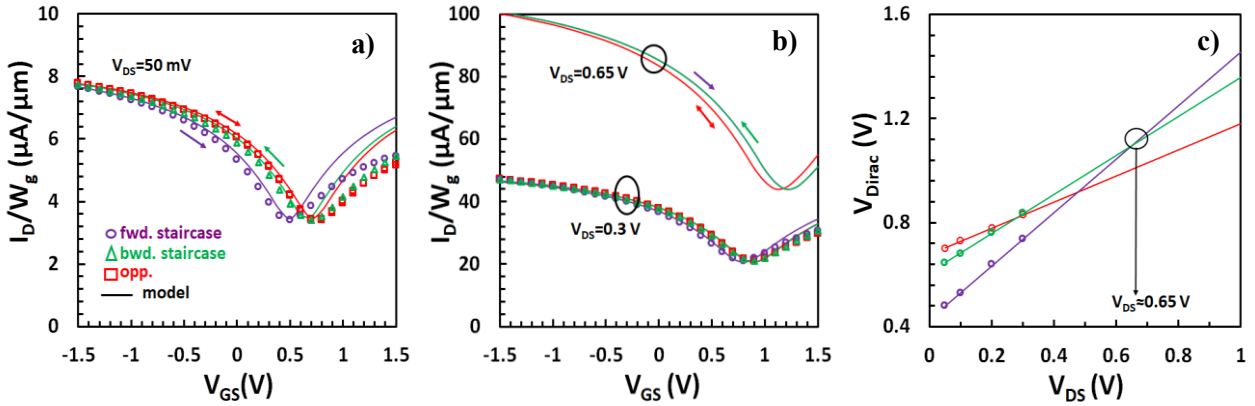

Fig.1. Transfer characteristics of the 300 nm-long GFET for a) V_{DS}=50 mV, b) V_{DS}=0.3, 0.65 V. c) Dirac voltage V_{Dirac} vs. drain voltage V_{DS} are shown for all available sweeps. Markers: data, lines: model.

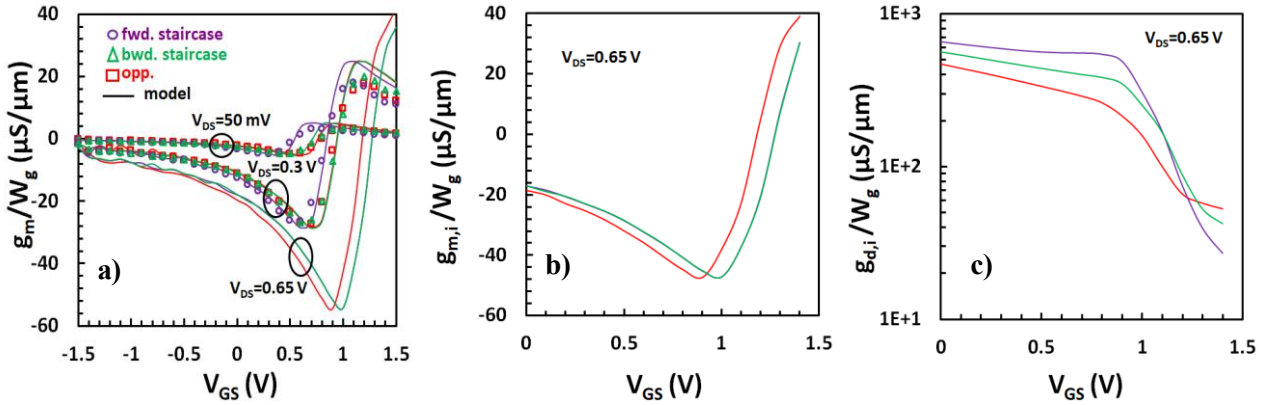

Fig.2. a) Extrinsic transconductance g_m vs. gate voltage V_{GS} with markers representing the measurements (V_{DS}=0.05, 0.3 V) and lines the model (V_{DS}=0.05, 0.3 and 0.65 V). Simulated b) intrinsic transconductance $g_{m,i}$ and c) output conductance $g_{d,i}$ vs. V_G at V_{DS}=0.65 V for all available sweeps.

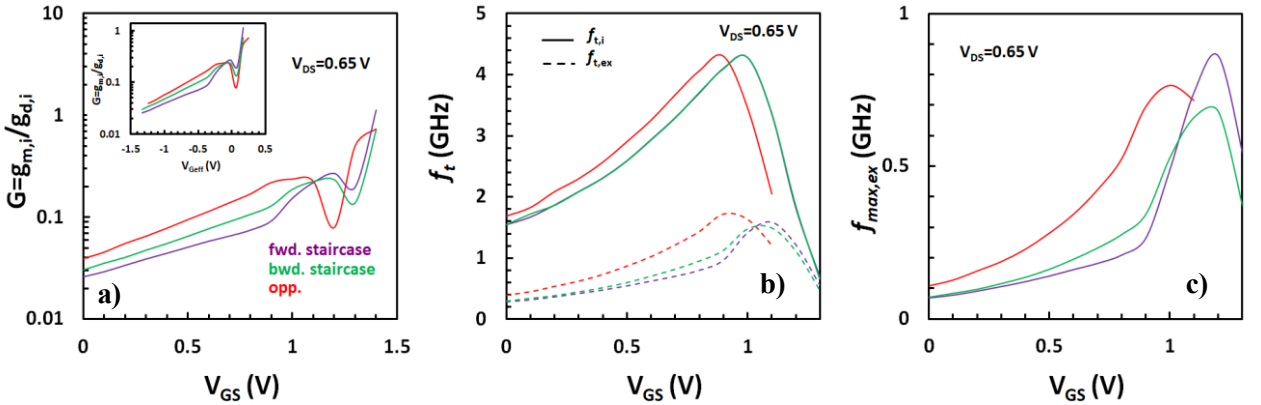

Fig.3. Simulated a) intrinsic gain G, b) intrinsic (solid lines) and extrinsic (dashed lines) cut-off frequencies $f_{t,i}$, $f_{t,ex}$ respectively and c) extrinsic maximum oscillation frequency $f_{max,ex}$ vs. V_{GS} at V_{DS}=0.65 V for all available sweeps. Inset in (a) shows simulated intrinsic gain vs. V_{Geff}.

Variability assessment of the performance of MoS_2 based BioFETs

J. Cuesta-Lopez, A. Toral-Lopez, M. C. Pardo, E. G. Marin, F.G. Ruiz, F. Pasadas, A. Godoy

Departamento de Electrónica y Tecnología de Computadores, Facultad de Ciencias,
Universidad de Granada, Granada 18071, Spain.
e-mail: jcuesta@ugr.es, agodoy@ugr.es

1. Abstract

We have developed a numerical simulator able to describe the processes that take place at the electrolyte-sensor interface. For this work, we focus on the performance variability of MoS_2-based Bio Field-Effect Transistors (BioFETs) specifically designed for the detection of DNA chains. To this purpose, we randomize the location of the receptor molecules attached on the sensing surface, analyzing the variability produced on the response of the sensor.

2. Introduction

Two-dimensional materials (2DMs) -based BioFETs are promising alternatives for sensing biological and chemical signals and processes due to their unique electrical and mechanical features [1]. We have developed an *in-house* simulator for 2DM-based BioFETs aiming at the detection of DNA molecules that implements a more realistic model than the commonly used box-based one [2]. In addition, in order to assess the impact of the inherent variability on the sensor response, we have included the possibility of randomizing the position of the surface receptors.

3. Methods

The simulated device is based on a 400nm-long semiconducting MoS_2 monolayer sandwiched between a 20nm-thick substrate and a 10nm-thick oxide layer, both made of SiO_2. The top oxide that electrostatically couples the 2D channel and the electrolyte, hosts the single-stranded DNA (ssDNA) receptors. For the electrolyte we assume either a 1×PBS or a 0.1×PBS solution. All geometry and materials parameters are collected in **Fig.1** and **Table 1**, respectively. The geometry of the ssDNA molecules is described by a sinusoid-shape that is finely captured by the spatial mesh. Its charge is -120q, i.e. -1q per nucleotide, where q is the electron elementary charge. When activated, receptors turn into double-stranded DNA (dsDNA) molecules, which are straight shaped and have twice the charge of ssDNA molecules [3]. Receptors are placed setting a random distance among them following a half-normal distribution. In addition to the uniform distribution, established as the control case, we consider three scenarios corresponding to a larger receptor density in different regions: centre of the channel, near the source and near the drain regions. For each of them, we selected 10 random distributions of $N = 12$ receptors (**Fig.2**). The activation percentage, α, is the parameter that defines the number of activated molecules: $N_{act} = \alpha N$. The numerical tool self-consistently solves the 2D Poisson - 1D Drift-Diffusion transport equations to obtain the I_{DS} - V_{FG} characteristics of the device for different N_{act} values.

4. Results and Conclusions

The MoS_2 BioFET I_{DS} - V_{FG} characteristics for a uniform distribution are depicted in **Fig.3**, showing a horizontal shift towards positive V_{FG} values as α increases for both 1×PBS and 0.1×PBS solutions. This can be associated to the increase of the negative charge when the ssDNA molecules switch to dsDNA. A comparison between the uniform distribution and the three scenarios described above reveals current differences of several nA/μm for every activation percentage α. The absolute current difference with respect to the uniform case for $\alpha = 50\%$ is plotted in **Fig.4**. The device sensitivity is defined as the current difference between the $\alpha = 0\%$ case and the selected α ($S = I_{\alpha=0} - I_{\alpha}$) at $V_{FG} = 0.3$V since this is the voltage that maximizes this difference for $\alpha = 100\%$ and both PBS concentrations. The sensitivity increases in all scenarios with respect to the uniform distribution (**Fig.5**).

Acknowledgements

This work has been supported by the Spanish Government under the projects TEC2017-89955-P (MCIU/AEI/FEDER, UE); the FEDER/Junta de Andalucía under project B-RNM-375-UGR18; and the European Commission under Horizon 2020 projects WASP (No. 825213). E.G. Marin also acknowledges Juan de la Cierva Incorporación IJCI-2017-32297. A. Toral-Lopez and J. Cuesta-Lopez acknowledge the FPU program under grants FPU16/04043 and FPU019/05132.

References.

[1] J. Lee et al., Scientific Reports, vol. 4, pp. 1-7, 2014.
[2] A. Toral-Lopez et al., Nanoscale Advances, vol. 1, pp. 1077-1085, 2019.
[3] A. Poghossian et al., Sensors and Actuators, vol. 111-112, pp. 470-480, 2005.

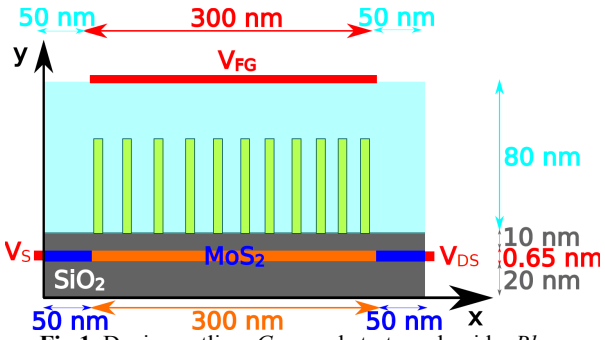

Fig.1. Device outline. *Grey:* substrate and oxide. *Blue:* source and drain. *Orange:* channel. *Cyan:* electrolyte. *Pistachio:* receptors. *Red:* metallic contacts.

$\varepsilon_{SiO2} = 3.9$	$\varepsilon_{MoS2} = 7.6$
$N_D = 10^{18}cm^{-3}$	$\mu_n = 50cm^2/(Vs)$
$\varepsilon_{elec} = 78$	pH = 7.4
$[H^+] = 3.98 \cdot 10^{-5}$ mM	$[OH^-] = 2.51 \cdot 10^{-4}$ mM
$[Na^+] = 140$ mM	$[Cl^-] = 140$ mM
$[K^+] = 2.7$ mM	$[NaH_3PO_4] = 1$ mM

Table 1. Device parameters.

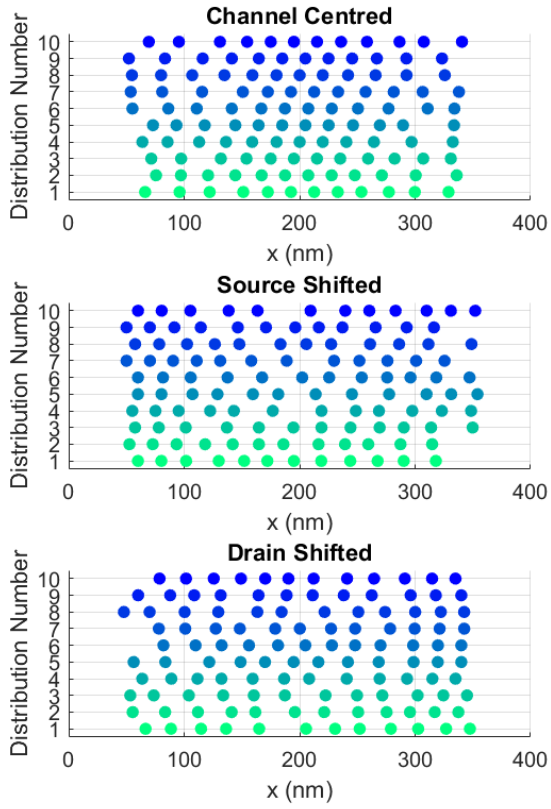

Fig.2. Simulated random distributions of receptors along the channel according to three different scenarios: (top) channel centred, (middle) source shifted and (bottom) drain shifted.

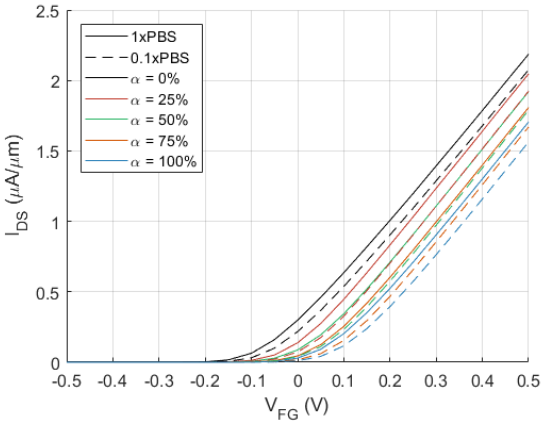

Fig.3. Transfer characteristics for uniformly distributed receptors ($N = 12$). Two PBS concentrations and varying α are distinguished by different line styles and colors, respectively. $V_{DS} = 0.1$V.

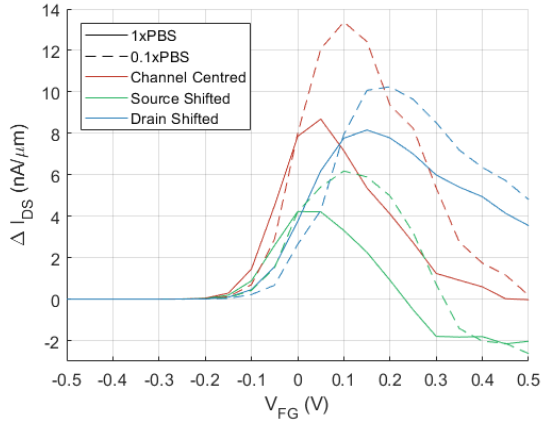

Fig.4. I_{DS} variation with respect to the uniform distribution for $\alpha = 50\%$. Two PBS concentrations and three distributions are depicted by different line styles and colors, respectively. $V_{DS} = 0.1$V.

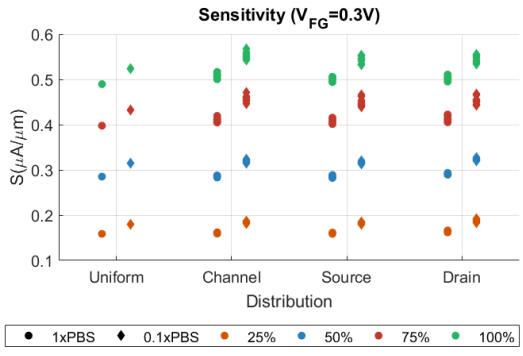

Fig.5. Device sensitivity for different distributions (abscissae), α values (colors) and PBS concentrations (shapes). 10 random distributions of receptors were considered for each non-uniform scenario. $V_{DS} = 0.1$V.

Impact of Self-Heating on Small-Signal Parameters of Graphene Field-Effect Transistors over a Wide Frequency Range

Pedro C. Feijoo*, Francisco Pasadas, Aníbal Pacheco-Sánchez, Ferney A. Chaves, David Jiménez

Departament d'Enginyeria Electrònica, Universitat Autònoma de Barcelona, E-08193 Bellaterra, Spain
*PedroCarlos.Feijoo@uab.cat

1. Introduction

Field-effect transistors with graphene as their ultra-thin channel (GFET) promise to stand out in high frequency (HF) applications [1]. However, thermal effects could limit device performance through self-heating and thermal coupling [2], so an analysis of them is necessary. This work studies the effect of self-heating on the small-signal parameters of the GFET with an architecture as the one shown in Fig. 1. In addition to the field-dependence of self-heating effects in GFET small-signal parameters shown in a previous study [3], this work enables to study the impact of such effects over a wide frequency range.

2. Methods

Our model for GFET DC performance, described in [4], defines drain current I_{DS} as a function of the graphene temperature T and the intrinsic bias point (the gate-to-source voltage V'_{GS} and drain-to-source voltage V'_{DS}). To study the HF performance, we consider the temperature-dependent two-port network [2] consisting of the intrinsic GFET embedded as in Fig. 2. We assume that the GFET presents a complex thermal impedance Z_{th} that depends on the small-signal frequency ω ($=2\pi f$) and the different paths i through which the power $P = V'_{DS} \cdot I_{DS}$ is dissipated out from the graphene channel towards its surrounding materials. The different paths are characterized by a thermal resistance $R_{th,i}$ and a thermal frenquency $f_{th,i}$.

$$Z_{th}(\omega) = \sum_i \frac{R_{th,i}}{1 + {j\omega}/{2\pi f_{th,i}}} \quad (1)$$

$R_{th} = \Sigma_i R_{th,i}$ is an effective thermal resistance that embraces all the dissipating paths, raising graphene temperature above ambient temperature T_A in a way proportional to P:

$$T - T_A = R_{th} P \quad (2)$$

When the self-heating affects HF behavior of the GFET, the small-signal parameters are described by the following equations [2]:

$$y_{11}(\omega) = y_{11,T}(\omega)$$

$$y_{12}(\omega) = y_{12,T}(\omega)$$

$$y_{21}(\omega) = \frac{y_{21,T}(\omega) + cZ_{th}(\omega) y_{11,T}(\omega) V'_{GS}}{1 - cZ_{th}(\omega) V'_{DS}} \quad (3)$$

$$y_{22}(\omega) = \frac{y_{22,T}(\omega) + cZ_{th}(\omega)\left[y_{12,T}(\omega) V'_{GS} + I_{DS}\right]}{1 - cZ_{th}(\omega) V'_{DS}}$$

where $y_{ij,T}(\omega)$ are the small-signal parameters calculated at a constant temperature T (that is, isothermal) and the coefficient $c \equiv \partial I_{DS}/\partial T$.

3. Results and discussion

For simulations, we used the parameters of a fabricated GFET [3]. The effect of self-heating at selected bias points is shown in Fig. 3 for the intrinsic transconductance g_m and output conductance g_{ds} assuming a one-path Z_{th}. Fig. 4 shows similar conditions but assuming two dissipating paths for Z_{th}. Notice the important impact of self-heating on the g_{ds} parameter, which can even go from negative to positive values for the gate overdrive voltage V_{GS} - V_{GS0} of -5 V.

Fig. 5(a) and (b) show the isothermal case ($g_{m,T}$ and $g_{ds,T}$) for frequencies higher above thermal frequencies, where heat dissipation cannot follow the oscillation of the electrical signal, and the non-isothermal case ($g_{m,0}$ and $g_{ds,0}$), for frequencies below thermal frequencies, where heat dissipation follows the oscillation of the electrical signal. Fig. 5(c) shows the GFET maximum oscillation frequency f_{max}, obtained from the isothermal parameters.

4. Conclusions

Self-heating raises the temperature of graphene, affecting both DC and HF device performance. Using the GFET as a two-port network, graphene temperature cannot follow a HF small signal at frequencies above thermal frequencies applied to the device, which must be considered when HF performance is analyzed.

Acknowledgements

This work was partially funded by the EU's Horizon 2020 R&D Program (GrapheneCore2 785219 and GrapheneCore3 881603), by the MINECO (TEC2015-67462-C2-1-R), and the MCIU (RTI2018-097876-B-C21), and by the European Regional Development Funds (ERDF) allocated to the *Programa Operatiu FEDER de Catalunya 2014-2020*, with the support of the *Secretaria d'Universitats i Recerca* of the *Departament d'Empresa i Coneixement* of the *Generalitat de Catalunya* for emerging technology clusters to carry out valorization and transfer of research results. Reference of the GraphCAT project: 001-P-001702,

References

[1] W. Wei, et al., 2020 IEEE Latin America Electron Devices Conference, pp. 1-5, Feb. 2020.
[2] N. Rinaldi, IEEE Trans. on Electron Dev. vol. 48, no. 2, 323, Feb. 2001.
[3] M. Bonmann et al., IEEE Trans. Electron Dev., vol. 67, no. 3, 2020
[4] P. C. Feijoo, et al., IEEE Trans. on Electron Dev., vol 66, no. 3, 1567, Mar. 2019.

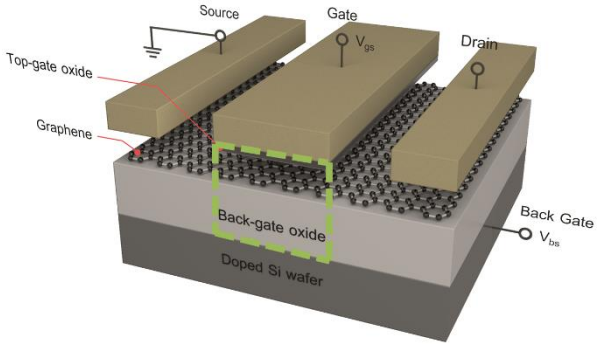

Fig. 1. Schematic of the GFET. In the studied GFET, top oxide corresponds to a 20 nm thick Al_2O_3 layer while the bottom oxide is a 285 nm thick SiO_2 layer. The length of the gate is 500 nm and the width, 30 µm. Electron mobility in graphene is 2000 $cm^2\ V^{-1}\ s^{-1}$, saturation velocity $2\text{-}3\cdot10^7$ cm s^{-1} and puddle concentration $3\cdot10^{11}$ cm^{-2}. R_{th} is $2.7\cdot10^4$ K W^{-1}.

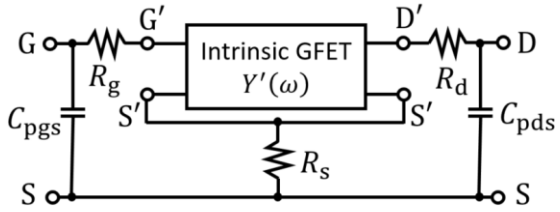

Fig. 2. Extrinsic network of the two-port GFET. Parasitic resistance R_g is 10 Ω, while $R_s = R_d = 5.5$ Ω. Parasitic capacitances C_{pgs} and C_{pds} are in the order of 10 fF.

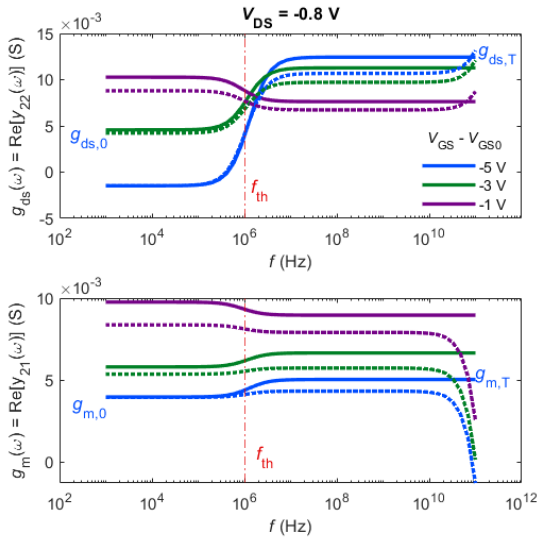

Fig. 3. Intrinsic (solid lines) and extrinsic (dotted lines) g_{ds} (top) and g_m (bottom) as a function of the frequency of the applied signal. Thermal impedance is assumed to present a pole at f_{th} = 1 MHz. Intrinsic $g_{m,0}$ and $g_{ds,0}$ are highly affected by self-heating effects (non-isothermal case), while $g_{m,T}$ and $g_{ds,T}$ are achieved where heat dissipation cannot follow the oscillation of the electrical signal (isothermal case).

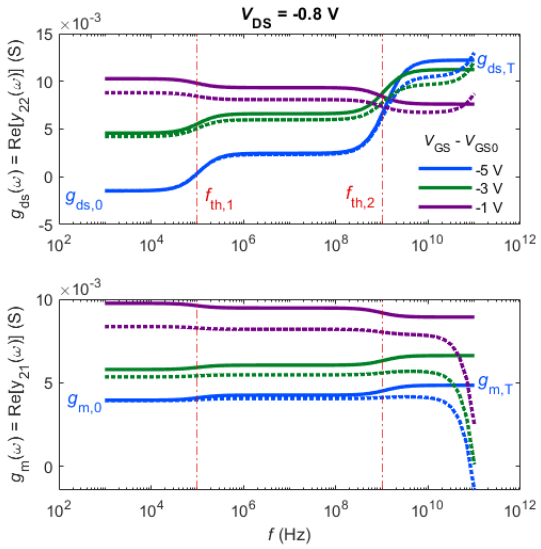

Fig. 4. Intrinsic (solid lines) and extrinsic (dotted lines) g_{ds} (top) and g_m (bottom) as a function of the frequency of the applied signal. Thermal impedance is assumed to present two poles at the frequencies $f_{th,1}$ = 100 kHz and $f_{th,2}$ = 1 GHz, which means two different paths within the GFET to dissipate heat.

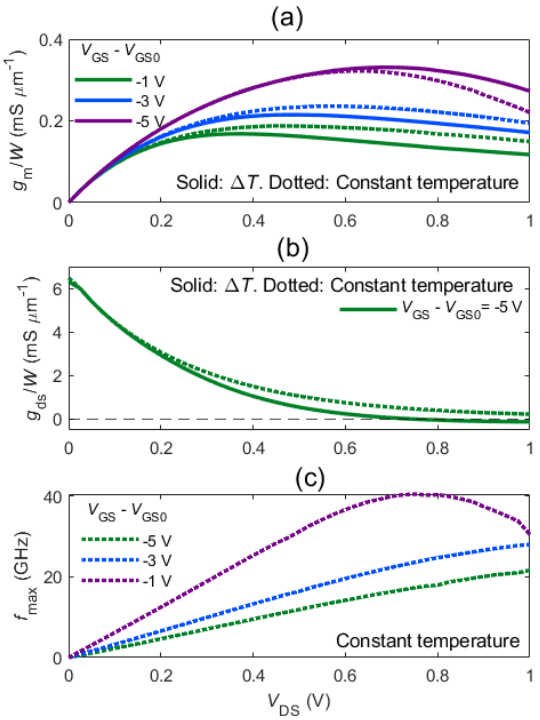

Fig. 5. (a) g_m, (b) g_{ds} and (c) f_{max} as a function of the extrinsic bias voltage. Solid lines correspond to the quasi-static approximation of the DC curves ($g_{m,0}$ and $g_{ds,0}$), the so-called non-isothermal case, while dotted lines assume a constant temperature at the bias point despite the varying small-signal voltage ($g_{m,T}$ and $g_{ds,T}$) known as the isothermal case. Calculating f_{max} with the non-isothermal parameters would lead to incorrect values since graphene temperature cannot follow small electrical signals with frequencies above thermal frequencies.

Electrically and Chemically Doped 2D lateral pn junctions: Equilibrium and out-of-the equilibrium properties

Ferney A. Chaves*, Pedro C. Feijoo and David Jiménez
Departament d'Enginyeria Electrònica, Escola d'Enginyeria, Universitat Autònoma de Barcelona, Campus UAB, 08193 Bellaterra (Barcelona), Spain.

*ferneyalveiro.chaves@uab.cat

1. Abstract

The need for miniaturization of structures in modern semiconductor electronics has directed significant attention toward the fabrication of pn junctions (fundamental electrical components) based on atomically thin materials such as graphene, phosphorene, silicene, germanene, etc., and the family of transition metal dichalcogenides (TMDs) [1,2]. This kind of 2D pn junctions (2DJs) takes advantage of the ultra-thin nature of 2D materials to offer new and exciting possibilities which are impossible to achieve by its 3D counterpart. 2DJs will be an essential part of the new generation of 2D crystal based electronic and optoelectronic devices such as photodiodes, transistors, solar cells, photo-detectors, etc. [3,4].

Some advantages of 2DJs are the thickness-dependency of the semiconductor band gap for some materials, the gate-tunable doping and rectification by external out-of-plane electric fields and the possibility of tuning some electrical properties such as the depletion region width and capacitance by changing the surrounding dielectrics. These advantages enable even more possibilities to create different pn junction concepts, compared with 3D materials.

2DJs can be integrated into a device either by a vertical or by a lateral configuration [5]. In particular, 2D lateral pn junctions are structures where the doping can be reached either electrostatically or chemically and useful for solar cells and photodetectors because the built-in potential created in the space charge region separates and drives the photogenerated e–h pairs to generate photocurrent.

However, while there are many reports of experimental studies on 2DJs, the same is not true for theoretical studies, where the impact of low dimensionality on their electrical properties and their differences with 3D junctions are reported. Thus, theoretical research studies of 2DJs at equilibrium and driven out-of-equilibrium, considering the impact of its low dimensionality, surrounding medium and external electric fields, remain to be developed.

Here, we report a study of the electrostatics and electronic transport of 2D lateral pn junctions based on numerical simulations, which sets the basis for gaining understanding of experimental measurements and for the assessment of analytical models. Our study has been focused on both chemically doped and electrostatically doped 2DJs (Fig. 1), leaving the investigation of vertical 2D pn junctions for a future study. To do so we implement a physics-based simulator that self-consistently solves the 2D Poisson's equation coupled to the drift-diffusion and current continuity equations. Notably, the simulator considers the strong influence of the out-of-plane electric field through the surrounding dielectric, capturing the weak screening of charge carriers and the differences between the two kinds of 2DJs. In addition, we have developed, for the first time, an analytical model for the electrostatics of the electrically doped 2DJ which fits very well to the numerical simulations.

Among the main results of our study we might remark: (i) a proposed Shockley-like equation for the ideal current–voltage (J–V) characteristics, (ii) an ideality factor close to 2 due to the impact of recombination–generation processes inside the effective depletion layer, consistently with experimental data [6], (iii) impact of the material dimensionality on the performances of single-layer MoS_2 (2D) lateral pn junctions against those of the Si (3D) junction, (Fig. 2) (iv) effects of interface states in the 2D semiconductor-insulator interface on the electrostatics and the transport properties, (v) analytical expression for the electrostatic potential and depletion layer width for the electrically doped 2DJ (Fig. 3), (vi) a comparison of the rectification factor between the two kind of 2DJs.

2. Acknowledgments

This work was funded in part by the EU's Horizon 2020 R&D Program (GrapheneCore2 785219 and GrapheneCore3 881603), in part by the MINECO (TEC2015-67462-C2-1-R), and by the MCIU (RTI2018-097876-B-C21). This article has been partially funded by the European Regional Development Funds (ERDF) allocated to the Programa Operatiu FEDER de Catalunya 2014–2020, with the support of the Secretaria d'Universitats i Recerca of the Departament d'Empresa i Coneixement of the Generalitat de Catalunya for emerging technology clusters to carry out valorization and transfer of research results. Reference of the GraphCAT project: 001-P-001702.

3. References

[1] F. Schwierz et al., Nanoscale, 2015, 7, 8261–8283.
[2] S. Kang et al., 2D Mater., 2020, 7, 022003.
[3] D. Jariwala et al., ACS Photonics, 2017, 4, 2962–2970.
[4] J. Sun et al., Adv. Mater., 2020, 32, 1906499.
[5] R. Frisenda et al.,Chem. Soc. Rev., 2018, 47, 3339–3358.
[6] F.Chaves et al. Nanoscale Adv., 2020, 2, 3252-3262

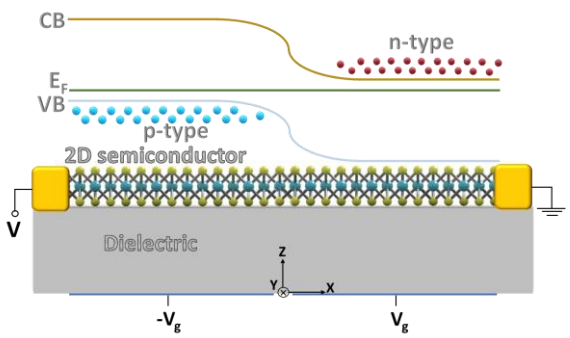

Fig. 1 Scheme of the electrically doped 2D lateral pn junction geometry. For the chemically doped junction, the gate electrodes do not exist.

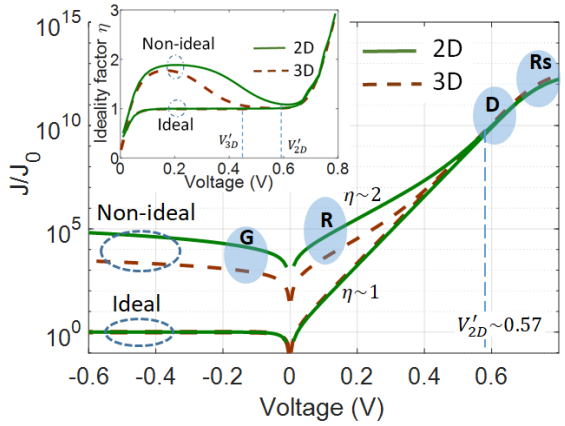

Fig. 2 J-V characteristics of chemically doped 2D lateral and 3D pn junctions showing the different components of the current. Energy gap of 1.12 eV and built-in potential of 0.8 V are assumed in both cases Inset: Ideality factor vs V. "Ideal" and "Non-deal" refer to consider zero and non-zero (Shockley-Read-Hall model) net recombination rate inside the effective depletion region, respectively. Labels "G", "R", "D" and "Rs" correspond to the region dominated by generation current, recombination current, diffusion current and current driven by series resistance, respectively. V'_{2D} and V'_{3D} are the crossover voltages separating the regime where current is driven by recombination from the regime where is driven by the diffusion.

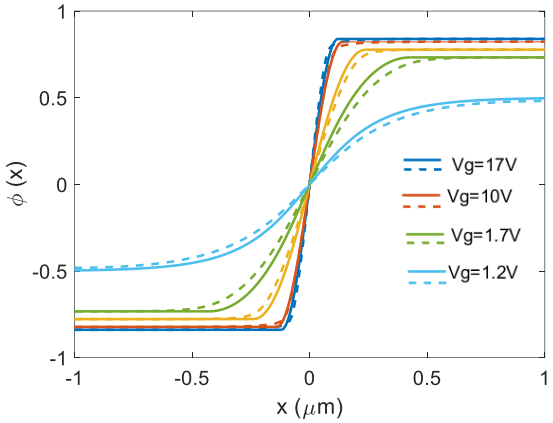

Fig. 3 Electrostatic potential of an exemplary electrically doped 2D pn junction for several applied gate voltages. Solid lines: analytical model. Dashed lines: Numerical model. A monolayer MoS_2 with energy gap 1.8 eV and 300 nm thickness SiO_2 gate insulator are assumed.

Electrical simulation of a QLED device based on quantum dots using the Transfer Hamiltonian approach

J.J.Santaella[†,‡], K.Critchley[*], S.Rodríguez-Bolívar[‡], F.M.Gómez-Campos[‡]

[†] VALEO Lighting Systems, Department of Electronics, Martos, Spain
[*] University of Leeds, School of Physics and Astronomy, Leeds, UK
[‡] Universidad de Granada, Dpto de Electrónica y Tecnología de Computadores, Granada, Spain

Abstract:
Light-emitting diodes or more commonly known as LEDs have great advantages relating to the power consumption and the long useful life they offer to the final applications. Moreover, style is key in some industrial sectors. Particularly, style plays an important role in automotive lighting systems[1,2] where the current and future trend target to achieve even greater lighting surfaces with flexible features and shapes in three dimensions (3D) as shown in Fig1.

Nevertheless, the present LED technology used in the automotive field is formed by discrete devices of point light sources, making it quite complex and expensive to accomplish large lighting surfaces. On the other hand, organic LEDs (OLEDs) are a real and validated technological solution[2] currently used in the automotive market. However, although the current automotive OLED complies with the car manufacturer requirements, the intrinsic instability of those optoelectronic devices under wide temperature ranges such as those in the automotive industry, reduces drastically their lifetime[3], when compared with other environmental conditions like consumer electronic devices. This forces to put in place complex manufacturing processes, which increase the final cost of the OLED device.

Nowadays, nanomaterials called quantum dots (QDs) could end the issues described above effectively due to the inorganic nature of those nanoparticles. In particular, quantum dots LEDs (QLEDs) present a promising perspective in the lighting field due to its purity of color, processability and stability[4]. Yet, the manufacturing QLED process has to be controlled so as to achieve an optimal device performance. Thus, the possibility to model the optoelectronic device in a previous design step before its experimental implementation, would offer the possibility to anticipate the electrical performance of the final QLED by assessing the critical manufacturing parameters to take into account during the fabrication process.

Hence, in this work we have developed a simulation tool in Matlab® based on the transfer hamiltonian method. Thus, we report the numerical simulation approach of an experimental electroluminescent QLED (Figure 2) based on $CuInS_2$/ZnS quantum dots as active layer[5], using the Transfer Hamiltonian approach[6], and following Illera's *et al.* previous works, to calculate the current density J(mA cm^{-2}) and the fundamental I-V curve of each pixel device independently. The experimental multilayer QLED device selected (Figure 3), followed a conventional structure[7,8]: ITO as anode, PEDOT:PSS as hole injection layer (HIL), TFB as hole transport layer (HTL), CIS/ZnS QDs as active or emission layer, ZnO NPs as electron transport layer (ETL) and Al layer as cathode.

Particularly, the junction capacitance between the distinct multilayer, specifically the Anode-Hole Injection Layer (HIL) interface and its influence in the I-V curve is deeply analyzed as shown in Fig4, highlighting the importance of this parameter during the QLED fabrication process and allowing the computational model to put that influence under control by the selection of the optimal thickness and transport layers during the experimental manufacturing of the optoelectronic device.

Thereby, this work achieves to correlate simulation with experiment results relating to the QLED device current variations, which is critical when designing automotive electronics modules to control this new nanotechnology lighting in the future.

Keywords: quantum dots, QLED, automotive applications, lighting systems, electroluminescence, transport layers, nanoparticles, transfer hamiltonian approach.

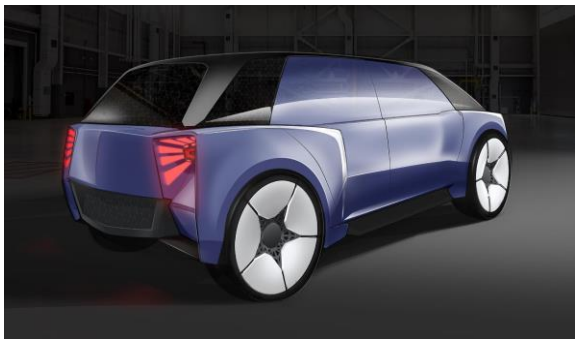

Figure 1: Figure illustrating the rearlighting function with different red-shape of a vehicle.

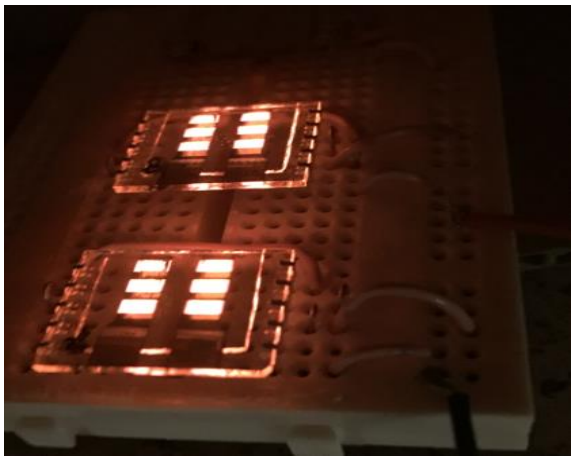

Figure 2: Figure illustrating the QLED fabricated following the structure: Anode/HIL/HTL/EL/ETL/Cathode.

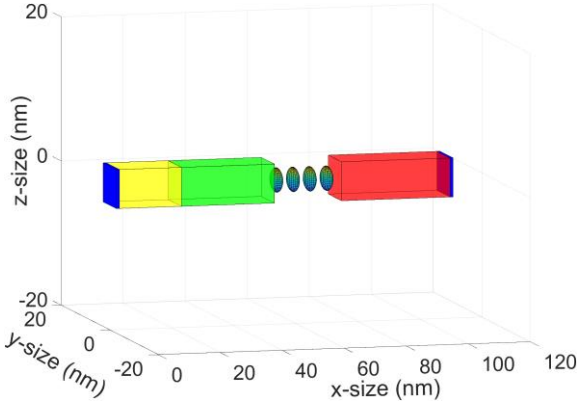

Figure 3: 3D view model of the experimental QLED device with all transport layer drawn[5] i.e. Anode(blue_left) / Hole Injection Layer (yellow) / Hole Transport Layer (green) / QDs / Electron Transport Layer (red) / Cathode (blue_right). NB: The quantum dots represented in the figure are spherical. Different scales were used in each direction for the sake of clarity.

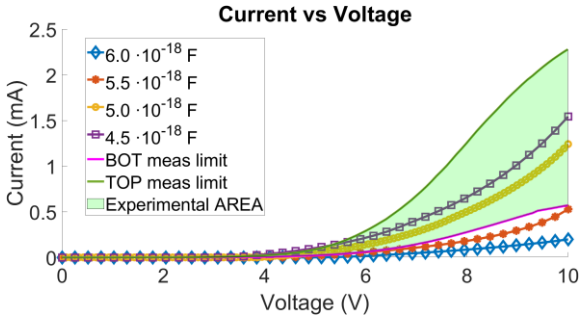

Figure 4: Figure illustrating the fundamental I-V curve plot[5]. Solid lines indicate the upper and lower measured curves corresponding to the individual pixels from Fig2. The green area in between shows the variability due to the manufacturing process. Marked curves correspond to the simulation, where the junction capacitance Anode-HIL of the QLED device was gradually varied.

Acknowledgements

This work was supported by VALEO, multinational automotive company. F.M.G.C and S.R.B were supported by Project P18-RT-3303 funded by the Spanish Junta de Andalucía. The authors thankfully acknowledge the computational assistance provided by Sergio Illera.

References:

1. M. Fachot, "Technology and applications of light emitting diodes, *LEDs Magazine*, Volume 10," p. 1, 2013.
2. P. Boulay, "Automotive Lighting Technology, Industry and Market Trends 2017 Report," no. October, 2017.
3. G. Konstantatos and E. H. Sargent, Colloidal Quantum Dot Optoelectronics and Photovoltaics, 1st ed. Cambridge: *Cambridge University Press*, 2013.
4. V. Wood and V. Bulović, "Colloidal quantum dot light-emitting devices," *Nano Rev.*, vol. 1, no. 1, p. 5202, 2010.
5. J J Santaella; K Critchley; S Rodríguez-Bolívar and F M Gómez-Campos. "Design and fabrication of $CuInS_2$/ZnS-based QLED for automotive lighting systems," *Nanotechnology*, vol. 32 p.105204, 2021.
6. Illera Robles, Sergio ; García Castelló, Núria ; Prades García, Juan Daniel ; Cirera Hernández, Albert. "A transfer Hamiltonian approach for an arbitrary quantum dot array in the self-consistent field regime" *Journal of Applied Physics* 112, 093701 (2012)
7. Jong-Hoon Kim and Heesun Yang, "All-solution-processed, multilayered CuInS2/ZnS colloidal quantum-dot-based electroluminescent device," *Opt. Lett.* 39, 5002-5005 (2014)
8. Zelong Bai, Wenyu Ji, Dengbao Han, Liangliang Chen, Bingkun Chen, Huaibin Shen, Bingsuo Zou, and Haizheng Zhong, Hydroxyl-Terminated CuInS2 Based Quantum Dots: Toward Efficient and Bright Light Emitting Diodes *Chemistry of Materials* 2016 28 (4), 1085-1091.

RTN study of TiN/Ti/HfO_2/Pt resistive switching devices based on neural network analysis

G. González-Cordero[1], M.B. González[2], F. Jiménez-Molinos[1], F. Campabadal[2], J.B. Roldán[1]

[1]Departamento de Electrónica y Tecnología de Computadores. Universidad de Granada. Facultad de Ciencias. Avd. Fuentenueva s/n, 18071 GRANADA, Spain. Email: jroldan@ugr.es

[2]Institut de Microelectrònica de Barcelona, IMB-CNM (CSIC), Campus UAB, 08193 Bellaterra, Spain

1. Abstract

The analysis of Random Telegraph Noise (RTN) signals in Resistive Random Access Memories (RRAMs) is of utmost importance as this phenomenon can lead to stochastic errors in the operation of these devices. In this work, we have measured and analyzed in depth different RTN (I-t) traces by means of self-organizing maps (SOM), a kind of artificial neural networks (NN) devoted to clustering. This technique is employed to perform an automatic classification of the RTN traces that have similar Locally Weighted Time Lag Plot (LWTLP) patterns.

2. Introduction

RRAMs have a great potential for applications linked to neuromorphic computing, non-volatile memories and hardware cryptographic security codes [1]. Among other advantages, these devices consume much less power than traditional non-volatile NAND flash memories, they are CMOS compatible, 3D stackable and show outstanding endurance, retention and latency features. Recent advances in the technological and modeling grounds have led these devices towards industrialization; however, there are still some issues to be addressed related to variability and noise [1]. In particular, RTN signals are under scrutiny since they can produce read errors limiting the device reliability and affecting memory ICs.

In addition, RTN can be used to study the physical mechanisms impacting reliability and variability [2-5]. The main mechanism responsible for the resistive switching phenomenon in RRAM devices is the formation and partial destruction of a filamentary conductive filament (CF) that leads to different resistance states [1]. Nevertheless, inside or close to the CF, traps can be found that can alter the charge conduction producing small current fluctuations (RTN) observed mainly in the high resistance state (HRS) [5]. In this work, the RTN signals produced by electrically active defects present in these devices are analyzed by means of the LWTLP, and the resulting patterns are classified by using SOM analysis.

3. Results and discussion

The TiN/Ti/HfO_2/Pt devices analyzed here and their electrical characteristics have been described in [6]. A typical RTN (I-t) trace measured in the HRS, at a voltage V_{RRAM}=0.2 V is shown in Fig. 1. To analyze the RTN results, we have used two techniques: the LWTLP [2] and self-organizing maps [4]. The LWTLP plots are shown on the right of Fig. 2. The main diagonal of the LWTLP show the number of current levels in the RTN (I-t) trace, the points outside of the main diagonal indicate current transitions, and the color scale indicates the number of events.

We have started our analysis making use of a long RTN trace (Fig. 1). We have segmented the corresponding (I-t) trace in consecutives pieces of 1000 points (see Fig. 2). The corresponding LWTLPs (a 100x100 pixel resolution image) is also given for each of the traces. The set formed by the LWTLPs of the RTN signals (Fig. 2) will be used as the database to train the NN. The SOM analysis is employed to classify the experimental RTN patterns obtained by the LWTLP. The application of the algorithm described in [4] allowed us to obtain a self-organizing map (NN non-supervised analysis), see Fig. 3. Several network sizes were tested and we found that a 5x4 neurons network is an acceptable compromise between the number of clusters or classes obtained, and the number of elements classified in each of the classes. The classes corresponding to the neurons of the SOM obtained are given in Fig. 4. Note that this classification identifies the LWTLP patterns that are most frequently found along the long trace shown in Fig. 1. The results show that there are traces with clearly differentiated current levels (e.g. #17, # 18, #13…) and others with a single level and a component of white noise (e.g. #1, #2, #15…). The time evolution of the classes corresponding to the RTN trace (Fig. 1) is shown in Fig. 5. This describes the RTN most frequent traces and allows a Markov chain approach to model RTN signals for circuit simulation purposes [4]. RTN signals are an interesting entropy source for the fabrication of random number generators for cryptographic circuits, in particular, for the implementation of physical unclonable functions.

5. Acknowledgements

The authors thank the support of the Spanish Ministry of Science, Innovation and Universities and the FEDER program through projects TEC2017-84321-C4-1-R, TEC2017-84321-C4-3-R.

References

[1] F. Pan et al., *Mat. Science and Eng.*, 83, pp. 1-59, 2014.
[2] G. González-Cordero et al., *J. Vac. Sci. Tec. B.* 37, 012203, 2019.
[3] J. Martin-Martínez, et al., IEEE EDL, 35, p. 479, 2014.
[4] G. González-Cordero et al., *SST*, 35, 025021, 2020.
[5] M. B. González et al., IEEE TED, 63, 3116-3122, 2016.
[6] M. B. González et al., Spanish Conf. Elec. Devices, 2021.

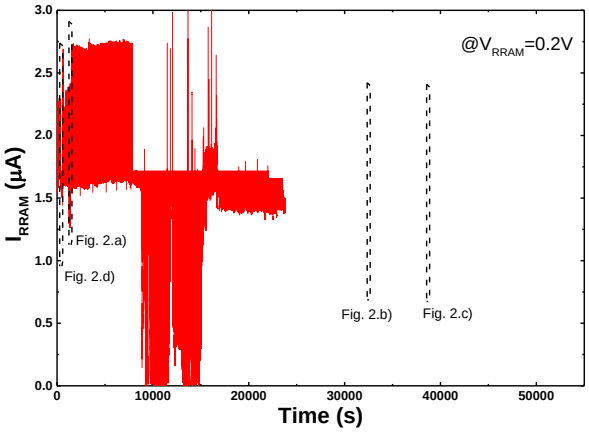

Figure 1 Current versus time trace for a TiN/Ti/8 nm-HfO_2/Pt device in the HRS at V_{RRAM}=0.2V (3.44 million data were measured in 55245.54 seconds).

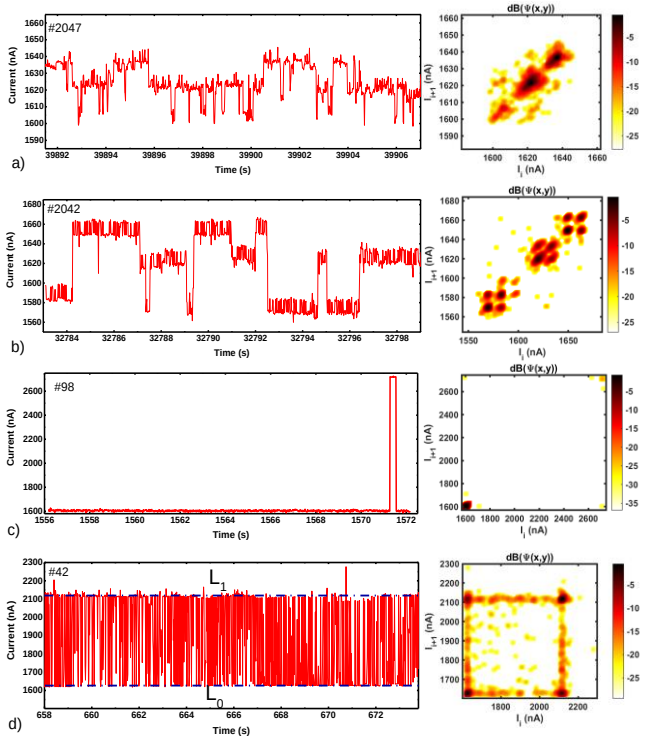

Figure 2 a-d) Measured RTN (I-t) traces (segmented from the long trace shown in Fig. 1) and the corresponding LWTLPs for a TiN/Ti/8 nm-HfO_2/Pt device in the HRS at V_{RRAM}=0.2V. In the d) case, two clear current levels can be distinguished (L_0, L_1).

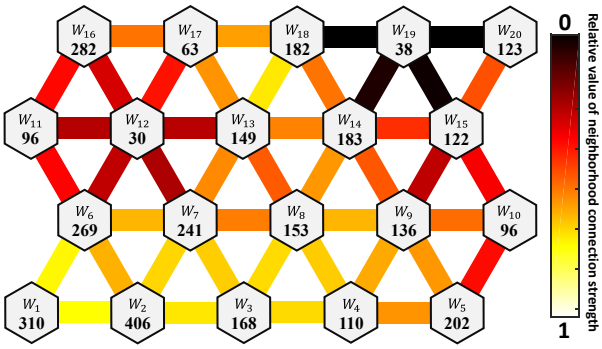

Figure 3. Self-organizing map obtained after the NN analysis of the LWTLPs. It is organized as the results of the pattern clustering performed [4]. The hexagons represent the neurons, the digits inside stand for the numbers of LWTLP patterns associated to each cluster head (neurons); i.e., the classes obtained in the classification process. A dark colour connection between the neurons corresponds to a large Euclidean distance between them [4] (a large difference in the LWTLP patterns and hence in the RTN trace features).

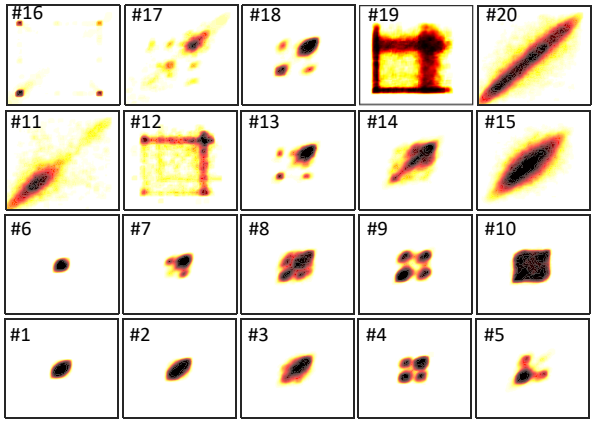

Figure 4 LWTLPs corresponding to the neurons (obtained after training the 5x4 SOM neural network) shown in Fig. 3. See in Fig. 2 the correspondence between the LWTLPs and the RTN traces.

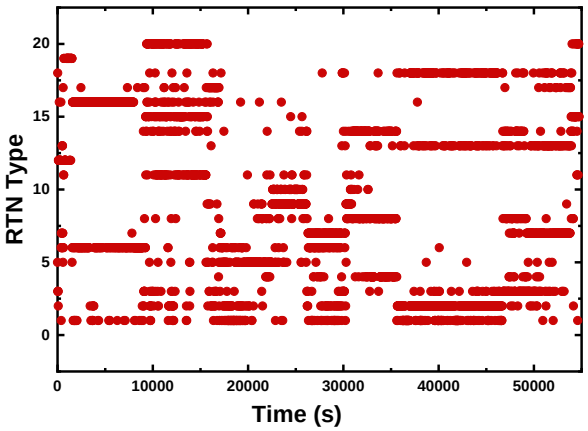

Figure 5 Evolution of LWTLPs clusters (NN classes) obtained along the segmented RTN trace shown in Fig. 1.

Threshold voltage variability study in a 12 nm gate length Nanosheet FET

Julian G. Fernandez [1], Natalia Seoane [1], Karol Kalna [2] and Antonio Garcia-Loureiro [1]

[1] Centro Singular de Investigación en Tecnoloxías Intelixentes, University of Santiago de Compostela, 15705 Santiago de Compostela, Spain (e-mail: julian.garcia.fernandez2@usc.es).
[2]Nanoelectronic Devices Computational Group, Swansea University, Swansea SA1 8EN, U. K.

1. Motivation

Nanosheet FETs are strong aspirants to substitute FinFETs in future nanoscale digital applications [1]. The variability in device characteristics is one of the limitations to the scaling and the integration of nanoelectronic devices [2]. The metal grain granularity (MGG) and the line edge roughness (LER) variabilities are the most harmful fluctuations in short channel transistors [3]. In this work, we perform a 3D simulation study of the influence of these variabilities on the performance of a 12 nm gate nanosheet FET.

2. Methodology

We present a 12 nm gate length nanosheet FET, based on an experimental structure [4], previously calibrated in [5]. In Fig. 1(a-b) the ideal device structure with its relevant parameters is shown.

We use a multi-method simulation toolbox called VENDES [6], which is an in-house-built 3D finite element (FE) software. This tool is capable to reproduce physics using the drift-diffusion (DD) transport method while applying quantum corrections through the density gradient (DG) approach to consider quantum effects.

To introduce MGG variability, the gate is modified by varying its work-function thus mimicking the different grain orientations and shapes observed experimentally [7]. The MGG depends on the grain size (GS) reproduced here by Poisson Voronoi diagrams [8]. Fig. 1(c) shows an example of a random MGG profile.

The LER variability consists of perpendicular deformations to the transport direction, due to lithography fabrication processes [9]. This deviation is reproduced by periodic z-deformations along x-direction. The LER is characterized by the root mean square (RMS) which indicates the amplitude of the deformation, and the correlation length (CL) which periodically propagates this deformation on the space. A LER deformation profile can be seen in Fig. 1(d).

3. Numerical Results

The simulation study is carried out at high drain bias, V_{DD}=0.7 V, to be consequent with the calibration against experiment [5]. We use the constant current criteria at a drain current, I_D=2.0 µm/µA, to extract the threshold voltage (V_{th}), and a large enough statistical sample to study variability. Therefore, 300 different devices with random profiles for each source and variability parameter are generated.

Fig. 2 shows the V_{th} distributions due to MGG variability as a function of the GS. The standard deviation (σV_{th}) and the mean value of the distribution, together with the V_{th} of the ideal device for a work-function (WF) of 4.52 eV, are also shown. Note that, σV_{th} increases from 10 mV to 33 mV due to a rise in the GS from 3 nm to 10 nm. The statistical mean V_{th} consistently decreases when the GS is increased. At a same GS=7 nm, σV_{th} is 52% lower than a similar gate length (L_g=10 nm) nanowire FET [6].

Distributions of V_{th} due to LER are shown in Fig. 3. σV_{th} increases with RMS. Unlike for the MGG, the statistical mean of V_{th} coincides with the ideal value of the device without any deformation. Note that σV_{th} increases from 22 mV to 36 mV due to a rise in the RMS from 0.6 nm to 1.0 nm at CL=10 nm. At a same RMS=0.6 nm and CL=10 nm, σV_{th} is 13% higher when compared to a L_g=10 nm nanowire FET [6].

Figs. 4(a-b) show the correlation between the subthreshold slope (SS) and the V_{th} for the two sources of variability. For LER, SS and V_{th} are highly correlated, with a Pearson's correlation coefficient CC=-0.969, unlike for the MGG which CC=-0.648. Figs. 4(c-d) show the I_D-V_G characteristics for the 300 device configurations affected by the MGG and the LER, respectively. The V_{th} was extracted using the constant current criterion (see blue lines). The LER variability induces changes in the SS that will directly affect the V_{th} (hence the strong correlation between both parameters), whereas MGG variability mainly induces a V_{th} shift with the SS remaining practically constant (as seen in Fig. 4(a)).

4. Conclusion

The 12 nm gate length nanosheet FET is significantly affected by LER (σV_{th} ranging from 22 mV to 36 mV as a function of the RMS at a fixed CL), and MGG (σV_{th} increases from 10 mV to 33 mV with the GS).

These MGG and LER σV_{th} results are 52% lower and 13% higher, respectively, than the ones observed in a similar gate length (10 nm) GAA nanowire FET.

These results are very promising for nanosheet FETs making them strong candidates to replace FinFETs in high-performance applications.

References

[1] IRDS, More Moore, https://irds.ieee.org/editions/2020
[2] G. Roy et al. doi: 10.1109/TED.2006.885683
[3] D. Nagy et al. doi: 10.1109/ACCESS.2020.2980925.
[4] N. Loubet et al. doi: 10.23919/VLSIT.2017.7998183.
[5] D. Nagy et al. doi: 10.1109/ACCESS.2020.2980925.
[6] N. Seoane et al. doi: 10.3390/ma12152391
[7] H. Dadgour et al. doi: 10.1109/IEDM.2008.4796792.
[8] Indalecio, G. et al. doi: 10.1088/0268-1242/29/4/045005.
[9] J. A. Croon et al. doi: 10.1109/IEDM.2002.11.

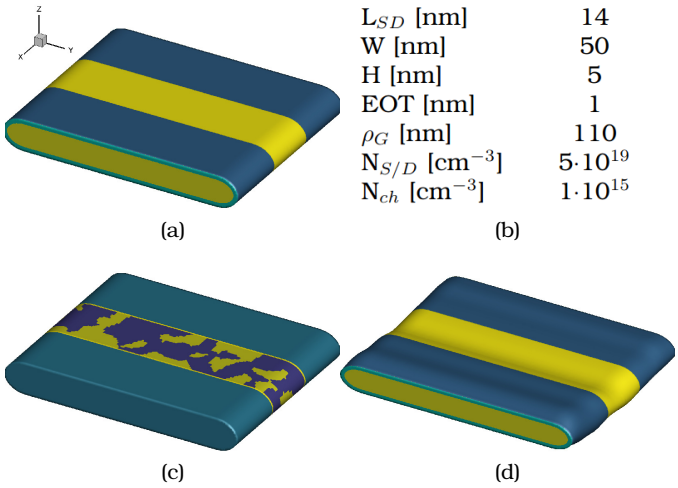

(a)

	Nanosheet
L_G [nm]	12
L_{SD} [nm]	14
W [nm]	50
H [nm]	5
EOT [nm]	1
ρ_G [nm]	110
$N_{S/D}$ [cm^{-3}]	$5{\cdot}10^{19}$
N_{ch} [cm^{-3}]	$1{\cdot}10^{15}$

(b)

(c) (d)

Fig. 1: (a) 3D scheme of the 12 nm gate length Nanosheet FET, (b) device parameters: gate length L_G, source and drain lengths L_{SD}, width W and height H of semiconductor, effective oxide thickness EOT, gate perimeter ρ_G, source and drain doping $N_{S/D}$, and channel doping N_{ch}, (c) an example of MGG variability, and (d) an example of LER variability.

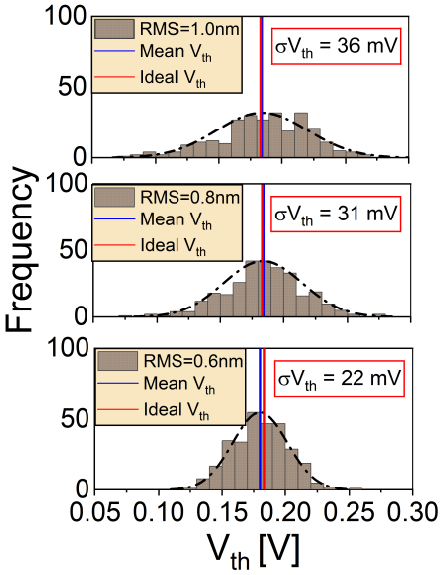

Fig. 3: V_{th} distributions due to LER variability for different root mean square (RMS) deformations and a correlation length (CL) of 10 nm. The σV_{th} is also shown, together with the mean values of the distributions and the V_{th} of the device without LER deformation (ideal).

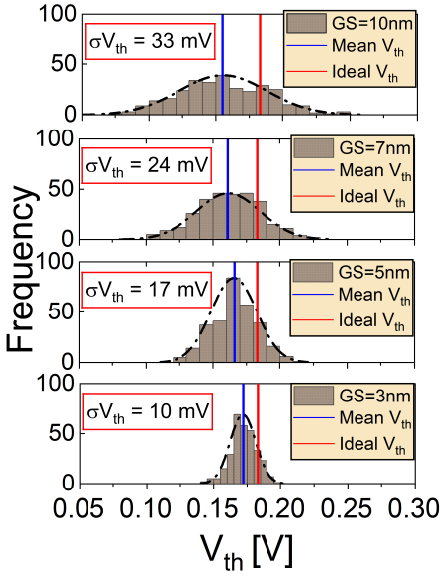

Fig. 2: Threshold voltage (V_{th}) distributions due to MGG variability for different grain sizes (GS). The threshold voltage deviation (σV_{th}) is also shown, together with the mean values of the distributions and the V_{th} of the device with a constant work-function (WF) of 4.52 eV (ideal).

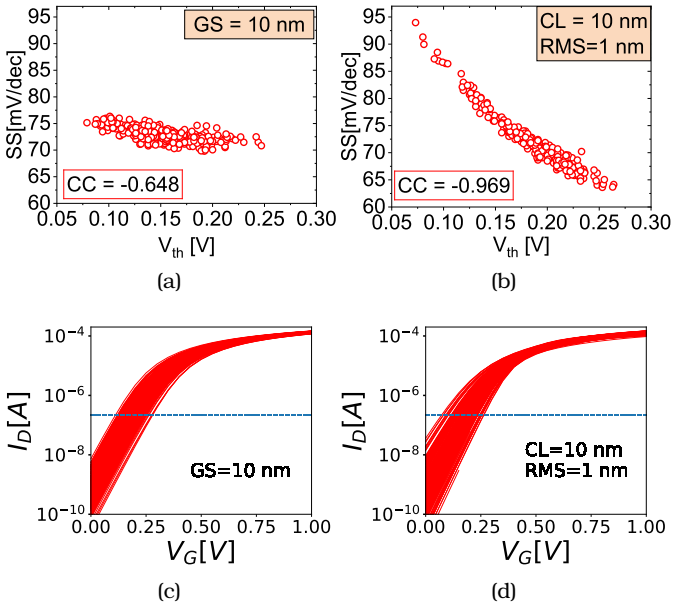

Fig. 4: Subthreshold slope (SS) versus V_{th} due to (a) MGG variability, and (b) LER variability. I_D-V_G variability characteristics due to (c) MGG, and (d) LER. The Pearson's correlation coefficient (CC) is also shown. Blue horizontal lines in (c) and (d) refer to the constant current criteria to set the threshold voltage: I_{CC}=$2.2{\cdot}10^{-7}$ A.

Complementary Resistive Switching in Anti-Serially Connected HfO_2-based Memristors

M. Saludes-Tapia[1], S. Poblador[2], F. Campabadal[2], J. Suñé[1], E. Miranda[1], M. B. Gonzalez[2]

[1]Departament d'Enginyeria Electrònica, Universitat Autònoma de Barcelona, 08193 Bellaterra, Spain
[2]Institut de Microelectrònica de Barcelona, IMB-CNM, CSIC. Campus UAB, 08193 Bellaterra, Spain
*Electronic mail: Mercedes.saludes@e-campus.uab.cat

1. Introduction

The versatile features of memristive devices lead to several potential applications such as non-volatile data storage, digital logic circuits, hardware security, and brain-inspired (neuromorphic) systems. When two bipolar mode memristive devices are anti-serially connected complementary resistive switching (CRS) arises [1]. The combined action of two resistive switching devices leads to the alternate appearance of high (HRS) and low resistance (LRS) states in the current-voltage (I-V) characteristics. This characteristic feature can be used to solve the sneak-path problem in crossbar arrays [2]. In this work, the electrical behavior of two anti-serially connected HfO_2-based resistive switching devices fabricated with a common bottom electrode is investigated. Special attention is given to the role played by the operating conditions on the resistance window and the gradual/abrupt resistance state transitions, being relevant features for a reliable performance in real applications.

2. Experimental

The fabricated devices consist of two anti-serially connected 200 nm-TiN/18 nm-Ti/15 nm-HfO_2/100 nm-W memristors with a common bottom electrode. The HfO_2 layer was deposited by Atomic Layer Deposition at 225°C using TDMAH and H_2O as precursors, and N_2 as carrier and purge gas. The top and bottom electrodes were deposited by magnetron sputtering. Notice that the Ti layer acts as an oxygen getter material. A schematic representation of the resulting structures is shown in Fig. 1. The electrical characterization of the devices was carried out using a *Keysight B1500* semiconductor parameter analyzer.

3. Results and Discussion

Fig. 2 shows typical I-V loops of single RS devices and of two anti-serially connected devices. The electrical characterization started with the electroforming process of each individual device that led to the formation of an oxygen deficient conductive filament (CF) connecting the top and bottom electrodes and driving the device to the LRS. This process was done by applying a positive voltage ramp to the top TiN/Ti electrode, while the W bottom electrode was grounded. After that, a RESET process was performed by applying a negative voltage ramp to the top electrode, which resulted in a partially broken CF and led the device to the HRS. Next, the RS cycling was done through subsequent SET and RESET processes. In order to assess the CRS behavior of two anti-serially connected RS devices, a double voltage ramp was applied from 0 V to $\pm|V_{lim}|$ (see Fig. 3(a)). As shown in Figs. 2(b) and 3(b) two regions with a lower resistance (crest regions) exist, one at each voltage polarity, characterized by the associated voltages, V_{crest}, and resistances, R_{crest}. In these regions, both devices are in the LRS, while in the other regions of the cycle, one device is in LRS and the other in HRS. The analysis of CRS behavior for different V_{lim} values (Fig. 3) reveals a strong dependence of the CRS window on the maximum applied voltage. Furthermore, at high V_{lim} the transitions between states become more abrupt due to the presence of snapback and snapforward effects during the SET and RESET processes of each memristor, respectively [3].

Fig. 4 shows the average and standard deviation values of R_{crest} and $|V_{crest}|$ as a function of $|V_{lim}|$ for both polarities. It is observed that R_{crest} decreases when V_{lim} increases, while V_{crest} increases as $|V_{lim}|$ increases. Notice that the observed experimental trends are similar for both voltage polarities. To assess the symmetry of the CRS I-V loop, the connection between R_{crest} and V_{crest} for both voltage polarities has been analyzed, and their corresponding Pearson correlation coefficients (ρ) have been extracted, giving values of ~0.96 and 0.82, respectively (Fig. 5). These high ρ values are related to the almost symmetrical behavior of the CRS (see Fig. 3a). Effects on the asymmetry of the CRS phenomenon will depend on the variations in the RS behavior of single devices. These variations can be attributed to the inherent variability of the main physical mechanisms responsible for the SET, and RESET processes of every single memristor, and to the device-to-device variability of a given technology.

In summary, this work demonstrates that the operating conditions and the inherent variability present in resistive switching structures must be carefully considered for reliable applications of CRS structures.

Acknowledgment

This work was partially funded by the Spanish Ministry of Science and Innovation and the ERDF program through Project Nos. TEC2017-84321-C4-1-R and TEC2017-84321C4-4-R.

References

[1] D. J. Wouters et al., "Analysis of complementary RRAM switching," IEEE Electron Device Lett., vol. 33, no. 8, pp. 1186–1188, 2012.

[2] E. Linn, R. Rosezin, C. Kügeler, and R. Waser, "Complementary resistive switches for passive nanocrossbar memories," Nat. Mater., vol. 9, no. 5, pp. 403–406, 2010.

[3] D. J. Wouters, S. Menzel, J. A. J. Rupp, T. Hennen, and R. Waser, "On the universality of the: I - V switching characteristics in non-volatile and volatile resistive switching oxides," Faraday Discuss., vol. 213, pp. 183–196, 2019.

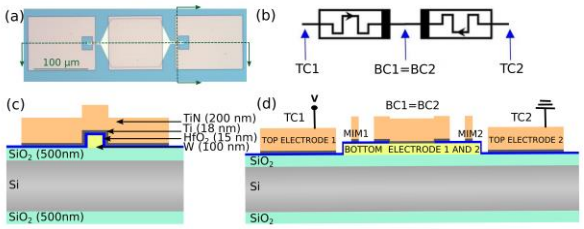

Fig. 1. (a) Optical image of the fabricated anti-serially connected TiN/Ti/HfO_2/W memristors with a common bottom electrode. (b) Electrical scheme. (c) Vertical and (d) horizontal schematic cross-sections (indicated by the dotted arrows in Fig. 1(a)).

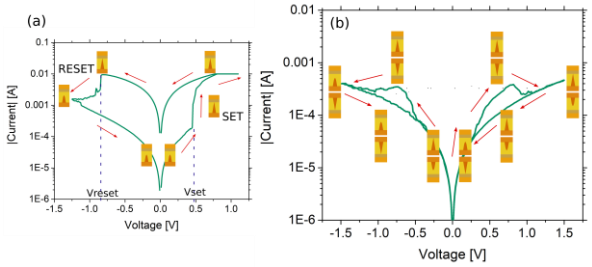

Fig. 2. Typical I-V characteristics obtained for (a) a single RS device and (b) two anti-serially connected RS devices. Arrows indicate the evolution of the RS and CRS phenomena in (a) and (b), respectively. The CF is represented by a truncated-cone with the smaller radius being adjacent to the Ti layer of the top electrode.

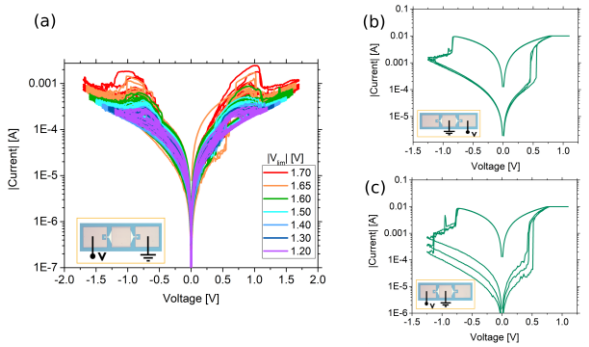

Fig. 3. (a) Experimental CRS behavior in anti-serially connected devices for several $|V_{lim}|$ values. Every 10 cycles $|V_{lim}|$ is decreased from 1.7 V to 1.2 V. (b)-(c) RS behavior of each single device for V_{lim} = [-1.4,1.1] V using a $I_{compliance}$ = 10^{-2} A during the SET process. The inset in each figure shows a top view optical microscope image of the structure, where the biased and grounded terminals are indicated.

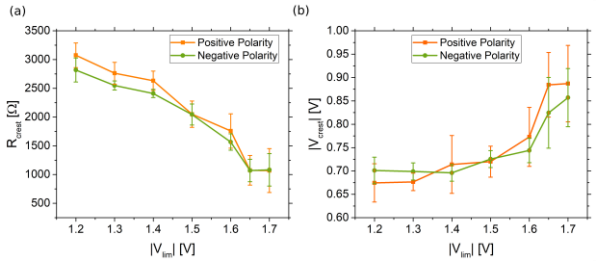

Fig. 4. (a) Average values for R_{crest} versus $|V_{lim}|$, and (b) $|V_{crest}|$ versus $|V_{lim}|$, for positive (orange squares) and negative (green dots) voltage polarities. The error bars indicate the standard deviation.

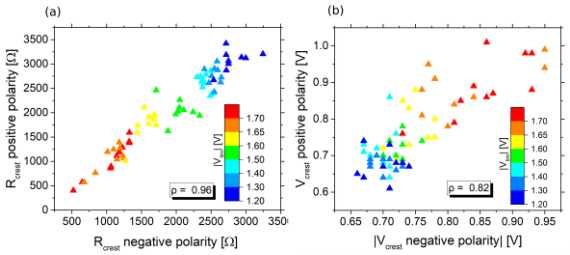

Fig. 5. R_{crest} at positive voltage polarity as a function of R_{crest} at negative polarity, and (b) $|V_{crest}|$ at positive voltage polarity as a function of $|V_{crest}|$ at negative polarity for several $|V_{lim}|$ values, and their corresponding Pearson correlation coefficients.

Towards a hybrid graphene device for Green Energy

J. Martínez[1], A. Velasco[1], Y.K. Ryu[1], A. Ladrón de Guevara[1], A. Boscá[1], J. Pedrós[1], S. Fernandez[2], J. Cárabe[2], J.J. Gandía[2], A. Molinero[2], J.M. Barcala[2], I. Arnedo[3,4], M. Fernandez[3], A. Inés[3], M.B. Gómez-Mancebo[2], R. Fernández-Martínez[2], R. Barrio[2], N. Brea[2], I. Torres[2], M.A. Bailador[2], I. Rucandio[2], A.J. Quejido[2], R. Fandan[1], M. F. Romero[1], F. Calle[1]

[1]ISOM, Universidad Politécnica de Madrid, Ciudad Universitaria, Madrid, Spain.

[2]CIEMAT, Avda. Complutense 40, Madrid, Spain

[3]Das-Nano, Polígono Industrial Talluntxe, Calle M-10, Tajonar, Navarra 31192, Spain.

[4]Dpto. Ingeniería Eléctrica, Electrónica y de Comunicación, Universidad Pública de Navarra, Pamplona 31006, Spain.

javier.martinez@isom.upm.es

1. Abstract

Graphene has attracted increasing attention in recent years due to its excellent mechanical, optical and electrical properties [1]. Its high theoretical specific surface area (SSA = 2630 m^2 g^{-1}) and high electrical conductivity make it an attractive material for many industrial applications [2,3]. Also, it is a flexible transparent material that can be used for solar cells, light emitting diodes (LEDs, OLEDs), touchscreens and LCD displays [4], and in the near future, its flexibility will let to create foldable and wearable devices. In particular, as a consequence of the increasing demand for more efficient, longer-lasting and more compact portable electronic devices, the use of graphene in energy storage devices is one of the most promising applications for this material [5].

We report on the precise fabrication of low cost, high-performance electrochemical supercapacitors with electrodes based in reduced graphene oxide(rGO)/polyaniline nanofiber composite electrode [5]. An infrared laser has been used to reduce the graphene oxide, converting the initial graphene oxide (GO) compact layer into a three dimensional open network of exfoliated graphene flakes (LrGO). This highly conducting porous structure is well suited for electrodepositing pseudocapacitive materials owing to its large surface area. Polyaniline nanofibers have been controllably electrodeposited [6] on the graphene flake network, not only extending further the electrode surface area and providing it with a strong pseudocapacitance but also preventing the restacking of the graphene sheets during the subsequent device processing and charge-discharge cycling.
The composite electrode (LrGO-PANI) presents specific capacitance of 442 F g^{-1}, as compared to 81 F g^{-1} of the bare rGO counterpart (Fig 1), and capacitance retention of 93% over 1000 cycles.

The progress in silicon-heterojunction solar cells requires to develop new architectures of transparent front electrodes in order to generate and extract current in a more efficient way [7]. State-of-the-art contacts for this application are a wide variety of transparent conductive oxides (TCOs). Among them, the one most commonly used is an 80-nm-thick indium tin oxide (ITO) layer. But the cost and scarcity of indium and its rather limited sheet resistance, not below 100 Ω/sq for such thicknesses, lead to the search of new strategies [8].

New architectures of indium-free TCO-based transparent electrodes incorporating one, two and three atomic graphene layers, respectively in different configurations were explored as possible approaches to improve silicon-heterojunction-cell front contacts. The results reveal that the transparent-electrode properties (Fig. 2) dramatically depend on the order in which the TCO and graphene layers have been deposited [9].

In conclusion, graphene can be used in energy generation and storage devices and it is possible to create a hybrid device that combine these two devices.

References:

[1] Luo et al,, Small., 8 (2012), 630
[2] Stoller el al., Nano Lett., 8(2008), 3498
[3] Boscá et al., Sci. Rep., 6(2015), 21676

[4] Cao et al., Small., 7(2011), 3163
[5] Ladrón de Guevara et al., Appl. Surf. Sci., 467 (2019), 691
[6] Pedrós et al., J. Power Sourc., 317(2016), 35
[7] Green, et al., Prog. Photovolt.:Res. Appl. 24(2016) 905.
[8] Terasako, et al., Surf. Coat. Technol. 201(2007) 8924
[9] Fernández et al., Micromachines 10 (2019) 402.

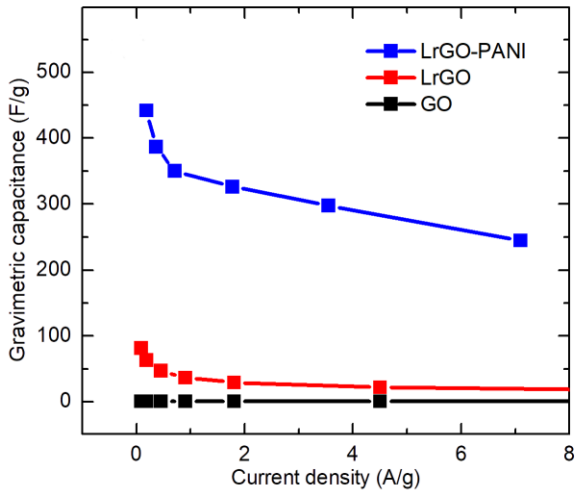

Figure 1: Gravimetric capacitance as a function of the current density for the GO, LrGO and PANI-LrGO electrodes.

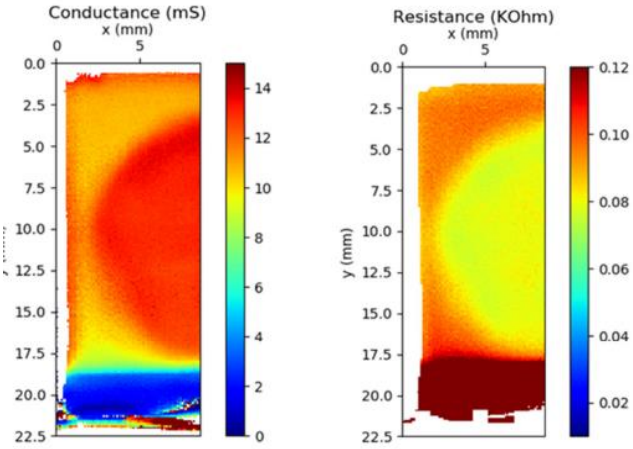

Figure 2: Conductance and resistance maps of three graphene layers transferred on top of the ITO/Si substrate system.

Acknowledgements:
This research was partially funded by the Spanish Ministry of Science & Innovation under the project DIGRAFEN, grant number (ENE2017-88065-C2-1-R) and (ENE2017-88065-C2-2-R) (MINECO/AEI/FEDER, UE) and A. V. FPU grant, as well as the Comunidad de Madrid through project NMAT2D-CM (S2018/NMT-4511). J.P. acknowledges support from Spanish MINECO (Grant RyC-2015-18968). R.S.F. acknowledges support from European Union's Horizon 2020 Research and Innovation Programme under Marie Sklodowska-Curie Grant Agreement No 642688. And The authors A.I., M.F., I.A. acknowledge support from the EU under Horizon 2020's EIC SME Instrument, under grant agreement No 829644. The author I.A. also acknowledges funding provided by FEDER and the Spanish Ministerio de Ciencia, Innovación y Universidades – Agencia Estatal de Investigación, under project TEC2017-85529-C3-2-R (AEI/FEDER, UE)

GaN-based HEMTs operating as zero-bias microwave detectors at low temperature

G. Paz[1], I. Íñiguez-de-la-Torre[1], H. Sánchez-Martín[1],
V. Hoel[2], Y. Cordier[2], T. González[1] and J. Mateos[1]

[1]Applied Physics Department, University of Salamanca, Salamanca 37008, Spain
[2]Institut d'Electronique de Microélectronique et de Nanotechnologie, University of Lille 1, France
gaupaz@usal.es

1. Introduction

The advances in transistor technology have made possible to reach the milestone of THz amplification with a 25-nm InP high electron mobility transistor (HEMT) [1]. When operating as detectors, HEMT transistors are able to detect RF signals much above their cutoff frequencies, what makes GaN-FET-based THz detection feasible despite the lower cutoff frequencies of GaN HEMTs [2,3]. In this contribution, we report on the experimental study of GaN-based HEMTs operating as zero-bias microwave detectors up to 43.5 GHz at low temperatures below 100 K. The injected RF signal is coupled to the drain terminal and the DC voltage output signal is recorded at the drain as well. The gate is only used to bias the device in the appropriate region. Responsivity (β) is just the ratio between the detected output voltage and the injected power. A very simplistic quasi-static (QS) model based only on the I_{DS}-V_{DS} curve is able to successfully fit the measurements in the entire gate bias sweep and for all the temperature range.

2. Device under test and experimental setup

In this work, we focus our study on an AlGaN/GaN HEMT grown on a high resistivity silicon substrate with two-fingers, a gate length L_G=75 nm, a drain-to-source distance L_{DS}=2.5 µm and a width of 25 µm [4]. For the measurements, the sample, located inside a LakeShore CRX-VF cryogenic probe station, is on-wafer connected to a VNA Keysight N5244A, used as RF source, and a two-channel SMU B2902A, which allows both biasing the device and record the output detected voltage. One channel of the SMU is connected to the gate and the other to the drain terminal, in this case through the internal bias-tee, making possible combining the RF input and the DC bias. The selected operating temperatures are 8, 20, 50 and 100 K. Figure 1 presents and scheme of the setup.

3. Results

Figure 2 shows the I_{DS}-V_{DS} at 8 K for various V_{GS} values in the region of interest for zero-bias detection applications. The threshold bias, V_{th}, is around -4.0 V, almost independent of the operating temperature. Based on the static DC curves, an analytical quasi-static (QS) model is able to predict the responsivity (β_{QS}) at low frequency based on the differential channel resistance R_{DS} and the bowing coefficient γ (see [5] for details). In Figure 3, the estimated values of β_{QS}= -0.5R_{DS}γ(1-|Γ|^2) (symbols) are presented together with the measurements of responsivity β at 1 GHz, showing an excellent agreement in the whole range of V_{GS}, even in subthreshold bias conditions. It is important to remark that β reaches its maximum for V_{GS} slightly above V_{th} (around 0.1-0.2 V higher). Note that R_{DS} significantly increases in the subthreshold region, while γ shows a maximum just above V_{th} (see inset of Figure 2) thus explaining the dependence of the responsivity on V_{GS}. On the other hand, the enhanced values of γ found at higher temperature also explain the increase of the responsivity. Interestingly, at higher temperatures (results not shown here), β exhibits a plateau in the subthreshold region (not reproduced by the QS model) and this peak is not observed. To analyze the frequency performance, Figure 4 shows the measured β up to 43.5 GHz for the optimum gate voltage, showing values of hundreds of V/W and a slow roll-off with cutoff frequency about 40 GHz, independently of the temperature. The slight increase of β at 100 K can be attributed to the higher value of γ observed in the inset of Figure 2. Finally, in order to evaluate the quality of the detector, the noise equivalent power (NEP) is calculated. Since we operate in zero-bias conditions, noise can be estimated using the Johnson-Nyquist formula, thus providing NEP=$\sqrt{(4k_BTR_{DS})}/\beta$. As observed in Figure 5, for each temperature the lowest NEP is reached again when V_{GS} is slightly higher than V_{th}, and also higher that the value providing the maximum β. NEP takes excellent values, 0.84 pW/Hz$^{1/2}$ for 8 K, increasing up to 2.2 pW/Hz$^{1/2}$ for 100 K.

For the sake of comparison, results in transistors with other gate lengths will be presented at the conference.

References

[1] X. Mei et al., IEEE Elec. Dev. Lett. **36**, pp. 327-329, (2015).
[2] J. D. Sun, et al., Appl. Phys. Lett. **100**, 013506 (2012).
[3] M. Bauer, et al., IEEE Trans. on Terahertz Science and Technology **9**, pp. 430-444 (2019).
[4] H. Sánchez-Martín et al., Semicond. Sci. Technol. **32**, 035011 (2017).
[5] A. M. Cowley and H. O. Sorensen, IEEE Trans. on Microwave Theory and Techniques **9**, pp. 588-602 (1966).

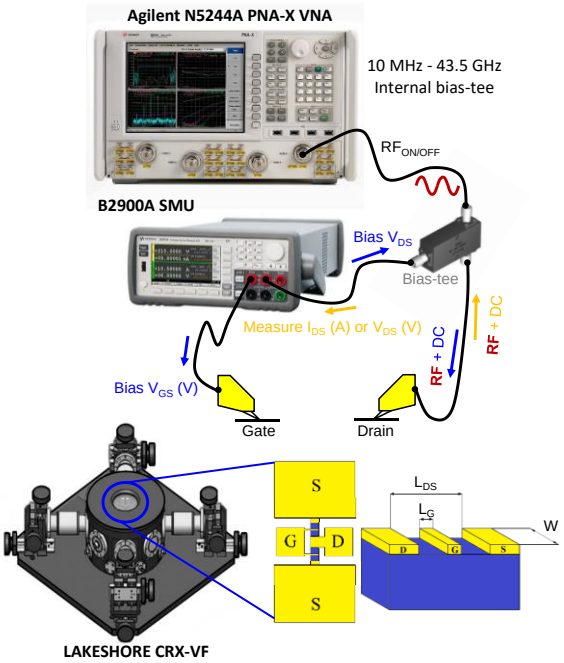

Fig. 1. Sketch of the measurement setup. The cryogenic probe station connects the transistor to the VNA and the SMU. Ground-signal-ground probes allow to access the device. All the system is controlled by means of a LabView code accounting for the losses of the cables and tips to ensure that a RF power of -15 dBm reaches the reference plane of the transistor.

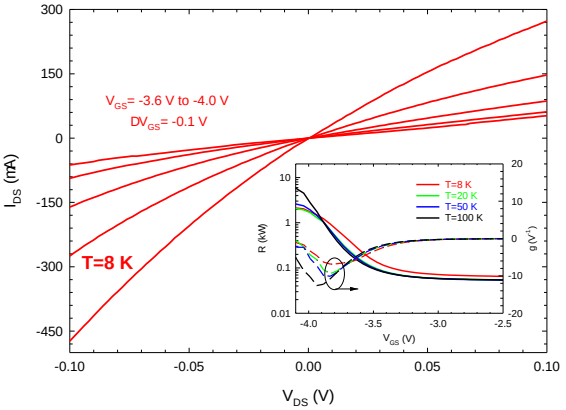

Fig. 2. I_{DS}-V_{DS} characteristics of the reference transistor at 8 K. Inset: Resistance R_{DS} and bowing coefficient γ from 8 K to 100 K.

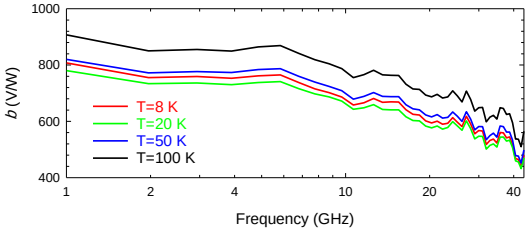

Fig. 4. β measured *vs.* frequency between 1 GHz and 43.5 GHz at temperatures from 8 K to 100 K for the V_{GS} providing the best responsivity in each case.

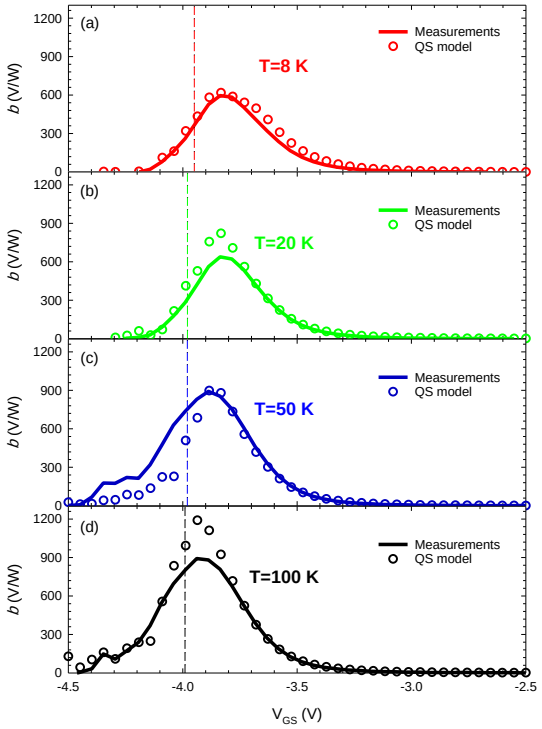

Fig. 3. β measured at 1 GHz (lines) and extracted using the QS model (symbols). (a) 8 K, (b) 20 K, (c) 50 K and (d) 100 K. Vertical lines indicate the threshold bias V_{th}.

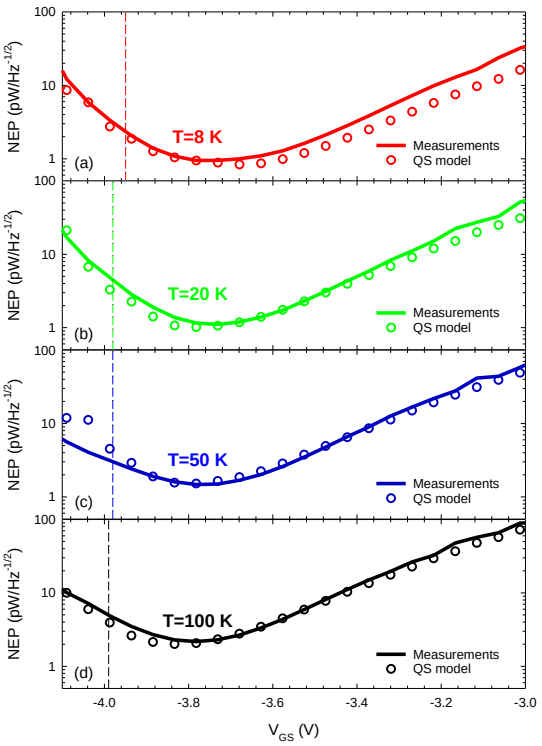

Fig. 5. NEP measured at 1 GHz (lines) and extracted using the QS model (symbols). (a) 8 K, (b) 20 K, (c) 50 K and (d) 100 K. Vertical lines indicate the threshold bias V_{th}.

Influence of dimensionality and stoichiometry in the electronic structure of InAs quantum dot solids

F.M. Gómez-Campos[†], E.S. Skibinsky-Gitlin[†], S. Rodríguez-Bolívar[†], M. Califano[‡], P. Rodosthenous[‡], J.A. López-Villanueva[†], J.E. Carceller[†]

fmgomez@ugr.es
[†] Departamento de Electrónica y Tecnología de los Computadores, Universidad de Granada, Spain
[‡] Pollard Institute, School of Electronic and Electrical Engineering, University of Leeds, Leeds LS2 9JT, United Kingdom

1. Abstract

Periodic quantum dot solids are new materials in which quantum dots are periodically distributed in space[1]. The properties of these materials are explored to find applications in new photovoltaic devices. In order to shed light on these future applications, investigating carrier transport[2] and light absorption are of paramount importance[3].
The first step to investigate these systems is to compute their electronic structures. In this work we present the electronic structure of one- (1D), two- (2D) and three-dimensional (3D) quantum dot solids made of 12 Å radius InAs quantum dots. Two different stoichiometries are studied. In the first case (system A) the quantum dot has an In atom in its center and the interdot contact surfaces along the (111) directions in the arrays are mainly arsenic atoms. In the second case (system B) the atomic positions are inverted, and therefore the contact surfaces between neighbours are mainly indium atoms.
The influence of dimensionality and stoichiometry in these quantum dot solids are discussed.

2. Theoretical framework

3. Results

Figure 1 depicts the systems studied in this work. They are linear (one-dimensional array), square (two-dimensional array) and cubic (three-dimensional array) lattices. The interdot distance is one-bond length. The systems A and B have different stoichiometry, interchanging all the In and As atomic positions in the whole solid.
Figure 2, 3 and 4 show the miniband structure of these systems. All the arrays show flat miniband structure in the valence band regardless dimensionality and stoichiometry. This is related with the weak coupling of the valence band wavefunctions in InAs between neighbouring dots, related to the greater valence band effective masses in this material.
About the minibands in the conduction band, system A shows wider minibands than system B. This is due to the greater interdot coupling in the former which can be attributed to the atomic distribution in the interdot facets.
About dimensionallity, three-dimensional systems exhibit greater miniband curvatures because of greater coupling with neighbours (6 neighbours vs 4 and 2 in two- and one-dimensional arrays). This will influence the effective mass for carrier transport in these quantum dot solids.

Acknowledgements

F.M.G.C, S.R.B, J.A.L.V. and J.E.C. were supported by Project P18-RT-3303, funded by the Spanish Junta de Andalucía.

References

[1] T. Hanrath, "Colloidal nanocrystal quantum dot assemblies as artifical solids" J. Vac. Sci. Technol. A, 30, pp. 030802, 2012.
[2] N. P. Brawand, M. B. Goldey, M. Vörös, G. Galli, "Defect states and charge transport in quantum dot solids" Chem. Matter., 29, pp. 1255-1262, 2017.

[3] A. A. Chistyakov, M. A. Zvaigzne, V. R. Nikitenko, A. R. Tameev, I. L. Martynov, O. V. Prezhdo, "Optoelectronic properties of semiconductor quantum dot solids for photovoltaic applications", J. Phys. Chem. Lett., 8, pp. 4129-4139, 2017.

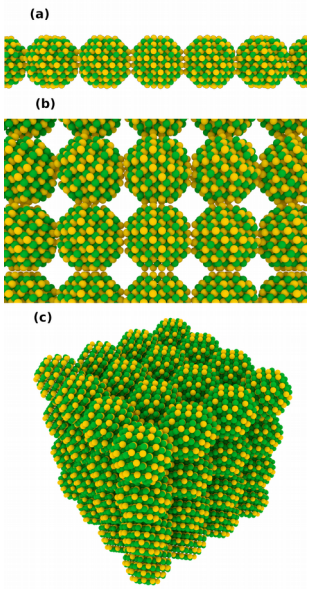

Fig.1. Quantum dot solids (a) one-, (b) two- and (c) three-dimensional arrays. Yellow and green spheres represent arsenic and indium atoms respectively in system A. In system B colours represent the opposite atoms because of the inverted stoichiometry.

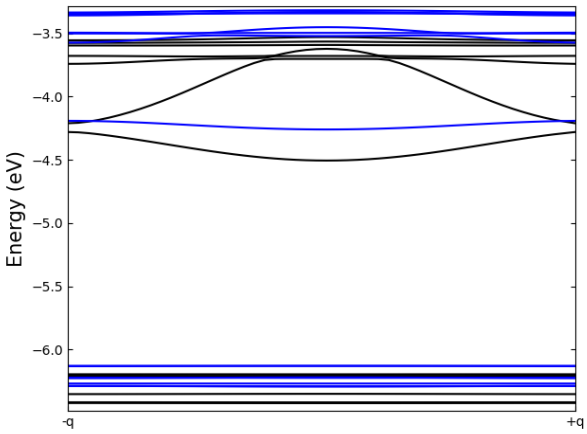

Fig.2. Miniband structure of a one-dimensional quantum dot solid. The minibands corresponding to system A (see text) are drawn in black; in blue, the ones corresponding to system B (see text). The horizontal axis sweeps the Brillouin zone. The energy in the vertical axis are referred to the vacuum level.

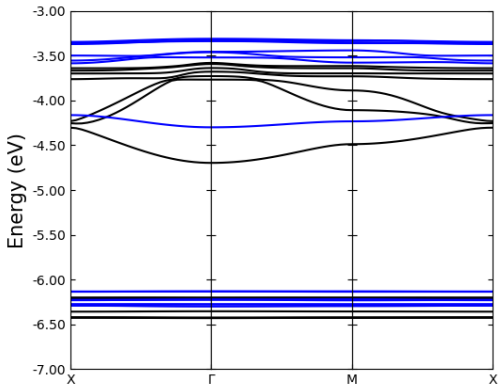

Fig.3. Miniband structure of a two-dimensional quantum dot solid. The minibands corresponding to system A (see text) are drawn in black; in blue, the ones corresponding to system B (see text). The energy in the vertical axis are referred to the vacuum level.

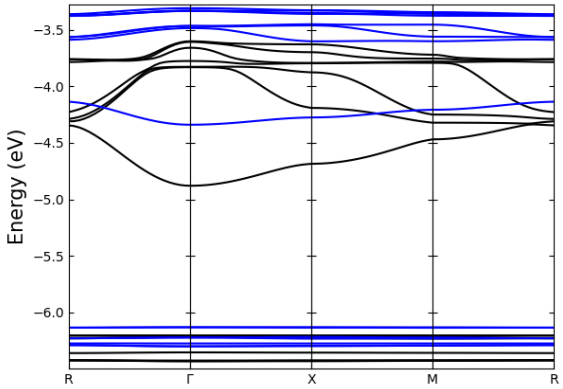

Fig.4. Miniband structure of a three-dimensional quantum dot solid. The minibands corresponding to system A (see text) are drawn in black; in blue, the ones corresponding to system B (see text). The energy in the vertical axis are referred to the vacuum level.

ORAL SESSION III

Device modelling, simulation and beyond

Thursday 10

15:45-17:00

Chairperson: A. García-Loureiro (Universidad de Santiago de Compostela)

Bias-dependence of surface charge at low temperature in GaN nano-diodes

E. Pérez-Martín[1], I. Íñiguez-de-la-Torre[1], T. González[1], C. Gaquiére[2] and J. Mateos[1]

[1]Applied Physics Department, University of Salamanca, Salamanca 37008, Spain
[2]Institut d'Electronique de Microélectronique et de Nanotechnologie, University of Lille 1, France
elsapm@usal.es

1. Introduction

In this work, with the help of a semi-classical two-dimensional Monte Carlo (MC) simulator, we study the DC current-voltage curves of Self-Switching Diodes (SSDs) fabricated on an AlGaN/GaN heterostructure from 100 K up to room temperature. Due to the very narrow channel of the SSDs, the presence of surface effects plays a key role not only on their DC behavior but also on their RF detection performance. The characteristic times and energies of such surface states have been determined through impedance measurements in [1]. The low-frequency dependence of the zero-bias responsivity at different temperatures (T), Figure 1, shows clearly the signature of the traps, also originating a change in the sign of the voltage response. The evolution with T of the negative surface charge density (σ) at the etched sidewalls of the SSD is the key magnitude to explain such behavior. In this work, we focus our attention at DC level, since it can also explain the low-frequency responsivity [2]. At 300 K, MC simulations with a constant value of σ are able to replicate very satisfactorily the experiments. However, to reproduce the shape of the I-V curve at low temperatures, a more realistic approach where σ depends not only on T, but also on the applied bias (V), is necessary, as we report in this contribution.

2. Device and surface charge models

The operation of SSDs lies on the high surface-to-volume ratio of its channel and the asymmetry originated by two L-shaped insulating trenches. The nanometer channel of the planar SSD produces a non-linear current-voltage relationship [3]. It is worth noting that the during the fabrication process, the etching of the sidewall trenches which define the channel creates surface traps at the semiconductor-air interfaces, partially depleting the conductive semiconductor channel, with a strong impact on the device performance. The more simplistic way to include the surface effects in the MC tool is to use a constant value of σ for each T. Based on the value of the net background doping N_{Db}=10^{17} cm^{-3} assigned to the GaN channel (see Ref. 4 for details), the lateral depletion at each side can be calculated as W_d=σ/N_{Db}. In this work, we simulate a 1 μm long and 80 nm wide single channel SSD (see the inset of Fig. 1). According to electrical measurements of SSDs with different widths (W), the value of W_d at equilibrium and 300 K is 18 nm [1]. For narrow channels and lower temperatures the channel is almost completely closed, and a more advanced algorithm is required due to the complex nature of the traps occupancy. The suggested method is to adjust the value of σ for each applied bias, i.e. $\sigma = f(V,T)$, which is computed by means of MC simulations using "reverse engineering", comparing the experimental I-V curve at each T with the simulations made with varying values of $\sigma(V)$.

3. Results

An inspection of the measured I-V curves (Fig. 2) reveals a surprising decrease of the current (and increase of the resistance, see the inset) at low T, most likely related to a significant increase of the surface charge at the sidewalls of the trenches, suggesting a thermal activation of the surface traps. We have simulated the mentioned SSD using different values of the constant surface charge density for each temperature. Circles of Figure 3 correspond to the simulations using the values of σ which correctly reproduce the zero-bias resistance (σ/q=18, 35 and 39.4×10^{15} m^{-2} for 300, 200 and 100 K, respectively). A fairly good agreement between such MC simulations and the experiments is found in the whole bias range under analysis for T above 220 K, indicating that a constant value of σ is able to model the behaviour of the device. For T<220 K, a good agreement can only be achieved if a bias-dependent surface charge density is employed. A series of MC simulations with constant σ have been compared with the measured I-V curve, so as to straightforwardly estimate the required value of σ to fit the current values at every bias point. The so obtained values of $\sigma(V,T)$ providing the good agreement with the experiments are plotted on the right axis of Figure 3. Also, Figure 4 shows the complete colour map of $\sigma(V,T)$. As expected, $\sigma(V)$ is practically constant for 300 K, but shows a maximum around zero-bias for lower T. It is also remarkable that $\sigma(V)$ is very asymmetric for 100 K (much higher for positive V), behaviour which is at the origin of the change of the sign in the response shown in Fig. 1, since it makes the bowing coefficient (inset Fig. 2) of the I-V curve to be negative at low T (the curve becomes concave, instead of the typical rectifying convex shape of the I-V). More details, and results corresponding to different SSDs, will be presented at the conference.

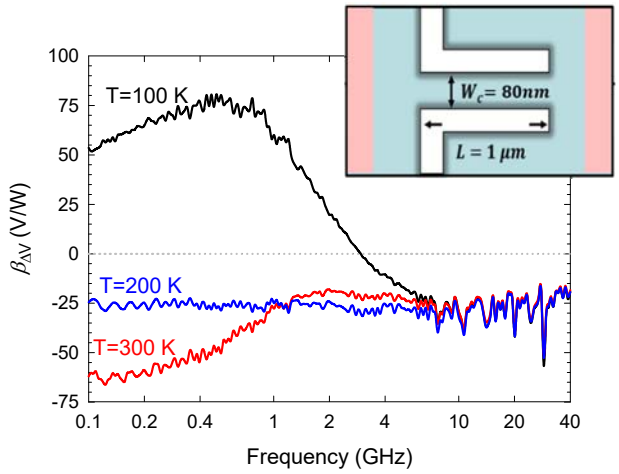

Fig. 1. Zero-bias responsivity, $\beta_{\Delta V}$, as a function of frequency between 100 MHz and 40 GHz for 100 K, 200 K and 300 K. The inset shows the geometry of the SSD under study.

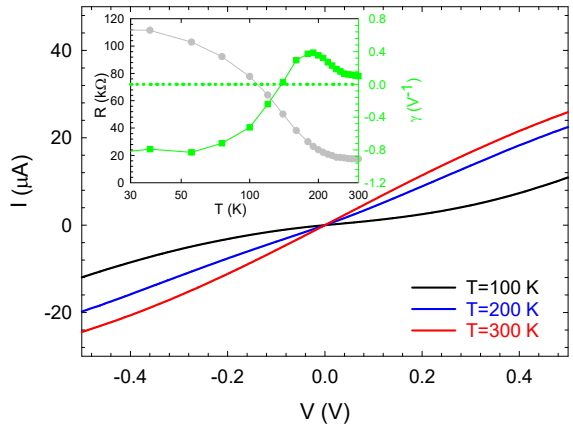

Fig. 2. *I-V* curves of the SSD under test for different temperatures. The inset shows the zero-bias resistance, *R*, and the bowing coefficient, γ, obtained with the QS model [2].

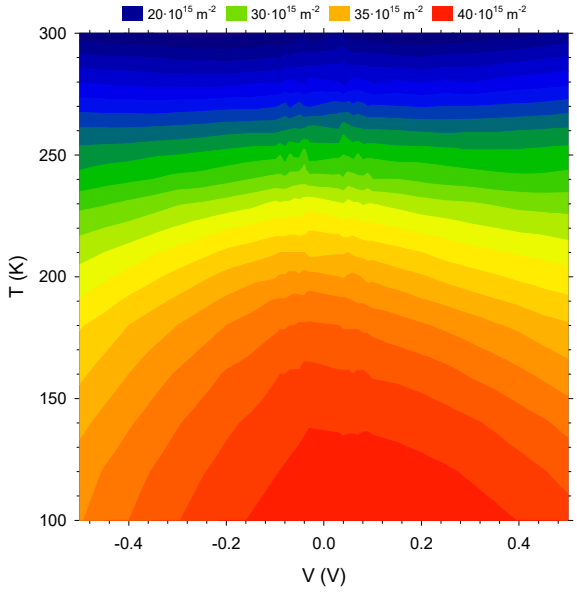

Fig. 4. Surface charge density color map as a function of temperature and applied bias. The lower the temperature the higher the surface charge values.

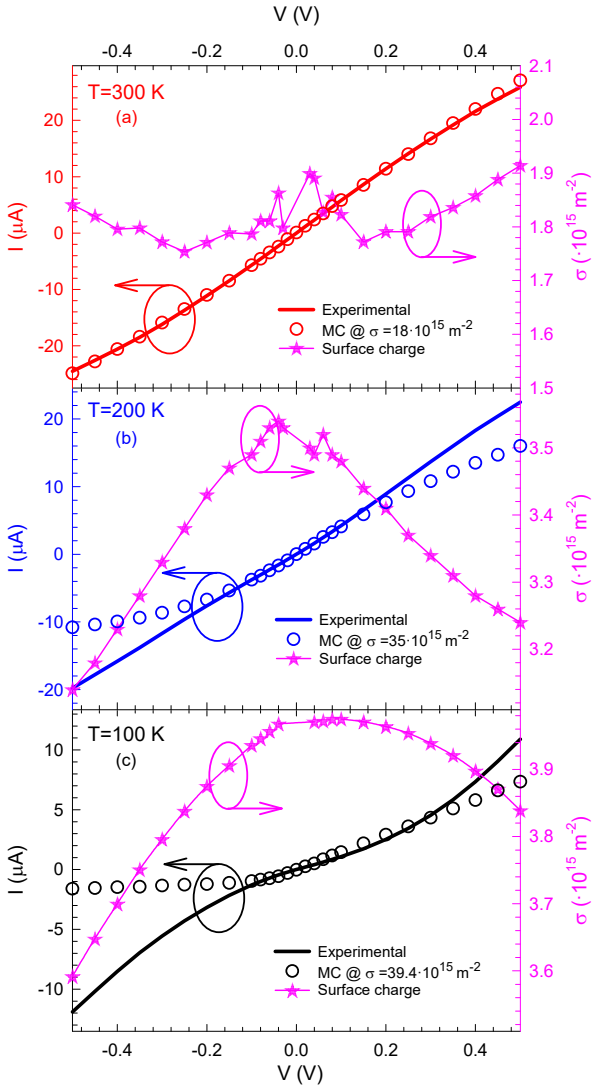

Fig. 3. Comparison of the measured (lines) and MC simulated (circles) *I-V* curves (left axis) for three temperatures (a) 100 K, (b) 200 K and (c) 300 K. Stars (right axis) represent the obtained values of surface charge density as a function of the bias.

References

[1] E. Pérez-Martín, T. González, D. Vaquero, H. Sánchez-Martín, C. Gaquière, V. J. Raposo, J. Mateos and I. Íñiguez-de-la-Torre, Nanotechnology **31**, 405204 (2020).
[2] A. M Cowey, and H. Sorense, IEEE Trans. Microw. Theory Tech. **14**, 588-602 (1966).
[3] A. M. Song, M. Missous, P. Omling, A.R Peaker, L. Samuelson, and W Seifer, Appl. Phys. Lett. **83**, 1881 (2003).
[4] J. Mateos, B. G. Vasallo, D. Pardo, and T. González, Appl. Phys. Lett. **86**, 212103 (2005).

Technological Parameters and Edge Fringing Capacitance in GaN Schottky Barrier Diodes: Monte Carlo Simulations

B. Orfao[1, *], B.G. Vasallo[1], D. Moro-Melgar[2], M. Zaknoune[3], G. Di Gioia[3], M. Samnouni[3], S. Pérez[1], T. González[1] and J. Mateos[1].

[1]Dpto. Física Aplicada, Universidad de Salamanca, Plz. Merced s/n, 37008, Salamanca, Spain.
[2]ACST GmbH, D-63457 Hanau, Germany.
[3]Institut d'Electronique de Microélectronique et de Nanotechnologie, France.
*E-mail: beatrizorfao@usal.es / Phone: +34-923-294500, Ext. 6339

1. Introduction and model

The nonlinearity of the *C-V* characteristic is the key parameter to optimizing the THz performance of the Schottky Barrier Diodes (SBDs) as frequency multipliers [1]. For high-frequency applications, where the anode surface needs to be significantly reduced, the intrinsic capacitance *C* dramatically deviates from its ideal value due to 2D edge fringing effects. The edge capacitance, C_{EE} has been modelled using the parameter β as $C_{EE}= \beta \cdot \varepsilon_{SC}$, where ε_{SC} is the dielectric constant of the semiconductor (8.9 in GaN) [2]. For the calculation of C_{EE} in realistic topologies, a semiclassical ensemble MC simulator of carrier transport self-consistently coupled with a 2-D Poisson solver has been used. The MC simulated structures (Fig. 1) are based in fabricated planar SBDs as those shown in the picture [3]. The layer structure consists of a highly doped substrate with doping $N_S=5\times10^{18}$ cm^{-3} and an epilayer with doping $N_E=3\times10^{17}$ cm^{-3}. The Schottky contact is placed on the top of the epilayer. Simulations with different values of some of the geometrical parameters have been carried out in order to find the optimal configuration to reduce edge effects. Silicon nitride (Si_3N_4), air, SiO_2 and a high-k dielectric, with dielectric constants of 7.5, 1.0, 3.9 and 25.0, respectively, have been considered as passivation dielectrics in the simulations in order to study their influence on the edge effects (EEs). For simplicity, the possible surface charge effects are not taken into account, thus a surface charge density $\sigma=0$ is considered at the semiconductor-dielectric interfaces.

2. Results and conclusions

The total depleted charge per unit length can be expressed as

$$Q(V)=Q_{Ideal}(V)+\beta \cdot \varepsilon_{SC} \cdot (V-V_b) \qquad (1)$$

with $Q_{Ideal}(V)=-L_{sch} \cdot q \cdot N_E \cdot W(V)$, being L_{sch} the size of the Schottky contact, q the electron charge, $W(V)$ the depth of the depletion region and V_b the built-in voltage of the Schottky contact [4]. MC simulations allow us to obtain the depleted charge, Q_{MC}, so that the β parameter is calculated from the slope of $(Q_{MC}-Q_{Ideal})$ vs $(V-V_b)$ (Fig. 2). We have studied how β is affected by the values of several technological parameters. First, related to the passivation dielectric (thickness, W_{diel}, and type of dielectric material), Fig. 3, finding that, as expected, the edge effects increase with W_{diel} and the permittivity of the dielectric. The effect of the epilayer lateral extension, L_{EP} (Fig. 4), is also important. For long enough L_{EP}, β remains almost constant, but when L_{EP} is shorter than given length, β significantly decreases. This geometrical limit depends on the dielectric, the higher the permittivity the higher the value at which L_{EP} starts decreasing. Fig. 5 illustrates the region where edge effects are relevant (red color means change in electron concentration with applied voltage) and how EEs are more pronounced for higher dielectric permittivity. We have also modified the size of the ohmic contact, its separation with the mesa, L_{diel}, and we have eliminated the L_{cap}, β not being affected in either case. Therefore, the optimization of the topology of the SBDs based on these results could be made, also taking into account the restrictions that the technological process imposes to the fabrication of the devices.

References

[1] J. T. Louhi, "The capacitance of a small circular Schottky diode for submillimeter wavelengths," IEEE Microw. Guided Wave Lett., vol. 4, no. 4, pp. 107–108, Apr. 1994.
[2] D. Moro-Melgar, A. Maestrini, J. Treuttel, L. Gatilova, T. González, B. G. Vasallo, and Javier Mateos, "Monte Carlo Study of 2-D Capacitance Fringing Effects in GaAs Planar Schottky Diodes," IEEE Trans. on Electron. Dev., vol. 63, no. 10, pp. 3900-3907, October 2016.
[3] G. Di Gioia, V.K. Chinni, M. Zegaoui, Y. Cordier, A. Maestrini, J. Treuttel, G. Ducournau, Y. Roelens, M. Zaknoune, "GaN Schottky diode for high power THz generation using multiplier principle", 43rd Workshop on Compound Semiconductor Devices and Integrated Circuits, WOCSDICE 2019, Cabourg, France, 2019.
[4] B. Orfao, B. G. Vasallo, D. Moro-Melgar, S. Pérez, J. Mateos and T. González, "Analysis of Surface Charge Effects and Edge Fringing Capacitance in Planar GaAs and GaN Schottky Barrier Diodes" IEEE Trans. on Electron. Dev., vol. 67, no. 9, pp. 3530-3535, Sept. 2020.

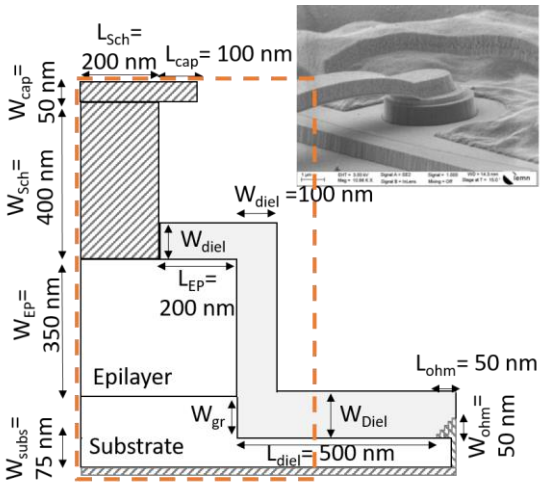

Fig.1. Schematic topology of the 2D MC simulated SBDs. Inset: *Image of a real SBD fabricated at IEMN.*

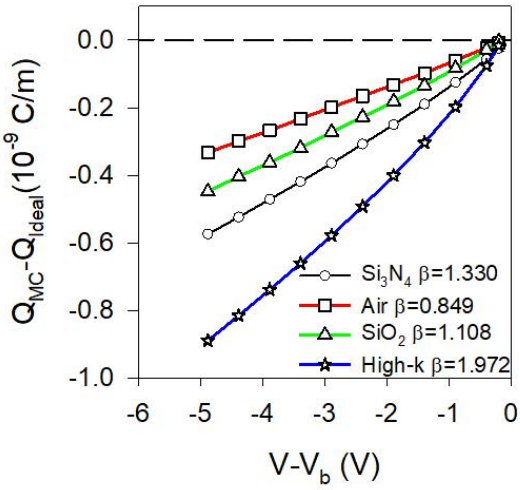

Fig.2. The depleted charge minus the ideal charge (Q_{MC}-Q_{Ideal}) versus V-V_b. The EEs parameter is calculated from the slope of this representation. For the calculation we use certain reverse bias points far from flat-band conditions, where there is a linear behavior.

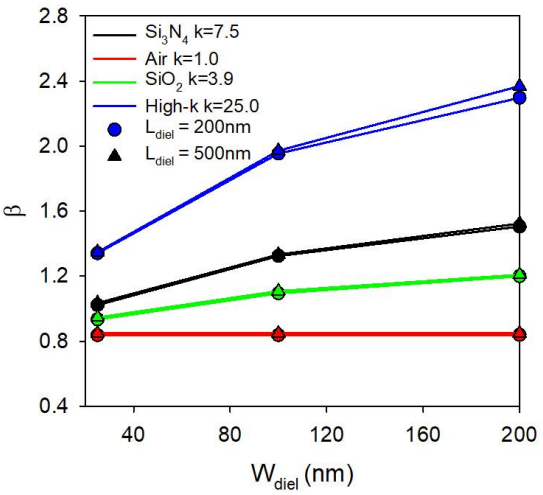

Fig.3. Dependence of the β parameter on W_{diel}, for two values of L_{diel} (200 and 500nm), with different dielectrics as Silicon nitride, (black), air (red), Silicon dioxide (green) and a high-k dielectric (blue).

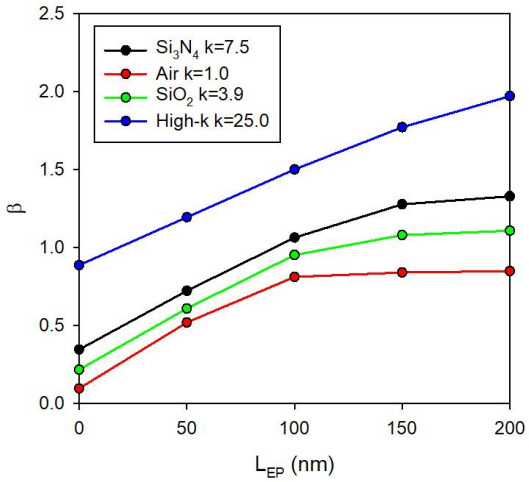

Fig.4. The β parameter calculated for different dielectrics versus L_{EP}.

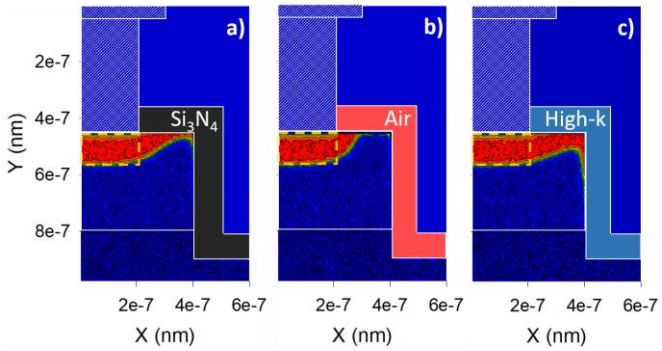

Fig.5. Map of the local contribution to the total capacitance per unit length, calculated as the variation of the electron charge per unit length between flat-band conditions and the bias point -4.0V, divided by the voltage difference, for different dielectric constants: a) silicon nitride, a) air and c) a high-k dielectric. Only the dashed rectangular zone in Fig 1 is represented. The red color represents the region where the electron charge is modified by the bias and the yellow dashed rectangular zone indicates the ideal depletion region, so the EEs region can be visualized.

Towards the experimental demonstration of non-quasi-static effects in graphene field-effect transistors

F. Pasadas[1,*], A. Pacheco-Sanchez[1], A. Mansouri[2,3], P. Kumar[3], G. Calabrese[3], K. Patel[3], A. Zurutuza[4], O. Habibpour[2], H. Zirath[2], R. Sordan[3] and D. Jiménez[1]

[1]Departament d'Enginyeria Electrònica, Escola d'Enginyeria, Universitat Autònoma de Barcelona, 08193 Bellaterra, Spain.
[2]Department of Microtechnology and Nanoscience, Chalmers University of Technology, Gothenburg, Sweden.
[3]L-NESS, Department of Physics, Politecnico di Milano, Via Anzani 42, 22100 Como, Italy.
[4]Graphenea, Avenida de Tolosa 76, 20018 Donostia/San Sebastián, Spain.
[*]email: francisco.pasadas@uab.es

1. Abstract

Taking full advantage of the radio-frequency (RF) performance of graphene field-effect transistors (GFETs) involves operating such devices around their cut-off frequency. In such operating frequency regime, when the transition time of the excitations applied to the device terminals is less than the transit time of carriers traveling from source to drain, the device suffers from significant carrier inertia so that it cannot follow the electrical variations and the so-called non-quasi-static (NQS) effects appear. In this work, we investigated requirements for the experimental demonstration of these effects. This requires a careful design of the experiments given the high frequencies involved. Specifically, we found that the influence of contact resistance could hinder the observation of the NQS effects. We explored this issue to pave the way for the observation of the NQS phenomena.

2. Quasi-static approximation

In the quasi-static (QS) regime, the channel charge is able to follow the voltage variations and serves as a reference to compare against the NQS behavior. The QS regime can be obtained from the equivalent circuit [1] depicted in Fig. 1a, where the small-signal elements are calculated by the previously developed model [2], [3].

3. Non-quasi-static approximation

The NQS effects are modeled by coupling the continuity equation to the transport description [4]. Fig. 1b shows the first-order (1^{st}) NQS equivalent circuit of a GFET, where the small-signal parameters are calculated [4]. In addition, we can numerically compute the NQS (N^{th}-order) or equivalently use the multi-segment approach that consists of breaking down the graphene channel to several sections, each section being short enough to be modeled quasi-statically [4], [5].

4. Results

A prototype GFET is described by the parameters collected in Table I. A thorough explanation about the meaning of the input parameters can be found in Ref. [2]. We have studied the frequency-dependent admittance $y_m=y_{21}-y_{12}$, which is widely used to explore the electrical gate control of the transistor channel over the frequency [6]. We have found that y_m has a zero and two poles in the frequency domain, as shown in Fig. 1c. The zero occurs at a frequency $f_1= g_m/(2\pi(C_{dg}-C_{gd}))$, while the frequency of the poles is proportional to the inverse of the metal-graphene contact resistance (R_c). Figs. 2a-c show the comparison of $|y_m|$ between the QS, 1^{st}-NQS and N^{th}-NQS, for $R_c \cdot W$ = 1, 0.28 and 0.1 kΩ·μm, respectively, where W is the channel width. Figure 2a shows that the three approaches predict the appearance of a pole at a frequency close to the intrinsic cut-off frequency ($f_{T,i}$). Figure 2b shows a particular situation where the specific value of $R_c=R_{c,limit}$ compensates a zero and a pole ($\tau_1=\tau_b$) in the QS case. Below such value ($R_c<R_{c,limit}$), the zero is dominant as shown in Fig. 2c. The upward-going magnitude predicted by the QS model at high frequencies is clearly unrealistic, since it suggests an enhancement in the forward gate-to-drain gain, contrary to the expectation that, at high frequency, electrical control of the gate on the drain current is gradually lost due to the carrier inertia in the graphene channel. A contact resistance $R_c<R_{c,limit}$ is required so the pole exhibited by $|y_m|$ is located at a frequency above $f_{T,i}$ which would allow to distinguish between QS (predicted to give an upward-going $|y_m|$) and NQS behavior (predicted to give a downward-going $|y_m|$). The fulfillment of this condition would help to demonstrate the appearance of the NQS effects in the graphene channel.

Acknowledgements

This work is supported in part by the Spanish Government under the projects TEC2015-67462-C2-1-R and RTI2018-097876-B-C21; by EC H2020 GrapheneCore3 881603; and by the European Regional Development Funds (ERDF) allocated to the Programa Operatiu FEDER de Catalunya 2014-2020, with the support of the Secretaria d'Universitats i Recerca of the Departament d'Empresa i Coneixement of the Generalitat de Catalunya for emerging technology clusters to carry out valorization and transfer of research results. Reference of the GraphCAT project: 001-P-001702.

References

[1] F. Pasadas, et al. DOI: 10.1109/TED.2017.2749503.
[2] F. Pasadas and D. Jiménez. DOI: 10.1109/TED.2016.2570426.
[3] F. Pasadas and D. Jiménez. DOI: 10.1109/TED.2016.2563464.
[4] F. Pasadas and D. Jiménez. DOI: 10.1109/TED.2020.2982840.
[5] Y. Tsividis. ISBN: 0195170148.
[6] M. Bagheri and Y. Tsividis. DOI: 10.1109/T-ED.1985.22284.

L	1 µm	V_{G0}	0 V
W	10 µm	μ	0.2 m²/Vs
C_t	7.97 mF/m²	T	300 K

Table 1. Physical and electrical parameters of the GFET under test. W and L are the graphene channel width and length, respectively; C_t is the geometrical capacitance per unit area of the gate oxide (10-nm thick Al_2O_3). V_{G0} is the offset voltage, μ is the carrier mobility and T is the temperature. A thorough explanation about the meaning of such input parameters can be found in Ref. [2].

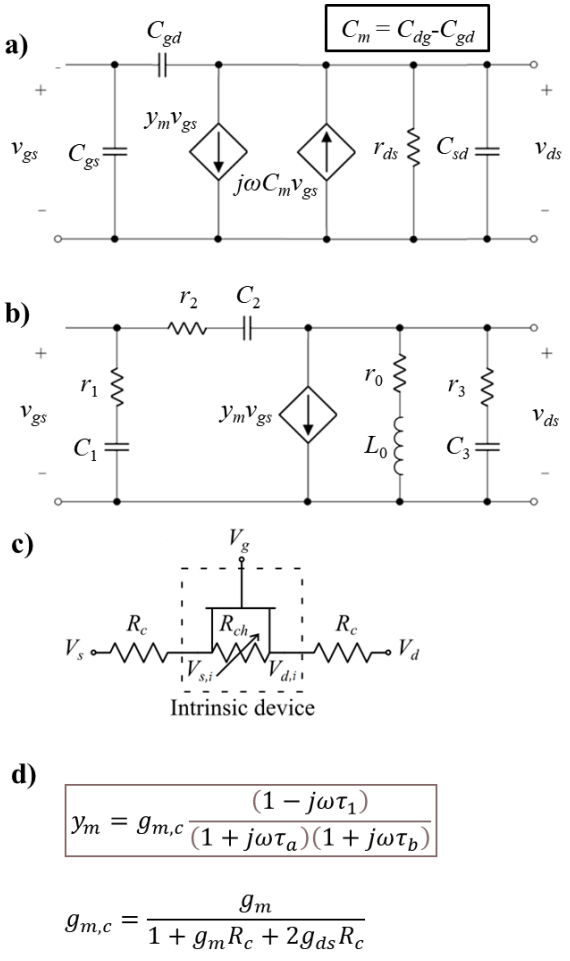

Fig.1. a) Complete charge-based QS intrinsic small-signal model of a GFET [1]. b) First-order NQS intrinsic equivalent circuit of a GFET in common-source configuration by means of lumped elements [4]. c) Schematics of the GFET resistive network. The extrinsic equivalent circuit is formed by an intrinsic description of the device (Figs. 1a-b) and two contact resistances (R_c) connected to the drain and source terminals, respectively. d) Explicit expression of the frequency-dependent admittance y_m=y_{21}-y_{12}. It results in the extrinsic transconductance at zero frequency, $g_{m,c}$, and presents a zero at a frequency f_1=1/(2πτ_1) and two poles at f_a=1/(2πτ_a) and f_b=1/(2πτ_b) that are highly dependent on the contact resistance.

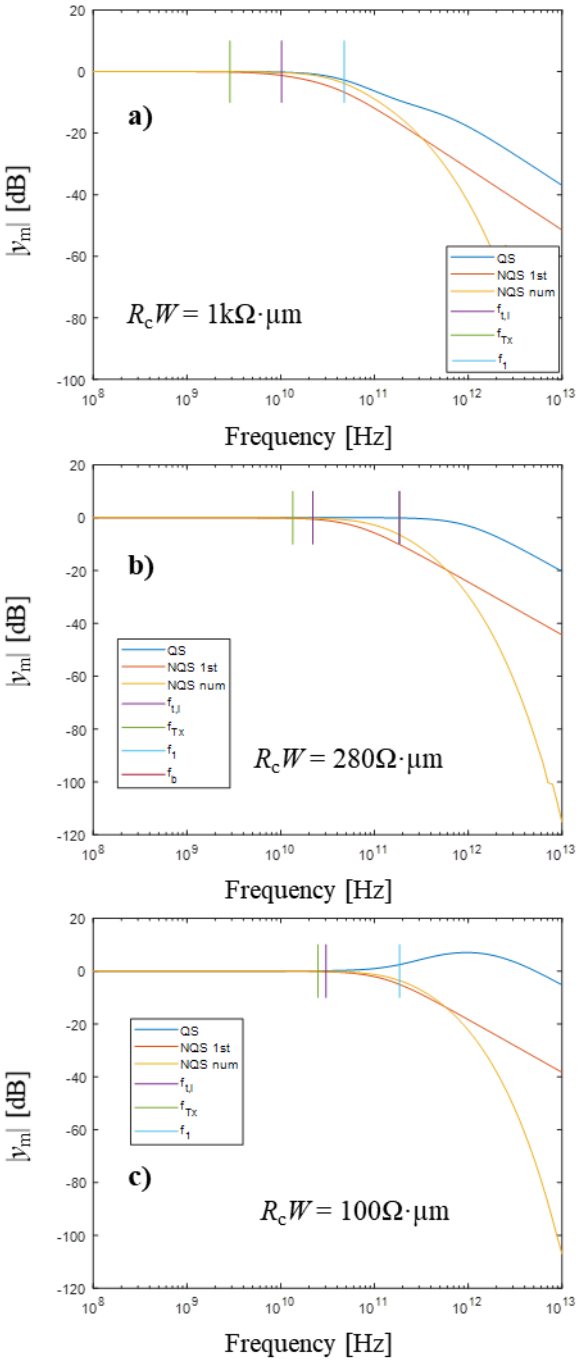

Fig.2. Graph of |y_m| vs. frequency for a contact resistivity of a) 1000; b) 280; and c) 100 Ω·µm. A comparison among the outcomes obtained by the QS (blue solid line), 1st-order NQS (red solid line) and the N^{th}-order NQS (yellow solid line) approaches is provided. The frequencies of interest are depicted by vertical solid lines. The device is biased at $V_{GS,ext}$ = 1.5V and a $V_{DS,ext}$ = 1V. The cut-off frequency is defined as the frequency at which the magnitude of the small-signal current gain (h_{21}=|y_{21}/y_{12}|) of the transistor drops to unity. We distinguish between the intrinsic cut-off frequency, $f_{T,I}$, calculated by neglecting the contact resistances, and the extrinsic cut-off frequency, f_{Tx}, calculated without neglecting the contact resistances. According to our results, the appearance of the NQS effects is linked to the $f_{T,I}$ which deals with the time that carriers take to travel from drain to source which is related to the intrinsic properties of the graphene channel.

Energy Based Analysis of Reset Transition in ReRAM Memristive Devices

M. M. Al Chawa and R. Tetzlaff
Technische Universität Dresden
Dresden, Germany
Email: mohamad_moner.al_chawa@tu-dresden.de

S. G. Stavrinides
School of Science and Technology
International Hellenic University
Thessaloniki, Greece
Email:s.stavrinides@ihu.edu.gr

C. de Benito and R. Picos
Universitat de les Illes Balears
Palma de Mallorca, Spain
Email: rodrigo.picos@uib.es

In this work, an energy-based analysis has been performed for the reset transition of ReRAM memristive devices. We have used a simple memristor model in the Flux-Charge ($\phi - Q$), extending previous work in [1], [2]. We have performed a quasi-static analysis for the reset transition of a bipolar ReRAM memristive device in order to relate the model parameters with a state variable, the temperature. We have considered a voltage ramp input with different slopes, and we have assumed that these ramps are slower than the physical mechanisms inside the memristor. A non-quasi-static model (NQS) could include, as a first approximation, the thermal capacitance that we have ignored, and this approach is currently under study.

In order to show that the proposed model follows the formalism in [3], we have written the corresponding equations side by side in Table I. It is worth mentioning that the POP equation implies that $dT/dt = 0$, so the system presents long term memory, as expected. The model correctly predicts the behaviour of the device, as can seen in Fig. 1, which shows the modeled memconductance (line) versus the experimental data (symbols). Figure 2 shows the modeled energy (lines) versus the one extracted from experimental data. As can be seen, the fitting is also fairly good. Figure 3 shows the effect of the variability on the model, depicting the final energy at the reset point for different cycles and different slopes.

TABLE I: Comparison between the formalism proposed in [3] and the model developed in this paper.

Ref. [3]	Proposed model
$Q = f(\phi, V, \mathbf{X})$	$Q = Q_{rst} \cdot (\frac{\phi}{\phi_{rst}})^n$
$\mathbf{X} = (x_1, x_2, .., x_k)^T$	$\mathbf{X} = T \qquad (T \leq T_{rst})$
$\frac{d\mathbf{X}}{dt} = \mathbf{g}(\phi, V, \mathbf{X})$	$\frac{dT}{dt} = \frac{2 \cdot n^2 \cdot Q_{rst} \cdot \alpha \cdot \theta}{\phi_{rst}^n} \cdot \phi^{n-1} \cdot V$

We have shown the effects of changing the slope on the reset point and model parameters, and introduced a method to estimate the new parameters, assuming that the important parameters are those that describe the process in the $\phi - Q$ space more than those in the $V - I$ domain. In any case, it has been shown that the total energy up to the reset point is dependent on the input ramp, thus strongly hinting at a thermally driven degradation mechanism as with a slower input signal more energy will be dissipated to the ambient.

TABLE II: Mean values and standard deviations of the obtained values for the reset energy and the calculated ones.

Slope	$E_{rst}(mJ)$	
(V/s)	Experimental	(**??**)
0.01	12.46 $\pm$ 0.71	12.33
0.0133	10.27 $\pm$ 0.82	10.11
0.0198	6.88 $\pm$ 1.03	6.71
0.0393	3.55 $\pm$ 0.41	3.47

TABLE III: Comparison between the calculated values for flux, time and, charge, respectively and those extracted from experimental values.

Slope	$\phi_{rst}(V.s)$		$t_{rst}(s)$		$Q_{rst}(mC)$	
	Exp.	Model	Exp.	Model	Exp.	Model
0.01	17.90	19	61.00	61.64	31.55	34.2
0.0133	14.22	14.29	47.10	46.35	25.17	25.71
0.0198	9.13	9.60	30.90	31.13	16.17	16.31
0.0393	5.04	4.83	16.20	15.69	8.45	8.22

Finally, we have found that the Q_{rst} multiplied by the slope of the signal is nearly a constant, as shown in Fig. 4. We have shown that the total accumulated charge is a function of the flux. This concept has also been shown by using different input signal slopes.

References

[1] M. M. Al Chawa, R. Picos, J. B. Roldan, F. Jimenez-Molinos, M. A. Villena, and C. de Benito, "Exploring resistive switching-based memristors in the charge–flux domain: a modeling approach," *International Journal of Circuit Theory and Applications*.

[2] M. M. Al Chawa and R. Picos, "A simple quasi-static compact model of bipolar reram memristive devices," *IEEE Transactions on Circuits and Systems II: Express Briefs*, 2019.

[3] F. Corinto, P. P. Civalleri, and L. O. Chua, "A theoretical approach to memristor devices," *IEEE Journal on Emerging and Selected Topics in Circuits and Systems*, vol. 5, no. 2, pp. 123–132, 2015.

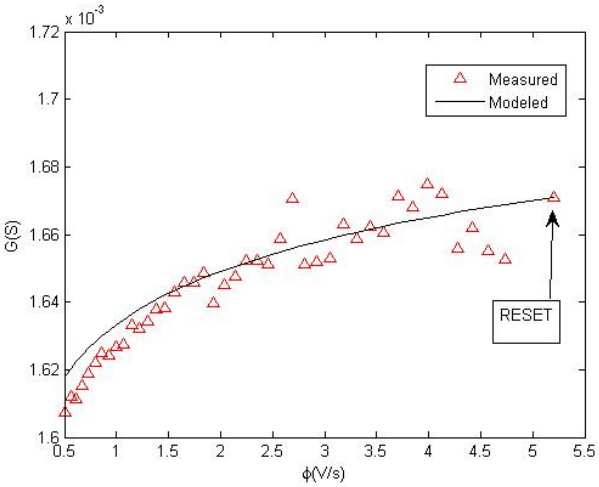

Fig. 1: Experimental (symbols) and modeled (line) conductance up to the reset point vs. voltage for a single cycle.

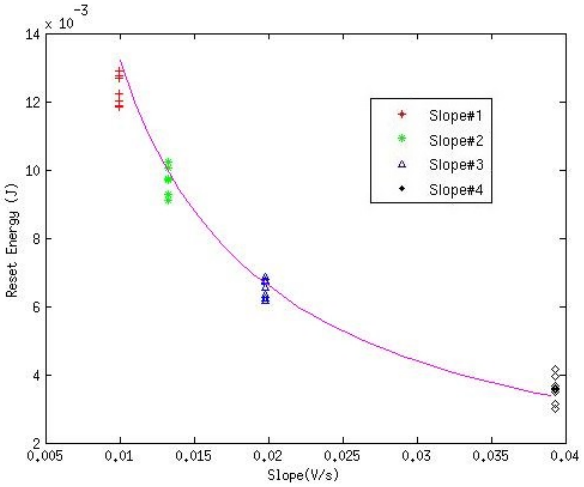

Fig. 3: Effect of changing the slope on the reset energy. Points correspond to data extracted from measurement with different slopes, while line shows the model.

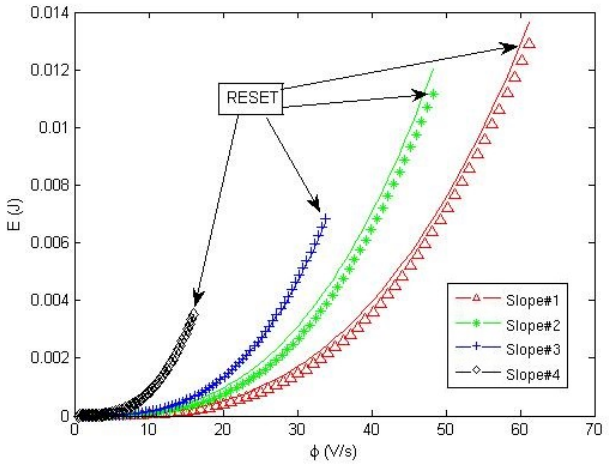

Fig. 2: Experimental energy (symbols) and model (continuous lines) vs. flux up to the reset point for different operating slopes.

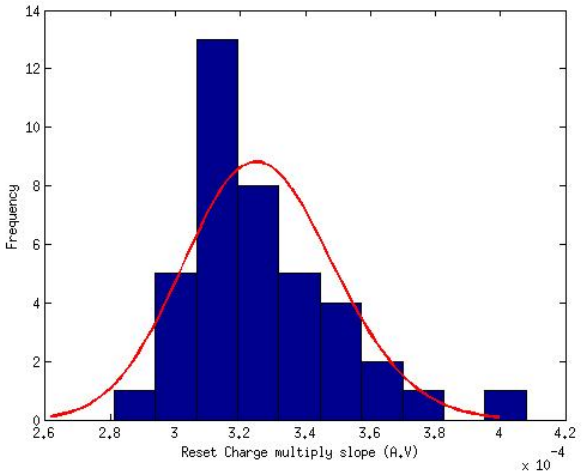

Fig. 4: Histogram of the product $Q_{rst} \cdot S$. The line is to $Beta\ distribution$ with mode 308μW and median 328μW.

In-depth Analysis of the Statistical Distribution of RRAM Electrical Parameters Intended for Compact Modeling

E. Salvador[1], M.B. Gonzalez[2], F. Campabadal[2], J. Martin-Martinez[1], R. Rodriguez[1], E. Miranda[1]

[1]Departament d'Enginyeria Electrònica, Universitat Autònoma de Barcelona, 08193 Cerdanyola del Valles, Spain.
[2]Institut de Microelectrònica de Barcelona, IMB-CNM, CSIC, 08193 Cerdanyola del Valles, Spain
E-mail address of corresponding author: emili.salvador@uab.cat

Abstract

This work deals with the incorporation of uncorrelated cycle-to-cycle (C2C) variability in the LTSpice memdiode model for RRAM devices. Variability in the *I-V* curves is addressed through an in-depth statistical characterization of the experimental data using the *fitdistribplus* package for the R language. The best candidate distributions for the most significant model parameters are included in the model script and used for performing Monte Carlo simulations.

1.Introduction

RRAMs are two terminal devices with a non-volatile switching resistance that are currently considered not only for memory arrays but also for a wide range of applications including neuromorphic computing, logic gates, etc. Nevertheless, one of the major drawbacks that faces this technology concerns with its inherent variability, which is associated with the formation and destruction of the filamentary conducting structure at atomic scale [1]. Since variability is at the heart of RRAM operation, inclusion of this phenomenon in any compact model intended for circuit simulation environments is of utmost importance. In this work, the introduction of uncorrelated C2C variability in the quasi-static memdiode model (QMM) [2] is explored. Importantly, uncorrelated C2C does not mean that the parameter estimators can be independently chosen. Since the *I-V* curve is evolutionarily generated by the input signal, there is a connection among the average and dispersion values of the model parameters called at each section of the *I-V* curve that must be addressed first in order to obtain realistic SPICE simulations.

2. Devices and experimental results

HfO_2-based MIM structures were investigated in this work. The oxide thickness is 10nm and the area of the devices 5x5μm^2. The bottom electrode is a 200nm-thick W layer and the top electrode is a 200nm-thick TiN layer on top of a 10nm-thick Ti layer acting as oxygen getter material [3]. Simulations are compared with experimental data obtained from 450 voltage sweeps. The complete set of experimental *I-V* curves and the median curve are shown in Fig. 1.a. High (I_{HRS}) and low (I_{LRS}) resistance state currents are extracted at V=0.2V. The snapback (SB) correction is calculated as $V_{SB} = V_{applied} - R_i \cdot I_{measured}$, where R_i is the SB series resistance. R_i is chosen so as to achieve a current increase at a constant transition voltage V_T (see Fig. 1.b) [4]. This correction is carried out for every cycle. The RESET voltage V_R is the voltage corresponding to the maximum current reached at negative bias and the SB current I_{SB} is found from the last data point before the occurrence of the SET jump. The extracted parameters for the whole set of curves were analyzed using the *fitdistrplus* package for the R language [5]. The Cullen and Frey skewness-kurtosis (SK) graph (Pearson plot) is used first as an indicator of the suitability of the different distributions available (normal, lognormal, gamma, Weibull, logistic). Notice the location of the observation (blue dot) with respect to the theoretical symbols and lines. Goodness of fit and criteria in combination with quantile-quantile (Q-Q) plots were used to determine the best candidate distribution. As examples, Tables 1.a and 1.b show the goodness of fit and criteria for V_T and V_R. Figs. 2 and 3 show the SK graphs and Q-Q plots for all the parameters analyzed: a) V_T, b) V_R, c) R_i, d) I_{SB}, e) I_{HRS}, f) I_{LRS}. The rest of the parameters, V_T, I_{HRS} and I_{LRS} follow a lognormal distribution while V_R and I_{SB} are better described by a normal one and R_i by a logistic one.

3. QMM with variability

Once the model parameter distributions are established, they are included in the header of the model script (not shown here). The *rand* and *gauss* functions in LTSpice and their transformations are used to generate the appropriate parameter values. In Fig. 4, experimental and simulated curves are compared. It is shown that simulations reproduce the main features of the experimental *I-V* curves.

References

[1] A. Chen and M. R. Lin, *IEEE Int. Reliab. Phys. Symp. Proc.*, pp. 843–846, 2011.
[2] E. Miranda, IEEE TNano, vol. 14, 787-789 , 2015.
[3] S. Poblador, M. B. Gonzalez, and F. Campabadal, *Microelectron. Eng.*, vol. 187–188, pp.148–153, 2018
[4] V. Karpov, D. Niraula, and I. Karpov, *Appl. Phys. Lett.*, vol. 109, no. 9, pp.1–5, 2016.
[5] M. L. Delignette-Muller and C. Dutang, *J. Stat. Softw.*, vol. 64, no. 4, pp.1–34, 2015.

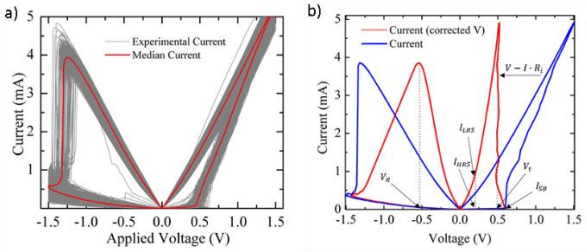

***Figure 1**: a) Experimental I-V curves: 450 cycles and median curve. b) Voltage correction to see the snapback effect in a single cycle and parameter specification.*

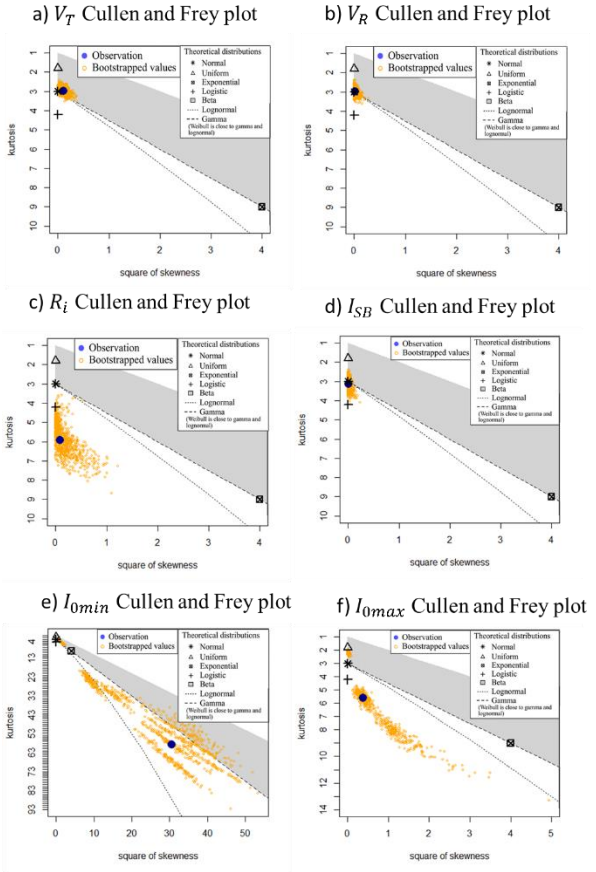

***Figure 2.** Show the Cullen and Frey SK plots for all the studied parameters: a) V_T, b) V_R, c) R_i, d) I_{SB}, e) I_{HRS}, f) I_{LRS}*

a)

	Method	Normal	Lognormal	Gamma	Weibull
Stat.	K-S	0.0375	**0.0295**	0.0298	0.0856
	C-vM	0.1289	**0.0576**	0.0696	0.9333
	A-D	0.9495	**0.3944**	0.5076	6.343
Cri.	AIC	-1654.55	**-1662.72**	-1661.04	-1585.18
	BIC	-1646.34	**-1654.501**	-1652.82	-1576.96

b).

	Method	Normal	Lognormal	Gamma	Weibull
Stat.	K-S	**0.0275**	0.0449	0.0393	0.046
	C-vM	**0.045**	0.1709	0.1149	0.2497
	A-D	**0.2707**	1.043	0.6944	1.858
Cri.	AIC	**-1500.53**	-1487.75	-1493.46	-1480.1
	BIC	**-1492.32**	-1479.532	-1485.25	-1471.89

***Table 1 :** Goodness-of-fit statistics (Kolmogorov-Smirnov, Cramer-von Mises, Anderson-Darling) and criteria (Akaike's and Bayesian) for a) V_T, b) for V_R.*

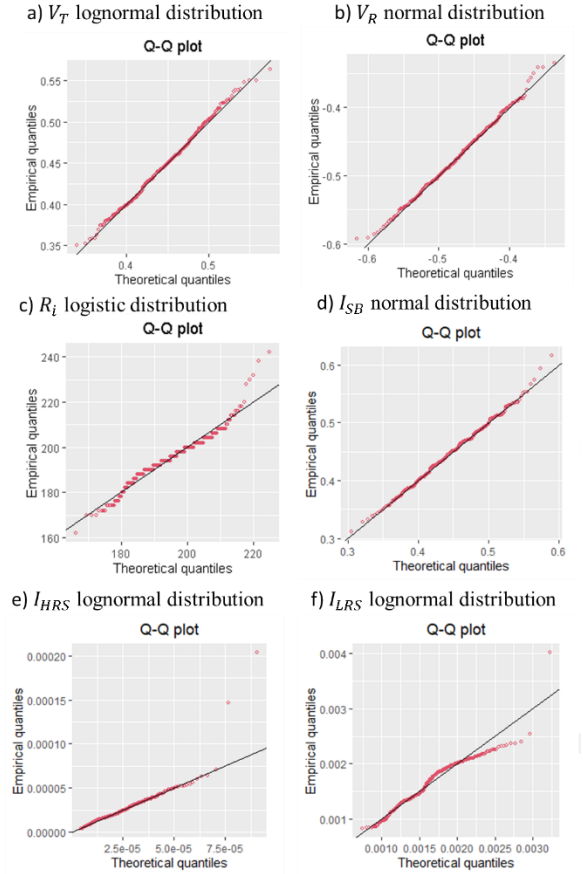

***Figure 3.** Show the Q-Q plots for all the studied parameters: a) V_T, b) V_R, c) R_i, d) I_{SB}, e) I_{HRS}, f) I_{LRS}*

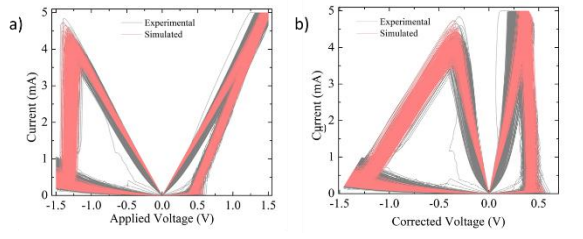

***Figure 4.** Experimental and simulated curves comparison. a) I-V curves and b) I-V curves applying the SB voltage correction.*

11 June 2021

Friday

ORAL SESSION IV

Sensors, actuators and biomedical devices

Friday 11

9:45-11:00

Chairperson: C. Aracil (Universidad de Sevilla)

Paper-based wearable patch for sweat biomonitoring

Meritxell Rovira[1], César Fernández-Sánchez[1], Silvia Demuru[2], Brince Paul Kunnel[2], Danick Briand[2] and Cecilia Jimenez-Jorquera[1]

[1] Instituto de Microelectrónica de Barcelona (IMB-CNM), CSIC, Campus UAB, Bellaterra, Spain,
[2] École Polytechnique Fédérale de Lausanne (EPFL), Switzerland
*Cecilia Jimenez: e-mail: cecilia.jimenez@csic.es; Meritxell Rovira: e-mail: meritxell.rovira@csic.es

1. Abstract

This abstract reports the development and characterization of a wearable sweat biomonitoring patch suitable for continuous assessment of the physiological state of individuals during the practice of exercise. Results demonstrate the feasibility of paper-based microfluidics and pH, sodium, and potassium ion selective field effect transistors (ISFETs) under continuous monitoring.

2. Introduction

During exercise performance, sweating leads to the loss of water and electrolytes due to thermoregulatory action. The monitoring of this electrolyte imbalance would enable personalized diagnosis and would help to prevent pathologies related to dehydration.[1] Several attempts have been reported in the last decade to achieve compact, affordable, and wearable platforms for healthcare and sport activities real-time monitoring. [2]
This work reports the development and evaluation of a wearable patch for monitoring biomarkers in sweat during the practice of exercise. The platform includes paper-based microfluidics to collect and drive sweat samples to an array of silicon solid-state sensors packaged on a flexible patch-like substrate.
Paper-based microfluidics enable working with the low sweat rates produced by an individual during exercise. Besides, microfabricated sensors allow integration with various interfacing electronic readouts being CMOS-compatible.

3. Experimental

A patch of 2,5 cm x 5 cm containing a microfluidic structure and an array of sensors has been designed and tested (Fig. 1a). The flexible substrate is made of polyimide (Kapton®) and includes the required electrical tracks for sensor connection to the electronics.
Sensors include ISFETs for pH, Na^+ and K^+ determination and two thin film microelectrodes (TFM) for conductivity and reference electrodes. The platinum reference electrode was coated with Ag/AgCl ink to perform as a quasi-reference electrode.
To fix and align the sensors and the paper, laminated materials like polymethyl methacrylate (PMMA) and silicone-based adhesive are used. Whatman® Grade 1 paper was used for microfluidics.
The synthetic sweat was prepared as described in [3].

4. Results and Discussion

The performance of the different sensors has been studied. ISFETs showed almost Nernstian sensitivities (average sensitivity of 55,5 mV dec^{-1}) in the range of concentrations of the ions in sweat (pH 4-8, 1-100 mM for Na^+, and 3-21 mM for K^+). They also demonstrated good sensitivities (average sensitivity of 51,0 mV dec^{-1}) in a synthetic sweat solution. Other parameters such as the matrix effect, the repeatability for consecutive calibrations (average standard deviation of 1,3 mV/dec in triplicates (n=13)) and the long-term stability (average standard deviation of 8 mV/dec in 46 days (n=13)) were also studied for Na^+ ISFETs to complete the model of the sensor's response.
The average time for a solution to reach the sensors through the microfluidic channels at the flow rate of real sweat (1,5 µL min^{-1} cm^{-2}) was about 15 min. Using this microfluidic design, Na^+ ISFETs responded dynamically to changes in concentration with sensitivities of 54,9 (1,6) mV dec^{-1} (n=3). In the case of artificial sweat, they showed sensitivities of 50,9 (8,3) mV dec^{-1} (n=3) (Fig. 1b).

5. Acknowledgements

This work is performed in the frame of the WeCare project (SNSF, Switzerland).

References

[1] R. A. Neal, H. C. Massey, M. J. Tipton, J. S. Young, J. Corbett, Front. Physiol. 2016, 7, 564.
[2] Mallika Bariya, Hnin Yin Yin Nyein, and Ali Javey, Bull. Nat. Electron. 2018, 1, 160-171.
[3] C.J. Harvey, Ryan F. LeBouf, Aleksandr B. Stefaniak, Toxicol. in Vitro 2010, 24, 1790–1796.

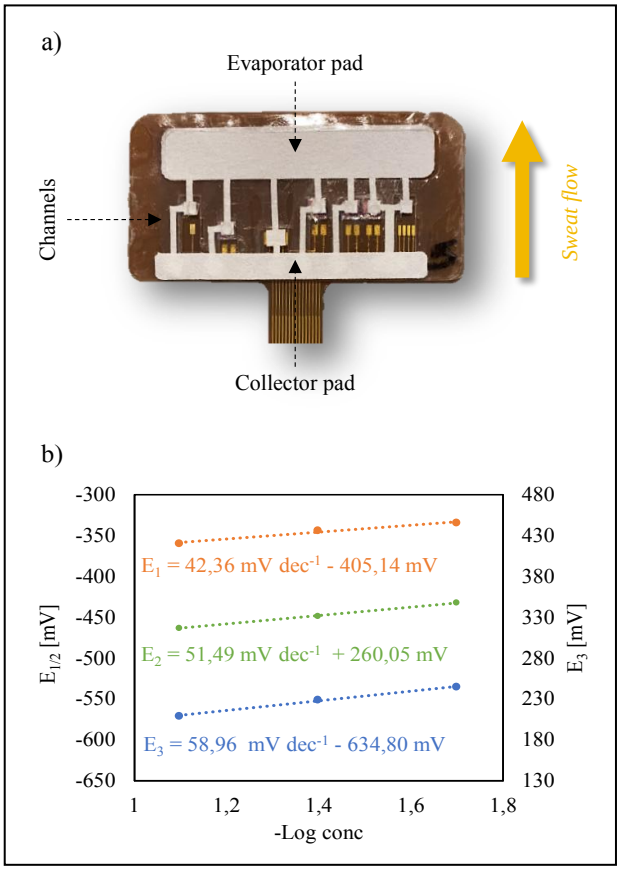

Fig.1. a, Wearable patch with sensors and microfluidics structure. **b,** Response of three Na ISFETs placed in the same patch with increasing concentrations of Na^+ in a synthetic sweat solution.

Detection of cytokines in skeletal muscle tissue using optical SPR sensing platform

Víctor Parra-Monreal[1], María A. Ortega-Machuca[1], Javier Ramón-Azcon[1], Winnie Svendsen[2], Albert Romano-Rodríguez[3], Mauricio Moreno-Sereno[3]

[1] Biosensors for Bioengineering Group. Institute for Bioengineering of Catalonia (IBEC), c/ Baldiri Reixac, 10-12, E-08028 Barcelona, Spain
[2] Bioengineering Department, Technical University of Denmark (DTU), Søltofts Plads, Building 221, DK-2800 Kongens Lyngby, Denmark
[3] Department of Electronics and Biomedical Engineering, University of Barcelona (UB), c/ Martí i Franquès 1, E-08028 Barcelona, Spain.

1. Abstract

In this work we have explored the use of a Surface Plasmon resonance (SPR) phenomenon for the detection of interleukin-6 (IL-6), a pro-inflammatory cytokine. It plays an important role in the muscle tissues, having direct relation with muscle contraction and, thus, it is considered a biomarker for some types of muscular dystrophies. Here we show that SPR can be used as a real-time monitoring of the shift of the reflectance dip of a gold diffraction grating in front to the antibody adhesion to Au.

2. Surface Plasmon Resonance

Plasmonic devices are based in light-matter interactions on metal-dielectric interfaces. For specific wavelengths, the interaction of the light with metals surfaces induces a collective oscillation of the free electrons of the metals, known as surface plasmon resonance (SPR). SPR-based sensing has shown great capability to detect all kind of molecular biomarkers as proteins, peptides, mRNA, DNA, etc. In this work, the Plasmon Resonance is excited in the gold layer thanks to the fabrication of a diffraction grating in gold layer [1], giving rise to resonance for visible light.

3. Materials and Methods

Optical sensor. The dielectric part of the sensor is a 100nm silicon nitride (Si_3N_4) layer over a 500mm thermal silicon oxide (SiO_2) on silicon substrate. Several diffraction gratings with subwavelength period have been fabricated in the Si_3N_4 layer using e-beam lithography and 20nm Reactive Ion-Etching. Finally, Cr/AU 5/45nm was deposited on top by electron-beam evaporation. Figure 1 shows the PDMS-encapsulated chip.

Functionalization of the gold surface was done by immersion in an alcoholic solution (18h) of Mercaptoundecanoic acid (MUA) to obtain an effective self-assembled monolayer (SAM). The SAM was activated by EDC/NHS reaction to obtain a covalent bond of the antibody. A Purified Rat Anti-Mouse IL-6 (BDPharmigen™) is the antibody used for a selective detection of the IL-6 protein.

Spectral interrogation has been used for characterization of reflectivity. Figure 2 is a scheme of the optical set-up. White light is focused in a fiber optics, and the light is collimated and divided with a beam-splitter (50%-50%), being one of the beams TM polarized and focused using a 4x objective. the light from the objective is focused in another fiber towards the spectrometer. The reflected spectrum is normalized to a reference spectrum in a flat area. Figure 3 is an example of the resonance reflectance dip.

4. Results and discussion

With reference liquids (water, ethanol, etc.), the measured bulk sensitivity of the SPR grating sensors is S=350nm/RIU and S=270nm/RIU for a grating period of Λ=500nm and Λ=400nm, respectively. Figure 4 shows the antibody (Ab) kinetics and saturation for two concentrations of 5 and 10 µg/mL. After this, a preliminary study with two IL-6 concentrations allowed observing the different interactions between proteins and antibodies: 1ng/mL (normal value when the muscle tissue is stimulated) and 10ng/mL (over-stimulation).

A full study will be presented to prove the feasibility of this technique and to discuss its limitation for IL6 detection.

References

[1] I. Abdulhalim, M. Zourob, and A. Lakhtakia, "Surface plasmon resonance for biosensing: a mini-review," Electromagnetics, vol. 28, no. 3, pp. 214–242, 2008.

[2] J. C. Love, L. A. Estroff, J. K. Kriebel, R. G. Nuzzo, and G. M. Whitesides, "Self-assembled monolayers of thiolates on metals as a form of nanotechnology," Chemical reviews, vol. 105, no. 4, pp. 1103–1170, 2005.

Fig.1 Photograph of the optical sensor (1.5cmx1.5cm). The grating area is 500µmx500µm. PDMS container and lid is also shown.

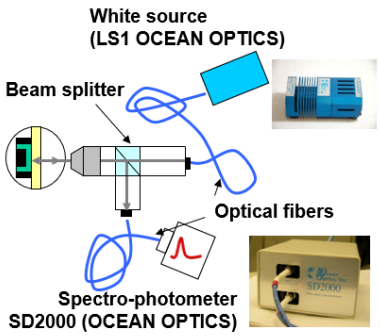

Fig.2: Schematic optical set-up, employing a LS-1 Optical source and SD2000 spectrometer from Ocean Optics.

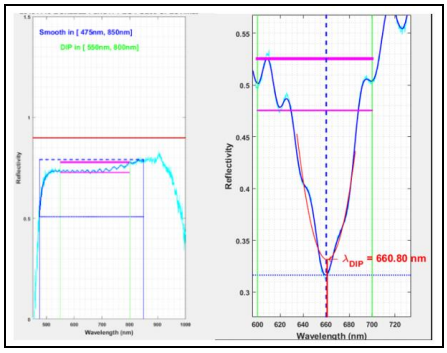

Fig. 3: Normalized reflectivity in a flat zone (left) and dip in a grating zone (right)

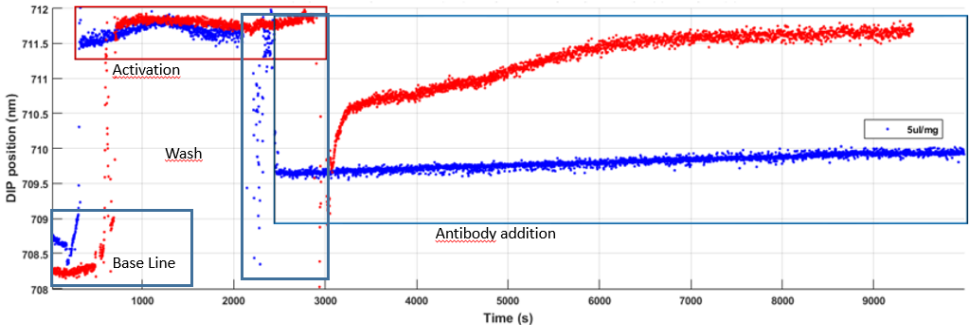

Fig. 4: SPR Measurements: Antibody Kinetics and Saturation
Blue: Ab 5 µg/mL Red: Ab 10 µg/mL

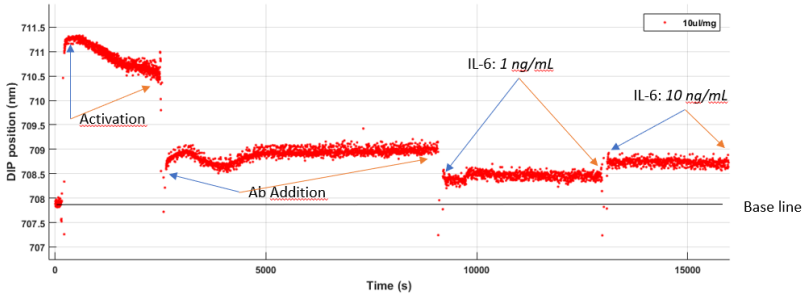

Fig. 5: SPR Measurements: IL-6 Samples

Study of magnetoelastic resonance for chemical sensors: Ribbons vs microwires

Álvaro Peña[1], Daniel Matatagui[2], Carlos Cruz[2], Patricia de la Presa[1], Pilar Marín[1, *], Carmen Horrillo[2, *]

[1] Instituto de Magnetismo Aplicado, Universidad Complutense de Madrid, Spain;
alvapena@ucm.es (A.P.); pmpresa@ucm.es (P.P.) mpmarin@ucm.es (P.M., *corresponding author)
[2] Instituto de Tecnologías Físicas y de la Información, Consejo Superior de Investigaciones Científicas, Spain;
carlos.cruz@csic.es (C.C.); d.m@csic.es (D.M.); carmen.horrillo.guemes@csic.es (C.H., *corresponding author)

1. Abstract

In this work, the magnetoelastic resonance behaviour has been studied in amorphous metallic ribbons and microwires using a custom-made setup. First, optimal setup conditions were determined for both materials, then the frequency shift dependence on polymer mass deposition was studied. Both materials show a predictable response to the mass deposition of the polymer tested, making them suitable for contactless chemical sensors.

2. Introduction

Magnetoelastic resonators allow for contactless sensing [1]–[3]. When a mass (Δm) is uniformly applied on the resonator of mass m_0, the resonant frequency f_0 shifts according to [2]:

$$\frac{\Delta f}{f_0} = -\frac{\Delta m}{2m_0} \qquad (1)$$

From Eq. (1) geometrical parameters are not relevant for this effect, however, microwires having higher f_0 would be better suited for sensing applications.

Polyepichlorohydrin (PECH) was used as a coating due to its sensitive capabilities[4].

3. Experimental

In this work two magnetoelastic materials have been studied i.e.: 37*6.6*0.02 mm amorphous magnetoelastic ribbons of composition $Fe_{40}Ni_{38}Mo_4B_{18}$ (Metglass 2826 MB) and 1cm long microwires with an amorphous metallic core of $Fe_{73}Si_{11}B_{13}Nb_3$, 67±1 µm in diameter, and a Pyrex shell 90±3 µm in diameter, as seen in figure 1.

The magnetoelastic resonance behaviour was characterized using a custom-made setup (figure 2). The system consists of a pick-up coil in which the ribbon or microwire is placed, the coil is fed with AC power through a Red Pitaya system controlled with LabView-based data acquisition software. The accuracy of the measurement can be adjusted by indicating the desired frequency range and the total number of samples in the acquisition. In doing this, high accuracies in steps of 1 Hz can be obtained for a specific frequency range.

In addition, Helmholtz coils are connected to a DC power source, which creates a steady uniform magnetic field around the pick-up coil. It is used as a bias field for the magnetoelastic material.

This system allows detection of vibrations through changes of the magnetic susceptibility, described in the Villari effect, obtaining the output signal amplitude versus frequency.

Ribbons and microwires were dip-coated on a PECH/acetone solution of 12mg/ml up to two times. Magnetoelastic resonance was measured for each coating.

4. Results

Figure 3 a) and b) show the dependence of the resonance frequency and its amplitude on the bias field for ribbon and microwire, respectively. This dependence is due to the ΔE effect [3]. as figure 3 shows, there is an optimal bias field where the signal amplitude is maximum. These fields, of 0.25-0.75mT for ribbons and 0.75-1.25mT for microwires, particularly 0.73 and 0.86mT as shown in figure 3 c) and d) for ribbons and microwires respectively, thus, these fields are used for the mass deposition measurements.

Plus, microwires show a lineal ΔE effect as opposed to the ribbons in this range, which suggests microwires also allow applied magnetic field sensing.

Figure 4 shows the resonance frequency shift and its amplitude for each coating. Both materials respond to the mass variance with a frequency shift as expected by equation 1. Furthermore, only a slight decrease in the resonance amplitude was observed. Thus, this finding indicates that both materials are suited for magnetoelastic based sensors.

5. Conclusions

Microwires were proven as a viable mass sensor, future work aims to test the sensors under toxic gas exposure.

References

[1] P. Marín, M. Marcos, and A. Hernando, "High magnetomechanical coupling on magnetic microwire for sensors with biological applications," *Appl. Phys. Lett.*, vol. 96, no. 26, pp. 11–14, 2010.

[2] C. A. Grimes *et al.*, "Wireless magnetoelastic resonance sensors: A critical review," *Sensors*, vol. 2, no. 7, pp. 294–313, 2002.

[3] J. D. Livingston, "Magnetomechanical properties of amorphous metals," *Phys. Status Solidi*, vol. 70, no. 2, pp. 591–596, 1982.

[4] D. Matatagui *et al.*, "Love-wave sensor array to detect, discriminate and classify chemical warfare agent simulants," *Sensors Actuators, B Chem.*, vol. 175, pp. 173–178, 2012.

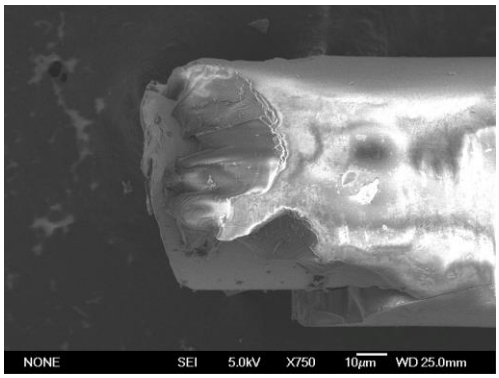

Fig. 1. *$Fe_{73}Si_{11}B_{13}Nb_3$ microwire seen under a scanning electron microscope.*

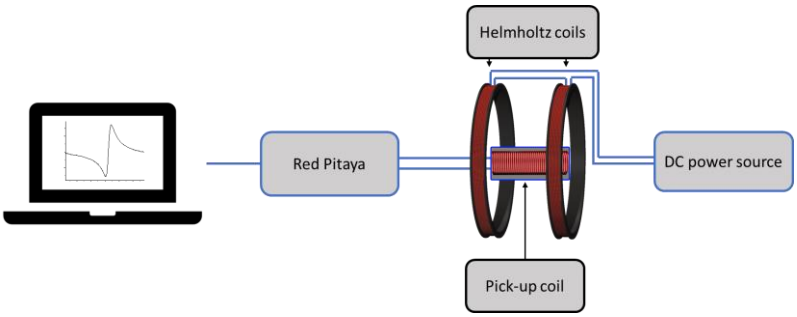

Fig. 2*. Experimental setup for magnetoelastic resonance measures*

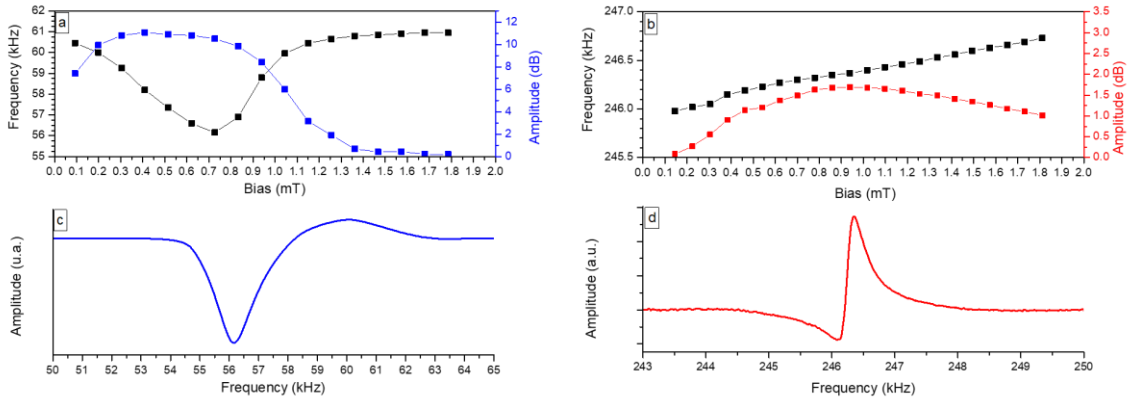

Fig. 3*. The magnetoelastic resonance frequency and its amplitude dependence on bias field for a) ribbons and b) microwires; Magnetoelastic resonance for c) a ribbon under 0.73mT and d) a microwire under 0.86mT bias field.*

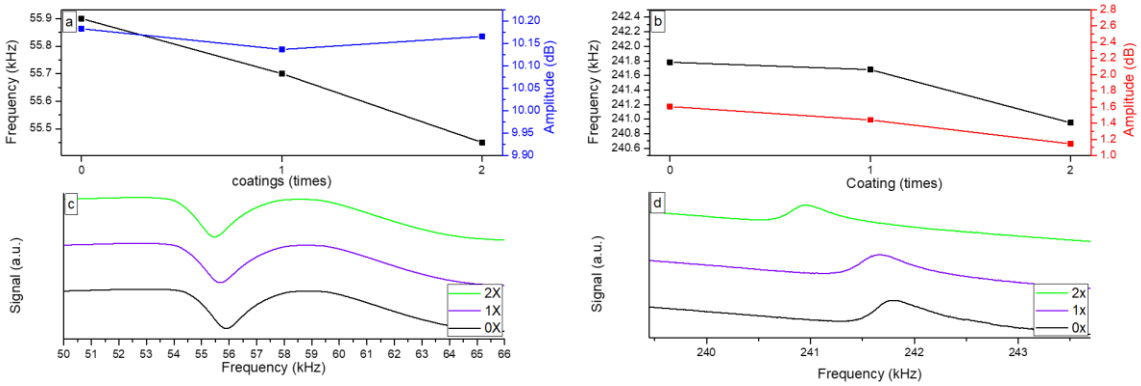

Fig. 4. *The magnetoelastic resonance frequency and its amplitude dependence on repeated coatings for a) ribbons and b) microwires; Magnetoelastic resonance for a clean (0x), dip-coated once (1x) and twice (2x) c) ribbon and d) microwire.*

Resistive gas sensors based on MoS_2 nanosheets with high response to low NO_2 concentrations

I. Sayago[1], C. Sánchez-Vicente[1], J.L. Sanjurjo[1], J.P. Santos[1], S.P. Ogilvie[2], H.J. Wood[2], A. Amorim Graf[2], M.J. Large[2], A.B. Dalton[2], R. Garriga[3] and E. Muñoz[4]

[1]Institute for Physical and Information Technologies (CSIC), 28006 Madrid, Spain
[2] University of Sussex, Brighton BN1 9RH, UK
[3] Departamento de Química-Física, Universidad de Zaragoza, 50009 Zaragoza, Spain
[4] Instituto de Carboquímica ICB-CSIC, Miguel Luesma Castán 4, 50018 Zaragoza, Spain

1. Abstract

This work reports on two-dimensional MoS_2 nanomaterial-based resistive gas sensors and their response to sub-ppm NO_2 concentrations. The sensitive material was prepared by drop-casting MoS_2 nanosheet dispersions on silicon substrates. Morphological characteristics of the fabricated thin films of MoS_2 nanosheets were analyzed by scanning electron microscopy (SEM). The fabricated sensors provided good responses to NO_2 concentrations as low as 50 ppb at room temperature.

2. Introduction

The use of nanomaterials has proven to be a convenient strategy to minimize the lack of sensitivity, selectivity and stability of gas sensors. Recently, two-dimensional (2D) materials such as graphene and transition metal dichalcogenides (MoS_2, TiS_2, WS_2, $MoSe_2$, etc.) have attracted interest due to their highly favorable properties for gas sensing applications [1,2]. Among these materials, MoS_2 is the most promising one due to its high surface-to-volume ratio, high adsorption coefficient and thickness-dependent electrical/chemical properties [3]. In this work, we report on the response to low NO_2 concentrations of a resistive-type gas sensor based on thin films of MoS_2 nanosheet assemblies.

3. Experimental

MoS_2 nanosheet dispersions were prepared by high-pressure homogenization of a mixture of MoS_2 powder and a solution of Triton X-100 in deionized water (4 $g \cdot L^{-1}$). Thin films of MoS_2 nanosheets were deposited onto micromachined silicon substrates with integrated heaters by drop-casting.

Prior to the detection processes, the sensors were annealed at 350 ºC for 4 h in an air atmosphere to remove surfactant traces, stabilize the sensing properties of the nanostructures, and improve their response.

Detections were carried out in synthetic air at different temperatures (25, 100 and 300 ºC), with a constant gas flow of 100 $mL \cdot min^{-1}$. NO_2 concentrations were varied from 50 to 2000 ppb and the exposure time was 15 min.

4. Results and discussions

SEM imaging of the fabricated sensor films reveals that MoS_2 flakes are assembled forming porous morphologies (Fig. 1).

The tested sensors are sensitive to NO_2 with high responses even at low temperatures. The best responses were obtained at moderate temperatures ($T \geq 200$ ºC) (Fig. 2). MoS_2 sensors present an n-type gas detection response, increasing its resistance upon exposure to oxidizing gases such as NO_2 (Fig. 3). The presence of active edge-sites in MoS_2 may enhance the gas and carrier exchange and transport, therefore contributing to improved detection performance. Previous works have shown that the edge sites of MoS_2 are highly chemical active over the inert MoS_2 basal planes [4].

References

[1] G. Neri, "Thin 2D: the new dimensionality in gas sensing", Chemosensors 5 (3), 2017, 21

[2] Choi, SJ., Kim, ID, "Recent Developments in 2D Nanomaterials for Chemiresistive-Type Gas Sensors". Electron. Mater. Lett. 14, 2018, pp 221-260

[3] M. Donarelli, L. Ottaviano "2D Materials for Gas Sensing Applications: A Review on Graphene Oxide, MoS_2, WS_2 and Phosphorene" Sensors 18(11), 2018, 3638

[4] Kibsgaard, J., Chen, Z., Reinecke, B. *et al.* "Engineering the surface structure of MoS_2 to preferentially expose active edge sites for electrocatalysis". Nature Mater 11, 2012, pp 963–969

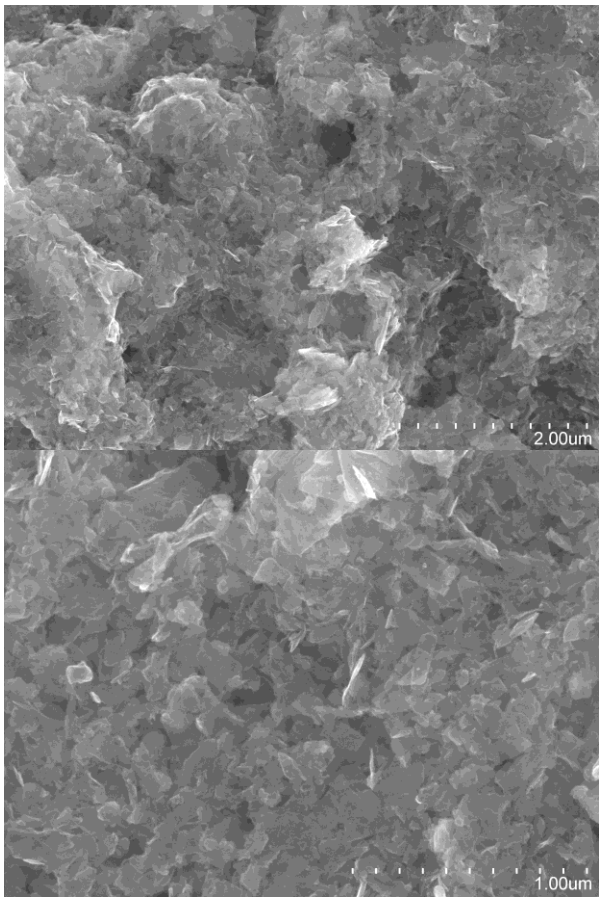

Fig. 1. SEM images of the fabricated thin MoS_2 nanosheet films.

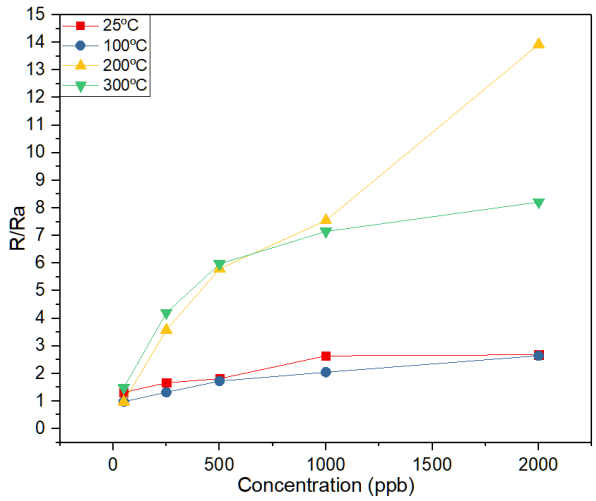

Fig. 2. Sensor response to NO_2 in air at different temperatures.

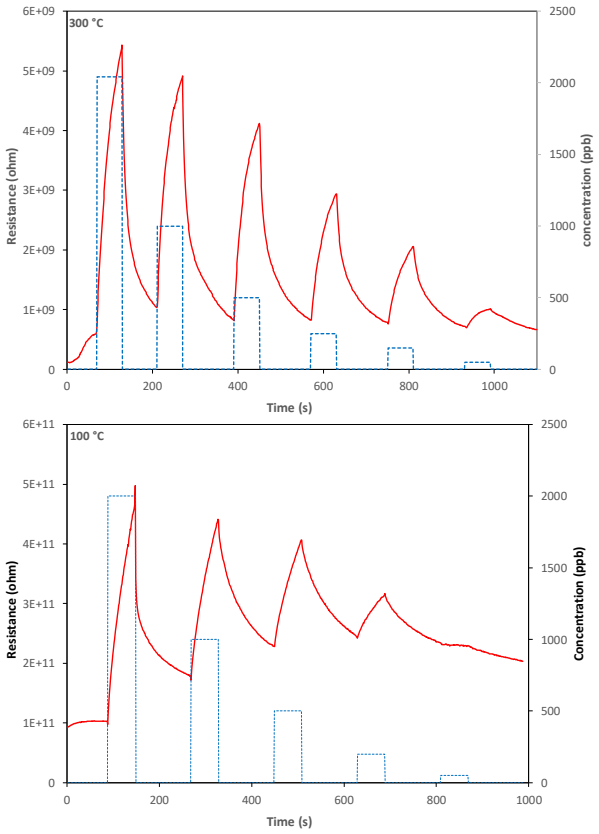

Fig. 3. MoS_2 sensor dynamic response in dry air to NO_2 (in the 20 ppb to 2 ppm range at 100 and 300 °C).

eHealth system with ISFET-based immunosensor for heart failure biomarker detection in saliva

Albert Alcacer[1,*], Hamdi Ben Halima[2], Abdelhamid Errachid[2], Joan Bausells[1]

[1] Institut de Microelectrònica de Barcelona, IMB-CNM (CSIC), Campus UAB, 08193 Bellaterra, Spain
[2] Institut des Sciences Analytiques, Université Claude Bernard Lyon 1, 69100 Villeurbanne, France
* Corresponding author: Albert Alcacer (albert.alcacer@imb-cnm.csic.es)

1. Introduction

Many technological advances have been accomplished by the overall healthcare community, improving detection methods and treatments for cardiovascular diseases (CVD). Nonetheless, this remains the most common cause of premature death in Europe with 19.9 million cases reported in 2017 and an estimated economic burden of €210 billion a year [1]. A chronic medical condition that can result from many forms of CVD, requiring of a lifelong treatment and monitoring with high associated costs, is heart failure (HF), a disease with a prevalence of 1-2% of adult population, rising to 10% among elder aged >70 years [2].

2. Objectives

The aim of this work is to present a label-free and rapid immunosensor based on an Ion-Sensitive Field-Effect Transistor (ISFET) with biofunctionalized sensing membrane, designed to measure Tumour Necrosis Factor-alpha (TNF-α) in saliva, a proinflammatory cytokine which levels correlate prematurely with HF severity [3]. An eHealth IoT-based system has been additionally implemented as a proof-of-concept for a real-time distributed monitoring ecosystem enhancing the probability of early detection, increasing the chances of long-term recovery with fewer complications, and reducing hospital-centred associated costs.

3. Biosensor

The ISFET devices have been fabricated as N-type FETs on 100 mm silicon wafers, with a gate dielectric of 100nm silicon nitride over 78nm silicon dioxide, and metal interconnect lines of platinum, showing a pH sensitivity of 33.5mV/pH [Fig.1]. Each diced Si-chip (8 x 8.4mm) integrates 4 ISFET devices and 1 Pt-based (pseudo-reference or counter) electrode [Fig.2]. The sensors are then biofunctionalized in the ISA laboratories by immobilizing monoclonal anti-TNF-α antibodies on the membrane. The immunosensor presents good response measuring TNF-α in PBS and artificial saliva (AS) with high selectivity and a low limit of detection of 5pg/mL [Fig.3].

4. Instrumentation

A constant-voltage constant-current (CVCC) readout circuit [4] measures changes in the ISFET threshold voltage (ΔV_T), which follows a quasi-linear relation with the TNF-α concentration in the range of 5-20pg/mL. Directing these measurements, an eHealth portable system for real-time monitoring of biomarkers has been implemented in an IoT-based environment [Fig.4], using a Bluetooth-paired Android-based smartphone as gateway, running an application for data representation and allowing the data storage and management through Google Cloud computing services.

5. Conclusions

An immunosensor device measuring TNF-α biomarker in artificial saliva has been developed and an eHealth system for the early detection of changes in concentration implemented, which may help improving the treatment quality of HF patients while reducing associated severe diseases and costs. Further research in limiting the cross-talking signals in real saliva samples and extending its range of detection is required, as well as implementing security protocols for health data management and AI decision-making systems.

This work is funded by EU-H2020 Framework Programme for Research and Innovation: KardiaTool Project "An integrated POC solution for non-invasive diagnosis and therapy monitoring of heart failure patients" (Grant No.768686)

References

[1] Adam Timmis, et al., "European Society of Cardiology: Cardiovascular Disease Statistics 2019", European Heart Journal (2020), vol. 42, pp.12-85.
[2] P. Ponikowski and A. Voors, et al., "Guidelines for the diagnosis and treatment of acute and chronic heart failure", European Journal of Heart Failure (2016), vol. 18, 891-975.
[3] Daiva Vozgirdaite, et al., "Development of an ImmunoFET for Analysis of Tumour Necrosis Factor-α in Artificial Saliva: Application for Heart Failure Monitoring", Chemosensors 2021, 9, 26.
[4] N. Moser, T. S. Landle, C. Toumazou, P. Georgiou, "ISFETs in CMOS and Emergent Trends in Instrumentation: A Review", IEEE Sensors Journal, vol. 16, nº 17. Sept. 2016

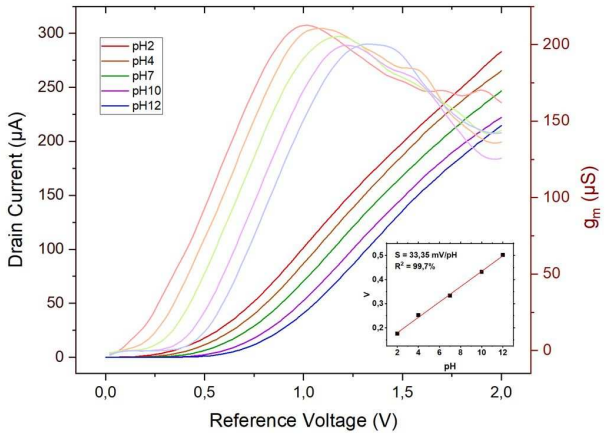

Fig.1. pH-ISFET

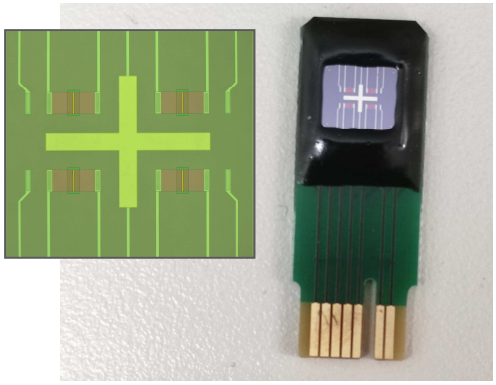

Fig.2. Sensor device

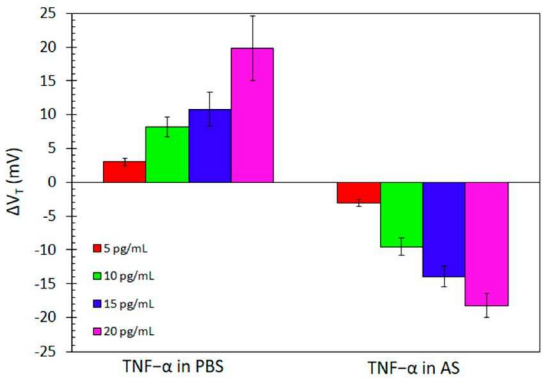

Fig.3. TNF-α immunosensor response

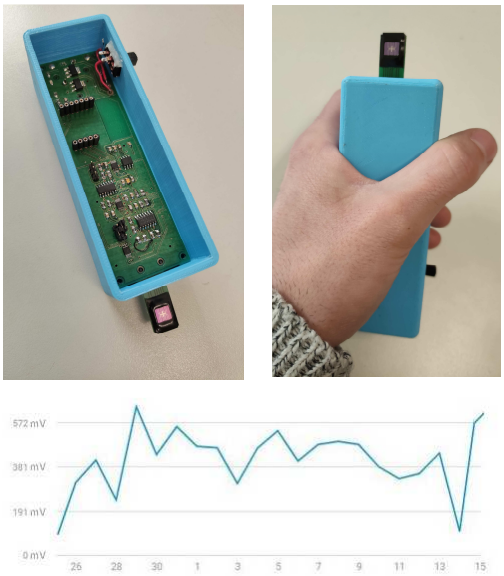

Fig.4. IoT-based eHealth prototype (top), Google cloud chart: V_T changes with pH (bottom)

POSTER SESSION IV

Sensors, actuators and biomedical devices

Friday 11

11:30-13:15

Chairperson: C. García Núñez (University of the West of Scotland)

In orbit data of miniaturized 2-axis sun sensors for attitude control applications in spacecrafts

Manuel Rodriguez[1], José Miguel Moreno[1], Pablo Ortega[2], Gema López[2], Gerard Masmitjà[2], Jose Manuel Quero[3], Juan García[3]

[1] Solar MEMS Technologies S.L. (SMT), Aerópolis, La Rinconada, Sevilla, Spain, jmmoreno@solar-mems.com
[2] Universitat Politècnica de Catalunya (UPC), MNT, Barcelona, Spain, pablo.rafael.ortega@upc.edu
[3] Escuela Superior de Ingenieros, Universidad de Sevilla (US), Sevilla, Spain, quero@us.es

1. Abstract

In this paper, the attitude data obtained in orbit from three different sun sensors developed by the authors is presented. These miniaturized devices were installed in different faces of a small satellite that was launched in a low orbit mission. During the experiments described in this work, the spacecraft pointed to the sun with each of these sun sensors, obtaining the angle measurements and the Sun radiation levels. Accuracy tracking obtained by the attitude control algorithm using sun sensor outputs has been successfully evaluated, as well as solar radiation stability when Sun pointing is achieved.

2. Introduction

A sun sensor is a device used to measure the incidence angle of sun rays with respect to a reference surface. Typical applications of sun sensors are the attitude control of satellites and the tracking control of solar power plants, among others [1]. Sun sensors can be classified as digital or analog, as well as coarse or fine depending on the accuracy of the measurement [2]. According to the sun sensor operating principle, the most common types for small spacecraft are cosine detectors and quadrant detectors. Cosine detectors are inexpensive, low-mass, simple and reliable devices but their accuracy is typically limited to a few degrees. Quadrant detectors appear to be gaining popularity in the CubeSat market due to their compact size and low cost. The sun sensor described in this work, which is based on previous developments [3],[4] and is commercially named as nanoSSOC-D60, is a quadrant type sun sensor. This unit is a miniaturized two axis sun sensor capable of measuring the incidence angle of a sun ray accurately in both azimuth and elevation. The sensor consists of four photodiodes fabricated monolithically in the same crystalline silicon substrate and placed orthogonally. The sunlight is guided to the detector through a window above the sensor, inducing photocurrents on each diode that depends on the angle of incidence [5]. A simplified scheme is illustrated in Fig.1. The measured currents from all four cells are then combined mathematically and processed in an internal microcontroller that provides the sun light incident angles through a digital interface. NanoSSOC-D60 has a field of view (FOV) of ± 60º, a weight of 6.2g and an accuracy of 0.5º (3σ).

3. In orbit results

Three of these sensors were integrated in a Cubesat satellite platform for a confidential mission, which was launched at 550 km altitude. These units (nanoFSS1, nanoFSS2 and nanoFSS3) were installed in the satellite as it is depicted in Fig.2, where Xp, Zp and Zn are the coordinate reference system of the satellite body. Doted lines represent the FOV of each sensor, which have been placed to guarantee that at least one sensor receives sun light during its normal operation when Xn is nadir pointing. During the following experiments in orbit, the spacecraft pointed to the sun with each of those sensors, one by one to check the pointing accuracy. Experiment results have been represented in Fig. 3, 4 and 5 for each unit, specifically the accuracy tracking achieved by the attitude control algorithm using the sun sensor X and Y angle outputs. Solar radiation levels detected by the sun sensors are represented as well, which is calculated as a summation of the four output voltages. When correct solar pointing is achieved, this value should be 5V and very stable. In the three experiments, accuracy tracking obtained is better than 1º or even 0.5º when stable sun tracking is achieved by the satellite (zoomed areas).

4. Conclusions

This paper shows the results obtained in orbit for three different sun sensors nanoSSOC-D60 installed in a Cubesat satellite. This unit uses four silicon photodiodes monolithically integrated in a quadrant detector structure, including a transparent cover glass on the same silicon die to prevent space radiation damage. Its fabrication combines microelectronics technology with a high efficiency solar cell fabrication process, allowing a miniaturized device. Different experiments have been successfully performed in orbit with the three units which telemetries were received and analysed, demonstrating than the sun sensors fulfil the accuracy requirements and functional targets of the mission.

References

[1] L. Salgado-Conrado. "A review on sun position sensors used in solar applications". Renewable and Sustainable Energy Reviews, Vol 82, Part 3, February 2018, Pages 2128-2146.
[2] "State-of-the-Art Small Spacecraft Technology", Small Spacecraft Systems Virtual Institute, Ames Research Center, NASA, Oct. 2020.
[3] P. Ortega, G. Lopez, J. Ricart, M. Dominguez, L. Castañer, J.M. Quero, C.L. Tarrida, J. García. "Fabrication of a Miniaturized Two Axis Sun Sensor for Satellite Applications". IEEE Sensors Journal, vol 10, nº10, pgs. 1623-1632, Oct. 2010.
[4] F. J. Delgado, J. Quero, J. Garcia, C. Tarrida, J. M. Moreno, A. G. Sáez, and P. Ortega, "SENSOSOL: MultiFOV 4-quadrant high precision sun sensor for satellite attitude control," in Electron Devices (CDE), 2013 Spanish Conference on, (IEEE, 2013), 123–126.
[5] https://www.solar-mems.com/nanossoc/

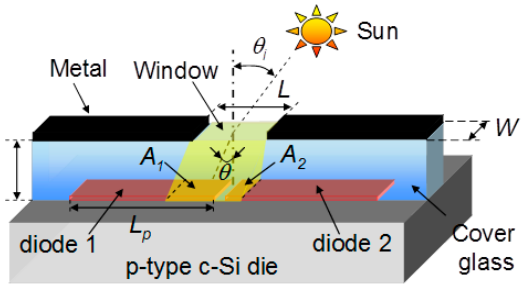

Fig. 1. Operating principle.

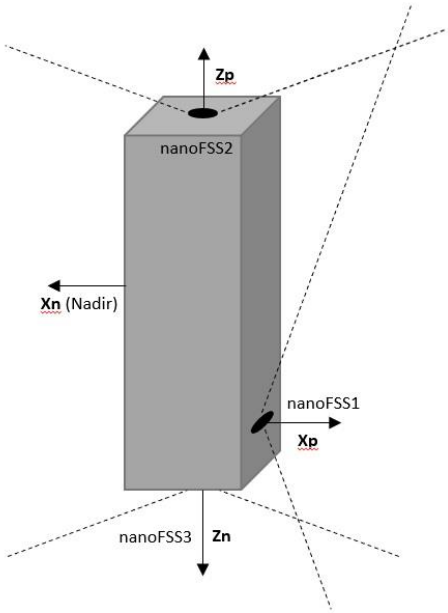

Fig. 2. Cubesat satellite body with the location of the three sun sensors.

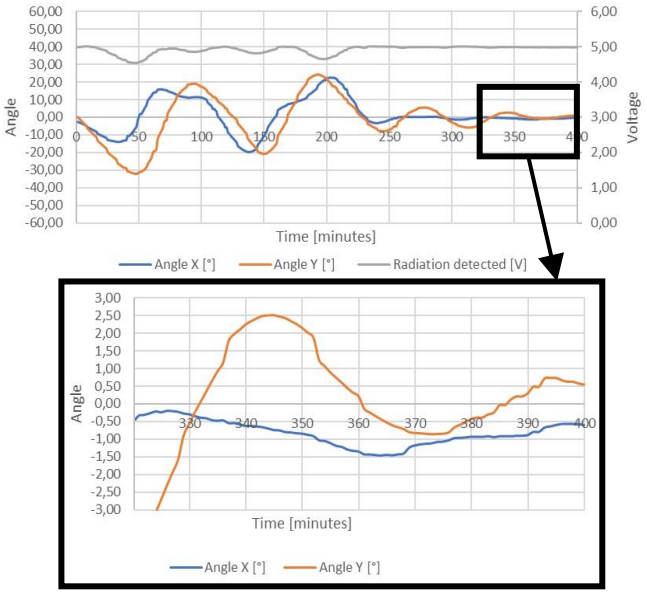

Fig. 3. In orbit experiment with nanoFSS1.

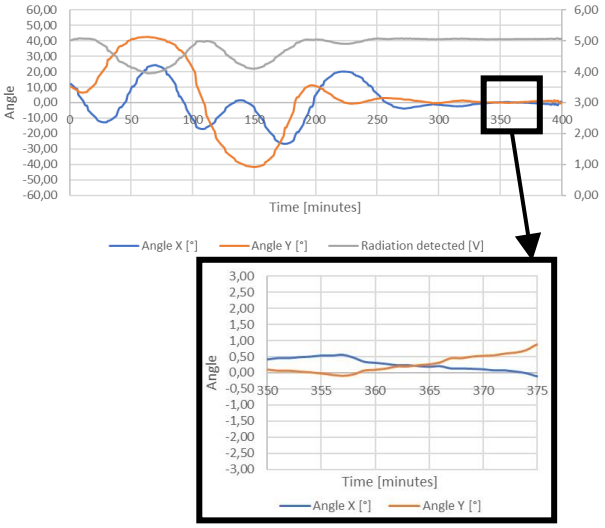

Fig. 4. In orbit experiment with nanoFSS2.

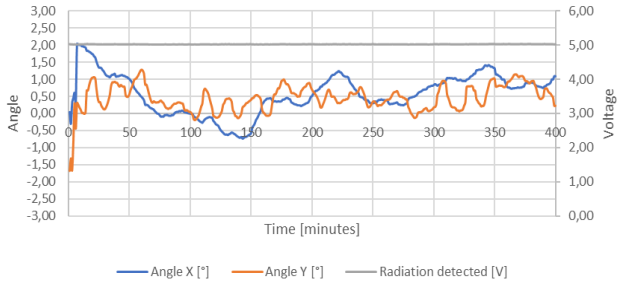

Fig. 5. In orbit experiment with nanoFSS3.

Study of the performance impact by fabrication imperfections in electrochemically etched macroporous silicon photonic crystals

Didac Vega Bru, Daniel Segura García, David Cardador Maza, Ángel Rodríguez Martínez

Micro and Nanotecnologies, Electronic Engineering Department, Universitat Politècnica de Catalunya,
C/Jordi Girona, 1–3, 08034, Barcelona, Spain.
E-mail: didac.vega@upc.edu. Tel: +34934016766

1. Abstract

Optical applications of macroporous silicon (MPS), for ex. gas sensing, require carefully prepared structures to achieve acceptable performance. In particular this paper deals with the **electrochemical etching** (EE) method and the imperfections inherent to such fabrication technique. Several structures with 700 nm pitch have been fabricated and their morphology studied to obtain the profile variations. Afterwards a theoretical study has been performed to assess the impact such variance has in optical performance of such structures.

2. Fabrication and Variability of EE MPS

Several MPS structures have been fabricated in n-type, ⟨100⟩ oriented silicon wafers with pores ordered using a square lattice with a 700 nm pitch. The fabrication method is EE (described in detail elsewhere[1]) which uses hydrofluoric acid (HF) as etching agent in an electrochemical process to dissolve silicon anisotropically. Etching of n-type samples requires illumination to generate the necessary carriers involved in the redox reaction. This provides an additional control variable giving great flexibility to design complex structures. In particular this capability is used to create 3-d structures such as the ones used here, and shown in **Fig. 1**.

In the electrochemical etching of silicon several sources of error can be found to cause deviations of the desired shape during the fabrication process. Intrinsic factors include crystal defects and impurity density gradients. Extrinsic factors include etchant concentration variations, illumination non-uniformity, temperature changes, and gas bubbles formation. The most important takeout is that many of these mechanisms involve *positive feedback* which may cause massive fabrication defects such as pore growth instability, premature pore death, etc.[2] Another significant aspect is that such defects have *long range* effects [3].

3. Characterization and Modelling

The SEM micrographs have been processed to obtain a mask image from which the pore profile can be reconstructed for *each individual pore*, as seen in **Fig. 2**. The pore profile is split for each modulation "layer" (see **Fig. 3**) and a *mean pore profile* obtained. From these data, a statistical model is derived, which is later used in a numerical study considering the pore *instantaneous* radius and vertical period as random variables. Several runs were performed and average results were obtained and compared with actual FTIR measurements.

4. Results

One first remarkable result is shown in **Fig. 4**, which highlights that features of the structure have an effect on subsequent pore features. Indeed, after the defect constriction, the pore radius is systematically smaller. This is attributed to a reduced [HF] after the defect. The photonic bandgap degrades fast with wider tolerances, as demonstrated in **Fig. 5**, which is a limiting factor. Similarly, a defect peak widens and shifts position due to fabrication errors. Comparing the theoretical model with FTIR measures shows good concordance, **Fig. 6**, for moderate tolerances (about 5%).

5. Conclusion

The effect of fabrication tolerances of EE MPS based PhC has been analysed. Some fabricated samples have been morphologically characterized and statistical models have been inferred from the data. The models consider the vertical period and the radius of the pore along its depth. It has been found that the samples fabricated in our typical conditions exhibit a vertical period tolerance with $\sigma_z \approx 5$ %. The models are described by i.i.d. Gaussian random variables, and this has been checked by numerical modelling. In these conditions the PBG shrinks about 20 %, from the ideal, and the resonance peak shifts less than 5 %. This results in a reasonably performing PhC for gas sensing applications.

References

[1] V. Lehmann, «The physics of macroporous silicon formation», *Thin Solid Films*, vol. 255, n.º 1, pp. 1-4, 1995.
[2] V. Lehmann, U. Grüning, «The limits of macropore array fabrication», *Thin Solid Films*, vol. 297 (1-2), pp. 13-17, 1997.
[3] S. Matthias, R. Hillebrand, F. Müller, U. Gösele, «Macroporous silicon: Homogeneity investigations and fabrication tolerances of a simple cubic three-dimensional photonic crystal», *J. Appl. Phys.*, vol. 99 (11), p. 113102, 2006.

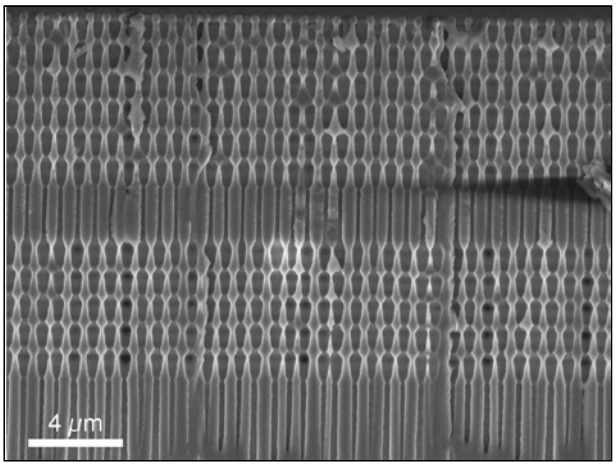

Fig. 1. SEM cross-section view of a fabricated 3-d MPS PhC.

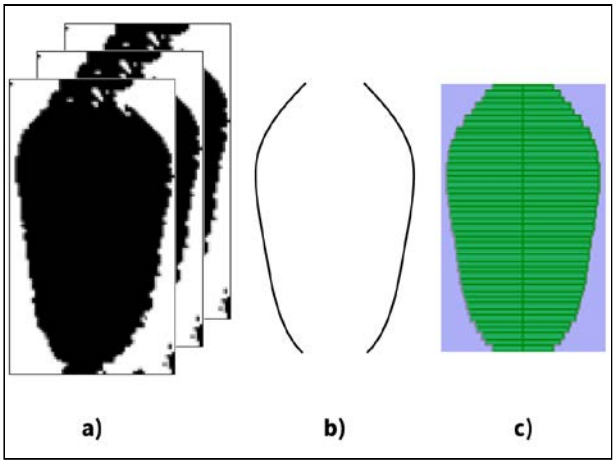

Fig. 2. Characterization of the microsturcture of the MPS pore profile. (a) The SEM image is processed to obtain a mask. (b) Shows the reconstructed profile obtained from the mask. (c) Slice model for numerical simulation.

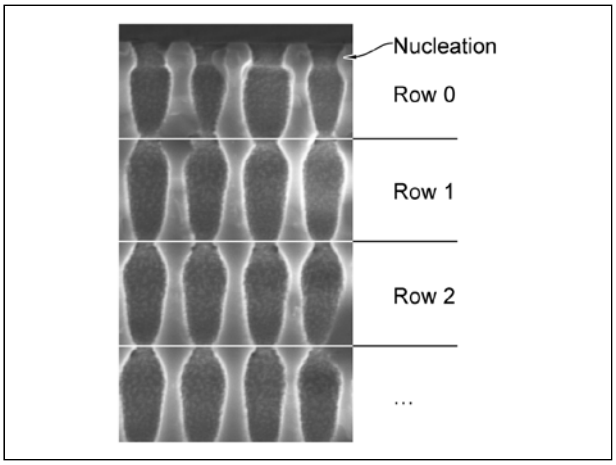

Fig. 3. Closeup view of the pore beginning. The row numbering used to group modulations is shown.

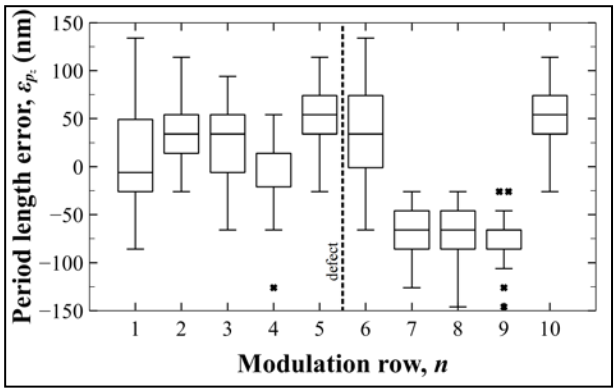

Fig. 4. Error distribution of the period depending on the modulation depth. The defect in the PhC is marked by the thick line, placed between periods 5 and 6.

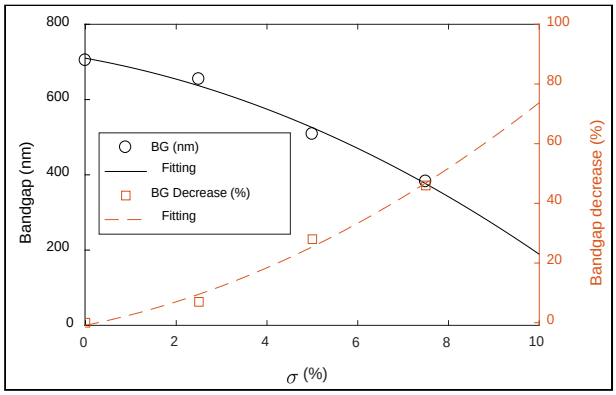

Fig. 5. Bandgap dependence on standard deviation of the period distribution.

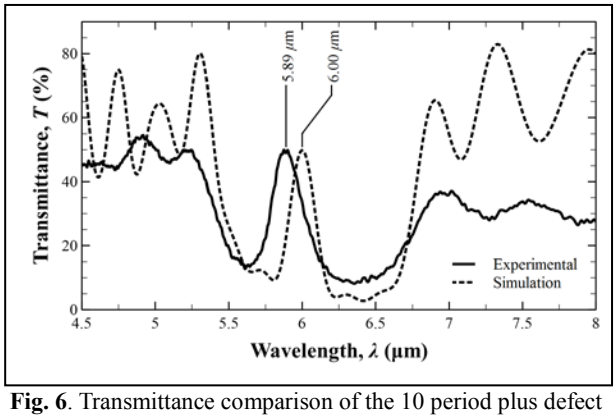

Fig. 6. Transmittance comparison of the 10 period plus defect PhC between the characterized fabricated samples and the ideal "mean" model..

ZnO nanorods and their modification with Au nanoparticles for UV-light activated gas sensing

M. Tomić,[1,2], I. Gràcia,[1] E. Figueras,[1] C. Cané,[1] and S. Vallejos[1]*

[1] Institute of Microelectronics of Barcelona (IMB-CNM, CSIC), Campus UAB, 08193 Cerdanyola del Vallès, Spain.
[2] Autonomous University of Barcelona (UAB), Campus UAB, 08193 Cerdanyola del Vallès, Spain.

***Corresponding Author:** stella.vallejos@imb-cnm.csic.es; Tel.: +34-935-947700

1. Abstract

Aerosol assisted chemical vapour deposited (AACVD) ZnO nanostructured films integrated into Si-based transducing platforms are modified with preformed Au nanoparticles (NPs) via impregnation. Characterization of these films using SEM, TEM, DRS, XRD, and XPS shows the incorporation of well-distributed and stable Au NPs at the surface of ZnO. Photoactivated gas sensing tests at room temperature (RT) demonstrate enhanced sensitivity and better speed of response for the Au modified ZnO films (AuZn) providing three-fold more response to ethanol and acetone as compared to unmodified ZnO films (Zn).

2. Introduction

Nanostructured metal oxides are attractive in gas sensing because they enhance the performance of these devices, not only due to their higher surface-area-to-volume-ratio, as opposed to bulk materials, but also due to the presence of specific crystal facets that provide a particular electronic structure to the surface. ZnO has been widely investigated for gas sensors due to its nontoxicity, stability, and low fabrication cost. Although ZnO based sensors have remarkable performances, it is possible to improve the gas sensing properties even further by decoration with noble metal NPs and photoactivation, among other strategies [1].

In this paper, the decoration of ZnO nanostructured film is achieved by using Au NPs and the assembled sensor devices are tested at RT with photoactivation toward ethanol, acetone, toluene, and hydrogen.

3. Materials and Methods

ZnO nanorods were directly deposited over Si-based transducing platforms using the AACVD method reported previously [2]. The modification of ZnO structures was achieved in a second step by impregnation with preformed Au NPs synthesized by Turkevich method [3]. Prior to the characterization, the samples were annealed in synthetic air at 450 °C for 1 h. The morphology of the film was examined using SEM and TEM, the optical properties using DRS, the crystallinity using XRD, and the chemical composition was determined using XPS. AuZn and Zn sensors were tested to ethanol, acetone, toluene, and hydrogen at RT via photoactivation (LED, 365 nm) in a continuous flow system with dry air as the reference. The sensor response (R) was defined as (Ra-Rg)/Ra, where Ra and Rg represent the electrical resistance in air and after 10 min of gas exposure.

4. Results and conclusions

The SEM images (**Fig.1**) display the Au modified ZnO structures, in which is noticed the uniform rod-like morphology (length of ~1.5 μm and average diameter of 200 nm) covered with well-distributed Au NPs with diameters between 5 and 40 nm. HRTEM (**Fig.2**) of these structures reveals the presence of highly ordered crystalline lattices with the interplanar spacing of 0.26 nm and 0.23 nm, consistent with the hexagonal ZnO (002) and cubic Au (111) planes. XRD (**Fig.3**) corroborates the presence of the hexagonal ZnO phase with absence of extra diffractions from Au most likely due to their small size, low amount, and high dispersion over the film. DRS results (**Fig.4**) display the band gap transition of ZnO at ~3.3 eV (estimated by Kubelka-Munk transformation for the adsorption wavelength of 375 nm) and the surface plasmon resonance band of gold at ~520 nm. XPS results (**Fig.5**) also confirms the presence of the typical Zn 2p, Zn 3p, Au 4d, and Au 4f core level spectrum.

Photoactivated gas sensing tests show enhanced responses with better recovery and response time for the AuZn sensor, as compared to the Zn sensor particularly to ethanol (**Fig. 6**).

References

[1] V.S. Bhati, M. Hojamberdiev, M. Kumar, Enhanced sensing performance of ZnO nanostructures-based gas sensors: A review, Energy Reports. (2020). https://doi.org/10.1016/j.egyr.2019.08.070.

[2] S. Vallejos, N. Pizúrová, J. Čechal, I. Gràcia, C. Cané, Aerosol-assisted Chemical Vapor Deposition of Metal Oxide Structures: Zinc Oxide Rods, JoVE. (2017) e56127. https://www.jove.com/video/56127.

[3] J. Turkevich, P.C. Stevenson, J. Hillier, A study of the nucleation and growth processes in the synthesis of colloidal gold, Discuss. Faraday Soc. 11 (1951) 55–75. https://doi.org/10.1039/DF9511100055.

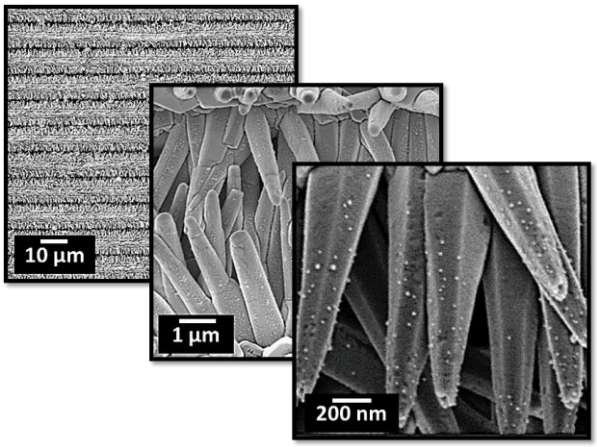

Fig.1. Low and high magnification SEM images of the AuZn structured films deposited over the transducing platform.

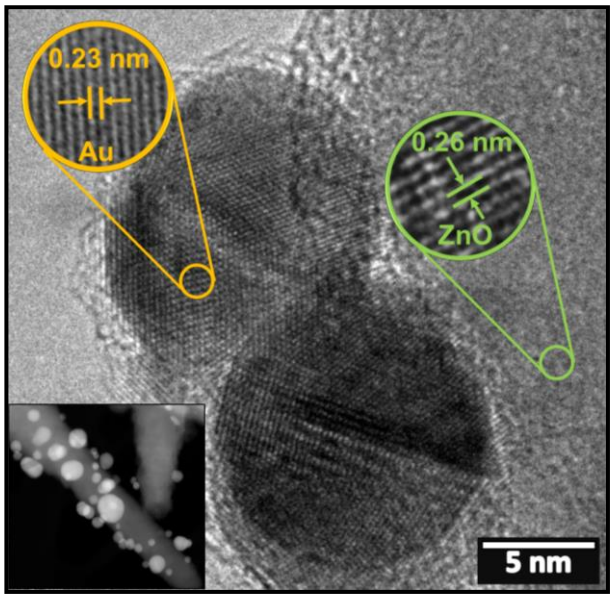

Fig.2. HRTEM image with the inset showing a STEM image of the ZnO nanorod modified with Au nanoparticles.

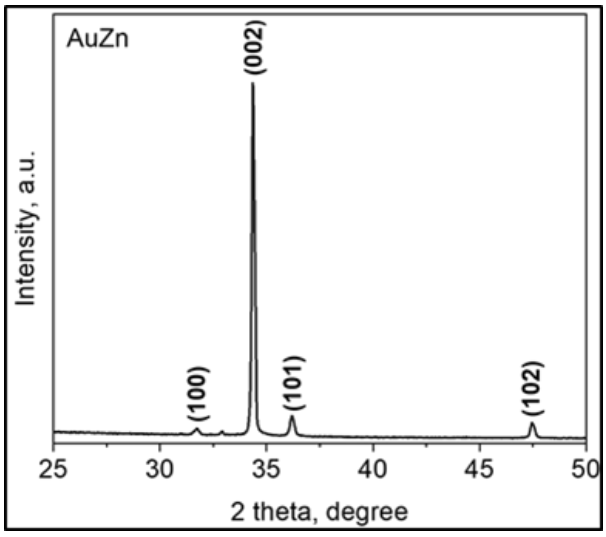

Fig.3. Typical XRD diffraction pattern of the AuZn films.

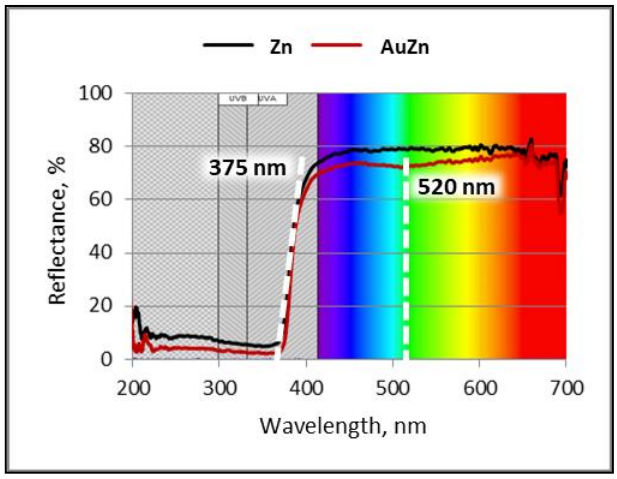

Fig.4. Diffuse reflectance spectra (DRS) of the Zn and AuZn structured films.

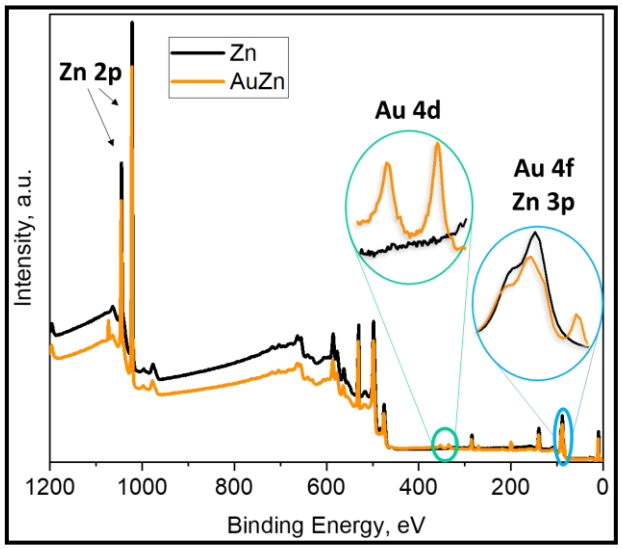

Fig.5. XPS spectra recorded on the Zn and AuZn films. Only the peaks of interest have been marked.

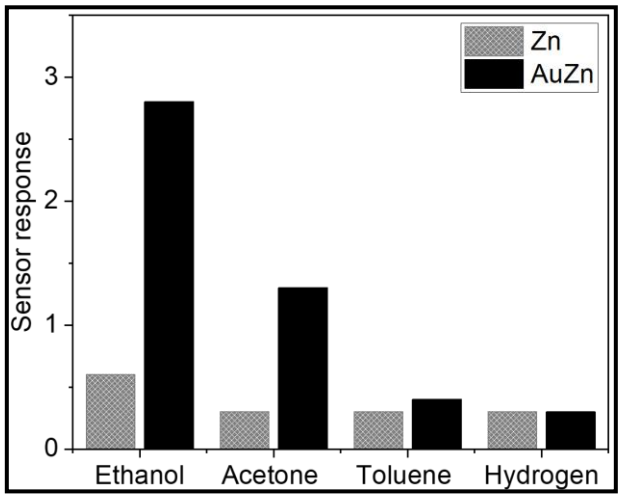

Fig 6. Photoactivated response towards 80 ppm of ethanol, acetone, toluene, and hydrogen.

3D Detectors for timing applications

O. Ferrer, G. Pellegrini, D. Quirion, M. Manna

Institute of Microelectronics of Barcelona (IMB-CNM)
Tel: (+34) 93 594 77 00, ext 2135
Oscar.ferrer@imb-cnm.csic.es

1. Introduction

The upcoming upgrade of the LHC, the High Luminosity - Large Hadron Colider, is going to push the requirements of its sensors further from where it stands now. One of the main characteristics of the improvement is the increase of proton flux which will result in a higher radiation damage for the sensors and an increase of the amount of events per time that have to be tracked. This talk will be centered on the explanation of some of the characteristics of the sensors that we at CNM are producing and some of the key fabrication steps.

2. 3D radiation silicon sensor

The basic working principle of a radiation silicon sensor is based on the collection of electrons (and holes) created by the ionization of the silicon atoms in the lattice. The quality of the signal depends on the noise, the charge collection efficiency (CCE), the breakdown voltage and, in our case, the time of arrival (ToA). The sensors that have been most used are planar sensors, which consists on layers of materials deposited and etched on top of the silicon wafer. While its fabrication is relatively easy, using the whole wafer thickness as the active area implies that the distance from the creation of the signal to the electrodes is quite large in comparison with the mean free path, which reduces the CCE and increases the ToA, especially after delivering the sensors the amount of non-ionizing radiation that those sensors are expected to receive. This issue is overcome using the 3D technology, which consists on electrodes etched perpendicularly to the surface (**Fig 1**) because of its shorter distance between electrodes, which makes them as a good candidate for the timing applications that is required for the ATLAS upgrade [1].

3. Device simulation

One of the key steps to be considered while producing the devices is its simulation in order to understand what are the expected characteristics and compare the actual results when fabricated. For example, in **Fig 2** we can see that after irradiation the charge collection because of a transient particle is lower than when not irradiated. Also, the electric field can be studied; full depletion is observed with just a few volts of bias voltage **(Fig 3)**.

4. Deep Reactive Ion Etching (DRIE)

A crucial step in the fabrication of 3D sensors is the etching of the perpendicular holes, which is performed with the DRIE, which is an anisotropic etching of the silicon alternating an etching step and a passivation step that, by making a higher etching ratio at the bottom of the wafer rather than on its lateral walls, a high aspect ratio (HAR) can be achieved [2]. Some of the key concepts and parameters will be explained in this section.

After the etching of the holes, highly doped polysilicon must be deposited so that the columns behave as an electrode.

References

[1] G. Kramberger, V. Cindro, D. Flores, S. Hidalgo, B. Hiti, M. Manna, I. Mandié, M. Mikuz, D. Quirion, G. Pellegrini, M. Zavrtanik “Timing performance of small cell 3D silicon detectors” Nuclear Inst. And Methods in Physics Research, A, Volume 934, p. 26-32, 2019.

[2] H. V. Jansen *et al* 2009, J. Micromech, Microeng, **19**, 033001

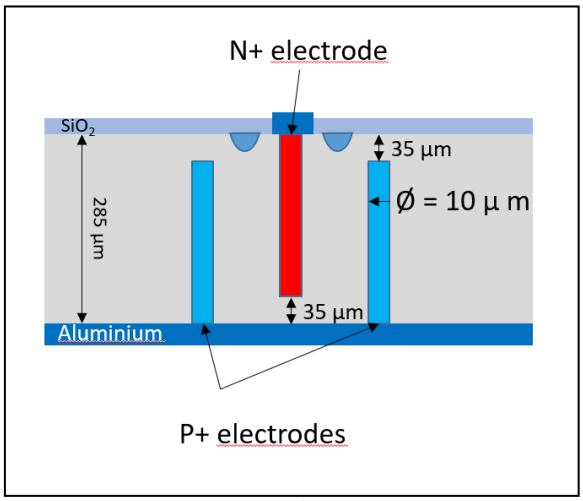

Fig.1. Scheme of a 3D sensor

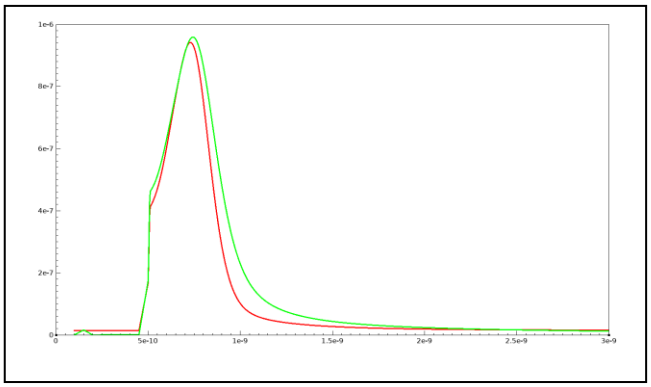

Fig.2. Simulation of the charge collection for not irradiated (green) and irradiated (red, f = $5e^{15}$ cm^{-2}) 3D silicon detectors

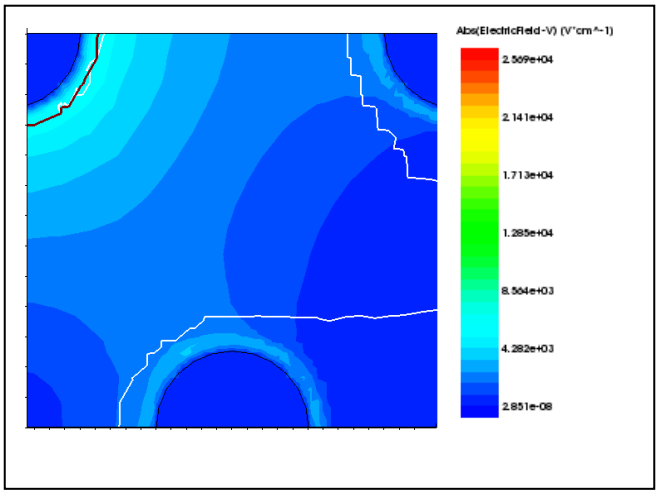

Fig 3. Simulation of the electric field – the white line represents the deletion region.

Glancing Angle Deposition of Nanostructured ZnO Thin Films for Ultrasonics

M. Pelayo Garcia, [1] Kevin McAughey,[2] D. Gibson,[1] David Allan Hughes,[2] and C. García Núñez[1]

[1]Institute of Thin Films, Sensors and Imaging, University of the West of Scotland, Scottish Universities Physics Alliance, Paisley, PA1 2BE, United Kingdom.
[2]Novosound Ltd, Newhouse, ML1 5UH, United Kingdom
Contact authors: manuel.pelayo@uws.ac.uk and carlos.garcianunez@uws.ac.uk

Ultrasonic sensors have demonstrated great potential for non-destructive testing (NDT) of materials, being widely applicable in health care/monitoring (biomedical, muscle recovery, cancer early detection), industry, and defence [1]. Most conventional ultrasonic sensors are based on monolithic piezoelectric ceramic materials (e.g. PZT, $PbTiO_3$ or PMN-PT) which are too bulky and non-conforming to enable their integration on flexible substrates. In spite of large piezoelectric coefficients, their high profile limits their operation frequencies below 100 MHz. To address these drawbacks, ZnO thin films have emerged as an alternative piezoelectric material for low profile and high frequency ultrasonic transducers due to properties such as low-cost, compatibility with flexible substrates, biocompatibility, and high piezoelectric coefficient. Moreover, the use of reactive sputtering techniques to deposit ZnO films has allowed resulting ultrasonic sensors to reach frequencies up to 1 GHz [2].

The existing procedures to deposit ZnO thin films, controlling crystalline structure, composition, and morphology of resulting piezoelectric material, have been further upgraded by techniques such as glancing angle deposition (GLAD) allowing the deposition of inclined nanostructured films (Figure 1(a)). In particular, GLAD has demonstrated great potential to control accurately the titling angle of nanostructured films which could be interesting for the partial or total suppression of certain S (shear) and L (longitudinal) acoustic modes [3]. This feature has a huge impact on ultrasonics utilised in different mediums, where only one acoustic mode couples into the medium, creating excessive ringing or damping (e.g. S-mode in liquid). Hence, the investigation of a single ultrasonic device allowing the modulation of S and L modes at certain frequencies is crucial.

This work presents GLAD ZnO thin films deposited at different reactive sputtering conditions optimised to meet the dual requirements of highly crystalline c-axis orientation while controlling the inclined angle of resulting nanostructured films for their application as piezoelectric material in ultrasonic sensors.

ZnO thin films are deposited by DC-magnetron reactive sputtering on Si(100) substrates, from a 100×300 mm^2 Zn (99.99% purity) target using O_2 and Ar as plasma gases. The sputtering system can allocate up to 56 samples of 20×20mm^2 using a dual magnetron system and a static/rotating drum (Figure 1(b)). In this work, ZnO nanostructured film characteristics are analysed as a function of: i) the gas flux angle with respect the normal vector of the target (α), ii) plasma power, iii) position of the substrate holder, and iv) total gas-flow, aiming to control the titled angle of the nanostructured film (β). Resulting films are characterised by SEM, EDX, XRD, Raman, stress, and piezoelectric measurements.

Figures 2 (a,b) show SEM images of ZnO films deposited at α of 60º and 86º, respectively. The analysis of the image cross-section demonstrates an increase of β from 5.5º up to 12º (Figure 2(c)) for α of 60º and 86º, respectively. This result proves the shadowing effect being characteristic of GLAD (Figure 1(a)) in comparison with the columnar structures (β = 0º) obtained under standard gas flow conditions (α = 0º).

EDX analysis shows a stoichiometric material ($Zn_{0.51}O_{0.49}$) independently on α. XRD characterisation confirms a highly crystalline ZnO film with wurtzite structure, showing a predominant (002) characteristic peak (2θ = 34.44º) for all films. The high crystallinity of the resulting nanostructured films leads to a great piezoelectric coefficient (d_{33}) of 56 pm/V (compared with 12.4 pm/V on bulk ZnO) measured by single-probe vibrometer (Figure 2(d)), and confirmed by finite elements analysis (Figure 2(e)). These results make the resulting titled nanostructured ZnO films to be promising as active material for the development of flexible ultrasonic sensors (Figure 2(f)).

References

[1] www.novosound.net/applications
[2] P. M. Martin, *et al.* "Piezoelectric films for 100-MHz ultrasonic transducers," *Thin Solid Films*, 379 (2000) 253.
[3] H. F. Pang *et al.*, "Annealing effect on the generation of dual mode acoustic waves in inclined zno films,"U*ltrasonics*, 53 (2013) 1264.

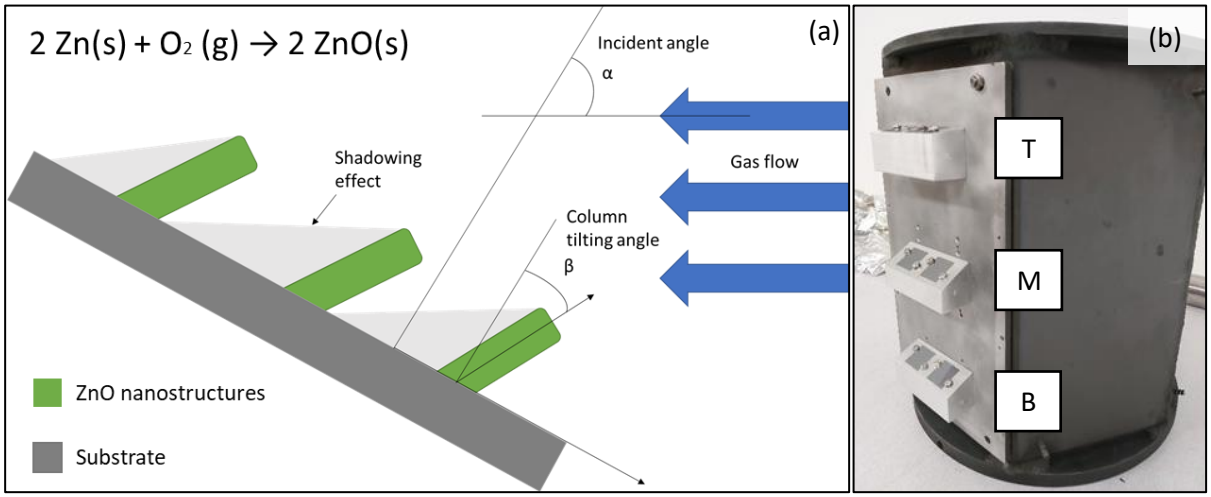

Figure 1. **(a)** Schematic of Glancing Angle Deposition (GLAD) technique. The diagram shows the characteristic angles belonging to GLAD. On the one hand, the incident angle (α) is defined as the angle between the incident molecular flow and the normal vector of the substrate. On the other hand, β represents the resulting column tilting angle. This angle is affected by the so-called shadowing effect. The front structures which gas reaches first act as a mask for the substrate behind, making the layer to grow in a tilted nanostructured manner. **(b)** Photograph of the drum utilised to support the substrate holders at different heights (top: T, middle: M and bottom: B). Each block is 70mm distant from each other.

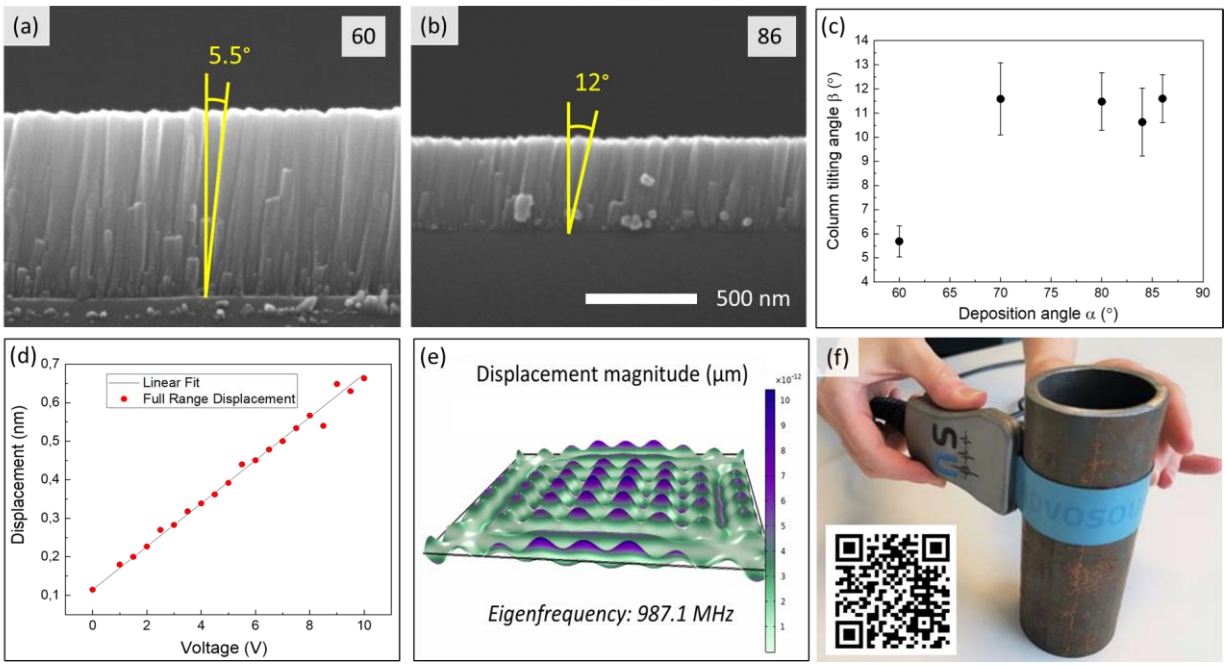

Figure 2. SEM images of ZnO films deposited at α of **(a)** 60° and **(b)** 86°, showing a thickness of 840 and 400 nm, and a β of 5.5°±0.6° and 12°±1°, represented in the image, respectively. **(c)** Graph depicting α vs β. An increase of the film tilting angle can be observed when the incident flux is increased. **(d)** Graphic representing the piezoelectric analysis, total displacement vs. voltage. It shows the piezoelectric behaviour of the grown layer, obtaining a great d_{33} coefficient of 56pm/V from the slope of the linear fit. **(e)** Image showing the FEA 3D displacement simulation of the 987.1MHz vibrational mode. **(f)** Novosound Kelpie, commercially available flexible ultrasonic detector, being used for corrosion mapping on a pipe. Its flexibility allows it to twist, bend and flex during the scan. The QR link leads to Novosound webpage demonstrating a wide range of applications for this sensor.

Development of a potentiometric bioelectronic tongue modified with gold nanoparticles for dairy industry

Clara Pérez-González, Coral Salvo-Comino, Cristina García-Cabezón, Fernando Martin-Pedrosa, María Luz Rodríguez Méndez

Group UVaSens, University of Valladolid, Escuela de Ingenierías Industriales Paseo del Cauce, 59, 47011 Valladolid.
e-mail: claraperez.biotecnologia@gmail.com; mluz@eii.uva.es

1. Introduction

Electronic tongues (ETs) have attracted considerable interest due to their capability to discriminate and analyse foods and beverages and to their potential to contribute to quality management. ETs are based on sensor arrays with low selectivity and high cross-selectivity combined with statistical tools that analyse the outputs from multiple sensors [1]. Compared to other analytical methodologies, this type of device has interesting practical characteristics such as possible online application, no need for pretreatment of samples, and the capability to assess several chemical compounds in a single analysis.

ETs can use arrays of sensors based on a variety of transduction principles. Potentiometric sensors are based on the study of the potential created across a selective membrane. This interphase potential depends on the electrode/solution interaction, which in turn, depends on the chemical compounds found in the studied solution.

The aim of this work was to construct an all-solid-state potentiometric e-tongue with an array of sensors based on polymeric membranes, to be applied in the dairy industry. Due to the complexity of milk samples and the presence of fats that induce interference in sensor responses, milk analysis is not a completely solved problem. In order to obtain an array of sensors with improved sensitivity, the membranes have been modified with gold nanoparticles [2]. In addition, enzymes as galactose oxidase, urease and lactate dehydrogenase have been covalent bonded to the PVC surface to increase the selectivity of the sensor.

2. Experimental

In this study, an ET composed by an array of 27 potentiometric sensors was developed. Sensors are based on a combination of gold nanoparticles, enzymes (galactose oxidase, urease and lactate dehydrogenase) and three plasticizers. Each of the polymeric mixtures was applied on solid conducting silver-epoxy supports. The set of sensors together with an Ag / AgCl reference electrode and a multiplexer for data acquisition formed the e-tongue.

The performance of the ET was evaluated by analysing six standard solutions of compounds usually found in milk (urea, lactic acid and galactose) with concentrations ranging from $1 \times 10{-}4$ to $1 \times 10{-}1$ mol / L. By applying the principal component analysis of the results obtained, 9 sensors were selected for the construction of the optimized e-tongue was applied to discriminate thirteen commercial milk samples.

In addition, correlations have been established with the chemical composition, obtained by traditional methods, through the application of PLS analysis.

3. Results

The responses of the sensors towards standard solutions indicate that sensors modified with gold nanoparticles and covalently associated enzymes showed a greater ability to differentiate between increasing concentrations of products of interest found in milk (urea, lactic acid, galactose, etc.) with variations of voltage up to 65 mV between samples. Moreover, the electronic tongue developed was able to perform the discrimination of milk with different nutritional characteristics using statistical analysis (PCA) showing as a result five differentiated groups, which are also ordered according to the fat content of the samples (Fig.1.). In addition, the results of the study showed that the electronic tongue developed could be used as a prediction system for different chemical parameters, such as pH, acidity, protein or fat, of future milk samples by applying partial least squares analysis with regression coefficients above 0.90 for two variables in the parameters studied (Table.1).

Acknowledgments

MICINN-FEDER (RTI2018-097990-B-100), Consejería de Educación JCyL- FEDER VA275P18 and «Infraestructuras Red de Castilla y Leon (INFRARED)» UVA01

References

[1] Ródriguez-Mendez, M.L., De Saja, J.A., González-Antón, R. “Electronic Noses and Tongues in Wine Industry” Frontiers in bioengineering and biotechnology, 2016, 4, 81.

[2] Yin, T., Qin, W. “Applications of Nanomaterials in Potentiometric Sensors.” Trends in Analytical Chemistry, 2013, 51, pp.79-86.

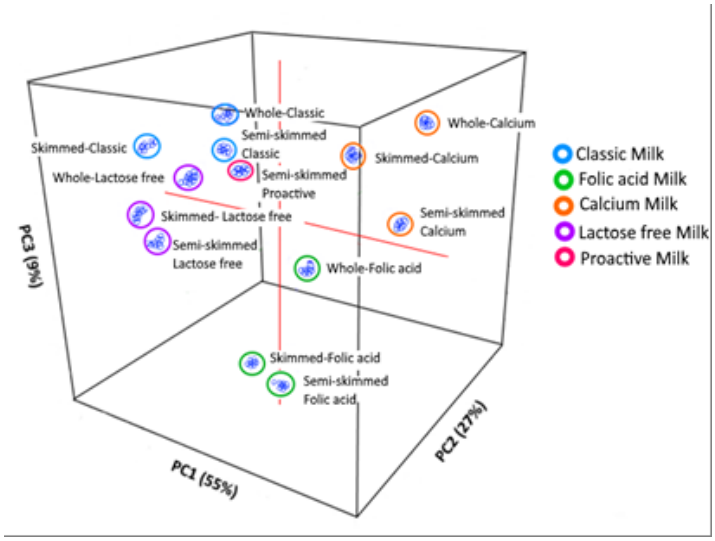

Fig.1. Classification of the milk samples studied according to the score diagram of the partial least squares (PCA) analysis.

Table.1. Parameters resulting from the regression of partial least squares analysis.

Parameters	**$R2_C$**	**$RMSE_C$**	**$R2_P$**	**$RMSE_P$**	**Latent variables**
Acidez	0.9683	0.2574	0.9683	0.2651	2
Density	0.9729	0.4672	0.9701	0.4916	2
%Proteins	0.9649	0.0527	0.9622	0.0555	2
%Fat	0.9112	0.3727	0.9094	0.3843	2
%Lactose	0.9695	0.0453	0.9658	0.0479	2
%ESM	0.9781	0.0946	0.9779	0.0986	2
%EST	0.9408	0.3285	0.9369	0.3436	3

Detection of 2,4,6 Trichloroanisole at low concentrations by means of machine olfaction

Jaime Gómez-Suarez, Félix Meléndez, Patricia Arroyo, Sergio Rodríguez, Sergio Palomeque, José Ignacio Suárez, Jesús Lozano*

Industrial Engineering School. Universidad de Extremadura, Av. Elvas s/n. 06006 Badajoz. Tel. +34924289600. Fax. +34924289601. *E-mail: jesuslozano@unex.es

1. Introduction

One of the main challenges when using natural cork stoppers is that they sometimes contain certain concentrations of 2,4,6-Trichloroanisole (TCA), a compound that gives wine a musty smell and ruins the bottle. It is estimated that up to 5.5% [1] of bottles of wine worldwide are "cork tainted", and, although harmless, this makes wine undesirable for costumers, leading to a huge economic impact in the cork industry.

Detecting TCA is not an easy task due to its low concentration. The main techniques used to detect this compound in cork stoppers production are chemical analyses, such as gas chromatography or mass spectrometry. These methods require a lot of time for the analysis, high prized equipment and specialised staff. Therefore, the cork industry demands an alternative method to detect TCA.

In this paper, an E-nose, is designed to detect a 2,4,6-Trichloroanisole at ppb level. E-Nose is an electronic system formed by an array of gas sensors combined with a pattern recognition system, they respond in real time, need low power supply and have low cost and size.

This paper is based on a previous work in which the authors used a similar ENose to categorize four different types of cork stoppers [2]. The following paper is a first approach to a similar problem but using an enhanced ENose and focusing on finding a specific concentration (3 ng/l) rather than categorizing samples.

2. Materials and Methods

The electronic nose designed includes an array of five non-specific digital sensors: BME680, SGP30, iAQ-Core, CCS811 and ZMOD4410. Each of these sensors measure different magnitudes of the stream flow or different concentrations, as shown in table I. The ENose is controlled by a 32-bit microcontroller, model PIC32MM0256GPM064, and it sends the data via Bluetooth to a Smartphone or PC. Fig 1.

To generate gas streams with low TCA concentrations, a calibration gas generator and a humidity generator (OVG-4 and OHG by Owlstone, respectively. Fig 2.) have been used. Using OVG-4 and OHG in addition to permeation tubes, it is easy to generate an air flow with a wide range of TCA concentrations and relative humidity. shows an image of the device. It was generated a gas flow of 300ml/min with a temperature of 25ºC. Switching the OVG split flow from 700 ml/min to 328 ml/min it was possible to reach TCA concentrations from <1.5 ng/l to 3 ng/l.

Once the signal is received, the data preprocessing stage begins. Since the original data set is usually too big to manipulate and contain irrelevant information, data preprocessing is aimed at finding a smaller data array that contains most of the relevant information [3]. A moving average method was also carried out to reduce noise and to smooth the shape of the signal.

3. Results and Conclusions

There were generated different concentration steps that allowed the authors to test the sensor array response. Figures 3 and 4 show the raw response and the processed response to TVOC's of the SPG30 to a step from 1.4 ng/l to 3 ng/l. The signal received and processed from CCS811 is shown in Figures 5 and 6. In both cases it can be concluded that the ENose detected the gap between 1.4 ng/l and 3 ng/l. Further researches must be carried out in order to test the behavior of the ENose in a variety of conditions.

References

[1] Peña-Neira, A., Fernández de Simón, B., García-Vallejo, M. *et al.* Presence of cork-taint responsible compounds in wines and their cork stoppers. *Eur Food Res Technol.* 211**,** 257–261(2000), doi: 10.1007/s002170000193

[2] Lozano, J.; Meléndez, F.; Arroyo, P.; Suárez, J.I.; Herrero, J.L.; Carmona, P.; Fernández, J.Á. Towards the Miniaturization of Electronic Nose as Personal Measurement Systems. *Proceedings* 2019, *14*, 30. https://doi.org/10.3390/proceedings2019014030

[3] R. Gutierrez-Osuna and H. T. Nagle, "A method for evaluating data-preprocessing techniques for odour classification with an array of gas sensors," in IEEE Transactions on Systems, Man, and Cybernetics, Part B (Cybernetics), vol. 29, no. 5, pp. 626-632, Oct. 1999, doi: 10.1109/3477.790446.

Sensor	BME680	SGP30	ZMOD 4410
Values	Temp.	CO2	CO2
	Press.	TVOC	TVOC
	H.R.	H2	Ethanol
	Resist.	Ethanol	Resist.
			IAQ
Sensor	iAQ-Core	CCS811	
Values	CO2	CO2	
	TVOC	TVOC	
	Ethanol	Resist.	

Table 1. Magnitudes and concentrations measured by each sensor. TVOC for total volatile organic compounds.

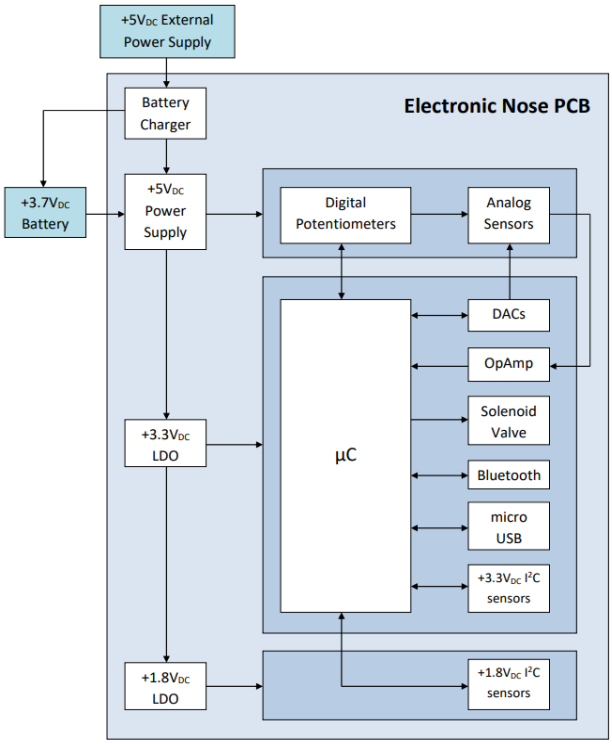

Fig.1. Schematic of the electronic nose

Fig.2. Owlstone vapour generator (OVG) and Owlstone humidity generator (OHG).

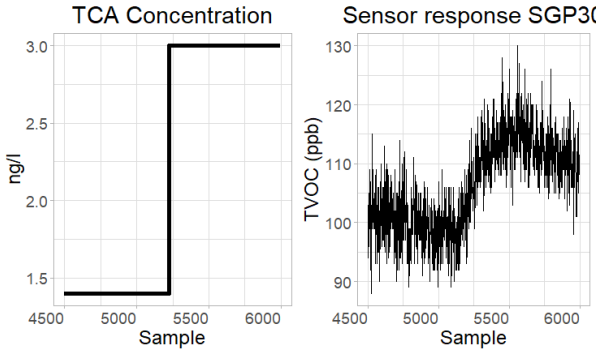

Fig.3. Raw signal received from SGP30 compared to generated TCA concentration.

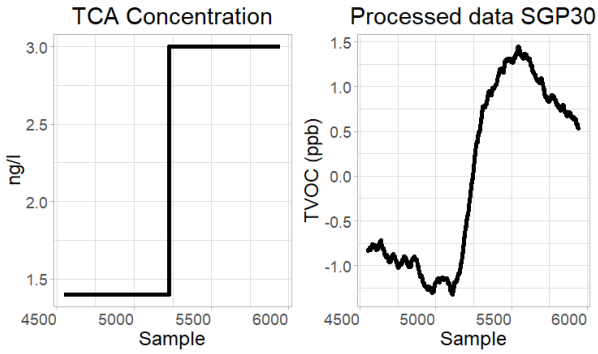

Fig.4. Processed data compared to generated TCA concentration.

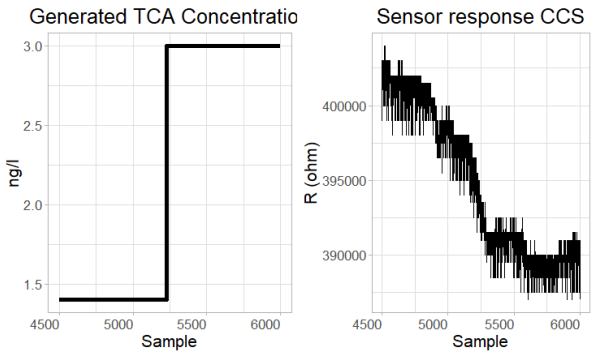

Fig.3. Raw signal received from CCS811 compared to generated TCA concentration.

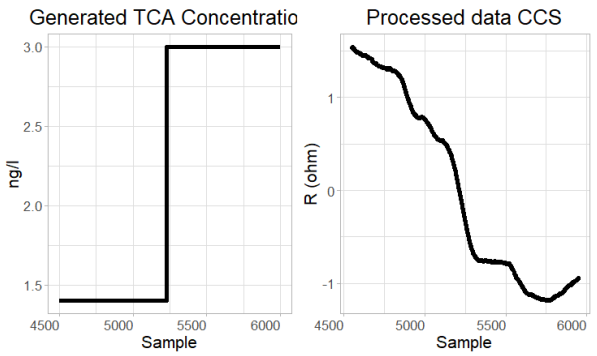

Fig.3. Processed data from CCS compared to generated TCA concentration

Modeling and simulation of a magnonic gas sensor to detect diseases in human breath

M. Pozo-Gómez[a,b], P. de la Presa[a], C. Cruz[b], P. Marín[a], M.C. Horrillo[b], D. Matatagui[b]*

[a] Instituto de Magnetismo Aplicado, UCM-ADIF, 28230 Las Rozas, Spain
[b] SENSAVAN, Instituto de Tecnologías Electrónicas y de la Información (ITEFI), CSIC, 28006 Madrid, Spain
*Corresponding Author, email: d.m@csic.es; Tel.: +34-91-561-88-06 (ext. 920422)

1. Abstract

A theoretical study of the interaction between magnetostatic spin waves (MSWs) and magnetic nanoparticles (MNPs) is presented. The propagation of the MSW occurs on an yttrium iron garnet (YIG) thin film, and the MNPs are encapsulated in a tube. The operation of the sensor is based on the fact that a gas interacting with the nanostructures produces a change in their magnetization, and this in turn produces a measurable change in MSW propagation.

The gas sensor structure is studied and characterized theoretically, through simulations. These simulations are also used in order to optimize the device through changes in the geometry, reaching sensitivities of 38 ppm in the magnetization of the sensitive material.

2. Introduction

Certain gases in breath can indicate health problems. Some of these gases, known disease markers, can be ammonia (NH_3), hydrogen sulfide (H_2S), nitric oxide (NO) and volatile organic compounds (VOCs) such as acetone (CH_3COCH_3), toluene ($C_6H_5CH_3$) and pentane (C_5H_{12}) [1].

Recently, magnonic gas sensors that takes advantage of the high sensitivity of MSWs to detect change in magnetic properties of nanoparticles, caused by an interaction with gases, were developed [2]. Due to the inherent properties of magnetic materials, new contactless sensors can be developed, where the sensitive material, MNPs, is separated from the transducer, YIG. A wide variety of magnetic materials, such as ferrites, can be used as sensitive layers. Thus, this device would allow the sensitive layer to be easily changed, increasing the number of responses.

3. Experimental

The transducer was based on a 2 cm x 1 cm ferrimagnetic sample consisting of a 7 μm thick YIG film on a gallium gadolinium garnet (GGG) substrate. The bias magnetic field is applied through a permanent magnet with a direction of magnetization perpendicular to the YIG plate, which results in the propagation of the MSW along the film. The design of the sensor consists of a cylindrical tube of 1 mm radius and 2 cm long, which would contain the MNPs ($ZnFe_2O_4$) on the YIG sample. The gases of interest would pass through the tube and their presence would be measured by the change in the frequency of the spin wave due to the variation of the magnetization of MNPS. A diagram of the sensor is represented in Fig. 1.

4. Results

Different simulations were carried out to optimize the response of the sensor. In order to achieve this, the placement of the MNPs tube with respect to the YIG was modified, and the resulting magnetic field in the YIG film was are calculated.

The frequency response of the MSW in YIG were used for the simulations (Fig. 2). To perform a sensitivity interpolation, the changes in the magnetic field on the YIG were studied. To this propose, the original BH curve was obtained and transducer sensitivity was characterized by changing the magnetization of the MNPs between 50% and 150% (Fig. 3), which was calculated for different distances of the MNPs with respect to the YIG layer. Fig. 4 shows the magnetic field due to interaction of the original MNPs. To calculate the magnetic sensitivity of the device, its noise was previously measured (100 Hz/min), and a minimum frequency response as three times higher than the noise signal was considered. An optimum design was obtained when nanoparticles are between the magnet and YIG at -0.15 cm from the YIG. Therefore, a sensitivity of 38 ppm in the magnetization of the MNPs was achieved, as seen on Table 1. According to this result, contactless chemical sensors with very high sensitivity could be developed.

5. Conclusions

This work proposes an innovative, simple and low cost contactless chemical sensor based on the combination of magnetic nanoparticles, as a sensitive material, encapsulated in a tube and a magnetostatic surface wave device as a transducer. Simulations showed a high sensitivity, 38 ppm, for perturbations in the magnetization of MNPs. Therefore, we believe that the solution presented opens a new and promising field of research in “contactless gas sensors”.

References

[1] Yoon, Ji-Wook, and Jong-Heun Lee. "Toward breath analysis on a chip for disease diagnosis using semiconductor-based chemiresistors: recent progress and future perspectives." Lab on a Chip 17.21 (2017): 35373557.

[2] D. Matatagui, et al. "Magnonic sensor array based on magnetic nanoparticles to detect, discriminate and classify toxic gases." Sensors and Actuators B (2017), 240: 497-502.

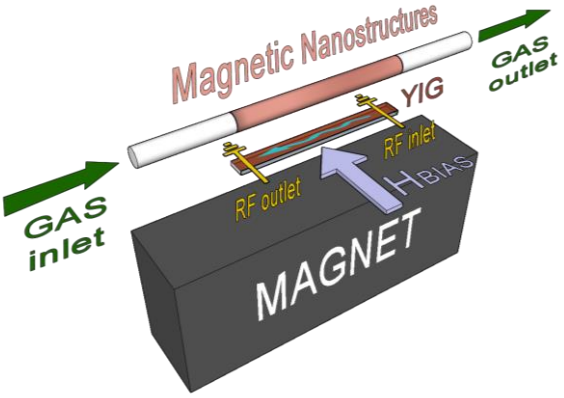

Fig.1. Diagram of the contactless gas sensor.

(a)

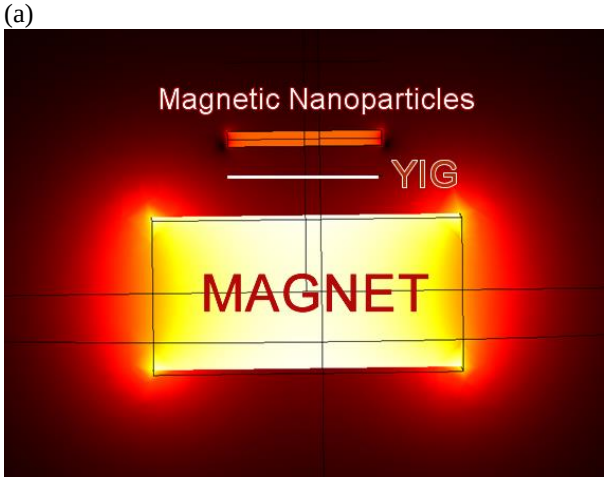

(b)

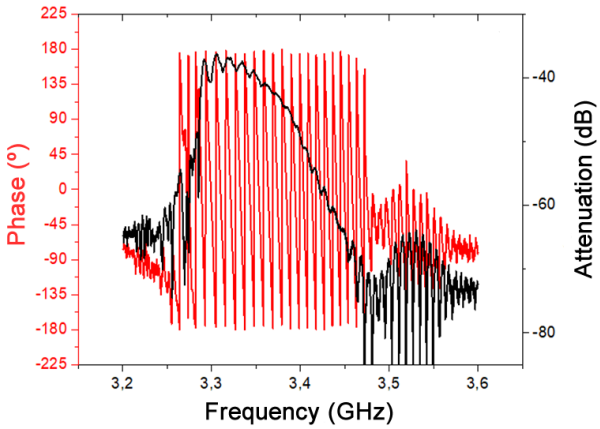

Fig.2. (a) Simulation of the experiment. The bias magnetic field on the YIG is generated by a magnet that is affected by MNPs. (b) Frequency response of the MSW device.

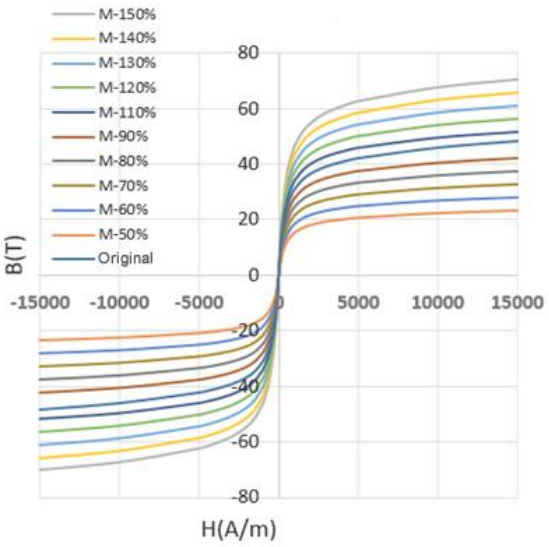

Fig.3. BH curves representing magnetizaion change of the MNPs between 50% and 150% from original measurement

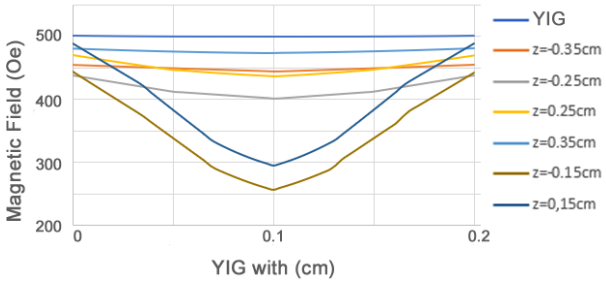

Fig.4. Magnetic field in the YIG for different positions of the original MNPs.

	Above		Below	
Position (cm)	0.25	0.15	-0.25	-0.15
Sensitivity (ppm)	229	63	82	38

Table 1. Sensitivity for different MNPs positions.

Automation and optimization device for the fabrication of sensors with nanomaterials.

Carlos Sánchez-Vicente[1,2], José Pedro Santos[1], Alfredo Azabal[2], Santiago Ruiz-Valdepeñas[2], Jesús Lozano[3], Isabel Sayago[1], José Luis Sanjurjo[1]

[1] Institute of Physics Technology and Information (ITEFI-CSIC), 28006 Madrid, Spain
[2]Up Devices and Technologies, 28021 Madrid, Spain
[3]Industrial Engineering School, University of Extremadura, 06006 Badajoz, Spain
Corresponding author: jp.santos@csic.es

1. Abstract

This work presents a device, dropcaster, developed to automate and optimize the deposition process of the sensitive layer of gas sensors by drop-casting [1]. It is designed for the development of sensors in the research phase of different materials and studying their behavior and response to different gaseous compounds.

As shown in Figure 1, this device is composed of a stepper motor controlled by a Raspberry Pi 4 Model B. In turn, this motor controls the advance of the plunger of the microsyringe (Hamilton 701 of 10µL and with a 26sG gauge needle), where the solution is located. The plate containing the sensor is placed under the syringe. In order to position the tip of the needle more precisely on the sensor, the equipment has a 1080p HD and 5MP mini webcam with manually adjustable focus. Figure 2 shows an image taken by the mini camera during deposition of the material on the sensor surface.

It also incorporates an LCD display with which different parameters of the deposition process can be programmed and configured. This equipment can be adapted according to the syringe type to be used depending on the sensor characteristics. With this device, a substantial improvement has been achieved in the sensor manufacturing process using the drop-casting technique. Two types of micromachined silicon substrates developed by CNM (National Microelectronics Centre, Barcelona) [2] and LAAS (Laboratory for Analysis and Architecture of Systems, Toulouse) [3] are used for the different projects. These devices incorporate four microhotplates with an area of less than 160 mm^2 each. The small size of the membranes and the fragility of the silicon substrate made manual deposition difficult. Therefore, by improving precision, we avoid possible electrical problems in the sensor contacts or that the tip of the needle may perforate the membrane in some of the depositions

Besides the time optimization achieved by automating the process, more precise depositions can be made only in the sensitive area of the sensor. This can be seen in Figure 3, which compares a deposition performed manually and another using the dropcaster. Besides, the precision of the dropcaster makes it possible to use different materials to deposit on each membrane. As observed in Figure 3.a, the materials deposited on each membrane overlap each other. Whereas in Figure 3.b, the deposited material is only in the sensitive zone of the sensor. In Figure 3.b, membranes with and without functionalization are shown.

It was also possible to observe an improvement in the distribution of the nanomaterials on the sensor surface and, therefore, improve the response, compared to previous results as shown in Figure 4 for TiO_2 nanoparticle sensor. Finally, this device has the advantage of being much cheaper than other commercial devices that can be used for this purpose.

This device was used to deposit different types of solutions with ZnO, TiO_2, SnO_2 or ITO nanoparticles, and in some cases with dopants such as Pd, Pt, Au or Rh. 2D materials such as graphene, MXenes or MoS_2 were also deposited.

References

[1] C. Van Nguyen, R. Bartali, L. Crema, and G. Speranza, "Effect of glass surface treatments on the deposition of highly transparent reduced graphene oxide films by dropcasting method," *Colloids Surfaces A Physicochem. Eng. Asp.*, vol. 498, pp. 231–238, Jun. 2016.

[2] C. Sánchez-Vicente *et al.*, "Graphene-doped tin oxide nanofibers and nanoribbons as gas sensors to detect biomarkers of different diseases through the breath," *Sensors (Switzerland)*, vol. 20, no. 24, pp. 1–12, Dec. 2020.

[3] A. Masa, Sergio; Robés, Diego; Hontanon, Esther; Lozano, Jesús; Eqtesadi, Siamak; Narros, "Sensors & Transducers Graphene-Tin Oxide Composite Nanofibers for Low Temperature Detection of NO," in *Conference: Sixth International Conference on Sensors and Electronic Instrumentation Advances (SEIA' 2020)*, 2020.

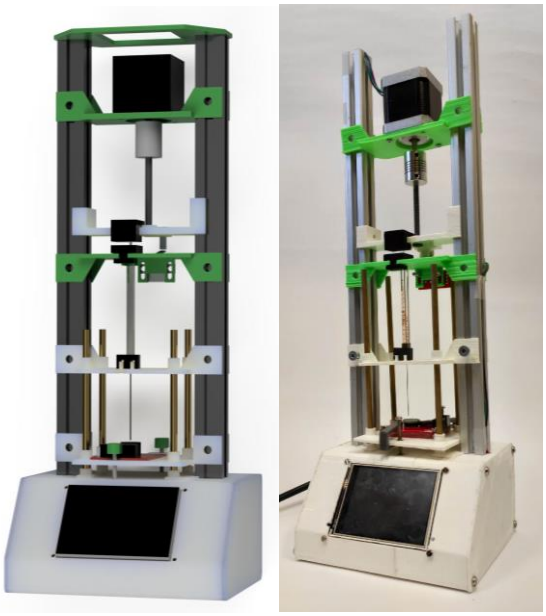

Fig.1. Dropcaster. (a) 3D design. (b) Dropcaster assembly

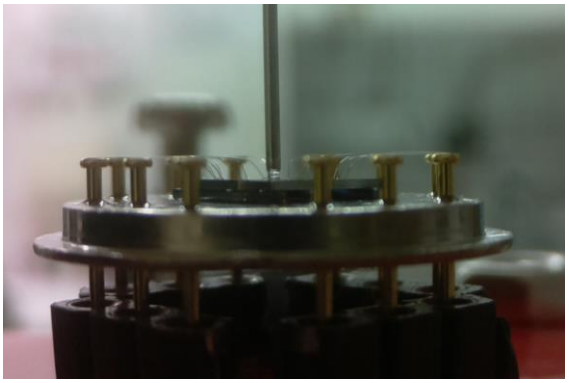

Fig.2. Deposition of the material on the sensor surface, as seen from the mini camera, incorporated into the dropcaster.

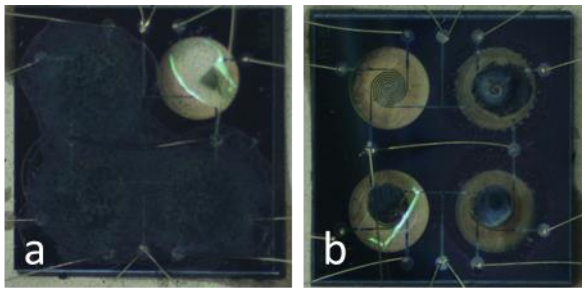

Fig.3. Deposition performed on a LAAS sensor.
(a) manually. (b) Using the dropcaster

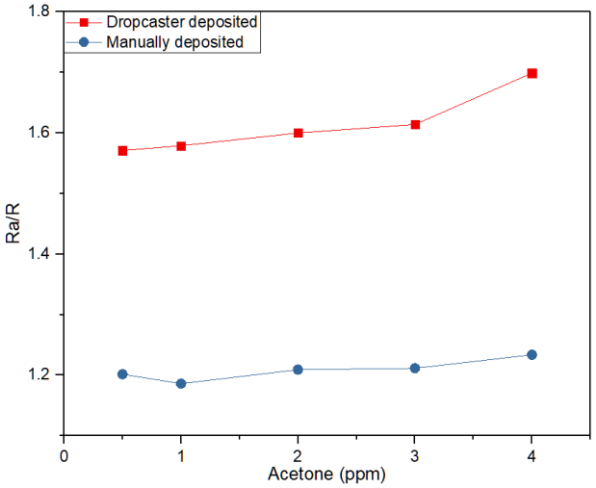

Fig.4. The difference in response between the manual deposition method and the dropcaster.

Technology Developments on iLGAD Sensors at IMB-CNM

Albert Doblas Moreno

A. Doblas [(1)*], D. Flores [(1)], S. Hidalgo [(1)], G. Pellegrini [(1)], D. Quirion [(1)] and I. Vila [(2)]
[(1)] Instituto de Microelectrónica de Barcelona IMB-CNM (CSIC), [(2)] Instituto de Física de Cantabria IFCA (CSIC-UC)
[*] Corresponding author e-mail: albert.doblas@imb-cnm.csic.es

1. Introduction

In this contribution, we will present the status of the technological developments at IMB-CNM to fabricate Inverse Low Gain Avalanche Detectors (iLGAD) for pixelated detectors. This iLGAD sensor concept is one of the most promising technologies for enabling the future 4D tracking paradigm that requires both precise position and timing resolution. In the iLGAD concept, based on the LGAD technology, the readout is done at the ohmic contacts, allowing for a continuous unsegmented multiplication junction. This architecture provides a uniform gain over all the active sensor area. This concept was successfully demonstrated in a first generation of 300 µm thick iLGAD sensors. In the second generation, we have fabricated thick iLGAD sensor optimizing the periphery for X-Ray irradiations. Currently, we are developing 50 µm thick pixelated iLGADs optimized for timing detection with a periphery design able to sustain higher electric fields and a simpler single-side manufacturing process.

2. LGAD Technology

Based on the APD concept, the Low Gain Avalanche Detector (LGAD) is an avalanche detector with the p-type diffusion less doped than an APD [1]. This p-type layer is called multiplication layer. This less doped diffusion provides the detector to have a lower gain which lead to a low readout noise, avoid cross talk and the gain is linear in the entire voltage regime. Therefore, we can achieve enough gain to amplify the signal without increase the noise. Energy and dose of the boron implantation for the multiplication layer are the most important parameters in a LGAD. Small changes can lead to huge modifications in the gain and the breakdown voltage of the devices. Therefore, the doping profile must be optimized to reach the optimal gain. In order to measure time and position simultaneously, LGADs can be segmented into strips or pixels. In that case, the n+/p region is segmented along all the active region, which is the area where all the current is multiplied.

3. Inverse LGAD Concept

Segmentation of a LGAD entail the appearance of the fill factor problem. Since the junction is segmented, a gap exists between pixels, where no multiplication takes place. Thus, fill factor is defined as the ratio between the multiplication area and the total active area. In order to reach a 100% fill factor, the Inverse Low Gain Avalanche Detector (iLGAD) was proposed [2]. Figure 1 shows a cross-section of the iLGAD design compared with the LGAD technology. Here, the ohmic anode is segmented into small pixels or strips. Therefore, the collection is be made by the anode and, as a contrary of LGADs, holes are collected.

4. Inverse LGAD for X-Ray Irradiations

In order to satisfy the demand of an iLGAD for X-Ray applications, we have designed a suitable periphery that has a better performance against X-Ray irradiations than the first generation of iLGAD. Figure 2 shows the cross-section of the second iLGAD generation.

5. Inverse LGAD for Timing Applications

In iLGADs, the collection is made by holes and then, the first generation of iLGADs is not suitable for timing applications. We are developing a new generation of iLGADs optimized for timing applications with an easier manufacturing process. Figure 3 shows a cross-section of this sensor concept.

6. Acknowledgements

This activity is carried out in the context of the RD50 (CERN) and AIDAInnova (EU) projects, with the participation of CERN-SDD, IFAE, IFCA, IMB-CNM, NIKHEF, University of Hamburg, University of Santiago de Compostela and University of Zurich. In addition, it is partially supported by the Spanish Ministry of Science under FPA2017-85155-C4-1-R and FPA2017-85155-C4-2-R grants.

References

[1] Pellegrini, G., et al. "Technology developments and first measurements of Low Gain Avalanche Detectors (LGAD) for high energy physics applications." Nuclear Instruments and Methods in Physics Research Section A: Accelerators, Spectrometers, Detectors and Associated Equipment 765 (2014): 12-16.
[2] Pellegrini, G., et al. "Recent technological developments on LGAD and iLGAD detectors for tracking and timing applications." Nuclear Instruments and Methods in Physics Research Section A: Accelerators, Spectrometers, Detectors and Associated Equipment 831 (2016): 24-28.

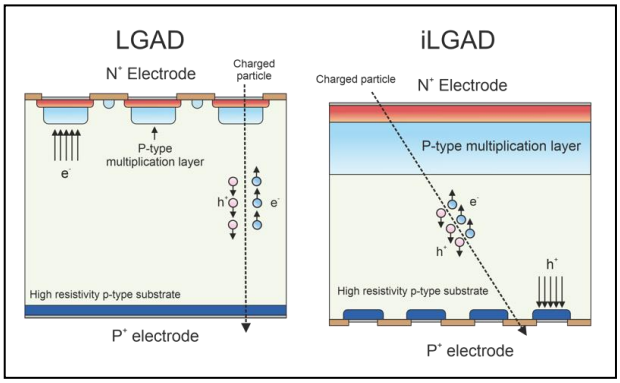

Fig.1. Comparison between LGAD and iLGAD technologies. In a LGAD, the multiplication region is pixelated collecting electrons, while p+ electrode is segmented in an iLGAD providing holes collection. A 100% fill factor is achieved in iLGAD technology. The sketch is not in scale.

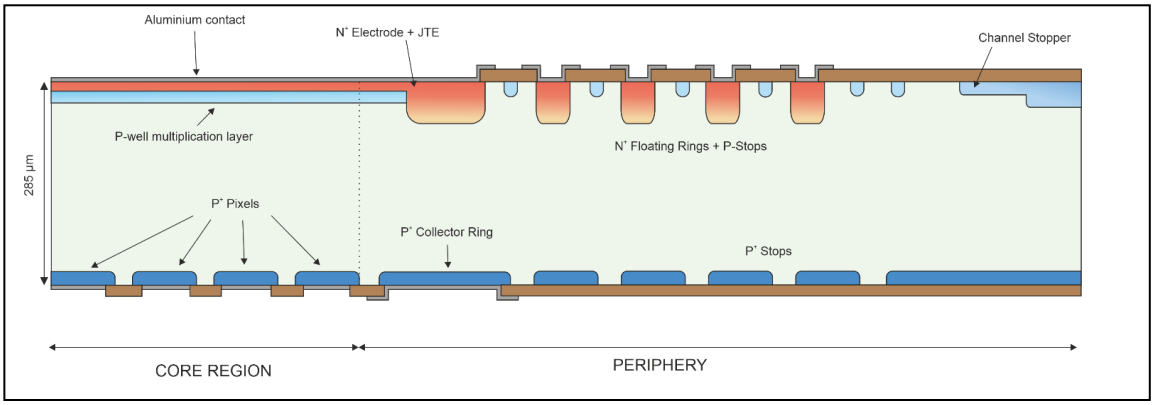

Fig.2. Schematic cross-section of the periphery design of the second generation of iLGAD at IMB-CNM. The periphery has been designed with TCAD tools in order to sustain higher voltages in the presence of X-Ray irradiations.

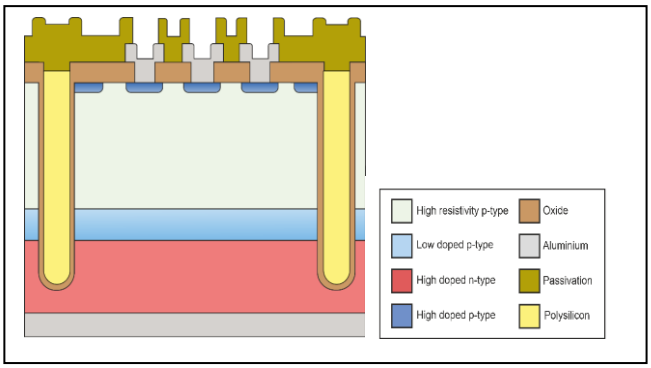

Fig.3. Schematic cross-section of the periphery design of the third generation of iLGAD at IMB-CNM. The manufacturing process is easier than previous generations since the process is single-sided. Active area is properly isolated with trench-technology.

Highly-packed arrangement of an all-Si based thermoelectric microgenerator

Denise Estrada-Wiese[a], Marc Dolcet[a], Robert Soriano[a], Joaquín Santander[a], Marc Salleras[a], Luis Fonseca[a], Jose-Manuel Sojo[b], Alex Morata[b], Albert Tarancon[b]

[a] *IMB-CNM (CSIC), C/Til·lers s/n Campus UAB, 08193 Bellaterra, Spain*

[b] *IREC, Jardins de les Dones de Negre 1, 2ª pl, 08390 San Adrian del Besos, Barcelona, Spain*

denise.estrada@imb-cnm.csic.es *luis.fonseca@imb-cnm.csic.es*

1. Abstract

An advanced and efficient interconnection between devices, systems and services through the Internet of Things (IoT) enables remote sensing and control for many applications. Powering IoT devices requires different strategies for energy autonomy, which can be realized in various ways. Energy harvesting techniques based on thermoelectric generators stand out as a sustainable, cost-effective and convenient alternative to batteries for long term autonomy when a heat source is present. When interacting with small-scale objects or phenomena, reducing these thermoelectric generators to the microscale and pursuing a low footprint is a challenge. Si-MEMS technology offers an interesting path to fabricate environmentally sound thermoelectric microstructures. Contrary to the typically used thermoelectric semiconductor materials, such as chalcogenides (e.g. Bi2Te3) with a high thermoelectric performance (but incompatible with miniaturization techniques), Si behaves poorly thermoelectrically limiting the performance of thermal- to- electrical energy conversion due to its high thermal conductivity. However, all-Si based µTEGs (a collection of interconnected micro-thermocouples) can be produced thanks to micromachining for better thermal management at device level and nanostructuring for lowering the thermal conductivity of Si at functional material level. In the past, single micro-thermocouples with an effective area of 2 mm^2 were fabricated in our group producing power densities of several tens of nW/cm^2 [1, 2]. Each micro-thermocouple is formed of a suspended microplatform surrounded by a bulk Si rim that are bridged together by bottom-up silicon nanowires acting as the thermoelectric active material. The nanowires capture a fraction of the available temperature difference transforming the heat flow into an electric current that is collected through tungsten (W) paths, closing the thermoelectric circuit in a uni-leg configuration. The obvious next step is to efficiently combine several of those micro-thermocouples to transform a promising power density into a usable absolute power.

The present work reports on the micro-thermocouples design modification that enables the reunion of up to 50 micro-thermocouples in a small footprint chip (0.5 cm^2) for maximum packing density and multiplied power output. Ten elongated micro-thermocouples, each one corresponding to the parallel arrangement of five units of the described micro-thermocouples, fits in this compact assembly, as shown in Fig.1.

When a heat exchanger is not present, the fabricated device reaches power densities of 60 nW/cm^2 if all micro-thermocouples are connected electrically in series for an available heat source at 125 ºC (Fig. 2). The power output can be significantly enhanced by integrating a heat exchanger, which contacts the suspended regions of the µTEG reducing the thermal resistance with the ambient and cooling them much more effectively. A proper way to assemble the heat exchanger to the µTEGs is currently being devised. When successful, devices in the cm^2 size will be able to produce absolute power of tens of µW in real harvesting scenarios, as has been shown in previous work [3]. Thus, the fabricated microgenerator provides a promising miniaturized all-Si thermal harvester for advanced IoT systems operating in low-grade waste heat environments.

References

[1] D. Dávila et al, " Monolitically integrated thermoelectric energy harvester based on silicon nanowire arrays for powering micro/nanodevices" Nano Energy, vol. 1, pp. 812-819, November 2012.

[2] I. Donmez-Noyan et al, "SiGe nanowire arrays based

thermoelectric microgenerator" Nano Energy vol. 57, pp. 492-499, March 2019.
[3] I. Donmez-Noyan et al, "All-silicon thermoelectric micro/nanogenerator including a heat exchanger for harvesting applications" J. Power Sources, vol. 413, pp.125-133, February 2019.

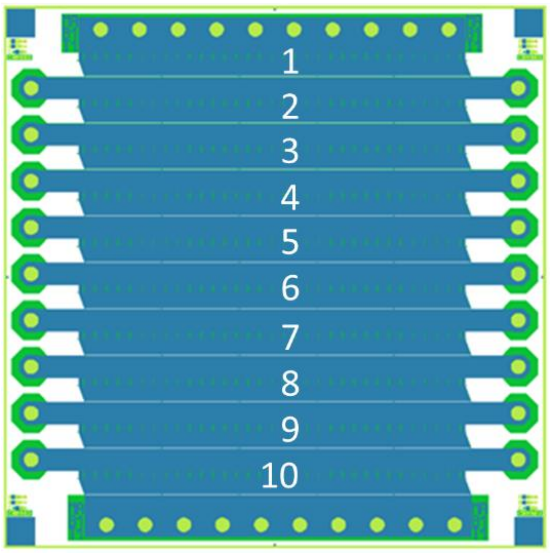

Fig.1. Scheme of the fabricated device featuring 10 long micro-thermocouples connected electrically in series and that can be independently tested.

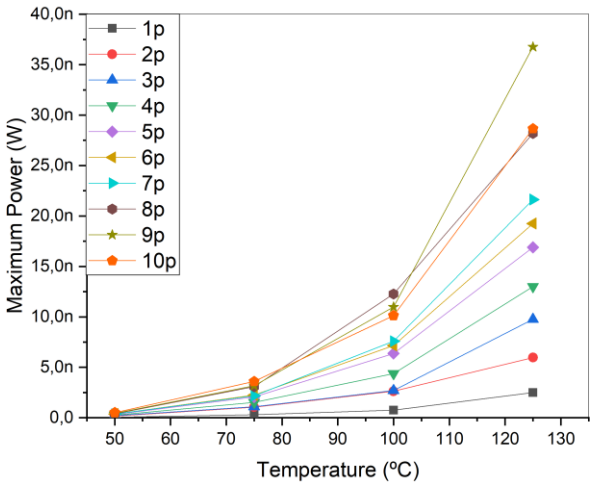

Fig.2. Maximum power obtained for the different number of series-connected micro-thermocouples (up to ten of them) at different hot source temperatures.

Proton Low Gain Avalanche Detector (pLGAD) for Low Energy Particles Detection

Albert Doblas Moreno

A. Doblas [(1)*], W. Khalid [(2)], D. Flores [(1)], S. Hidalgo [(1)], G. Pellegrini [(1)], D. Quirion [(1)], M. Valentan [(2)]
[(1)] Instituto de Microelectrónica de Barcelona IMB-CNM (CSIC)
[(2)] Stefan Meyer for Subatomic Physics of the Austrian Academy of Sciences (OAW)
[*] Corresponding author e-mail: albert.doblas@imb-cnm.csic.es

1. Introduction

Semiconductor detectors have been widely used as radiation detectors in High-Energy Physics (HEP) and in synchrotron radiation. Due to their intrinsic and linear gain, Low Gain Avalanche Detector (LGAD) sensors were proposed as radiation detectors for HEP experiments [1]. In order to fulfill a fill factor of 100% in segmented detectors, Inverse Low Gain Avalanche Detectors (iLGAD) were first proposed and successfully fabricated by IMB-CNM [2]. Here, the segmentation is made by the ohmic contact and then holes are collected. With the LGAD technology, we have been able to detect high-energy particles. Nevertheless, in order to detect low penetrating particles, we propose the so-called Proton Low Gain Avalanche Detector (pLGAD), which is based on the LGAD technology and it is adapted for low energy particles detection (~ 15 keV), specially for proton experiments. In this contribution, we are presenting the pLGAD concept, the design simulations and the proposal for the first pLGAD generation.

2. Proton LGAD Concept

Low energy particles penetrate 1µm in silicon, and therefore, the detection will be made at the surface of the detector. For this reason, a collection layer is included in the pLGAD design, as a difference of the LGAD technology. Figure 1 shows a comparison between the pLGAD and iLGAD technologies. Since the low penetrating particles do not damage the bulk of the detector, we use n-type substrates, as contrary of the LGAD technology. Therefore, in the pLGAD we have a n-type multiplication layer underneath a p-type collector layer and the collection is made by electrons at the segmented ohmic contact. On top, a p+ layer is diffused. Since we detect the particle in 1µm, we must define a shallow junction between the p+ contact and the p-type collection layer. Moreover, the entrance window must be as thinner as possible in order to assure that all the energy is deposited in the sensor and not in the non-active layers.

3. Proton LGAD 1D Simulations

The most important technological parameters in LGAD technology are the dose and energy of the p-type multiplication layer. The values of these parameters are critical and small changes can lead to huge differences in terms of the device performance. There is a trade-off between gain (G) and breakdown voltage (V_{BD}). We expect that the device is able to sustain a low gain during a high voltage regime. One-dimensional simulations have been used in order to determine the optimal trade-off of the pLGAD. Figure 2 shows the G-V_{BD} trade-off for the simulated pLGAD.

4. Proton LGAD First Generation at IMB-CNM

We propose the pLGAD first generation at IMB-CNM. For the first approximation, we use standard pad-like detectors (without segmentation at the ohmic side) in order to test the n-type LGAD technology. We are using high resistivity n-type 285 µm wafers and the fabrication steps are the same as LGAD technology. In the first generation, we are not including the p-type collector layer in order to determine first the optimal n-type multiplication layer dose. Later, we are preparing the second generation of pLGAD. Figure 3 shows a cross-section of the pLGAD second generation. Here, we are including the p-type collector layer, the ohmic contact is segmented and we are using BF_2 for the p+ shallow contact. The shallow contact has a depth of 90 n and therefore all the charge will be deposited in the collector layer.

5. Acknowledgements

This activity is carried out by the Spanish Ministry of Science under FPA2017-85155-C4-2-R grants.

References

[1] Pellegrini, G., et al. "Technology developments and first measurements of Low Gain Avalanche Detectors (LGAD) for high energy physics applications." Nuclear Instruments and Methods in Physics Research Section A: Accelerators, Spectrometers, Detectors and Associated Equipment 765 (2014): 12-16.
[2] Pellegrini, G., et al. "Recent technological developments on LGAD and iLGAD detectors for tracking and timing applications." Nuclear Instruments and Methods in Physics Research Section A: Accelerators, Spectrometers, Detectors and Associated Equipment 831 (2016): 24-28.

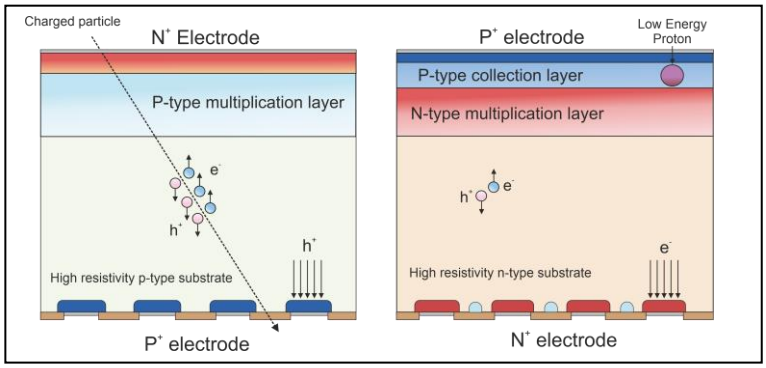

Fig.1. Comparison between iLGAD and pLGAD technologies. In the pLGAD electrons are collected, as contrary of iLGAD, where holes are collected at the segmented ohmic contact. In pLGAD we use n-type high resistivity substrate and a p-type collector layer is added to collect all the charge deposited by the low energy particle.

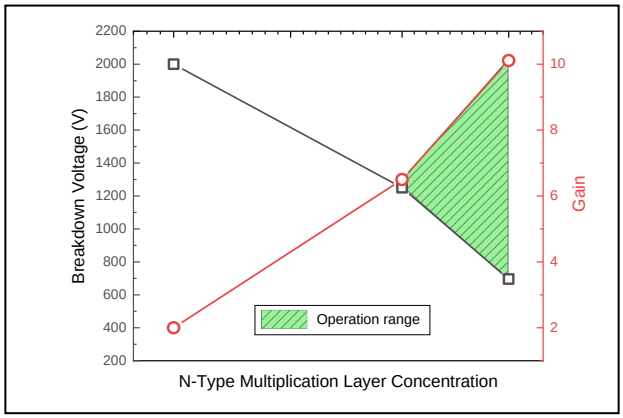

Fig.2. Breakdown voltage and gain trade-off for a simulated pLGAD. We have been able to find an operation range in which the device can sustain high voltages with a low gain.

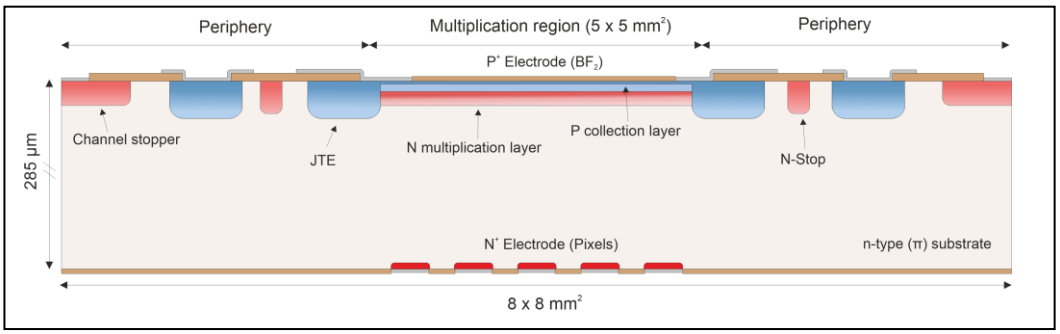

Fig.3. Schematic cross-section of the periphery design of the second generation of pLGAD at IMB-CNM. The manufacturing process is similar as the iLGAD, but there is an added complexity due to the necessity to define a shallow entrance window and two dose/energy values for both p/n collection/multiplication layers.

Development of a Highly Sensitive and Flexible Graphene Foam Based Pressure Sensors

C. Iain Douglas,[1] C. García Núñez,[1] D. Gibson,[1] M. Caffio[2]

[1]Institute of Thin Films, Sensors and Imaging, University of the West of Scotland, Scottish Universities Physics Alliance, Paisley, PA1 2BE, United Kingdom.
[2]Integrated Graphene Ltd., Euro House, Stirling, FK8 2DJ, United Kingdom
Contact authors: connor.douglas@uws.ac.uk and des.gibson@uws.ac.uk

Pressure sensors are widely used devices in a variety of industries from automotive, medical, industrial and consumer devices. These applications can range from ultra-sensitive e-skin, touch screen displays, medical diagnostics and health monitoring [1]. To compete with current industrial pressure sensors, a new easily fabricated, reproducible, and highly sensitive pressure sensor compatible with temperature sensitive substrates (plastic, fabrics, paper etc) is required. Currently flexible pressure sensors are primarily based on capacitive, resistive and piezoelectric methods. Capacitive presents advantages such as the ability to operate with no power supply. However, drawbacks include non-linear output and sensitivity to the surrounding environment. Piezoelectric sensors are durable and self-powering. Resistive pressure sensors provide advantages over the latter designs having simpler construction, robustness and long-term stability.

Advanced materials such as graphene have been proposed as a promising material due to enhanced electric properties (fast device response, low recovery time and low power consumption), mechanical properties (high durability, conformability) providing compatibility with flexible substrates. Graphene foam (GF) is a three-dimensional (3D) high surface area nanostructure exhibiting excellent potential for development of pressure sensors. Currently graphene based resistive pressure sensors have shown high sensitivity at low pressures (<5kPa) enabling ultrasensitive detection [2]. It has also been shown that the use of graphene electrodes for capacitive pressure sensors provides a high sensitivity of $3.19 kPa^{-1}$ [3].

In this work, we show the growth of GF by a catalyst free method onto a flexible substrate without the use of a transfer process (Integrated Graphene Ltd proprietary process), and a novel structure consisting of GF embedded in polydimethylsiloxane (PDMS) used as an active layer in resistive pressure sensors.

GF were directly grown on polyimide substrates (supplier Integrated Graphene Ltd, Figure 1(a)). Morphology of the samples was characterised using SEM (Figure 1(b)). Resulting nanostructure structures, as well as the analysis of the defects density were characterised using Raman spectroscopy.

Pressure sensors were fabricated with two configurations: i) co-planar and ii) vertical structure (Figure 2(a,b)). For the co-planar configuration, inkjet printing is used to pattern two Ag electrodes at both ends of the GF pattern (Figure 2(a)). In the vertical configuration, only one electrode was inkjet-printed, whereas the other electrode consisted of a metallic electrode was deposited on top of GF surface (Figure 2(b)). Finally, PDMS was embedded in GF structure aiming to enhance the sensitivity, increase the response time and provide more robustness to resulting sensors. The sensitivity of GF sensors was studied using an electronic circuit designed to measure the voltage drop in a load resistor (*see* inset Figure 2(c)). In order to test over a variety of different pressure ranges, a precision motor mounted on a vertical stage and controlled by a home-made software, was used to actuate on top of the sensor area through a mechanical "finger" made of software material (PDMS).

GF porous structure is observed by SEM (Figure 1(b)). Further analysis determines action of the GF, particularly when voids in the GF are compressed closer together and relaxed. From applying a constant input voltage (V_{in}) of 5 V and using a load resistor with a value similar to the resistance of GF (i.e. R_{load}=25Ω) the V_{out} was observed to decrease with the applied pressure (Figure 2(c)), indicating that the resistance of GF (R_{GF}) increases with pressure. From this result, it is postulated that the voids size increased with the pressure due to the expansion of the PDMS layer integrated in GF. PDMS layer presented various roles, comprising protection to GF, faster recovery times, and more sensitivity to a wider range of pressures compared to bare GF. Characterisation showed a sensitivity of 0.0418 mV/kPa over a range of pressures from 1 to 50 kPa.

References

[1] Y. Zang et al. Materials Horizons 2 (2015) 140.
[2] H. Tian et al. Scientific Reports 5 (2015) 1.
[3] J. Yang et al. ACS Appl. Mater. Interfaces 11(2019)14997.

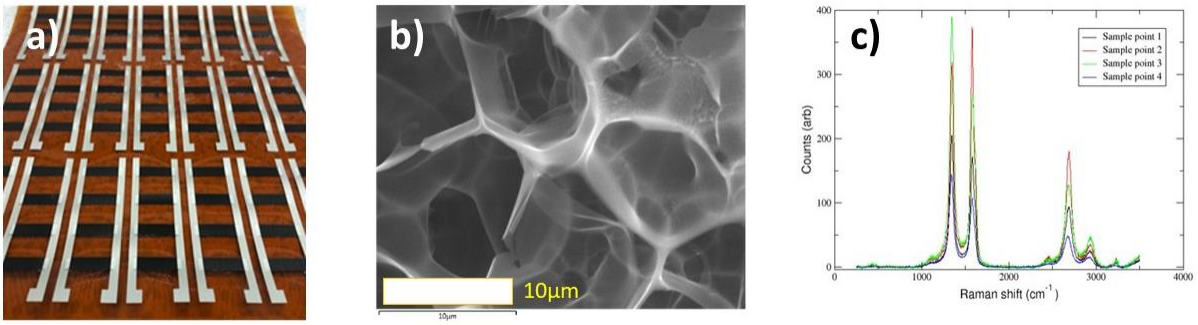

Figure 1. (a) Array of GF samples grown on polyimide substrates. Ag inkjet printed electrodes can be seen at each end of the GF pattern. (b) SEM image of GF, showing porous structure providing the high sensitivity of the pressure sensors. c) Raman spectra of the GF measured at four different points (mapping).

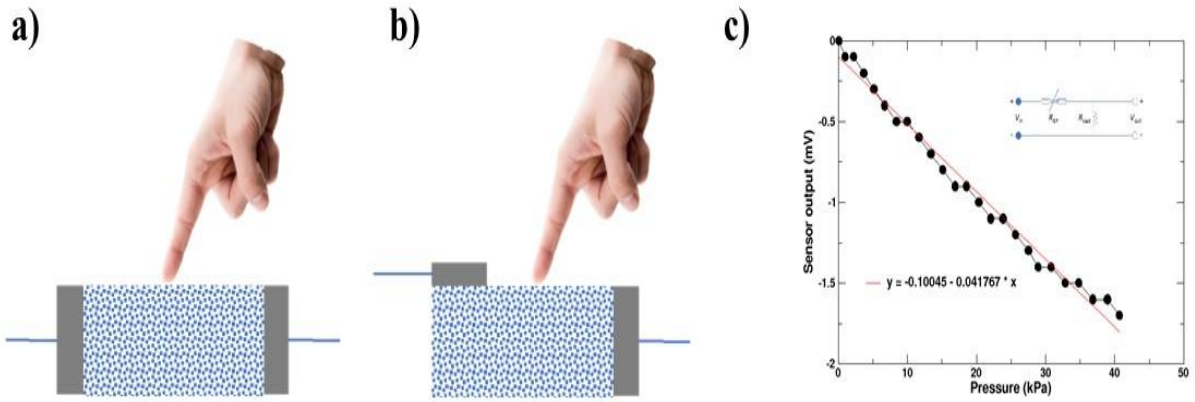

Figure 2. 2D schematic of pressure sensors with (a) coplanar (b) vertical configurations. (c) Graph of sensor output (mV) vs pressure (kPa) for the planar configuration; inset: electric circuit used to characterise the electric response of sensors subjected to pressure.

DEVELOPMENT OF HYBRID PIEZOELECTRIC MICRODEVICES FOR BIOAPPLICATIONS

Laura Lefaix[1], Andreu Blanquer[2], Lucie Bacakova[2], Jaume Esteve[1] and Gonzalo Murillo[1*]

[1]Instituto de Microelectrónica de Barcelona (IMB-CNM, CSIC), Barcelona, SPAIN
[2]Institute of Physiology of the Czech Academy of Sciences, Prague, CZECH REPUBLIC
*Dr. Gonzalo Murillo, tel. +34 935947700; email: gonzalo.murillo@csic.es

1. Introduction

The transmembrane potential is the voltage difference across the plasmatic cell membrane. Ion channels in the membrane allow a balance of the intracellular and extracellular ionic concentration. Several channels can be controlled through electrical stimuli. Thus, by affecting these signals, processes on cellular behaviour and intercellular communications can be guided [1].

This is the field of study of bioelectronic medicine, where the use of electrodes is extended for the recording and application of these signals. To reach a single-cell transmission of the electrical impulse, the use of acoustic energy transmission among piezoelectric transducers is being explored. Piezoelectric materials allow a reduction on the size without the negative side effects that may entail the use of wireless electromagnetic devices. Piezoelectric nanogenerators (NGs) are able to convert mechanical energy produced by tiny strain into electricity. Among piezoceramics, which have a stronger piezoelectric effect, zinc oxide (ZnO) is easy to synthesize through hydrothermal growth and has been proved to be biocompatible in several studies [2]. We propose the use of hybrid piezoelectric microdevices, which consist of piezoelectric ZnO nanosheets (NSs) integrated on silicon microparticles, for their use in bioelectronic applications (Fig. 1).

2. Fabrication of Microparticles

In this work, millions of silicon microparticles with volumes below 100 μm^3 were fabricated at a wafer level through microfabrication techniques.

The microfabrication process comprehends (1) the oxidation of the wafer (1 µm SiO_2); (2) aluminium deposition through e-beam evaporation; (3) sputtering of aluminium nitride, AlN (100 nm); (4) patterning of an array of squared 3 x 3 μm^2 micro particles, by using 6512 positive resist; (5) an anisotropic etching step to create regular microparticles and (6) an isotropic DRIE etching of sacrificial SiO_2 to allow the peeling-off of the microparticle.

3. Synthesis of ZnO Nanostructures

After the microfabrication process, 2D ZnO NSs were grown on top of the microparticles through hydrothermal growth. The wafer was fixed in a borosilicate glass reactor by using polyetheretherketone screws and immersed upside-down in a solution of 2:1 $ZnNO_3 \cdot 6(H_2O)$:HMTA. The reactor was later placed in an oven at 80 ºC for 9 h. Hexagonal ZnO NSs with a crystalline wurzite structure and a thickness of 72 ± 25 nm and diameter of 443 ± 76 nm were grown covering the AlN surface [3,4]. Then, the resulting hybrid microdevices were peeled off from the wafer by using a patented technique. After the collection, a suspension of more than 10^6 microdevices/mL per 1 x 1 cm^2 chip was obtained.

3. Finite Element Modelling (FEM)

FEM simulations using COMSOL Multiphysics 5.4. (COMSOL, Stockholm, Sweden) allowed to model the electromechanical behaviour of the cell-NS interphase. We could determine the electrical response of the ZnO NSs to different forces applied by the cells. Through FEM simulations it was shown that these microdevices were able to produce electric fields in response to mechanical stresses or ultrasonic waves. The voltage produced depends on the NS thickness and the cell force (Fig. 2.).

4. Biological Assessments

Human osteosarcoma cells (Saos-2 cells) were cultured with a concentration $1 \cdot 10^5$ microdevices/well and incubated for 1, 3 and 7 days. We validated the microdevice cytocompatibility by means of a live/dead staining. An internalization assay was carried out to study the different positions that the microdevices can take with respect to the cell: internalized or outside the cell, facing up or upside down. Several microdevices can be in contact with a single cell, and thus, a large number of NSs are able to stimulate it. We observed that a 49% of cells were in contact with one microdevice, the 25% with two and the 12% with three. The 47% of the cells that had a single microdevice in contact did not internalized it.

References

[1] Mycielska, M. E. & Djamgoz, M. B. A. *J. Cell Sci.* 117, 1631–1639 (2004).
[2] Murillo, G. *et al*. *Adv. Mater.* 29, 1605048–160555 (2017).
[3] Murillo, G., Rodríguez-Ruiz, I. & Esteve, J. *Cryst. Growth Des*. 16, 5059–5066 (2016).
[4] Murillo, G. *et al. Nano Energy* 60, 817–826 (2019).

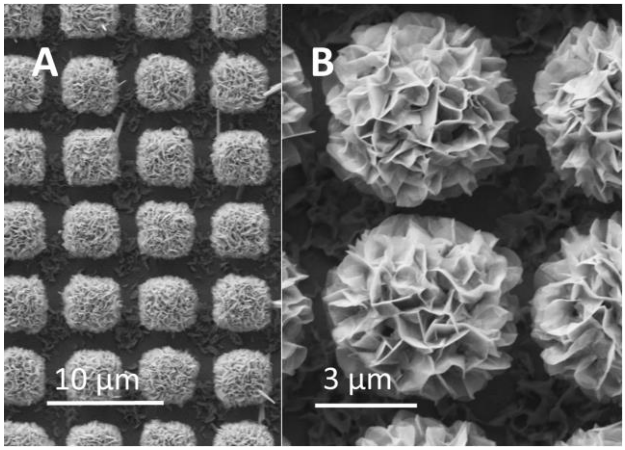

Fig.1. SEM images of the microdevices. (A) Wafer with microdevices at 5K X magnification. (B) Closer view of the microdevice with ZnO NSs grown on the top of silicon microparticles at 15K X.

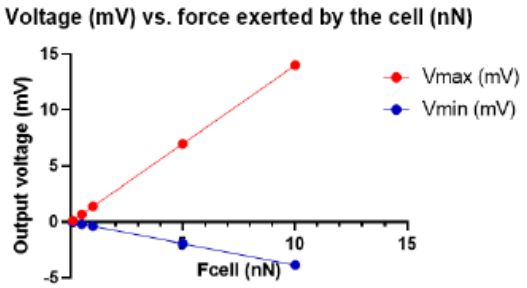

Fig.2. Graph of the simulated output voltage values produced by a single NS when a force is exerted in the perpendicular direction (y-axis) of the NS.

Low-cost voltage amplifier for biological signal acquisition through generic micro-electrode array

José A. Fontanilla, A. Luque

Dpto. Ingeniería Electrónica, Universidad de Sevilla
jfontanilla@us.es, aluque@gte.esi.us.es

1. Summary

This paper presents a generic voltage amplifier intended to be used in a platform for acquisition of electrophysiological signals through a multi-channel micro-electrode array (MEA). The design is compatible with commercially available MEAs and is intended to be used in generic experimentation platforms with multiple parallel channels for signal acquisition. The design and the preliminary experimental results, which confirm the feasibility of the design, will be presented.

2. Introduction

Micro-electrode arrays (MEAs) are devices used for the study of cellular dynamics and electrical exchanges between cultured cells, or the response of these cells to different external stimuli. A simple and reliable voltage amplifier able to interact with a variety of MEAs is required in order to provide an accessible and affordable research platform for cell study.

The electrophysiological signals of interest acquired in a MEA are in the order of tens of microvolts to some millivolts, depending on the configuration of the experiment or the type of cell or group of cells to be studied, so an amplifier with a gain between 60 and 80 dB, a good SNR, and capable of reliable and repetitive measures is needed for most applications.

Multi-stage amplifiers are typically used [1], including band-pass filters to reduce the final noise. However, few previous designs focus on providing different gains for different types of cultures, making them less flexible. Also, typical experiments require the simultaneous amplification of up to 60 signals, which makes the cost of each individual amplifier an important factor to consider.

3. Design

The design presented here will include two types of channels with different gains that can be used for different biological signals. They are a channel with a 60-dB gain using a single stage, and an 80-dB gain channel using two amplifier stages, each one with a gain of 100 times for a total voltage gain of 10.000. Both channels have fixed gains in order to simplify the design and reduce noise level. Both will be passed through a band-pass filter to reduce noise and remove unwanted DC level. Typical resistance of MEAs electrodes and traces is of hundreds of kΩ and the input impedance of the designed amplifier has been chosen to be much higher.

In the first stage of the 80-dB amplifier channel, an INA333 amplifier is used with a bandwidth of around 3.5 kHz, which is the adequate for neuron and heart cells. The amplified is then filtered by a first-order passive band-pass filter, and then amplified again using a TLC074 opamp, whose output is then filtered again with a capacitor in order to remove unwanted DC level shifts that may occur at this stage (Fig. 1).

4. Experimental results

The first test setup consists of a simple 5Vpp PWM signal with a period of 20ms and a duty cycle of 95% that was inverted in order to match the polarity of neuron spikes and then reduced in voltage, generating a 1ms, 50 μVpp pulse signal akin to that of a neuron spike. This signal was then fed to the 80-dB gain amplifier channel, and could be measured with an amplitude of around 0.5 V

For a second verification a MEA signal emulator (60MEA2100-SG, Multi Channel Systems GmbH) was used with different emulated signals representing several types of cellular activity, such as hippocampal population and neuron spikes, heart ECG and retina ERG (Figs. 2 and 3). All the signals were able to be displayed on both channels, but the 80-dB channel became saturated with the heart ECG and artificial sine signals, so in order to display them fully the 60 dB channel came into play in order to obtain accurate measurements of the different signals.

Finally, the frequency response of the amplifier was obtained (Figs. 4 and 5). Frequencies of interest of electrophysiological signals lie in the range 1-3kHz.

5. Conclusions

Preliminary tests show that the designed amplifier channels are adequate for electrophysiological signal acquisition from MEAs. The next steps are the testing with actual cell cultures with the amplifier, and the design and manufacturing of an integrated and fully functional 60-channel amplifier that can interface with any standard 49x49 mm MEA.

References

[1] F. Fambrini, M. A. Barreto and J. H. Saito, "Low noise microelectrode array signal headstage pre-amplifier for in-vitro neuron culture," 2014 IEEE Conference on Computational Intelligence in Bioinformatics and Computational Biology, Honolulu, HI, 2014, pp. 1-6, doi: 10.1109/CIBCB.2014.6845522.

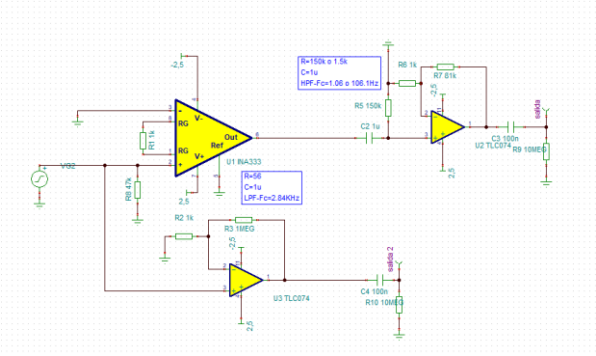

Fig. 1: Amplifier schematic

Fig. 2: Heart ECG ventricle signal after being amplified

Fig. 3: Hippocampal slice signal after being amplified

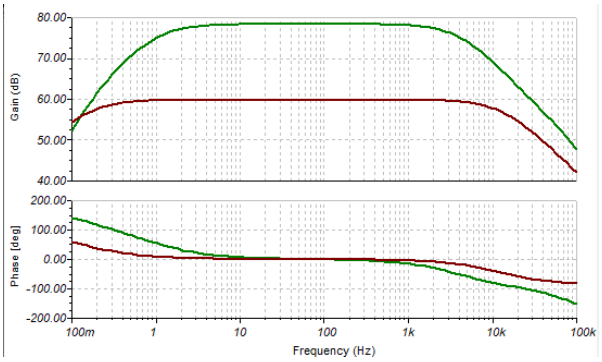

Fig. 4: Simulated frequency response diagram of the 80-dB amplifier channel (green) and 60-dB amplifier channel (red)

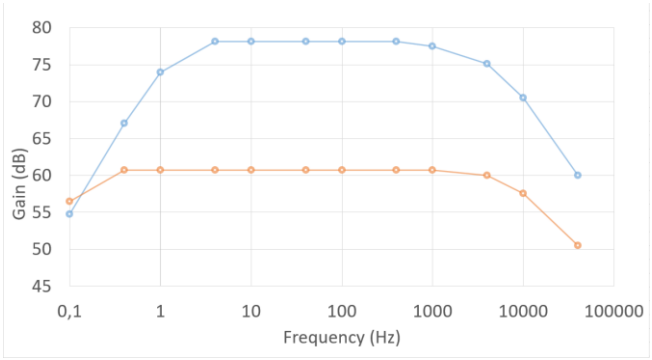

Fig. 5: Experimental frequency response of the 80-dB amplifier channel (blue) and 60-dB amplifier channel (orange)

Towards a 3D-Printed and Autonomous Culture Platform Integrated with Commercial Microelectrode Arrays

Jesús David Urbano-Gámez, Carmen Aracil, Francisco Perdigones, José Antonio Fontanilla, José Manuel Quero

Universidad de Sevilla, jurbano1@us.es , caracil@gte.esi.us.es , perdi@zipi.us.es, jfontanilla@us.es , quero@us.es

1. Abstract

Biologists and physicians need tools that may study the biological mechanisms involved in the degeneration of tissues to understand and slow down the effects of the diseases. In this way, systems able to maintain a culture in its appropriate conditions, even long term, and compatible with electro-stimulation and acquisition, open a wide field of applications. The proposed design is a low-cost portable system that accomplishes all these requirements. It is based on the integration of an MEA with electronic systems, and a culture platform, offering the possibility of electro-stimulation of a cell or tissue culture and studying its electrical activity.

2. Introduction

Focusing on the long-term cultures, most applications involve the use of incubators to maintain the culture in good conditions [1], and the use of electronic systems like Multi Channel Systems MCS GmbH where the electro-stimulation and acquisition are performed. However, there is a lack of integrated systems where both functions are combined. The development of integrated platforms with the benefits of having the contribution of nutrients, and even drugs to study their effects, while the acquisition and electro-stimulation can be carried out is fundamental [2], and would allow obtaining all the relevant information for doctors and biologists.

Regarding the culture platform, the cultures need an adequate environment to evolve in good conditions. This implies that nutrients have to be supplied in a controlled manner, and the design should be compatible with the addition of other liquids, to add drugs if required. On the side of electronics, an electrical interface is required to be in direct contact with the culture, and an electronic system has to be designed in a bidirectional manner, so the culture could be stimulated for studying its effect and being able to capture the evolution of the culture along the time of the experiment. This particular requirement should be highlighted, since monitoring the activity of the culture would allow feedback in real-time, achieving interesting results before the end of the experiment. The integration of electronics and microfluidics is the key to the challenge, using a low-cost technology easy to customize. In this way, it could be applied to many different cultures, even long term ones, which are the more stringent ones. Figure 1 shows the setup of the integration between the culture platform and MEA.

3. Microelectrode Array

The electrical module is based on two elements: the MEA one side, where the culture is in direct contact, and an electronic system, on the other, in charge of the generation and acquisition of signals.

Regarding the MEA, this device provides the substrate where the culture is deposited and offers the electrical connections to the external electronic system. For biomedical applications, obviously, the MEA has to be biocompatible.

The proposed design is based on the use of 60MEA500/30iR-Ti of Multi Channel Systems MCS GmbH [3], although it is compatible with other models. This specific model is composed of 60 microelectrodes, distributed in an array of 6x10 lines, with a separation of 500 µm. This MEA can be used for both organotypic or cell cultures.

4. Culture platform

The following requirements have to be considered in the design of the culture platform. First of all, it has to contain the nutrients, encircling the culture, so one or more wells have to be included, where the culture is deposited. Moreover, it has to be connected to the pump system in charge of controlling its delivery along with the experiment. In long-term cultures the flow used to be very slow, so a controlled syringe pump, connected to this culture platform, can be used. The culture platform must therefore have two ports, an inlet for nutrients and an outlet of waste.

Another important requirement is to design the platform for avoiding the creation of bubbles since they would result in the culture lacking nutrients and could deteriorate. In this way, a tilted surface has been designed between the inlet and outlet ports, so that in the purging process, the bubbles that are created move

towards the outlet port.
The choice of the material for the culture platform has to consider many aspects. First of all, the material has to be biocompatible, low cost, and easy to manufacture. The material chosen was a biocompatible Uniz zSG amber resin. The manufacture has been performed with 3D Anycubic Photon printer.

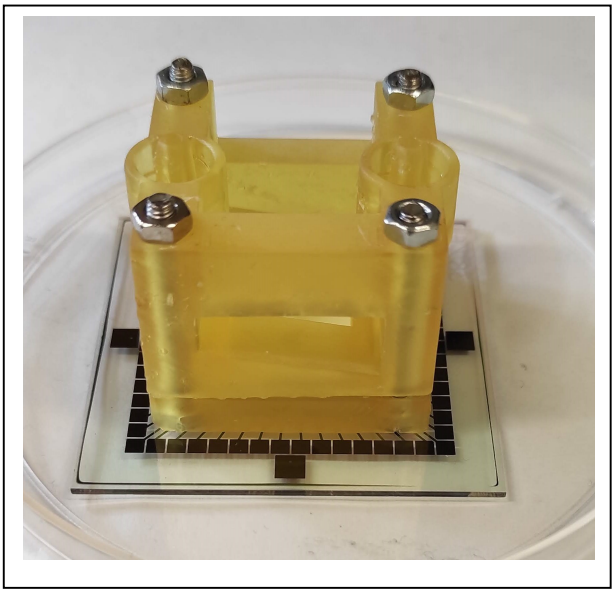

Fig.1. Integration of the culture platform and MEA.

5. Conclusion

A culture platform has been designed and fabricated. The culture platform consists of a transparent window to follow the evolution of the culture along with the experiments, and a 3D biocompatible structure with inlet and outlet ports to manage the medium. This part is assembled to a commercial microelectrodes array to electro-stimulate and acquire biological signals.

References

[1] Danisovic, L., et al. "Effect of long-term culture on the biological and morphological characteristics of human adipose tissue-derived stem cells." J Physiol Pharmacol 68.1 (2017): 149-158.
[2] Langhans, Sigrid A. "Three-dimensional in vitro cell culture models in drug discovery and drug repositioning." Frontiers in pharmacology 9 (2018): 6.
[3] https://www.multichannelsystems.com/ (accessed on 01/02/2021